University of Nottingham

UK | CHINA | MALAYSIA

Geometrical Modelling of Braided Textiles

By

Matthew Thompson

MEng (Hons)

Thesis submitted to the University of Nottingham for the Degree of Philosophy

April 2023

I. Abstract

Increasingly great pressures on design engineers to develop and manufacture lightweight and stiff structures can be seen across multiple industries. This has been achieved through the increase in the use of fibre reinforced composite materials. This is expected to continue with the added pressure of new and innovative solutions to such problems. Current trends have been towards using pre-impregnated woven or unidirectional fabrics with an increase in out-of-autoclave solutions being adopted. Alternative fabric geometries have been used in some small areas of the industry with examples of 3D woven and braided fabrics being used in some niche applications. Typically, the lack of use is due to the difficulty in the prediction and uncertainty surrounding the use of non-standard fabric architectures.

The main objective of this study is to address this problem with the development of novel tools for design engineers for the prediction of biaxial braided fabric geometries and resultant composite mechanical properties.

To address this objective a series of studies are presented, aiming to initially understand the fibre architecture and the effects of pre-preparation of the yarns on the resultant fabric. This study has shown the significant effect of winding twist on the geometry of the yarns post-braiding. The inclusion of 5 twists per metre of yarn can be seen to reduce the yarn width by 20% with a corresponding 27% increase in the thickness of the braided fabric. This can lead to significant effects during the infusion process with an increase in the number and severity of resin-rich regions within the composite panel. Additional imaging of the surface of the braid has shown increased damage to the surface of the yarns when twist is not applied, caused by an increase in friction between yarns during the braiding process.

In addition to yarn preparation techniques, mandrel complexity has been investigated with the inclusion of converging and diverging conical sections to the mandrel. Observations have shown a substantial impact on the braid geometry from the inclusion of a conical section. Fabric thickness and braid angle are both affected, showing instability in the braid during these regions. Diverging sections are shown to lead to the most significant impact on the braid geometry. Large levels of yarn

slippage on the mandrel are observed in these regions. This leads to difficulties in the prediction of properties and the repeatability of results. The detrimental effects on the braid architecture are seen to reduce for a reduction in the slope angle of the conical section, indicating gradual changes in mandrel geometry can lead to minor or negligible effects on the braid geometry.

Further to these studies, the scale of the braiding machine has been investigated with the use of a 48-carrier and 192-carrier braider. Investigations into yarn width and braid angle for the range of braiders on both circular and conical mandrels have shown minor differences between the braiders. This result is significant as it allows for results from braid geometry on reduced scale, and pre-production models to be interpolated for full-sized components, reducing the requirement for expensive manufacturing trails.

The research presented has been developed into a braiding tool for design engineers using TexGen modelling software. Through novel functions users are able to input process variables into TexGen, such as braider speeds and configurations, to simulate a 2D biaxial braided textile. Key parameters of the braid such as braid angle, coverage and yarn paths are predicted using established models. Custom refinement functions have been implemented to accurately model changes in the cross-section on the yarn along the undulations within the fabric. These fabrics have been compared to braided samples using a variety of inspection techniques such as optical microscopy as well as novel non-contact methods such as structured white light scanning and laser scanning.

Studies into the mechanical performance of sample fabrics have been investigated, with studies into mandrel geometry and yarn twist levels presented. A novel approach to modelling fabrics with a small radius of curvature has been implemented. CTextileBraidCurved has been developed to model unit cells which follow the curvature of the mandrel using a polar coordinate system, which is vital when modelling fabrics on small radius mandrels. Evaluation of elastic properties compared to equivalent flat unit cells show a difference of up to 10.5% in the axial modulus for radii of 10mm, reducing significantly for larger radii. Further studies present the effects of yarn twist level on the mechanical performance of the

composites with a good level of agreement between experimental and simulated results. Results show minor reductions in the mechanical performance in tensile modulus and strength with the inclusion of twist.

II. Acknowledgements

As always there are too many people to thank in making this thesis possible and getting me to the end of my PhD.

Firstly, I have to thank my supervisors, Prof. Nick Warrior and Dr Kishen Rengaraj. They have guided me through each step, offering input when needed and making me challenge myself throughout.

Thanks go to all the technical staff in the Composites lab at the University of Nottingham, Liam Sparke, Paul Johns and Ben Jennison, for enabling me to develop all the practical methodologies and collect the data within this study.

To everyone in the Composites Research Group at the University of Nottingham. There are too many to mention by name but everyone who helped me develop methods, sanity check my code, build up my knowledge and supported me. Particular thanks to Ant Evans, for keeping me sane when working on the robot, and Louise Brown for all the help in TexGen.

To all the fellow PhD students I have worked with over the last few years for the help and support through some of the strangest times of our lives. In particular Jamie Turnbull, Albert Gibbs, Joe Eastwood, Grace Owen, Guy Lawrence, Dan Wilson and George Spackman. I could not have finished this wouldn't your unwavering support and ability to listen to me drone on about braids. Special thanks to Beth Grimes who is the only other person who actively wants to talk about braids as much as me!

Special thanks to all my friends and family who have got me across the line, especially my parents for supporting me as I decide never to leave university and encouraging me throughout this.

Finally thank you to you for taking the time to read this thesis! More work than you can imagine has gone into this.

Contents

Table of Figures

Nomenclature

$\boldsymbol{\alpha}$	**Braid angle**
$\boldsymbol{R}$	Mandrel radius
$\boldsymbol{P_m}$	Mandrel perimeter
$\boldsymbol{N_h}$	Number of horn gears
$\boldsymbol{n_c}$	Number of carriers
$\boldsymbol{v}$	Mandrel take-up velocity
$\boldsymbol{\omega}$	Spool angular velocity around the spool plane
$\boldsymbol{\omega_h}$	Horn gear angular velocity
$\boldsymbol{CF}$	Coverage factor
$\boldsymbol{V_f}$	Volume fraction
$\boldsymbol{w_y}$	Yarn width
$\boldsymbol{t_y}$	Yarn thickness
$\boldsymbol{t_f}$	Fabric thickness
$\boldsymbol{x_g}$	Distance between parallel yarns
$\boldsymbol{\varepsilon^0 = \{\varepsilon_x^0, \varepsilon_y^0, \varepsilon_z^0, \gamma_{yz}^0, \gamma_{xz}^0, \gamma_{xy}^0\}}$	Macroscopic strains
$\boldsymbol{\sigma^0 = \{\sigma_x^0, \sigma_y^0, \sigma_z^0, \tau_{yz}^0, \tau_{xz}^0, \tau_{xy}^0\}}$	Macroscopic stresses
$\boldsymbol{F_x, F_y, F_z, F_{yz}, F_{xz}, F_{xy}}$	Generalised forces applied to unit cell to produce microscopic stresses in the same direction
$\boldsymbol{E}$	Young's Modulus
$\boldsymbol{G}$	Shear Modulus

1 Introduction

As the usage of composites grows within multiple industries, various manufacturing techniques will be required to expand to meet the new demand. The unique fibre structure of braided composites, with continuous fibres from start to end of the component and controllable fibre angles, have been used in small scale, niche products. For example, in 2017 Porsche released a newly developed braided carbon wheel as an option for the Porsche 911 S [1], advertised as a 20% weight saving whilst being 20% stronger. Additionally, Dowty Propellers developed a triaxial braid for use on an industrial scale in propeller blade design [2]. Further examples of braided composites include BMW 7-Series cant rails [3] and rail passenger hand rails [4].

Whilst there has been industrial usage of braiding technology, it is clear from a review of the literature in Chapter 2 that the technology has not been utilised to its full potential. Braiding has often been overlooked with designers opting for the use of known materials such as woven fabrics. This is in spite of braiding offering the designers greater freedom to develop efficient use of composite materials, enabling the tailoring of fibre angle and fabric architecture to the required loading cases within the component. Research and understanding of the formation of the braid from process parameters is lacking the depth required, in addition to the lack of prediction of properties of resultant fabric and composites.

This chapter describes the process of braiding and key terminology used with the sector and outlines the themes of work and aims presented within this thesis.

1.1 Braiding Process

Braiding has been used in the construction of ropes for thousands of years and was more recently industrialised in the textile industry during the industrial revolution. Since the 1980's, with A&P Technology leading the development [5], braiding has been used as a technique for the manufacture of composite components. The process of braiding involves several yarns of fibrous material being interlaced together to produce a fabric. This technique has been of interest due to the high fibre deposition rates with a near net share production method, enabling improved production rates and reduced costs.

1.1.1 Overbraiding

Overbraiding is the process of braiding around a shaped mandrel to produce a near net shaped component from the braider. This is common when braiding for structural parts as it allows for the braid angle and coverage to be directly controlled at various parts along the mandrel. Alternatively a pre-braided sleeve can be produced, a process in which no mandrel is used and a sleeve of braided material is produced and manipulated into shape after production. If a pre-braided sleeve is used, the properties are directly linked to the shape of the mandrel, often leading to problems with coverage and incorrect braid angles. During overbraiding there are a number of parameters used to explain the braiding process. *Figure 1-1* demonstrates these parameters.

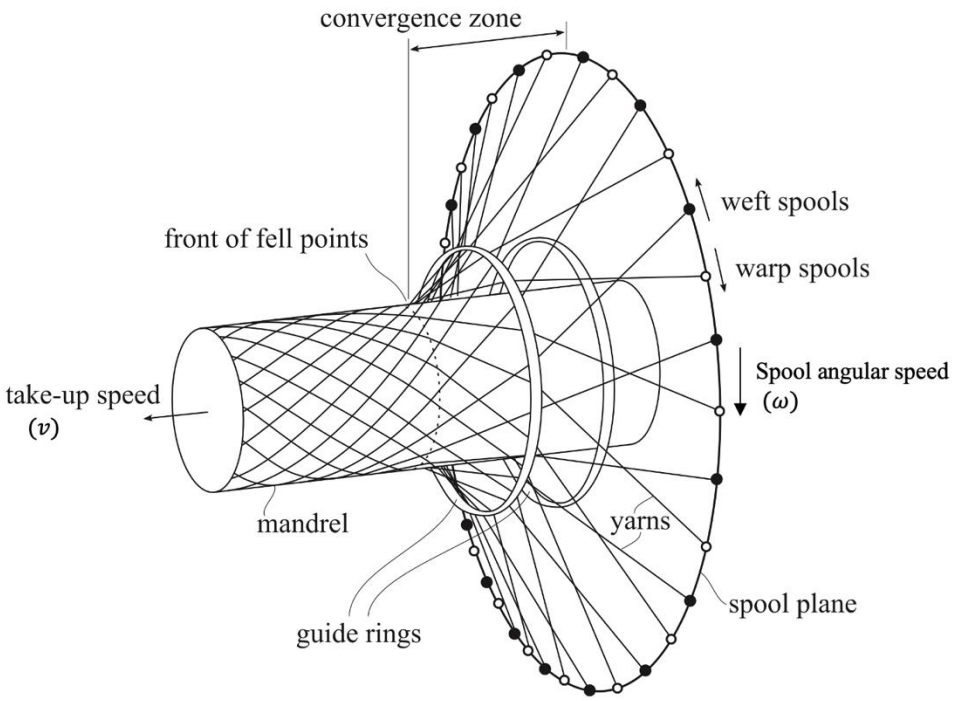

Figure 1-1. Principle features of overbraiding. Adapted from [6]

It is common within the analysis to ignore the motion of the yarns within the carrier and simplify the carriers to points on the spool plane.

- The take-up speed, *v*, is defined as the translational velocity of the mandrel running through the braider, often robotically controlled.

- The fell points are the points at which the yarns first touch the mandrel, this is not always the final deposition point of the yarns due to slippage between the yarns and mandrel, especially on complex mandrels.
- The convergence zone is defined as the distance between the fell point and the spool plane. Alternatively, if the guide ring position significantly alters the direction of the yarns, the convergence zone is redefined as the distance between the guide ring and the fell point. This length is directly linked to the angle of the yarns on the surface of the mandrel.
- The angular velocity of the spools, ω, is defined as the angular velocity around the braider perimeter.

Whilst braiding sleeves will allow for constant braiding until the carriers run out of materials, overbraiding is limited by the mandrel length. The maximum length of the mandrel is defined by two factors: (1) the size of the room and (2) the amount of material the bobbin is able to hold. Typically, the mandrel is moved using robotic control or a gantry. In 1991 Rosenbaum [7] described a machine where the braider would move with a fixed mandrel, typically requiring the room to be only 10 to 20% larger than the mandrel length, however this limits the complexity of the mandrel. Some modern arrangements include a blend of approaches, with a movable robot and a moveable braiding machine.

1.2 Braiding Machine

Although many different categories of braiding machines exist, two high level categories are flat and tubular braiders. As their names would suggest, they are used for producing flat and tubular structures respectively. Within this thesis only tubular braiders will be considered due to the research focusing on overbraiding, the act of braiding over a shaped mandrel for the production of near net shaped components.

The number of yarns within the process is dependent on the size of the braiding machine being used, typically ranging from 8 bobbins for tabletop braiders up to 800 bobbins for some of the largest braiders in the world [8].

To achieve the ‘over and under’ motion required for the fibres to interlace together, the bobbins follow a sinusoidal path around the braider with half of the bobbins

travelling in a clockwise (warp yarns) direction, and the other in an anti-clockwise direction (weft yarns) as shown in *Figure 1-2*.

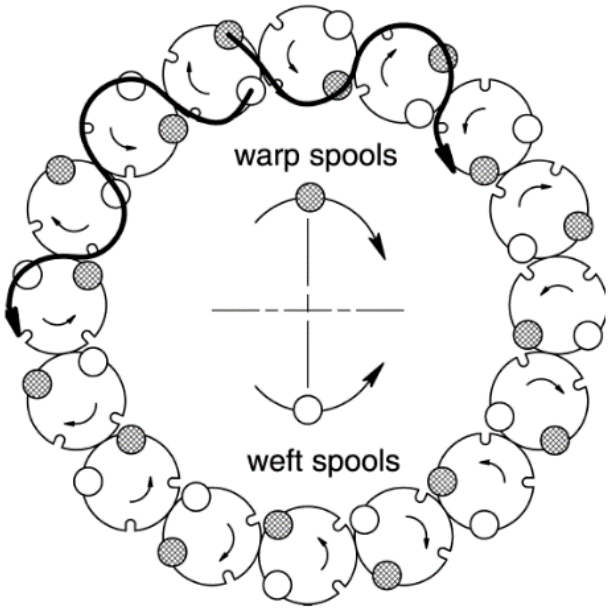

Figure 1-2. Bobbin movement around a tubular braider. Bold arrows show the carrier path. [9]

To enable this movement, a series of horn gears rotate in opposite directions with carriers travelling between, each holding a bobbin of fibres. The path of the carriers can be modified to change the pattern of the interlacement of the fibres.

1.2.1 Axial and Radial Braiders

Within the category of tubular braiders there are two main styles, axial and radial braiders. This refers to the direction of the bobbins with regards to the spool plane, defined as the plane in which the yarns leave the carriers. *Figure 1-3* shows an example of both an axial and radial braider. Axial braiders are defined by bobbins which are positioned facing outwards from the spool plane, whereas radial braiders have bobbins that face towards the centre of the spool plane. Axial braiders have traditionally been used for tubes and sock like fabrics, however recently axial braiders have been used for more complex geometries, a role typically fulfilled by radial braiders.

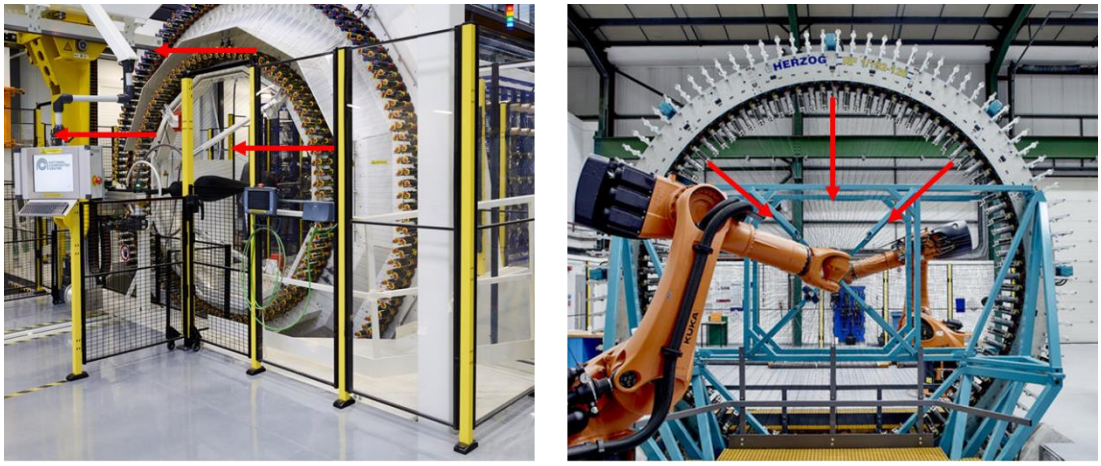

(a) (b)

Figure 1-3. Examples of (a) axial braider and (b) radial braider with the direction of bobbins in respect to the spool plane shown by red arrows.

A major benefit of radial braiders is the reduction of relative movement between the yarn outlet and the braiding point as the bobbins are facing towards the mandrel. Within axial braiders there is a greater change in distance between the bobbin and the mandrel due to the carriers travelling in a sinusoid path on the spool plane. This has led to the need for a compensation mechanism to allow for this change in length, whilst maintaining tension within the yarns. Additionally, within radial braiders, the yarn consumption usually exceeds the change in length, meaning there is no pullback of the yarn into the bobbin. This eliminates repetitive crinkling and straightening of the yarns [10] and reduces the likelihood of damage to the yarn. In axial braiders the carrier must be able to keep the tension within the fibres over the amplitude of the bobbin path, typically around 120 mm. On average each segment of the yarn is pulled back and forth over the rollers and guiding elements 30 times before it leaves the carrier [10].

Radial braiders are typically required to be larger than equivalent axial braiders. This is due to the limitations in the radius of the track to ensure bobbins do not touch, whilst still being able to hold a significant amount of material.

The following sections provide an overview of the critical parts of the braiding machine.

1.2.2 Horn Gears

Horn gears are used to transfer carriers around the braider and pass on the carrier to the next horn gear rotating in an opposite direction. Typically, each horn gear will have 4 to 6 slots capable of carrying carriers, as seen in *Figure 1-4*. The pattern in which these carriers are placed on the horn gears will determine the braid pattern produced. In theory, the radius of the horn gear should be equal to the curvature of the tracks in which the carriers travel, however this is often larger to improve the stability of the carriers. Combined with deeper slots in the horn gear, there is a larger contact surface to support the carrier and ensure the driving force is applied in the same direction as the velocity of the carrier, enabling smooth movement around the braiders [11].

It is common for carriers to have two small plates, seen in *Figure 1-4*, to enable stability as they move around the braider, reducing wear and noise of the machine. The carriers are passed from horn gear to horn gear, using a small channel to guide the carriers in the correct direction. The base of the carrier has a small foot inserted into this channel to guide the carrier to the next horn gear.

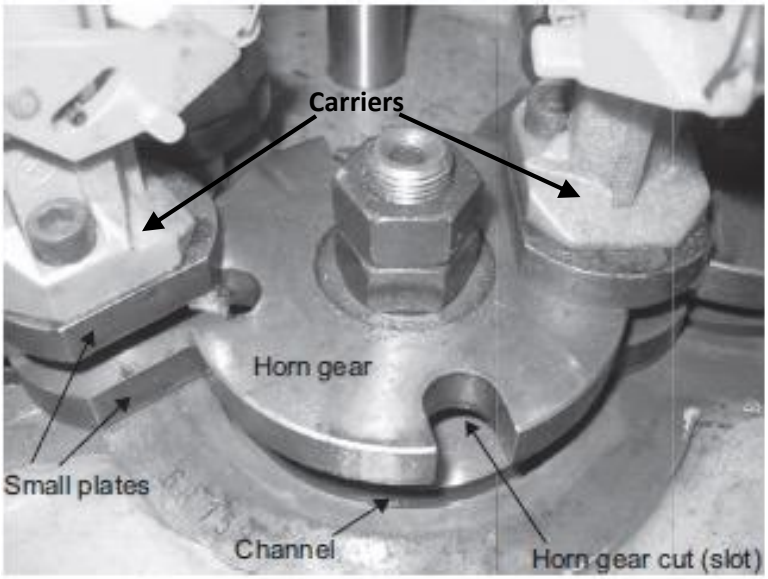

Figure 1-4. Key elements of the horn gear system for carrier motion. Small plates keep the carrier stable on the horn gear with the channel guiding the carrier in the desired sinusoidal path. Adapted from [11]

1.2.3 Carriers

The carriers are used to move the bobbins of yarns in a sinusoidal path around the braider. W.A Douglas summarises the main functions of the carrier [12] as:

1. Hold a bobbin with yarn material (as much as possible).
2. Compensate for the differences in length during the braiding process and maintain yarn tension.
3. Pay out the correct quantity of yarn as required.
4. In the event of a yarn running out or becoming broken, the carrier should produce a signal to the operator.

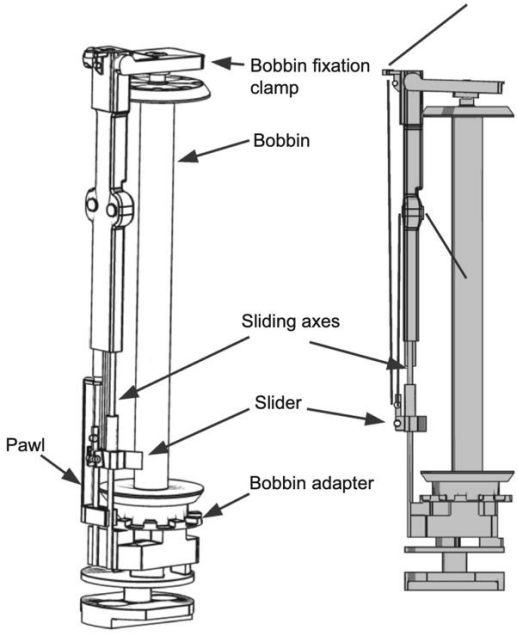

Figure 1-5: Slider-balanced carrier system used in this study. [13]

For function 2, maintaining tension, a detailed comparison of the systems for maintaining tension is given by Kyosev [13]. It is typical within the composites industry to use a slider-balanced carrier, as seen in Figure 1-5, consisting of a spring-loaded system with a lever to ensure the yarn tension is maintained and the carrier is able to compensate for the change in length. The main components of such carriers are highlighted in *Figure 1-6*. The yarn is unwound from the spool, through pulley 1, a static pulley, into pulley 2, a rotating pulley, and out of the top of the carrier. The black lever is used to constrain the rotation of the spool until more yarn is required, at which point pulley 2 rises upwards, with tension held from spring 1. When enough

yarn is required as to require rotation of the bobbin, pulley 2 will reach the level of pulley 1 and will rise together. This movement releases the latch constraining the bobbin and allowing it to rotate. This rotation will reduce the tension within the yarn, causing both pulleys to fall, locking the rotation of the bobbin. This process will happen cyclically over the braiding process.

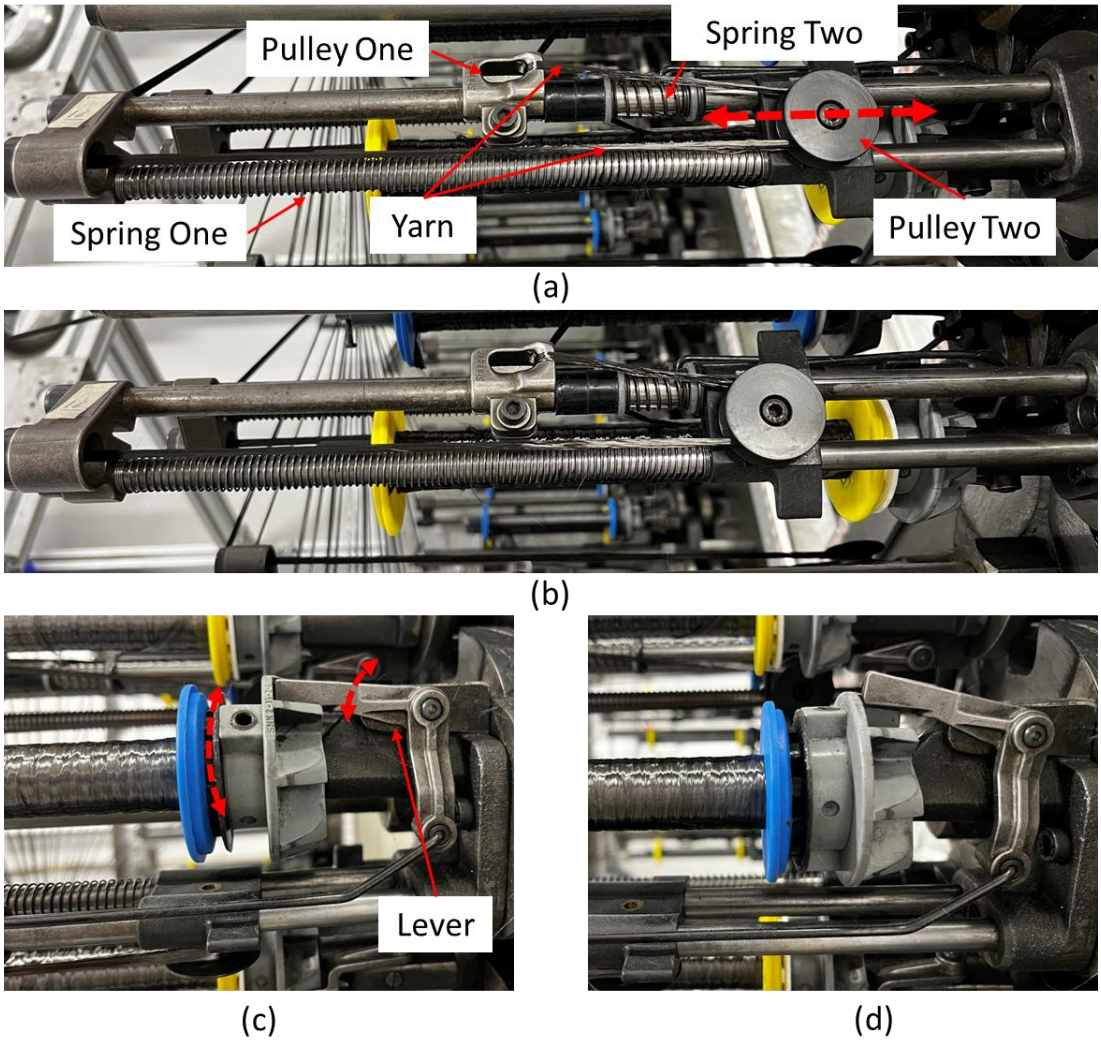

Figure 1-6. Movement and Tension Mechanisms of a carrier. Dashed red arrows show movement direction. (a) tension increased in yarn raising Pulley Two, (b) Pulley Two raised to maximum height, (c) Pulley Two is attached to Lever and (d) Lever raised to allow for movement.

The dynamic behaviour of the system was investigated by Ma et al. [14] showing how the tension of the yarn varies throughout the take-up of the yarn at a constant speed, with the mathematical model showing good agreement with the experimental data. The study showed a fluctuation in the tension of the fibre during

the braiding process, as seen in *Figure 1-7* (b). The sudden drops and rise in the tension of the yarns causes damage within the yarns, ideally tension would be kept constant throughout the braiding process. Additionally, it is noted that this style of carrier tensioning system relies on a large level of tension within the yarns, making this unsuitable for fine or delicate materials, where a slide-balanced carriers are more appropriate.

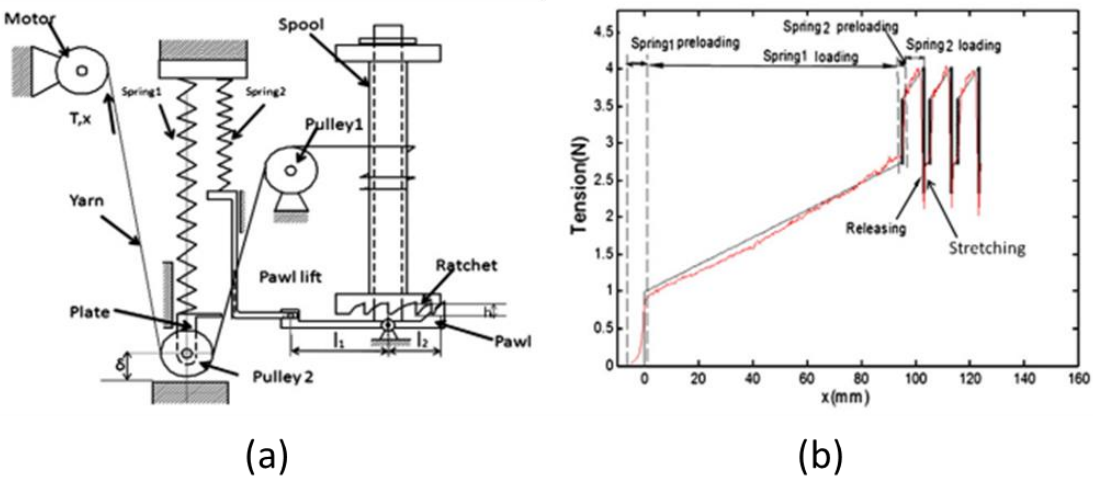

Figure 1-7. (a) schematic model of the carrier system with yarn and (b) comparison of simulation (black) and experimental (red) of tension within the yarn. [14]

1.2.4 Yarn Winding

Bobbins within the braiding machine must be loaded with the required yarns through a process of yarn winding. Yarns are taken from larger spools and re-wound onto the bobbins, a process is typically carried out using a winding machine, the likes of which are shown in *Figure 1-8.* Kyosev gives an detailed description of the winding process and the range of technology used in [15]. Within this study parallel winding of the bobbins has been used. In this the yarns are wound directly next to each other along the length of the bobbin, before laying on top of the layer below. The alternative method, cross winding, is typically used when winding yarns with little to no sizing within the fibres. The more fragile nature of these yarns requires the need for cross-winding during the braiding process.

Key to ensuring a successful wind of the bobbins is to maintain tension within the yarn during the process. This ensures yarns lie flat on the bobbin and greatly increases the success of unwinding of the bobbin during braiding as the yarns cannot

tangle together. This may be done through a range of processes including tension plates, guide rings and motor controls. Additionally other factors such as twist within the yarn and yarn placement on the bobbin must be controlled during this process.

The maintenance and preparation of the yarns within this rewinding process is vital to the success of the resultant braid using the bobbins. Delicate yarns must be able to be unwound without snagging or breaking during braiding.

Figure 1-8: Herzog bobbin winding machine to wind yarns for braiding.[16]

1.2.5 Guide Ring

The guide ring is a small, smooth ring placed parallel to the spool plane to help guide the fibres onto the mandrel. The guide ring is usually positioned close to the fell point, defined as the point at which the fibre first touches the mandrel, aiding in guiding the yarns onto the surface of the mandrel. The take-up speed and braider angular speed effect the natural fell point, with the guide ring being able to adjust position relative to the spool plane. Research shows that the guide ring can be used to encourage a consistent braid angle on complex mandrels. For prismatic mandrels with sharp edges, a smaller braid angle is often measured on the edges compared to that of the centre. This results in an S shaped yarn as seen in *Figure 1-9*. Research by SLG Carbon [17] shows how the guide ring shape can influence the braid angles on prismatic shaped mandrels. Results showed a minor reduction in the deviance of the

braid angle around the cross-section of a rectangular mandrel, however no conclusive relationship between guide ring shape and braid angle was given.

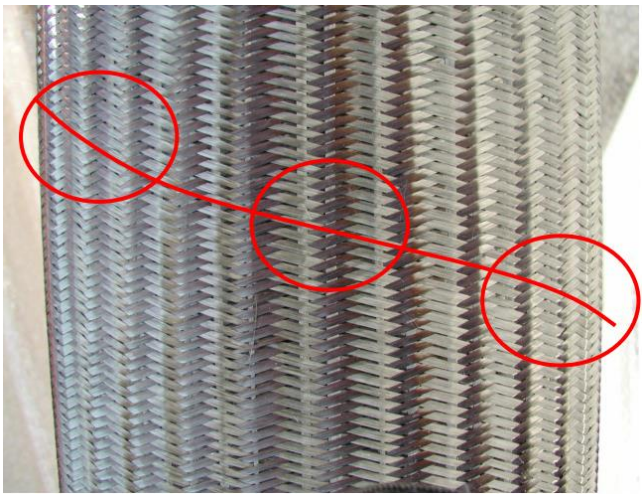

Figure 1-9. Braid formed on squared cross-section mandrel. S-shaped yarn path is shown in red. [17]

To gain a close, tight braid on the mandrel the guide ring should be as close to the mandrel diameter as possible, however this leads to problems when braiding complex mandrels where the diameter of the mandrel can change dramatically along the length of the mandrel. To address this, A&P Technology Inc has been issued with a patent [18] for a braiding ring with an adjustable diameter as shown in *Figure 1-10*. It is noted this is yet to be seen on a commercially available braiding machine.

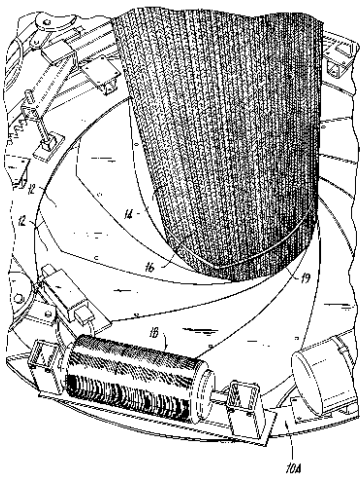

Figure 1-10. Adjustable inside diameter guide ring from A&P Technology Inc Patent. [18]

In more recent studies the effects of vibration on the guide ring have been investigated as discussed by Kyosev [19]. In this study, different vibrational frequencies and amplitudes were investigated when braiding with carbon fibres and glass fibres. This showed an increase in vibrational frequency leads to an increase in yarn roving. Work echoed by Reiner et al. [20] showed a peak coverage at 13.75 Hz. Both studies were completed using radial braiding machines and it is yet to be seen if the same effect is found on axial braiding machines. However, deviances in the results for axial braiders may occur due to reduced contact with the guide ring.

1.2.6 Mandrel

Typical materials and considerations necessary when deciding on a mandrel are outlined in Braided Reinforcements for Composites [21]. Ideally the core material would be lightweight, able to withstand the braiding forces and suitable for the temperatures and pressures experienced during the curing and de-moulding process. In some applications, the mandrel will remain within the composite component, with the mandrel often made of a closed cell foam to ensure the foam does not absorb the resin during the infusion process.

In cases where the mandrel needs to be removed post curing the removal method will depend on the material used. Unless a large draft angle is used, the mandrel will often be melted or made from compacted sand or salt which can be dissolved post curing. Recent advances have enabled smart materials to be used, which will retain a complex geometry until heated and softened. Upon cooling the material will return to its complex shape, allowing for another braiding process. Additionally, additive manufacturing techniques, such as Fused Deposition Modelling, have been used for the production of complex mandrel shapes in an efficient and cost-effective method. Mandrels can be printed in sections and bonded together. The closed surface allows for the infusion process without absorption into the surface. Structural integrity and low melting temperatures with PLA (typically used in Fused Deposition Modelling) must be considered before usage.

1.3 Themes of Work

As discussed, a greater demand for composites is predicted as current use cases increase and new products and components, requiring the need for composites

within their manufacturing, are developed. Braiding technology allows for highly automated, near net shaped production on complex geometries to contribute to lowering manufacturing time and cost, whilst allowing for tailor made solutions with fibres highly aligned with the loading path to maximise the efficiency of the material.

Currently, there is a further need for the understanding of yarns during the braiding process to determine how process parameters affect the final preform. Much of the knowledge within the braiding industry is held within a small set of manufacturers and technical staff. Additionally, design engineers require tools to ease the prediction of the properties at the early stages of design. This allows for the evaluation and comparative analysis of braided fabrics to known techniques such as forming and weaving.

1.3.1 Aims and Objectives

As discussed there is a need for engineers to be able to predict the geometry and properties of a braided fabric, comparable to methodologies used for woven fabrics during the design stage. Therefore the aim of this these is to develop a methodology to accurately predict the yarn geometry in biaxial braided fabrics from process parameters and develop a framework for the prediction of mechanical properties of the resultant fabrics. To address these aims the objectives of this thesis are to:

- Develop a link between the geometry of a braided preform and the preparation of the fibres before winding on simple and complex mandrel geometries and investigate the effect of alternative fibre preparation on the properties of the composites.
- Develop an understanding of the effect of machine size on the braided fabric.
- Develop a novel geometrical modelling technique for biaxial braided fabrics.
- Develop a novel understanding of the relationships between the curvature of the composite and the elastic mechanical properties.

Within this research, braided fabrics have been produced using two different scale braiders, a 48-carrier axial braider and a 192-carrier axial braider.

This work has been conducted in collaboration between the University of Nottingham (UoN) and the National Composite Centre (NCC) in the UK. The findings

presented in this thesis are part of a larger braiding investigation within the EPSRC Future Composites Manufacturing Hub.

2 Literature Review

This chapter consists of a comprehensive literature review within the area of overbraiding, focusing on a critical review of the methodologies for predicting architectural properties of the braid such as the braid angle and coverage factor using a wide range of technologies and models at a range of scales. An evaluation of the literature is presented in relation to the prediction of mechanical properties, reviewing both experimental and simulation-based results. Conclusions of the latest work and limitations that this research aims to address in subsequent chapters are also examined.

2.1 Braid Architecture

The versatility of the braider enables a wide range of braid architecture to be possible. This section explains the mechanisms for manufacturing various braid architectures.

2.1.1 Braid Pattern

Three common braid architectures used in composite manufacture are diamond, regular and Hercules shown in *Figure 2-1*. However, with adjustments to the carrier locations it is possible to develop more complex patterns. There are a number of naming conventions for braids [22], the modern standard is the following:

X:X-Y

This is read as “over X groups, under X groups as a group of Y yarns”. For the braids shown in *Figure 2-1* this would be given as (a) 1:1-1, (b) 2:2-2 and (c) 3:3-3. For a more complex braid pattern such as that shown in *Figure 2-1 (d)*, the notation would be 2:2-1 as each yarn passes over and under 2 yarns, in groups of 1 yarn.

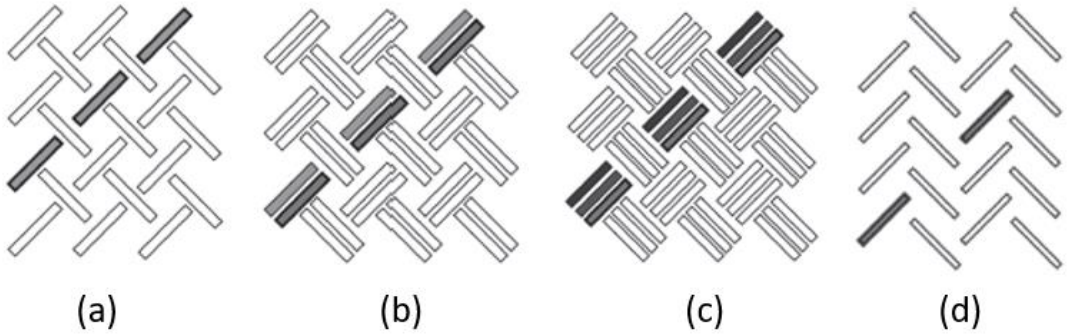

Figure 2-1. Typical braiding patterns (a) diamond, (b) regular, (c) hercules and (d) 2:2-1.

2.1.1.1 Architectural Styles

In addition to the braid pattern, the architectural style can be altered within a braided fabric to tailor the properties to the required loading. This section explains the main architectural styles and the benefits and drawbacks of their properties.

The one division in braid architectures is between 2D and 3D architectures. 2D braids are defined as braids where each layer of the braid is independent of the layer below, there are no through-thickness yarns attaching the layers together. Alternatively, 3D braids contain yarns that run between the layers of the braids. To achieve this, a dedicated 3D braiding machine is used. In these machines, the bobbins run between multiple braiding rings. This can either be in a circular configuration, as shown in *Figure 2-2*, or as a square platform. The connections between the horn gears are a series of switches that can be changed to direct the carrier in the desired direction. A simplified model of this is shown in *Figure 2-3*. These braiders are especially efficient at producing parts with a specific shape such as a T, I or H section. This is due to the flexibility of the bobbin path within the square grid. Sontag et al. [23] presents a review of recent advances in 3D braiding technology with particular emphasis on bifurcation of the 3D braided architecture.

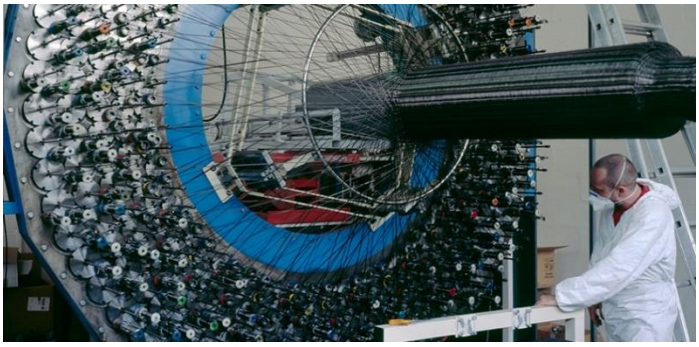

Figure 2-2. An example of a 3D braiding machine, the bobbins are able to move between multiple rings.

Némoz et al. [24] investigated the mechanical property differences between 2D and 3D braided performs. This showed that under static compression tests, both braid architectures exhibited similar elastic behaviour but with a higher plateau for 3D braids and greater strength than 2D braids. Upon failure, it is evident that delamination of the 2D tube resulted in failure, which was less prevalent within the 3D tube. Additional fatigue loading was completed, which showed significant improvements for 3D braids, completing 11,200 cycles until rupture. This is reduced to 1500 cycles for 2D braided samples. This reduction is expected due to the decreased ability of crack propagation between layers of the composite. Although initially 3D braiding seems to be superior compared to that of 2D braids, there is limited industrial usage due to the increased cost of a 3D braid. The complexity of the machine increases the capital cost, and the slower deposition rate increases the manufacturing cost.

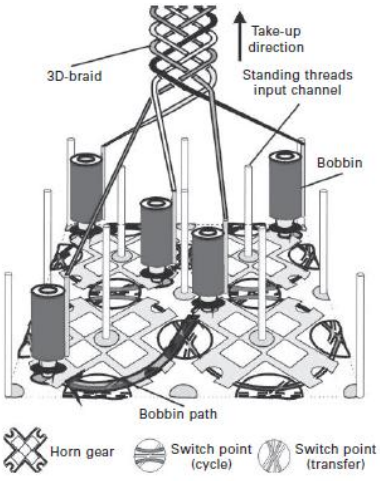

Figure 2-3: A simplified 3D braider with switches to control the directions of the bobbins.

Additionally, limited simulations of 3D braids are presented within the literature, limiting industrial confidence. Grave et al. [25] developed two methods for the simulation of 3D overbraiding; a finite element model and an algorithmic model. Although the algorithmic model is significantly less computationally expensive, it is unable to adapt to changes in mandrel geometry. Supplementary work by Guader et al. [26] presented an analytical model for 2D and 3D braiding. Key parameters such as braid front during the transitional period, slippage on the mandrel and relaxation of the yarns can be described using this model. However further validation is required for complex mandrel cases and is limited by requiring a linear yarn trajectory within the convergence zone.

Within the categories of 2D and 3D braids, there are two further architectural styles; biaxial and triaxial braids. Biaxial braids only have +/- bias yarns whereas triaxial have additional axial yarns present, interlaced into the structure of the braid, as seen in *Figure 2-4*. Birkefeld et al. [27] investigates the mechanical and fibre architecture differences between the two layups. The results obtained showed an increase of more than 400% in longitudinal modulus (E_x) for the triaxial braid compared to the biaxial layup, due to the increased fibre concentration in the direction of the loading. Comparable results were obtained by Wolfahrt et al. [28].

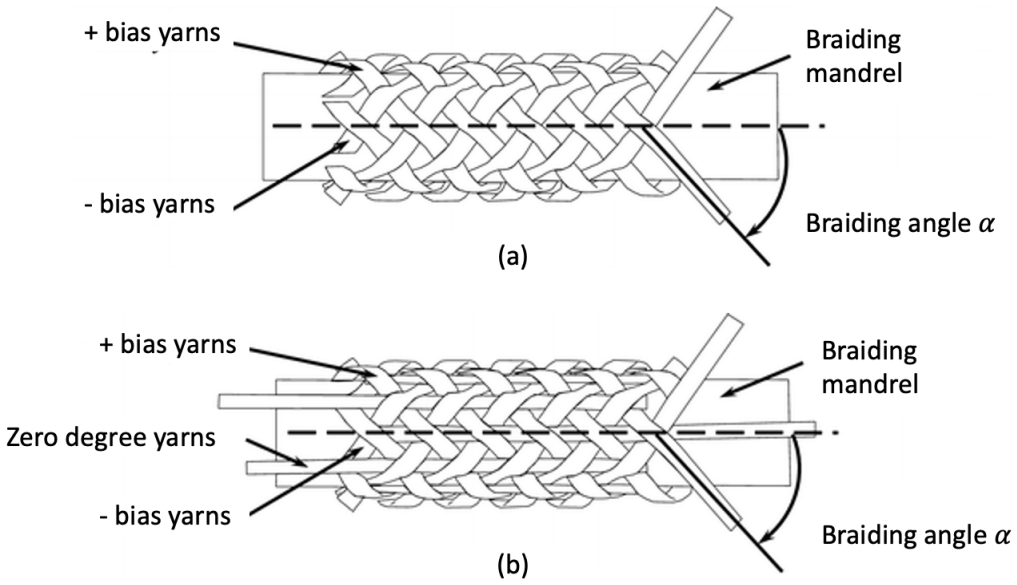

Figure 2-4: (a) Fibre layup for biaxial braid, (b) Fibre layup for triaxial braid. Adapted from [27]

Due to the geometry of the structure within triaxial braids, there are higher levels of fibre crimp in the bias yarns, which can reduce the in-plane shear properties of the material and reduce volume fraction. Furthermore, there is a limit to the number of axial fibres that can be interlaced into the braid, this is limited by the number of horn gears on the machine. Axial fibres can alternatively be placed along the mandrel either before or after the braiding process [10]. This method allows for a greater number to be added but does not gain the same performance as the fibres are not laced together. Further problems arise around fibre slip when this technique is used, reducing the effectiveness even further.

Large levels of yarn undulation are present within traditional braided fabrics which impacts the in-plane stiffness of the composite. Recent developments in braid architectures have led to non-crimp or unidirectional braided fabrics [29]. These braids are produced through an imbalance in the number of weft and warp yarns. Two approaches exist for the production of such fabrics. The first uses all structural yarns (i.e carbon or glass) to produce a nearly non-crimp fabric. This produces a fabric with a large number of yarns in one direction, subsequent layers can be reversed to produce a balanced composite structure if required with minimal undulation to the fibres. As shown in *Figure 2-5* there is a small amount of undulation of the fibres and the weft yarns cross over the warp yarns. Alternatively as developed by Advani et al. [30], the warp yarns can be made of a dissolvable material such as a Grilon co-polymeric auxiliary. Using this method, the warp yarns are dissolved during the infusion process and a nearly idealised non-crimp fabric is produced.

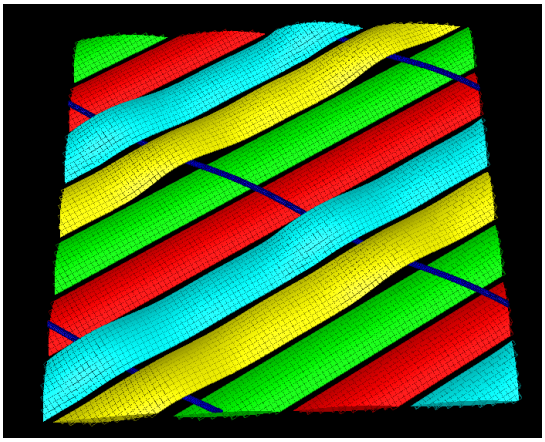

Figure 2-5: Example of a nearly non-crimp fabric - 24 weft yarns and 6 warp yarns.

Metzner et al. [31] studied the effects of non-crimp braids compared to conventional braids and unidirectional tapes. In this example, there are 72 CF yarns and 36 support yarns (72 CF yarns in both directions for the conventional braids).

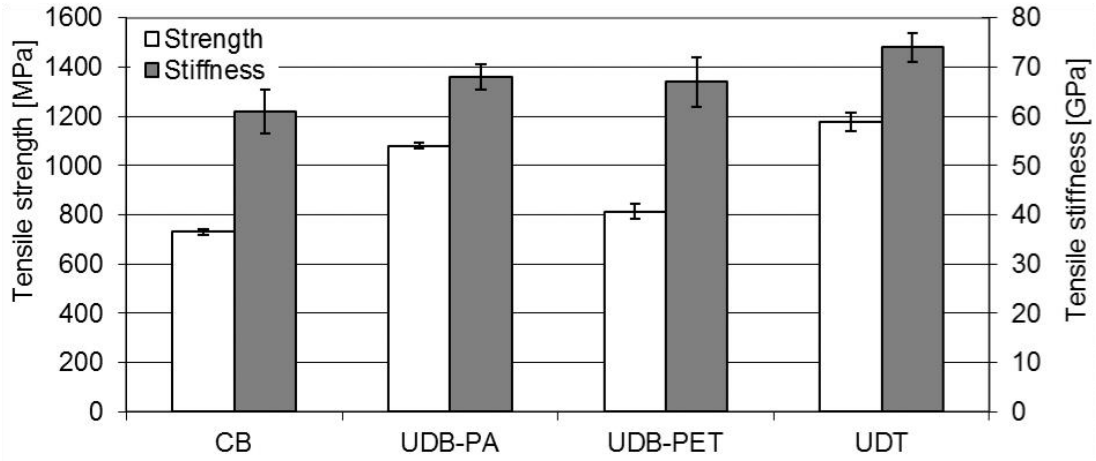

Figure 2-6: Tensile strength and stiffness data for CB (conventional braids), UDB-PA (Unidirectional braid with PA support yarn), UDB-PET(Unidirectional braid with PET support yarn) and UDT(Unidirectional tape). [31]

Figure 2-6 shows the results of tensile testing of a range of braids. This work illustrates an increase in both tensile strength and stiffness for the unidirectional braids compared to the conventional braid, but a reduction compared to the unidirectional tape (UDT). These differences can be explained through the inspection of the crimp presented within each fabric. As seen in *Figure 2-7* there is a large reduction in the fibre undulation when comparing the unidirectional braids (UDB-PA/UDB-PET) to the conventional braids, with further reduction in the UDT.

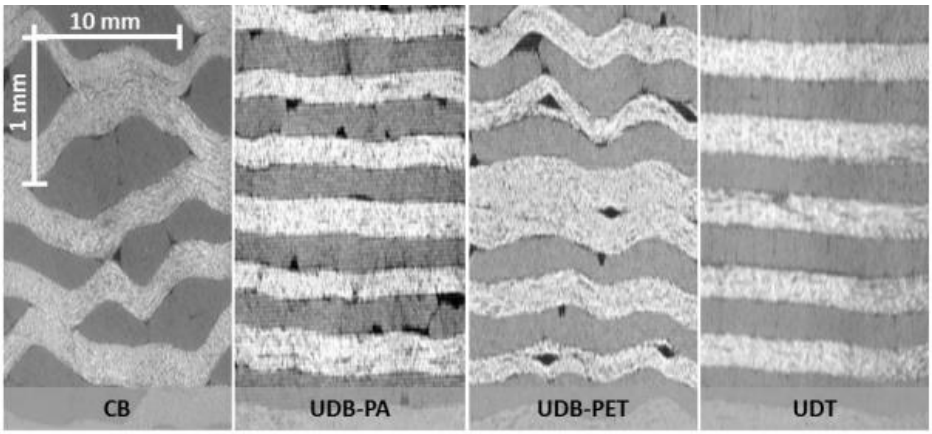

Figure 2-7. Representative micrographs of CFRP laminate of CB, UDB-PA, UDB-PET and UDT [31]

2.1.2 Braid Angle

The braid angle is one of the most influential features of the structure, affecting the mechanical and permeability properties of the structure. The braid angle (α) is defined as the angle between the bias yarns and the central axis. Birkefield et al. [27] states that in practice it is only possible to braid with angles from 20 to 80° with the braid angle affected by the machine configuration. Du & Popper [32] derived Eq. (2.1) to refine the braid angle using the Perimeter length of the mandrel, P_m, the average angular velocity of the carriers, ω, and the take-up velocity of the mandrel, v.

$$\alpha = tan^{-1}\left(\frac{P_m \omega}{2\pi v}\right) \tag{2.1}$$

This was redefined by Potluri et al. [33] to account for more controllable parameters of the machine, given in Eq. (2.2). ω_h is defined as the angular speed of the horn gear, usually a controllable speed on braiding machines, R is the mandrel radius and N_h is the number of horn gears on the braider.

$$\alpha = tan^{-1}\left(\frac{2\omega_h R}{N_h v}\right) \tag{2.2}$$

The ISO 10122 standard – Section 7.2.5.1 [34] outlines how to measure the braid angle of a tubular braided sleeve. This requires the measurement of the length of the braided sleeve (L_t) as it sits on the mandrel. A single yarn is extracted from the braided form and its length is measured (L_v). The braided angle can then be calculated from Eq. (2.3). This method relies on the braided yarn following a perfect helical path and does not account for local variations in the braid angle.

$$\cos(\alpha) = \frac{L_t}{L_v} \tag{2.3}$$

A more robust method often used is through digital image analysis. The braid angle is determined using a high quality image of the braided surface and software such as ImageJ [35], or a custom programme written using the Image Processing Toolbox in MATLAB [36, 37]. Pipan et al. [38] developed an adaptive algorithm to control the quality of a braid. This was implemented in MATLAB to detect any imperfections such as missing yarns, hooped yarns or knotting in the structure. The concept works through analysing an IR image of the braid architecture and comparing to the

expected intensity in specified regions of the image. Hunt & Carey [39] proposed a machine vision system for measuring the braid angle of a tubular braided structure. This method requires using 2D-DFT (2-Dimensional Discrete Fourier Transform) to process the image. The study showed that to gain an accurate representation of the braid angle, only the middle 20% of the image should be analysed due to distortion of the braid angle in relation to the camera lens. When compared to experimental and mathematical models the developed process shows good agreement. Ravenhorst used photogrammetry to measure the braid architecture of a braided mandrel [6]. This involves taking multiple images of the braided surface to build a 3D model. It is estimated by Ravenhorst that this has an accuracy in the order of ±2°, however, it has been shown that such methods can take 15-30 minutes to produce a rendered model. Monnot et al. [37] uses an automated process of photographing the surface of the braid at various inspection points. This system uses a simple system of edge detection and Hough transform to detect the braid angle. The reliability of this method depends on the quality of the images captured. Zambal et al. [40] explains the difficulty in using machine vision to capture carbon fibre. The material has very difficult optical properties due to their high absorption of light with distinct reflection angles. This issue is overcome using multiple distributed light sources. This causes yarns in different directions to be illuminated differently, giving the impression of even lighting.

2.1.3 Coverage Factor

In addition to braid angle, coverage factor is an important parameter for defining the properties of braided structures. Ravenhorst [41] defines this as the fraction of the substrate area covered by bias yarns. A generalised expression for cover factor is presented in Eq. (2.4). For mono material axisymmetric braids where $w_{y,X,1} = w_{y,O,1} = w_{y,X,2} = w_{y,O,2} = w_y$, $p_x = p_O = p$ and $a_x = a_O$ this can be simplified to Eq. (2.5). (Terms defined in *Figure 2-8*)

$$CF = 1 - \frac{(2p_x - w_{y,X,1} - w_{y,X,2})(2p_o - w_{y,o,1} - w_{y,0,2})}{\sin(\alpha_x + \alpha_o)} \tag{2.4}$$

$$CF = 1 - \left(1 - \frac{w_y N_h}{4\pi R cos(\alpha)}\right)^2 \tag{2.5}$$

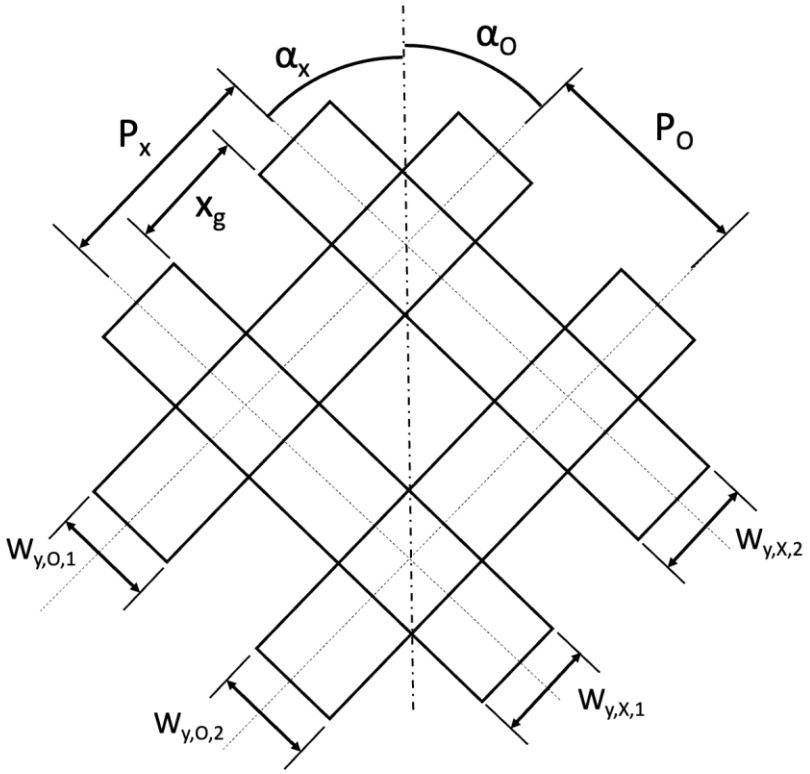

Figure 2-8. Coverage factor definition for biaxial braided fabrics.

Eq. (2.5) is only valid whilst the braid has not jammed, this happens when the coverage exceeds 100% causing bunching of the fibres and overlapping to occur. This is usually undesirable within the composites industry due to limitations in post-processing and excess damage or crimp in the fibres. Du and Popper [32] defined a maximum angle when braiding on a desired mandrel before the braid would become jammed, as expressed in Eq. (2.6).

$$\cos\left(\alpha_{jammed}\right) = \frac{W_y \sin(\gamma)}{2R_m \sin\left(\frac{2\pi \sin(\gamma)}{N_c}\right)} \tag{2.6}$$

W_y is defined as the yarn width, N_c is the number of yarn carriers. R_m is the mandrel radius and γ is the half cone angle between the braid guide ring and the deposition plane.

2.1.4 Factors influencing braid architecture

There are a number of parameters that can affect the final braid architecture, this section reviews the current research in these areas.

It is shown in Eq. (2.2) and (2.5) the radius of the mandrel effects both the braid angle and the coverage factor. For simple, constant cross-section mandrels, it is expected

for the braid to stabilise and produce a constant fabric. In reality, this is difficult to achieve for braided components due to the need for change in the cross-section of the component. Du et al. [32] investigated the change in cross-section for two conical shaped mandrels. This showed a more consistent braid architecture for the shallower sloped mandrel, giving the braid the ability to adapt to the change in cross-section without slipping on the mandrel. Additionally, the direction of the braiding was investigated, showing a more stable braid when braiding on a converging conical section. This is explained by an increase in yarns slipping on the mandrel for the diverging conical section, creating an unstable braid. The complexity seen in the architecture on complex mandrel shapes often requires a complex model to predict the braid architectures [9, 41, 42]

2.1.5 Yarn Preparation

Material preparation prior to braiding is seen to influence the resultant architecture. Large levels of damage are expected to occur during the winding process due to the tight angles and changes of direction the yarns are subjected to. For natural fibres it is required for high levels of twist to be introduced during this stage to help stabilise the yarn and prevent breakages. Torun et al. [43] discusses the changes in yarn geometry due to twisting commingled yarns, showing a significant reduction in yarn diameter with an increase in twist levels, effecting coverage factor. Cheung et al. [44] used twisted fibres within 2D braiding. Tubular braided composite tubes were produced with twisted fibres, untwisted fibres and half and half. Mechanical properties of the tubes were tested with an increase in modulus and about a 40% increase in tensile load capacity for twisted samples. A significant difference in architecture is seen for twisted samples with increased gap regions in the yarns due to a decrease in yarn width.

Currently there is limited conclusive research highlighting the effect of yarn preparation on the yarn geometry and the resultant effect on coverage factor and braid angle. These two factors have been previously identified as key parameters in the prediction of braided properties.

2.2 Review of Modelling Braided Fabrics Architecture

The strength of the composite is mainly determined by the fibre used, size of the yarns, style of braid, braid angle and coverage factor. This was first investigated by Brunnschweiler [45] in 1954 with a study investigating the tensile properties of cotton braids at various braid angles. This section explains the different approaches to modelling the architecture of braided fabric that have been developed, with their strengths and weaknesses outlined. The three approaches that are taken by the literature are:

- Analytical
- Kinematic
- Finite Element

Analytical uses a series of equations, often in a spreadsheet to calculate the braid. This gives a very fast result, typically in the range of milliseconds. However, due to relying on a number of assumptions, this result can often have large errors. A Finite Element approach is the most complex approach and takes the longest time to run, depending on the model size it can take days or weeks to run. These models allow for yarn tension and bending, yarn interaction, friction, guide ring friction, gravity, fibre slippage on the mandrel and bridging on concave mandrels [41]. However, it is not usual for these simulations to be able to predict cross-sectional changes as the fibres are braided as well as the effects of a broken fibre and fibre damage throughout the process. The kinematic approach is a compromise between the two. It neglects yarn to yarn interaction, yarn deformation and slippage. Instead, it assumes the fibres move in straight lines between the bobbins and mandrel but is able to reduce the calculation time, which makes it useful in the design stage.

2.2.1 Scales

There are three main scales in which the braid can be investigated with each used for a different analysis of the braid and characterisation;

- Micro
- Meso
- Macro

The micro scale corresponds to the impregnated yarns. The main analytical models include rule of mixtures, Chamis formulae [46], Hill-Hashin-Christensen-Lo formula [47] with further development in finite element (FE) modelling [48]. FE modelling can be used to predict strength and failure within composite yarns [49-51].

The meso scale corresponds to the representative unit cell (RUC), the smallest single cell that can represent the braid architecture, as shown in Figure 2-9. Numerous studies have used unit cell analysis to determine the mechanical properties of a braid [27, 52-54] using programmes such as TexGen and Abaqus. Meso-scale modelling is typically used for strength and failure prediction of braided properties [55-57], showing the ability to predict failure locations and degradation of the composite post failure. It is important that the unit cell is accurately formed and is different for each type of braid. The unit cell is often presumed to be the same for a whole structure, but it may be necessary to represent a structure with multiple unit cells if there are large changes in fibre angle or geometry of the mandrel.

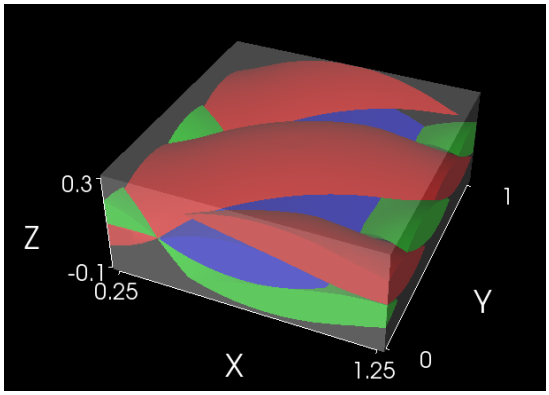

Figure 2-9. Meso-scale triaxial braid unit cell.

The macro scale corresponds to the whole structure of the braided part. This is often conducted during the late design stage to ensure the fibre architecture is capable of withstanding the loading. Zhang et al. [48] conducted a multi-scale study on the design of a helicopter arm. For the micro-scale study, the impregnation of the fibres with the matrix is analysed to predict the elastic constants and strength values of the fibre bundles. For a meso-scale analysis, the RUC is developed for a 3D braid with the interaction between the fibres and the matrix being modelled. From this Abaqus is used, along with failure mechanisms related to yarn breaking, matrix cracking and interface debonding, to predict the mechanical behaviour of 3D braided composites.

The main purpose of the macro scale analysis is to investigate the influences of braid angle on the full-field mechanical behaviours and thus determine the braiding parameters.

2.2.2 Analytical Models

Analytical models are a quick way of calculating the braid angle dependant on the geometry and process parameters. They are usually limited due to only being suitable for simple axisymmetric geometry parts and are not able to consider any yarn friction or slippage on the mandrel. The initial analytical solution was proposed by Ko [58] in the closed form classical solution given in Eq. (2.1).

Du & Ko [59] developed a model for the prediction of braid angle using Eq. (2.7). This model is run until steady state is achieved from the braiding machine. In comparison to experimental data, the model had an error of 5° lower than the true value. This is thought to be due to neglecting yarn interaction causing curved yarn paths. Additionally in this study, the relationship between braid angle and volume fraction for a variety of λ_a/λ_b ratios (Axial fibre linear density/bias fibre linear density) is presented. This shows that for an initial increase in braid angle, the volume fraction will increase (pre-jamming phase) until the jamming limit is reached (dependent on the ratio) at which it will reduce forcing an increase in yarn thickness.

$$\alpha(z) = \tan^{-1}\left[\frac{R_g}{h(t)}\sqrt{1 - \delta^2}\right] \tag{2.7}$$

Taking the work from Du & Ko further, Du & Popper [32] developed a model for the prediction of the braid angle, coverage factor and volume faction. This model assumed the yarns were straight within the convergence zone and the mandrel shape is a surface of revolution. As well as the prediction of these three factors, the model is able to calculate the maximum braid angle achievable whilst still maintaining a coverage factor of 1. The model was compared to experimental data for a baseball bat shaped mandrel with an average error of 5° apart from around the handle which showed a significantly higher average error of 10°.

2.2.3 Kinematic Models

Analytical models may be quick and easy solutions, but they have limited use in the design of braided composite structures due to the inaccuracy of the models.

Therefore, kinematic models have been developed to account for yarn interaction and frictional forces.

Zhang et al. [60] started to develop the model from Du & Popper through an investigation of the kinematics of braiding, initially looking at straight yarns, then evolving to account for the curvature of the yarns in the convergence zone. Zhang et al. [61] then expanded this model into a mechanics analysis through the influence of frictional forces between the yarns. Kessel and Akkerman developed a prediction model of the yarn trajectories on a complex mandrel [9]. This model is built upon the assumptions the yarn trajectories are continuous and differentiable, there is no yarn slippage on the mandrel and the yarns are straight in the convergence zone. Due to the yarns being assumed as straight, that friction is ignored from the system as this causes bending of the fibres. The model is additionally designed to handle eccentricity of the mandrel within the braider. This is compared to the classical solution Eq. (2.1) as well as experimental data showing a reasonable agreement on both complex mandrels tested. The model proposed is able to calculate braid angles with reasonable accuracy for a braid with a high coverage factor. However, this starts to break down when an open braid is produced. At this point there is a higher degree of yarn slippage on the mandrel, thus leading to larger errors. Additionally, the experimental data for this study shows a large difference (7°) in the braid angle between different faces of the complex mandrel.

Building upon this Akkerman and Ravenhorst [6] designed a novel inverse model. Rather than using take-up speed and spool angular velocity as inputs and outputting the braid architectures, the inverse solution does the opposite. The desired braid architecture is inputted with the take-up speed and spool angular velocity outputted. This is more useful in the design of components, as the desired braid architecture can be determined from the load conditions with the machine settings being given. This model assumed no fibre slippage, yarn interaction with the guide ring and other yarns and the yarn thickness is neglected. The same complex mandrel is used as [9]. The maximum error measured was 7°, which was predominantly due to the braider being unable to satisfy the desired braid angle on all sides at once. Ravenhorst additionally hypothesises that the complex mandrel shape is leading to large degrees of fibre

slippage in the cross-sectional changing areas which the model is not able to take into account. In addition to this, limitations with the machine hardware limited the speed variation. Discrete velocity steps of 7 mm/s were used, showing a lower degree of resolution to the mathematical model.

This model was further tested by Ravenhorst in [41] for a range of different complex mandrels. This includes a cone, nozzle, curved centre line, and a step change in braid angle along a circular mandrel. Each of these examples are analysed with and without feedback. For examples without feedback, *Figure 2-10*, there is a ramp up to changing the braid angles, whereas with feedback, *Figure 2-11*, the braider reverses direction at dramatic braid angle changes to achieve a fast change. With feedback there is agreement between the kinematic and analytical solutions.

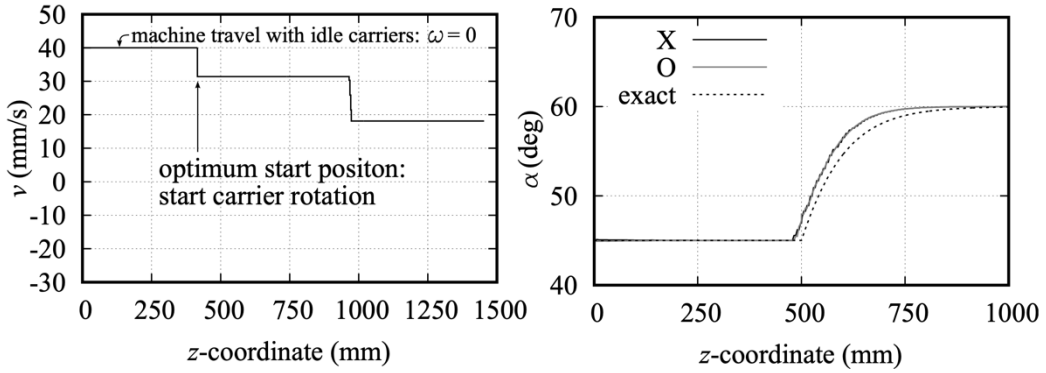

Figure 2-10: Cylindrical mandrel with step change in braid angle at 500 mm - No feedback. Left: Take-up speed profile. Right: Analytical solution and kinematic model braid angle for both yarn groups. Note ramp change in the braid angle. [41]

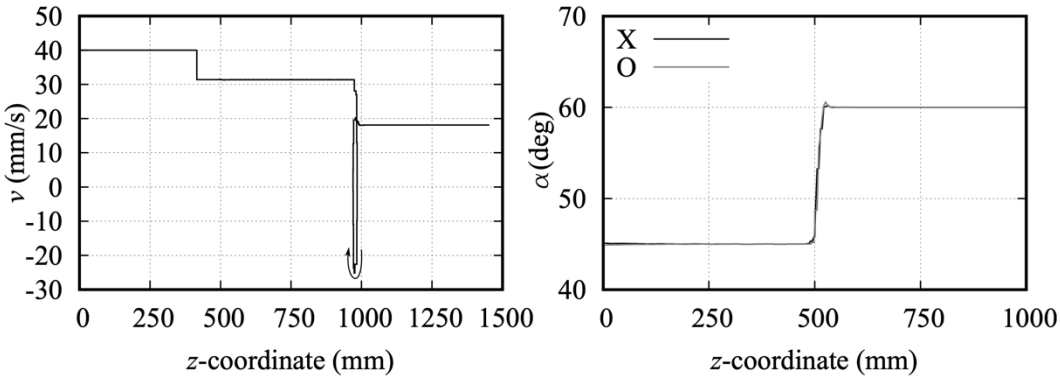

Figure 2-11: Cylindrical mandrel with step change in braid angle at 500 mm - With feedback. Left: Take-up speed profile. Right: Analytical solution and kinematic model braid angle for both yarn groups. Note: Reversal of the speed profile.

It was hypothesised in [9] that yarn interaction plays a large factor in the errors present, leading to Ravenhorst and Akkerman investigating yarn interaction in braiding [62]. Within this model Coulomb friction between the yarns is estimated. The fibres are assumed to be rectangular and of constant cross-sectional area with any fibre breakage, detachment and entanglement neglected. Through validation with experimentation a modelled coefficient of friction value of 0.3 for carbon yarns provided the closest match between model and experiment, causing a reduction of the convergence zone by 25%. It is observed by Ravenhorst that during the braiding process there was a significant amount of fibre damage around the guide ring. This effect is not yet currently modelled and could be significant in improving the accuracy of the model.

Hajrasouliha et al. [63] developed a kinematic model paying particular attention to the two main parameters that effect braid angle; position of the fell point and the yarn length between this and the carrier. This model assumes that the yarn path between the fell point and carrier is a straight line and is tangential to the mandrels surface at the fell point. The results of this model were compared around the perimeter (x_m) of different mandrels with two of these results shown in *Figure 2-12*. This clearly shows the model gives a greater error when dealing with elliptical mandrels. It is noted that to measure the braid angle, a single white thread was braided into the composite to clearly see the angle. The effect of this change in single yarn geometry and material on the braid angle has not been presented.

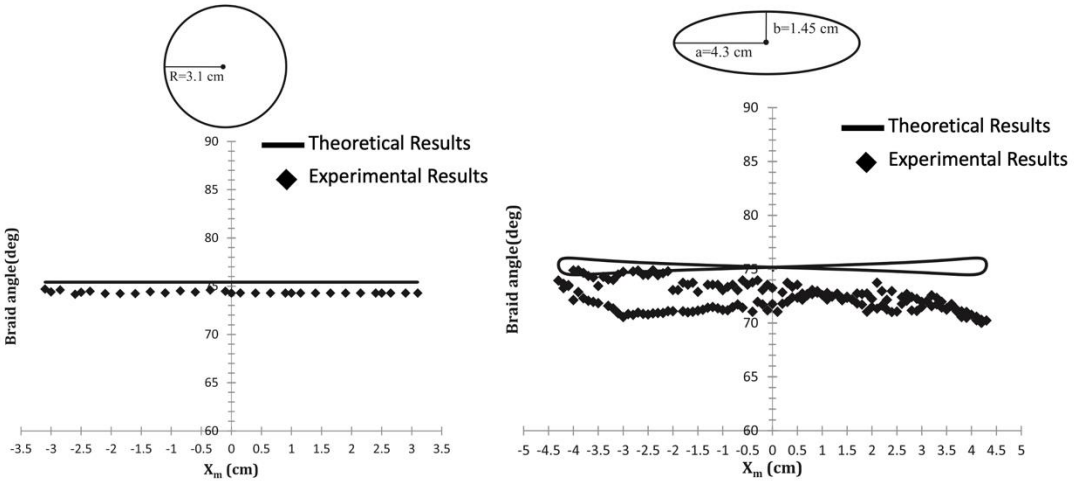

Figure 2-12: Experimental and theoretical braid angle versus X_m for: (a) circular cross-section, (b) elliptical cross-section with a/b = 2.96.

2.2.4 Finite Element Models

For further advanced modelling, finite element models need to be considered. These models are able to take into account material deformation, yarn interactions, fibre slippage, tension and gravity. By adding more variables into the model the time to run is significantly increased, often taking days or weeks to run a full simulation.

Pickett et al. [64] developed an explicit FE method for simulating the braiding process and predicting the mechanical properties of the final braided composite. Through simulation, it is shown that a Smooth Particle Hydrodynamic (SPH) method is the most accurate way to model the interface between the fibres and the matrix. This is a mesh free particle method with the ability to handle very large deformations and is advantageous when dealing with complex shapes and multi-scale resolution. Initially the yarns are modelled as circular, which upon observation of braided preforms is incorrect. To ensure there is no penetration of adjacent yarns, a specialised technique that uses a scaled representation of the yarn structure together with the unscaled version is used. Picket describes the method as 'internal stresses are generated to deform the yarns to the scaled size, whilst contact and external tooling ensure correct compaction and nesting of the braid'. The result from this method is shown in *Figure 2-13*.

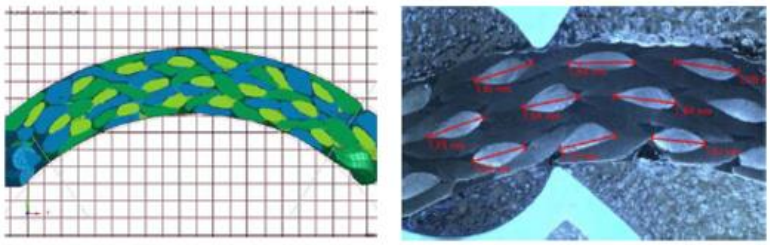

Figure 2-13: (a) FE model of the cross section of tri-axial braid (3 layers), (b) micrograph of tri-axial braid [64]

The accuracy of the model produced is not fully verified. The only comparison presented is for a shear stiffness test, in which a 29% difference was observed, which suggests errors within the model. Further testing of tensile and compression tests could help identify if this is the case. Hans et al. [65] developed a FE simulation for arbitrary mandrel shapes, creating a truss element model of the yarns, simplifying their elliptical cross section to a circle. Friction between elements in the model have been categorised and measured. Yarn to yarn friction is dependent on the orientation of the yarns with respect to each other, leading to a perpendicular value and parallel value. Experimental values for the braid angle on a complex mandrel show good agreement with simulation data, however no comparison of yarn shape can be conducted due to the truss elements being used. Chen et al. [42] developed a FE model to predict yarn location on complex mandrel shapes, enabling deformation post braiding to achieve concave geometry using a braid.

2.3 Simulation Packages

Previously the current state of academic predictive models has been reviewed for analytical, kinematic and FE models. However, for these to be useful in the production of braided composites, the models need to be built into commercially available software for designers to use to evaluate the components. This section gives an overview of what is currently available and where possible, what assumptions the software is built upon.

There are many software packages available at the time of writing each designed from different approaches to define the braid. As with mathematical models there are three factors which each software package (or combination of) needs to be able

to simulate to allow for the evaluation of the component; braid angle, coverage factor and braid thickness. This is done in two different approaches: either through simulation of the braiding process, including positions of bobbins and fibre placement, or as a simulation of the final braid architecture. Both are useful in designing braided composite.

2.3.1 BraidSim

Ravenhorst and Akkerman developed a kinematic model (as explained in Section 2.2.3) which was implemented into BraidSim [41, 66]. This is capable of simulating the overbraiding process for complex shaped mandrels for both biaxial and triaxial braids. The software can be run in three different modes:

1. Conversion – A non-kinematic part of the software, which converts the geometry and laminate plan to a composite layup used for structural analysis.
2. Simulation – The forward solution calculates the braid angle distribution from the machine speed profiles.
3. Optimisation – This is the inverse solution that calculates the take-up speed from the target braid angle and fixed carrier rotational speed.

It is possible to import the 'ply book' from conversion mode into Abaqus for structural analysis of mechanical properties. It is noted that the software is not commercially available and further work is needed to give it a GUI.

2.3.2 Multifilament Modelling

Meso-scale modelling of a textile yarn usually use 3D solid structural elements arranged to give the yarn a lenticular or elliptical cross section. These are capable of modelling yarn-scale deformation and local yarn effects such as nesting and yarn buckling. New developments of higher resolution modelling have enabled fibre bundles within the yarn to be modelled. The technique called digital element method models or multifilament modelling was first developed by Wang et al. [67] to model the yarn as a pin-connected digital rod element chain. As the element length is reduced to near zero the chain becomes fully flexible. This was expanded on by Zhou et al. [68] by using multiple chains to represent the yarn. This allows for yarn cross-section shape to be traced during textile forming or fabric deformation. This method

has been used in a range of studies including Thompson et al. [69] showing deformations in non-crimp fabrics in addition to Joglekar et al. [70] to show the compressive behaviour of 3D woven composites. A comparison of a range of simulation techniques was conducted by Sun et al. [71] shows that although multifilament modelling provided the best resolution to fibre shape during forming it required the most computational resources for simulations.

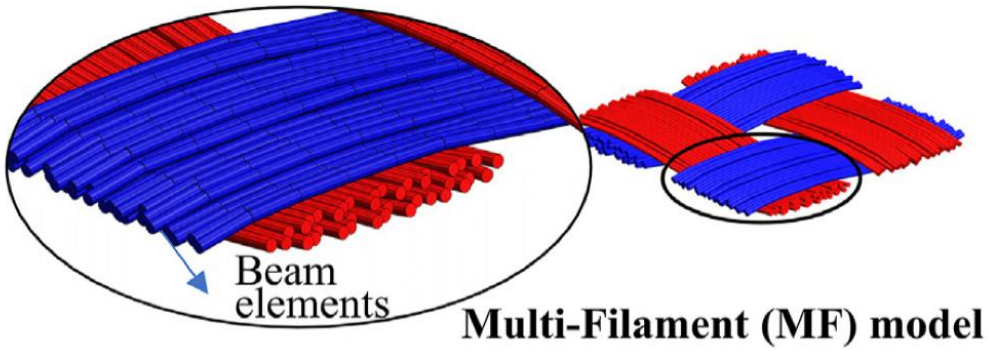

Figure 2-14: Example of multifilament modelling of woven unit cell. Adapted from [71]

2.3.3 CATIA

CATIA [72] is a CAD package from Dassault Systems that offers a composite braiding designer. This allows for the simulation of the whole braiding process from the braider, bobbin movement and fibre placement on the mandrel. Users are therefore able to visualise fibre paths on complex surfaces and optimise machine parameters to achieve the desired braid angle, coverage factor and thickness. This is a powerful tool for designing braiding composite parts, however it is noted that it is not clear what mathematical model is used for the braiding simulation.

2.3.4 Braid CAM

Braid CAM [73, 74] is an open source software developed by Melenka and Carey to predict the mechanical properties of a braided structure. This software is developed in MATLAB with a GUI. The goal of the software project was to develop a user-friendly software tool for the design and manufacture of tubular braided composites. The mathematical model used to develop the software is explained in [75, 76]. The software allows the user to enter the braid angle (specific value or range), mandrel diameter, yarn width, yarn thickness and number of yarns and braid pattern. It also

requires the mechanical properties of the yarns to be inputted with the software, predicting the elastic and shear modulus of the composite for a range of braid angles. Due to limitations in the inputs only simple circular mandrels can be predicted, limiting its usage in the design of braided components.

2.3.5 TexMind

TexMind [77] is a braiding simulation software developed by Y. Kyosev that is able to model in 3D a braided structure. This allows for the user to analyse the final braided structure with information about the float length, minimal machine requirements and the carrier arrangements. A sub-section of the software, Braiding Machine Configurator, allows for the investigation of carrier arrangement and the braided structure this will produce. TexMind is limited due to:

- Inability to model yarn intersections
- Unable to change yarn geometry along the length of the yarn
- Unable to input braider machine parameters

Although the geometry can be imported into TexGen for further analysis, difficulty in modifying the geometry within TexGen limits its usage.

2.3.6 SolidWorks

Although Solidworks does not have a braiding simulation tool, Ning et al. [78] modelled a finalised tubular braided structure using Solidworks and a generalised rose curve. As shown in *Figure 1-2*, the path of the carriers on a braider is sinusoidal. In using a generalised rose curve this path is able to be simulated along the length of the tubular braid. This allows for a 3D model to be produced of the braided structure. As the rose curve structure can be modified the mandrel shape, complex mandrel components can be simulated through this method. Additionally, this method is not limited to Solidworks, and the mathematical model can be implemented into any CAD software. The paper shows that both circular and tape yarns can be modelled, with good consistency in appearance and interlacing pattern.

2.3.7 Braided Composite Design App

J. P. Carey developed an app for the Google Play Store [79] as a tool for the design and manufacture of braided composite materials. The key features of the software are outlined in by Carey et al. [80] as:

- Micro-mechanics calculations for unidirectional lamina
- Strength prediction for unidirectional lamina
- Coordinate system transformation matrix used for angle ply lamina
- Key braided composite manufacturing prediction equations
- Imaging-based braid angle measurement
- Braid machine configurations to produce the three fundamental braiding patterns.

A full description of the capabilities of the software is available in Chapter 2 in Handbook of Advances in Braided Composite Materials: Theory, Production, Testing and Applications [80], with the main mathematical models explained in Chapter 3.

2.3.8 WiseTex

WiseTex [81] is a software package used to model the internal structure and deformability of various fabrics including woven, braids, weft-knits and NCF fabrics. This is part of a suite of software packages for modelling. This includes LamTex for modelling of laminates, TexComp for calculation of stiffness, FlowTex for permeability of textiles using Navier-Stokes equations. In a review of geometrical modelling software Martin Sherburn [82] explains the advantages of WiseTex over TexGen include:

- Geometry calculation based on physical properties
- GUI for creating a wider range of fabric types
- Built-in analytical models for fabric mechanics predictions
- Built-in analytical models for composite material stiffness predictions
- Ability to model gaps created through yarns during stitching

2.3.9 TexGen

TexGen [83] is a simulation software package for analysing RUC. The software is primarily used for developing unit cells of varying fabrics and analysing the geometry,

investigating permeability, and calculating mechanical properties. Currently in version 3.12 TexGen is being developed by researchers at the University of Nottingham. Predominately setup for weave architectures, it is possible to program custom python scripts to generate braided unit cells (example in Appendix D).

TexGen is written in C++ with cross platform support for Windows and Linux. *Figure 2-15* shows the UML class diagram for TexGen. **CTexGen** is split into three main sections, **CLogger** which deals with the warning and error messages issued by other classes, **CDomain** which is responsible for the production of the domain (The area of the textile being looked at). This is usually the size of the unit cell but can often be larger if required. **CTextile** is responsible for generating the textiles. This is split into multiple sections, however, only the key sections are discussed here. **CTextileWeave** is the assembly of yarns from either **CTextileWeave3D** or **CTextileWeave2D**. Much of this data comes from the weave setup wizard. **CYarn** is responsible for the geometry of the yarn, position of master and slave nodes and the interpolation between these notes. The two interpolation methods used in TexGen are Bezier and Cubic.

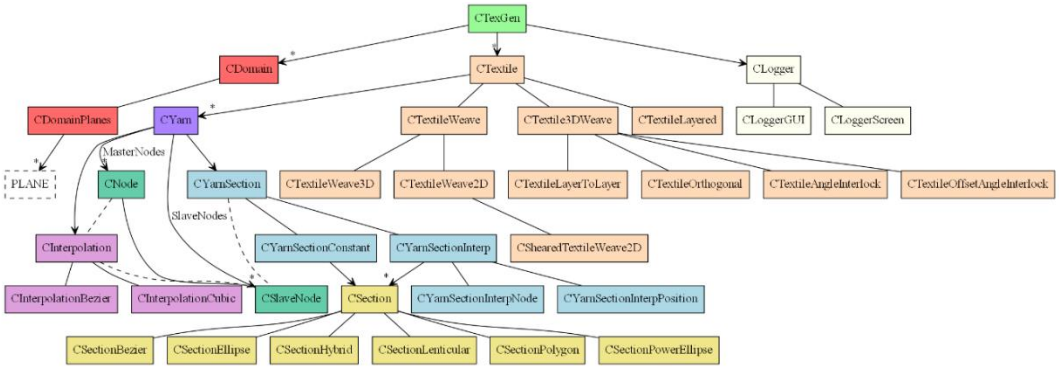

Figure 2-15: Unified Modelling Language (UML) Class Diagram for TexGen [60]

TexGen has integration with Abaqus CAE for the prediction of mechanical properties based on boundary conditions defined by Li et al. [84] as well as allowing the user to export the files as step or IGES files.

This section has highlighted the range of methods and simulation packages available for the prediction of composite braided fabrics. Critically no single package is able to predict properties based on process parameters, produce a realistic yarn and fabric

geometry and allow the freedom designers require when investigating the use of braided composites in component design.

2.4 Mechanical Properties of Braided Fabrics

The mechanical properties of braided structures depend on a number of different parameters including braid angle, braid architecture and coverage factor. Various studies have been done over the past 30 years to compare the mechanical properties and build models to help predict values. This section contains a critical review of these studies.

2.4.1 Experimental Results

Wolfahrt et al. [28] studied the effect of preform architecture on the mechanical and fatigue behaviour of braided composites. In this study 4 different fibre architectures were investigated, 45° biaxial, 45° triaxial, 60° triaxial and 70° triaxial. Fabrics were braided onto circular mandrels and cut to form flat composite panels. No discussion is given for a variation in braid architecture after being cut from the mandrel. For the monotonic tensile testing the results showed a significant increase in tensile strength and modulus in 0° testing between the 45° biaxial to triaxial samples, with a slight reduction for the 60° and 70° triaxial. With the fatigue testing it is seen that 45° biaxial samples showed the worst results with 45° and 60° triaxial showing very similar results.

In 1996 Swanson et al. [85] compared the strength of braided composites to traditional laminates. This showed braided composites to have up to a 30% lower tensile strength in the axial direction when compared to unidirectional laminates. It is noted by the author that up to half of this value may be due to the lower volume fraction of the braided composite (V_f=50% for braided compared to 60% for the laminate) with the rest due to the fibre architecture. Upon inspection of the braided composite there appears to be a waviness to the fibres in the axial yarns. This may be due to the braiding parameters or the RTM process. The most significant strength loss in the braided structure is in the transverse direction, with losses of around 60-70%. This is likely due to two factors; (1) the undulation of the braided yarns giving rise to stress or strain concentrations and (2) there is evidence to suggest the discrete nature of the axial yarns are giving rise to strain concentrations. A similar test was

undertaken by Falzon and Herszberg [86] which largely agreed with the data found by Swanson. The tensile test showed the braided composites to have a 10% lower longitudinal tension modulus when normalised to 60% volume fraction. It is suggested that much of this comes from the crimp within the fibre yarns for the braided composite, which is not present in the UD lamina.

The difference between braided and woven composites and the effects of fibre orientation on mechanical properties was studied by Dauda et al. [57]. This showed the maximum tensile strength of the composite reduces by as much as 20% with an increase in braid angle from 45 to 65°, with similar results shown for the maximum flexural strength. It is shown that although the tensile strength between the woven and braided composites is comparable, the flexural strength of the woven composite is as much as twice that of the braided composite. This is due to the loading cases of each of the tests and the fibre orientation of woven composites compared to that of the braided structure.

Heieck et al. [87] investigated the influence of coverage factor on in-plane mechanical properties of both 2D biaxial and triaxial braids. For biaxial braids this showed that the tension modulus reduced at lower coverage factors, however the compressive modulus fluctuated around the same values. On the other hand, with triaxial braids, both the tensile and compressive modulus are reduced with a reduction in coverage factor. All values in the study were normalised to V_f= 60% and for biaxial braids, two different injection systems were used (RUM235/RTM6) which led to significantly different results in some tests. The range of coverage factors is between 100 – 92.9% which does not show a large enough range of values to produce a correlation between coverage factor and mechanical properties.

A study by Charlebois et al. [88] looked at the tensile compressive and shear properties of 2D biaxial braided composites at 3 braid angles (35°, 45° and 50°) compared to UD laminate. Within this study it was shown that in the tension test the braided composite exhibited a higher modulus than the UD laminate, contradictory to other studies [85, 86], due to the undulation of the fibres reducing the in-plane properties. The shear modulus of the samples was tested using the Iosipescu

method. Though the test was deemed to be unsuitable due to the scatter of the data, it was observed that the braided specimen seemed to be loaded by a combination of shear and bending. This is due to the low bending stiffness and high shear stiffness of the material.

Whilst most studies on mechanical properties focus on the elastic modulus, Potluri et al. [89] studied the flexural and torsional properties of both biaxial and triaxial braided tubes. Each of these was tested at 3 different braid angles and the comparison of 1 layer to 2 layers. For the flexural tests, it showed that all samples at 45° exhibited the lowest bending stiffness with, as expected, triaxial samples having a higher bending stiffness than biaxial due to the presence of axial yarns to take the loading. Whereas in torsional tests it showed that there was very little difference between triaxial and biaxial as the axial yarns take very little of the load.

2.4.2 Simulation Results

Kier et al. [90] developed an analytical model for predicting the mechanical properties of 2D triaxial braided textile composites. A MATLAB code is developed for the prediction of the mechanical properties through the analysis of experimental and FE data. This analytical model is built upon work published by Quek et al. [91]. The model is a stiffness-based model and thus produced higher than expected values for some mechanical properties. However, upon comparison the model shows good agreement with the experimental results for tensile and shear modulus.

When designing the fibre architecture for a component, the loading cases need to be considered to achieve the most effective design. Gurley et al. [92] has outlined a process to determine the optimum structure. The model used to simulate the loading process was compared to experimental data with good agreement between values. It is suggested that the main reason for variation in the data is due to manufacturing inconsistencies due to the machine used to produce the samples. Further quality control and higher braiding tensions may mitigate this. Additionally, the work conducted in this study was completed on open braided structures, which have a very low coverage factor. This has been shown by previous studies [87] to have detrimental effects on the mechanical properties.

Whilst most studies of mechanical properties are interested in the linear behaviour Wehrkamp-Richter et al. [50] investigated the non-linear mechanical response of triaxial braided composites. Through RUC models and experimental data, the failure modes are determined for loading cases at a variety of angles.

Yu et al.[93] applies the two-scale method to predict the mechanical properties of a 4-step 3D braided composite. Both stiffness and strength parameters are compared against experimental results and show good agreement with up to 11% deviance. This may be due to the lack of interface boundary between fibres and matrix within the FE model.

Numerous studies have been conducted to measure the mechanical response of 2D braided composites. Miravete et al. [94] developed an analytical meso-mechanical approach to predict the strength of triaxial braided composites. Xiao et al. [55] used FEM analysis of sub-cells of the RUC of triaxial braids to predict the strength. Strength and failure response of triaxial flat braided fabrics was predicted by Quek et al. [95] using a micro-mechanics based approach. Xu et al. [51] used a multi scale approach, using a micro-scale model to predict the response within a meso-scale model. Wang et al. [96] used Hashin's Failure Criteria and a degradation model to predict failure within 2D biaxial braided composites at a range of braid angles. This showed good agreement with experimental values at low strain values, however some deviance was noted once failure had occurred within the model.

2.5 Conclusion

Through a review of the literature to date, areas for further development have been identified and are addressed within this thesis. Studies into mechanical properties has highlighted the requirement to understand the braided geometry including the fibre undulations and coverage, to accurately predict the properties. With regards to fibre preparation, in-particular the twist level within the fibre, academic research is limited, with the main focus on the effect on mechanical properties. Little research has been conducted to show the effects this may have on the yarn geometry and the overall architecture of the braided fabric. Research presented within this thesis will investigate how twist level effects the geometry of the yarn and the overall braid architecture.

Additionally, the requirement for a predictive meso-scale modelling technique has been shown. Commercially available software, such as CATIA and TexMind, has been shown to have limitations in the prediction of the geometry. This is either through the assumption of constant yarn cross-sectional shape or is unable to predict larger fabric architecture such has braid angle or coverage. Therefore, this thesis addresses this gap in the literature, building a new method for both the prediction of fabric geometry such as braid angle, and predicting the complex yarn cross-sectional shape and geometry throughout the braided fabric.

The effect of the scale of the axial maypole braiders is lacking within the literature. Studies have been conducted on a range of braider sizes but little comparison of these has been presented. The thesis presented will use two scales of axial braider to investigate the effect this may have on the yarn and braid geometry, allowing for any modelling technique to be validated on multiple sizes of braider.

3 Methodology

The present work is split into 3 main areas of research. Firstly, an investigation into the effect of twisting yarns during the winding process on the braid architecture in single and multilayer preforms on simple circular mandrels (Chapter 4) and on complex prismatic conical mandrels (Chapter 5). Secondly, a geometrical modelling technique has been developed within TexGen to predict key braid architectures and model a Representative Unit Cell (RUC) in both a flat and curved domain (Chapter 6). Finally, a methodology has been developed to predict the mechanical properties of the composites, investigating the effect of curvature on elastic properties (Chapter 7) and the effect of twist on the mechanical properties (Chapter 8). This chapter outlines various experimental methods used within these studies for data collection, with a validation of the methods shown.

3.1 Braiding Machine

Braids have been analysed from two different braiders within this thesis: a 48-carrier braider at the University of Nottingham and a 192-carrier braider at the National Composites Centre (NCC). This section explains the methodology for the manufacturing of braids using each machine.

3.1.1 48-carrier Braider

The 48-carrier braider used at the University of Nottingham is a Steeger 140/48 HS axial braider, as shown in *Figure 3-1*. The braider can hold 48 individual carriers, each with its own tensioning system. Carriers are positioned within the horn gears to enable a 2:2-1 braid pattern when using a fully loaded braider.

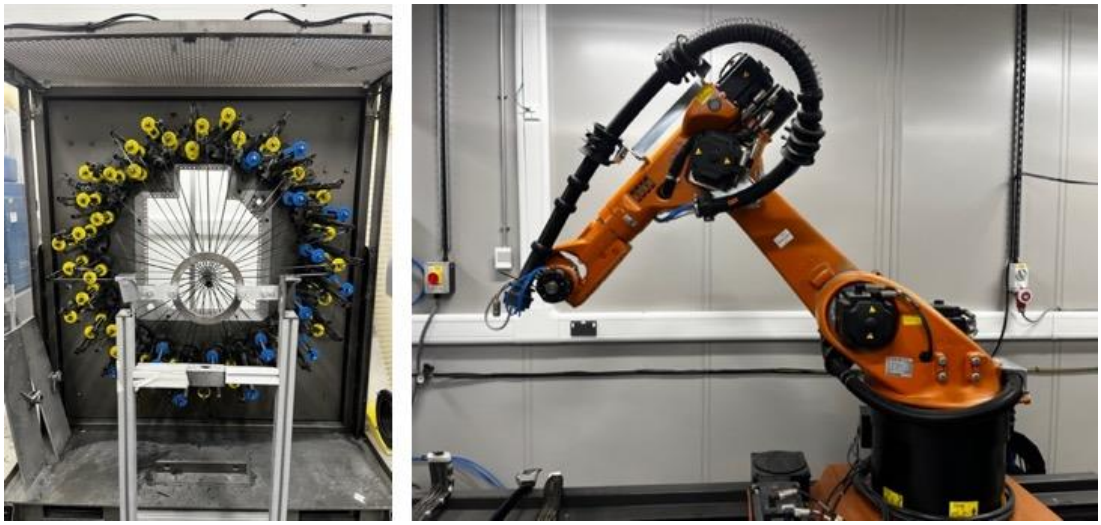

Figure 3-1: 48-carrier Steeger 140/48 HS axial braider and Kuka KR30-60 robotic arm at the University of Nottingham.

The control system for the braider uses a Kuka KR C2 controller [97]. To control the speed and direction of the braider, an analogue voltage output is used from the KR C2 controller. The analogue signal is processed with a Hitachi Inverter to send synchronised signals to 3 DC motors within the braiders.

To calibrate the system, a rotational encoder has been attached to an output shaft on a horn gear to measure the rpm at various voltages. The results of this are shown in *Table 3-1.*

Table 3-1. Braider speeds resulting from voltage defined within the Kuka control unit.

Voltage (V)	Horn Gear Speed (RPM)	Horn Gear speed, ω_h (rad/s)	Carrier Speed (RPM)	Picks per Minute (PPM)
0.90	47	4.92	3.92	94
0.85	44	4.61	3.67	88
0.80	40	4.19	3.33	80
0.75	38	3.98	3.17	76
0.70	35	3.67	2.92	70
0.65	32	3.35	2.67	64
0.60	28	2.93	2.33	56
0.55	25	2.62	2.08	50
0.50	22	2.30	1.83	44

Mandrel positions within the system are controlled via a KR30-60 robotic arm mounted on a linear rail track for precise manoeuvrability of the mandrel when braiding. This enables 6 axes of movement for the robot during braiding. The control of the robot gives a repeatability of 0.07 mm. This system is controlled via the same control panel as the braider speed which allows for in-programme changes during the braiding process.

A 180 mm diameter guide ring has been used to guide yarns onto the mandrel and reduce the convergence zone of the braider. *Figure 3-2* shows the formation of a braid with each yarn undulating under two yarns of the opposite direction before undulating over two yarns.

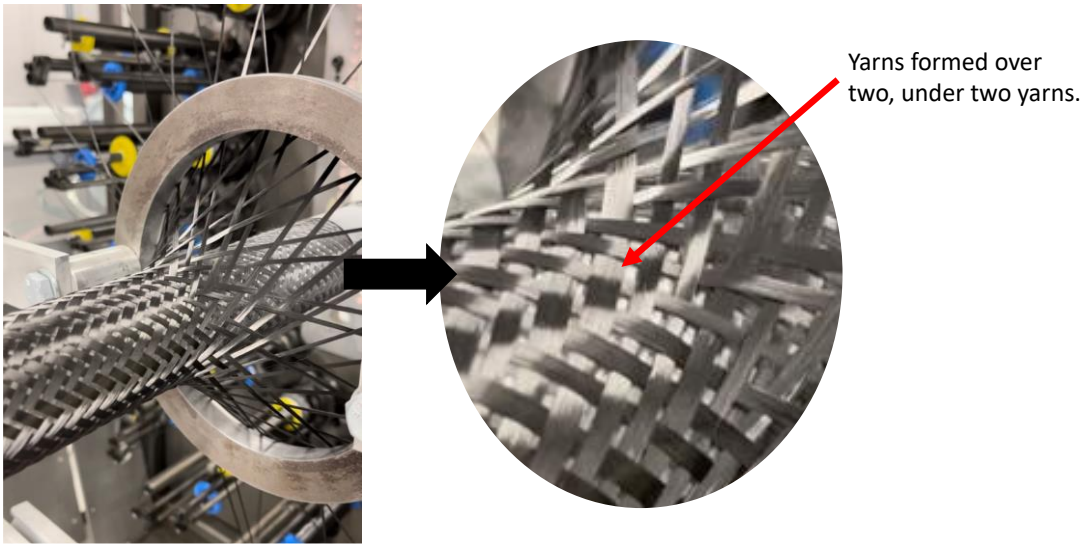

Figure 3-2: Formation of braided fabrics using a 48-carrier Steeger 140/48 HS braider and 12K carbon fibre yarns.

3.1.2 192-Carrier Braider

In addition to a 48-carrier axial braider at the University of Nottingham, a 192-carrier Eurocarbon axial braider [98] has been used at the National Composite Centre, Bristol. This braider comprises of 192 individually tensioned yarns in a 2:2-1 braid pattern with achievable braid angles between 15°-80°. This forms part of a larger system capable of braiding using either a 192-carrier or 288-carrier braiding ring as seen in *Figure 3-3*. Control of the mandrel and braider is conducted via precise CNC control, using a large gantry system to support larger mandrels at both ends.

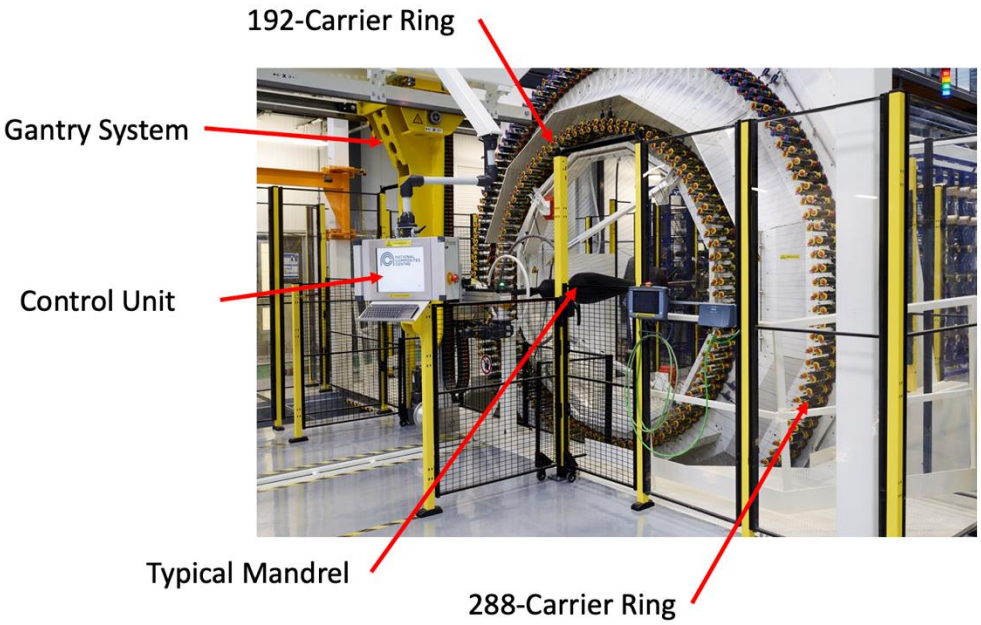

Figure 3-3: NCC Braiding System

3.2 Winding

Kysov [15] gives an overview of the multiple methods of winding fibres with a variety of advantages and disadvantages. The method used within the thesis has focused on parallel winding with flanged bobbins, negating the requirement of the yarn to hold itself onto the bobbin. The winding has been completed using the Cezoma VLS-87 bobbin winder. The system allows for a constant speed, tension, and material feed rate to maintain high-quality winding.

During the winding phase, additional twist has been induced into the yarns. This is in addition to any pre-twist applied by the manufacturer. Twist has been added using the Eurocarbon twisting machine, with an explanation of the kinematics below.

Twist is applied to the material through a differential in rotation speed between the spool of stock material and the bobbin in which the yarn is being wound. During the set-up of the machine the user specifies a winding velocity (wind) in mm/s and a level of twist in twist per meter (tpm). The twisting machine receives continuous pulses from the bobbin winding machine (PulsFreq), with each pulse representing one rotation of the bobbin. (Note this has a circumference of 20.01 mm). The twisting machine then uses this data to calculate the required rotational speed of the stock material to achieve the desired twist within the material. This relationship is given in Eq. (3.1) and (3.2).

$$Wind\ \left[\frac{mm}{s}\right] = 201[mm]\ x\ \frac{PulsFreq\left[\frac{puls}{s}\right]}{1} \tag{3.1}$$

$$SP\ RPM\ [RPM] = SP\ Twist\ [tpm] x\ Wind\ \left[\frac{mm}{s}\right] x\ \frac{60}{1000} \tag{3.2}$$

The set-point spool speed (SP RPM) is then sent to the frequency inverter, which then sends a signal back converted into an actual spool rotational speed. Note the motor for the spool does not contain and encoder and therefore is an estimate of the speed of the spool, considering electrical characteristics of the motor and the actual power consumption and frequency.

To increase stability during the braiding process, it is recommended to use alternative S-twist and Z-twist for the warp and weft yarns on the braid. This refers to the direction of the twist on the fibres as shown in *Figure 3-4*. This is achieved by reversing the direction of the rotational speed of the spool bobbin during winding.

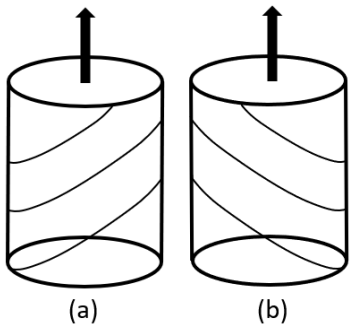

Figure 3-4. Twist configurations, (a) Z-twist or (b) S-twist.

3.3 Optical Microscopy

Optical microscopy has been used within this study to image and measure the internal structure of the braids in various states. Velez-Garcia et al. [99] outlined methods to prepare samples of fibre composites for optical microscopy. Using this method and sample data a set procedure was developed and implemented to ensure consistency in specimen preparation. The procedure is as follows.

1. Cut samples and cast them in polyester resin in 40 mm diameter pots.
2. Cast samples ground on both the top and bottom surfaces to reveal the internal structure and produce flat surfaces

3. Wet polish samples on a range of grit papers P240 – 4000, becoming finer in each iteration. This is followed by a final stage using a cloth wheel with a 1.0 µm silica solution. Details of times are outlined in *Table 3-2*.

Table 3-2. Sample polishing procedure for samples.

Grit Paper	Time (min)	Objective
240	5	Removal of material until plane of interest is reached
400	5	Gradual removal of surface layers to eliminate grooves
600	10	
800	10	
1200	10	
2500	10	
4000	10	
Silica Solution	15	Final polish. Over polishing during this phase may impact the definition of the fibres during microscopy.

Samples were imaged using a microscope with a 5x magnification lens. Image Capture Pro was used to set focal lengths for samples and tile images together. An example of the output images can be seen in *Figure 3-5*. From this data the yarn width, yarn thickness and cross-sectional shape is able to be determined.

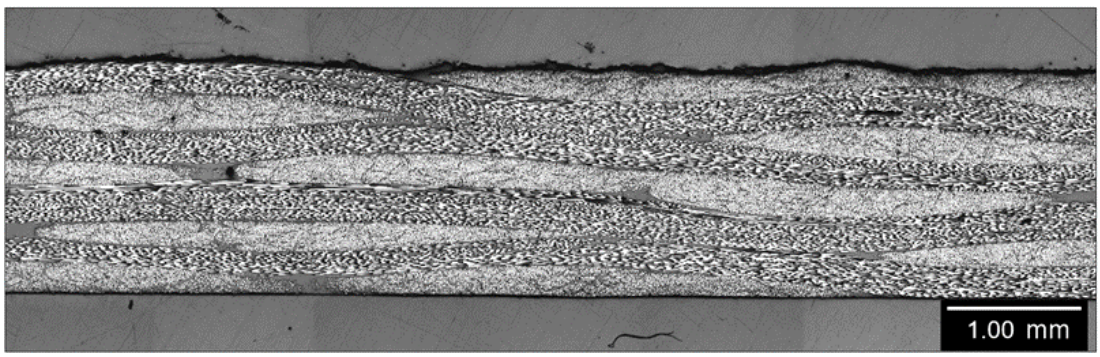

Figure 3-5. Sample image using optical microscopy and procedure outlined above.

3.4 Surface Analysis

Sherburn [82] gives an overview of the techniques used for the measurement of parameters such as fabric thickness. Traditional methods rely on either contact with the surface or only use small samples of the braid, such as optical microscopy or µCT. Several methods have been developed to analyse the surface of the braid using non-contact methods to capture data such as braid angle, yarn width and fabric thickness.

3.4.1 Structured White Light Scan

A HP 3D Scan Pro S3 dual camera system has been used to capture the surface of the braid, based on coherence scanning interferometry (CSI). Through a series of images captured with a range of structured white lines projected onto the sample, the system measures deviations within the projected image due to irregularities in the surface of the object. The programme analyses these changes in the fringe to reconstruct the surface shape of the specimen. Using several scans around the perimeter of the mandrel, scans are able to be stitched together to build a 360° model of the braid surface. 3D point clouds were then acquired with a precision of up to 0.05% over the scan area. A scan area of 200 mm^3 is used within this study, giving an accuracy of 0.1 mm^3. This method is used for yarn width and fabric thickness measurements. As seen in *Figure 3-6(b)* the texture, as well as topology, is captured within the model. This can be used to calculate the thickness of the braid as well as manually measure the braid angle and yarn width.

(a) (b)

Figure 3-6. Comparison of (a) photography and (b) structured white light scan model of braided fabric.

3.4.2 Apodius 3D Scan

The Apodius Vision system 3D developed by Hexagon has been used to capture the structural topology of the surface and measure surface images for fibre angle. The system is built from 3 main components, an absolute arm 85, an RS6 scanner and an HP-C-V3D vision sensor, as shown in Figure 3-7. Initially, the surface of the mandrel is scanned using the Absolute Arm and RS6 scanner within the Apodius 3D software. This produces a point cloud of the surface of the braid, which is then meshed with an element size of 3 mm. This mesh is determined by the system to create an overall topology of the surface. It is not able to determine geometrical features such as yarn width. As this system is not designed to capture an accurate topology and relies on image data to calculate fibre angles, a finer mesh is not required. The HP-C-V3D sensor is used to capture low reflective images of the surface of the fibres. As the system is connected to the Absolute arm, the location position of the images is known and are mapped onto the surface of the mesh previously produced, as shown in *Figure 3-8(a)*.

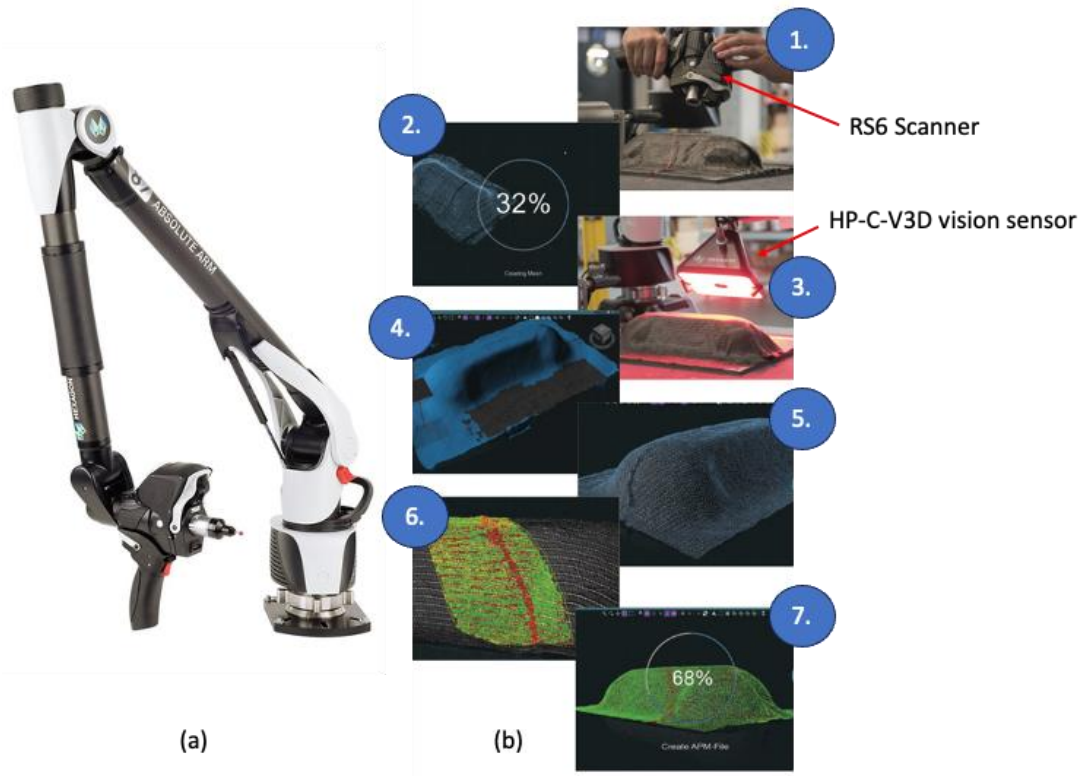

Figure 3-7: (a)Hexagon Absolute arm with (b) process flow for Apodius (1) laser scanning, (2) meshing, (3) Image scanning of the surface, (4) plotting images on the mesh, (5) completed surface map with mesh and images, (6) fibre angle analysis display and (7) complete component fibre angle analysis.

To define the fibre orientations within the images captured, a reference image must be defined in the software. The system uses regions with similar optical appearances to group areas together into fibres with the same orientation. Each local area is then examined using a texture segmentation algorithm to detect the edges of the yarns. This can then be corresponded to a reinforcement direction manually by the user. The system is able to use this value to recognise local fibre orientations using the grey value found within the spectra. As the system knows the global location and orientation of the images captured, the local fibre orientation can be mapped into the global system.

Figure 3-8 shows the type of analysis that can be completed from an inspected component using the Apodius system. *Figure 3-8(b)* shows the *'Angular Orientation Advanced Check Two Peaks'* used to confirm the uniformity of the braid along the length. The analysis is completed over the whole 3 mm element, calculating an

orientation vector for each pixel that lays on the mesh triangle within the picture area. This is then able to consider each mesh triangle in comparison to the surrounding triangles to display a quality check. *Figure 3-8(c)* shows the results of the *'Angular Orientation High Resolution Check'.* This algorithm defines the orientation for each and colours each pixel separately depending on the angle analysis and quality criteria. This data is then compiled within the graph seen in *Figure 3-8(d)* showing the range of angles seen in the example. Typically for a braid, two peaks would be expected, one for weft yarns and another for warp yarns. Individual areas can be further inspected with the average orientation vector for each triangle superimposed onto the 3D images as seen in *Figure 3-8(e & d)*.

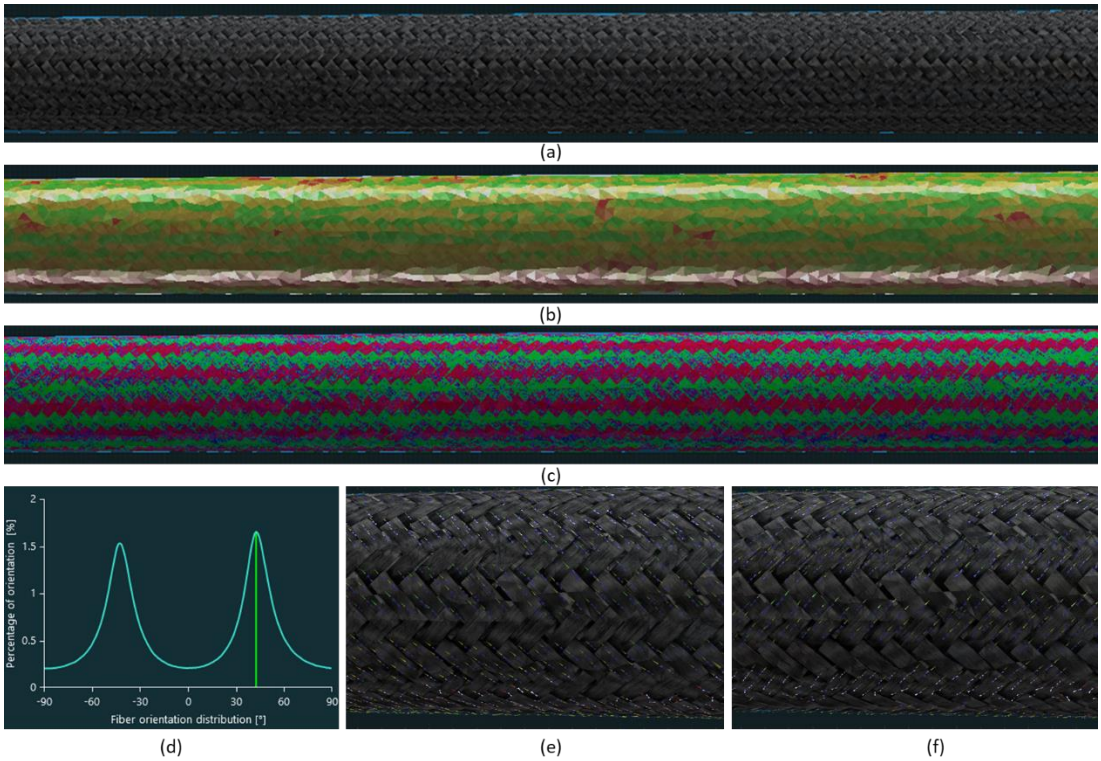

Figure 3-8. Captured data using Apodius Scanner. (a) Images mapped onto 3D geometry, (b) angle validation, green shows angle agreement, red shows outside of the quality range, (c) Angular orientation high resolution check, (d) Graph showing frequency of angle orientation during analysis in (c), (e and f) showing visual confirmation of angle orientation for weft and warp yarns superimposed on 3D images.

3.4.3 Laser Scan

For greater accuracy in measuring the surface topology of the braided mandrel over a larger area, a method has been developed using a Hexagon RS6 laser scanner attached to the Hexagon Absolute Arm 85 with a calibrated accuracy of +/- 0.0031 mm. Although a red-light laser is used by this system, preferred for scanning carbon fibre, the reflectivity of carbon fibres has led to inaccuracies when using light scanners to capture the surface. Therefore, a layer of matt-white powder, with negligible thickness, is applied to the surface of the fabric using an aerosol spray. The braided component is removed from the braider, with a full 3D scan taken of the surface using the RS6 Scanner mounted to the absolute arm shown in Figure 3-7(a). Scan data is gathered within Polyworks Inspector package for the whole length of the mandrel. These 3D point clouds are analysed using a MATLAB script to identify the thickness of the braid. Slices along the axis of the mandrel are taken to determine the thickness of the braid at specific points. These typically range between 5-15 mm, calculated from Eq. 3.1, and are determined from the braid angle and coverage.

$$x = 2x_g \cos(\alpha) \tag{3.1}$$

Where x is the minimum slice width, x_g is the spacing between the centre of the yarns and α is the braid angle.

From this, the maximum diameter is determined at 15° internals around the perimeter of the mandrel, and the overall thickness is determined to be the average of this. This process is outlined in *Figure 3-9*, showing a full 3D point cloud of the braided mandrel and segments taken for analysis. Using a scan of the mandrel with no braid and the same method outlined the thickness of the fabric can be determined along the length of the mandrel.

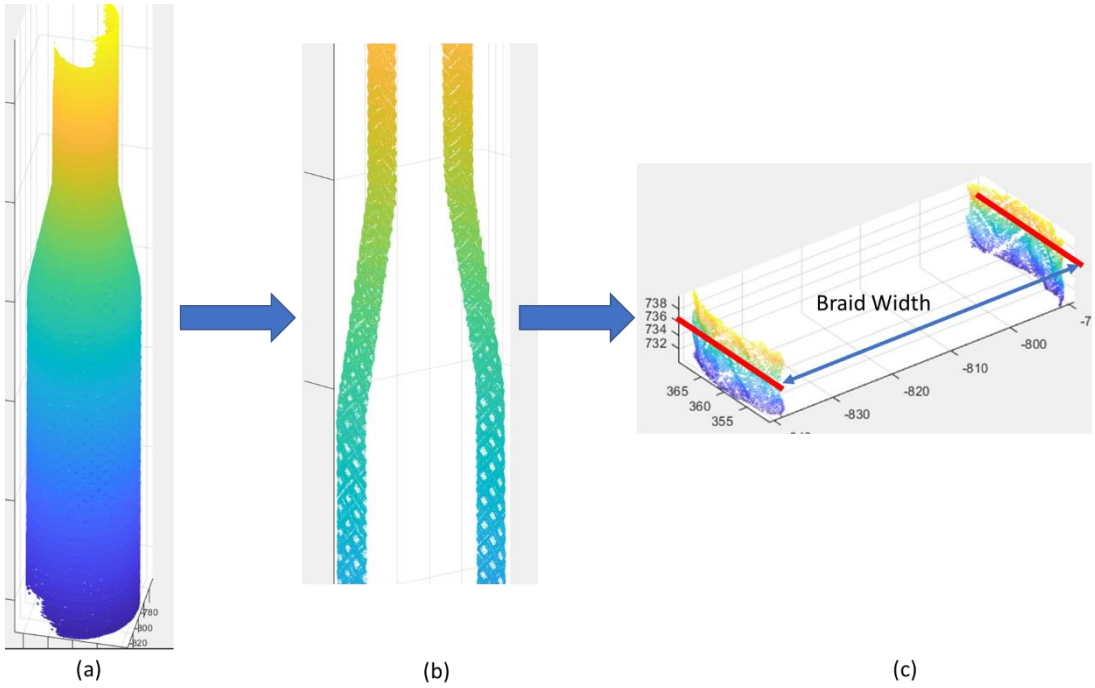

Figure 3-9. Points cloud analysis methodology. (a) overall point cloud for braided mandrel, (b) slice taken in the z-direction to reduce the number of points and (c) sample image of height x (from Eq. 3.1) with braid width indicated.

3.4.4 Braid Angle Measurement

Chapter 2, Section 2.1.2 defined the standard ISO 10122 – Section 7.2.5.1 [34] for measuring braid angle. Building upon the methods outlined in the literature, a method has been developed to automatically measure the braid angle at any point in the structure using a Python script and the OpenCV library [100]. Images are taken of the surface of the braid and cropped to the location of interest for the analysis shown in *Figure 3-10(a)*. A bilateral filter is then applied to the image. This has been chosen to ensure the edges of the yarns remain sharp but remove noise from the image and reflective artefacts within the yarns. This effect is shown in *Figure 3-10(b).* Using this smoothed image, a canny edge detection function is implemented to detect the edges of the image and remove all other details. The outcome of this is shown in *Figure 3-10(c)*. Following this, a Hough transform is conducted to detect large uninterrupted straight edges within the image and calculate the angle of these edges. Due to damage that occurred during the braiding process, there are often stray fibres on the surface of the braid which may not be removed during the filtering process and other artefacts are occasionally detected by the algorithm. Therefore,

an initial filter is used to remove all edges that have been detected outside the 'reasonable' range for the braid angle. Finally, the detected lines that fall within the accepted range are superimposed on the original image, *Figure 3-10(d).* This can be manually checked to ensure only yarns are detected. This method allows for a reliable and repeatable method to measure the braid angle.

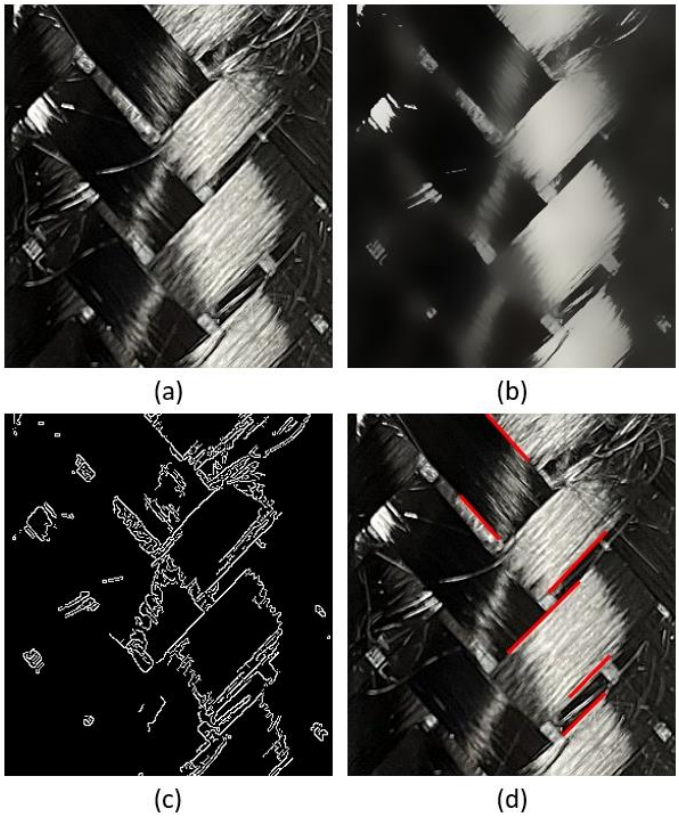

Figure 3-10. Process of automatic braid angle measurement (a) Image taken of braid, (b) bilateral filter applied, (c) canny edge detection and (d) outcome of hough transform transposed onto original image.

3.4.5 Apodius 2D Scanner

In addition to the custom Python script, the Apodius 2D scanner has been used to calculate the braid angle. This system comprises of a low reflectivity imaging camera and the Hexagon 2D image analysis software to measure the fibre orientations within each pixel of the image. Validation between this method and ImageJ analysis was conducted with the agreement of the braid angle to be within 1.0°. Data for this validation can be found in Appendix A, Section A.4. *Figure 3-11* shows the typical image captured of the surface of carbon fibre braids. The low reflectivity of this is key in the calculation of the fibre orientations, as it negates the need to apply smoothing

filters, as seen in the method outlined in Section 3.4.4. The 2D system has been integrated into the braiding setup to allow for post-braiding fibre analysis of the braid on the mandrel. This allows for measurement of braid angle within each layer of the braid at discrete points along the length of the mandrel. Limitations to this system include the braid surface needing to be perpendicular to the camera system, limiting usage on sloped sections.

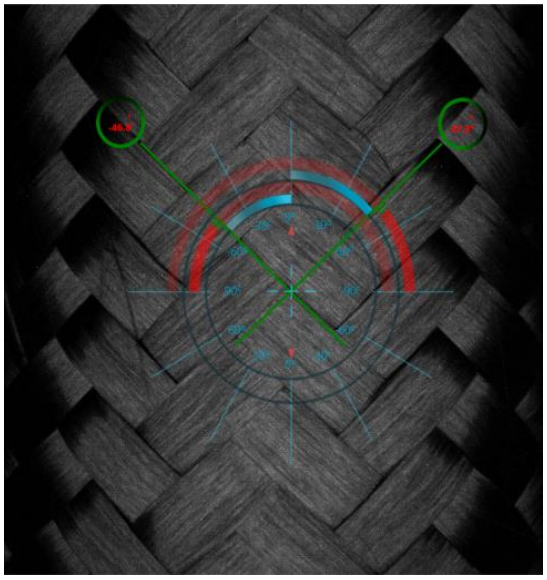

Figure 3-11. Image taken using Apodius 2D scanning software with braid angle measured indicated on the image.

3.5 Comparison of Methods

Outlined in previous sections are established and novel methods for characterisation of the braid architecture. This section provides a comparison of those methods for the same braided fabric.

Within this section, a piece of fabric has been braided using a 48-carrier axial braider with HTS40 12K carbon fibres with no additional twist added during the winding process. This was braided on a 50 mm diameter mandrel with a 2-2:1 pattern. Photos were taken along the length of the mandrel for braid angle analysis. The braid was scanned using the Apodius 3D scanner and laser scanner for braid angle and thickness measurements. Additionally, sections were cast and potted using the methodology outlined above for microscopy thickness analysis.

3.5.1 Results

3.5.1.1 Braid Angle

Three methods for braid angle measurements are compared: Apodius 3D scanning, Image J analysis and the automated braid angle analysis. 2D Apodius has not been included as it has been previously validated against ImageJ, showing alignment between methods. *Figure 3-12* shows an agreement on the braid angle between the multiple methods with an average of 41.3° for the Apodius system, 41.9° for the image J analysis and 40.6° for the automated braid angle detection method. Each method can describe changes in the braid angle along the length of the part, however only the Apodius system does not rely on discrete measurement locations. Discrepancies between the Image J measured angle and the automatic braid angle measurements are explained by the scope of the measurement system. With ImageJ, only a single weft and warp yarn is measured, with the braid angle taken as the average. Whereas with the automatic system, multiple yarns can be taken into consideration with the average taken from all measured yarns in a single image.

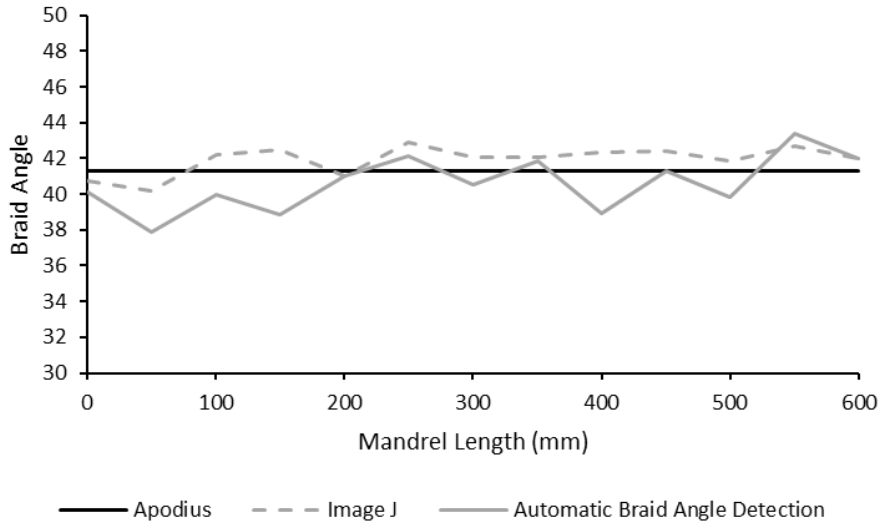

Figure 3-12. Braid angle measurements compared for the same fabric.

Braid angle analysis from the Apodius 3D scanner is shown in *Figure 3-13*, demonstrating a consistent braid angle along the length of the mandrel. Analysis of fibre orientation distribution shows two peak angles at -44.98° and 52.50°. Due to the orientation definition within Apodius, a 90° translation is required, giving a true

braid angle of 41.26°. A small peak is seen at 31° relating to the tape at the end of the samples and can be ignored for this analysis.

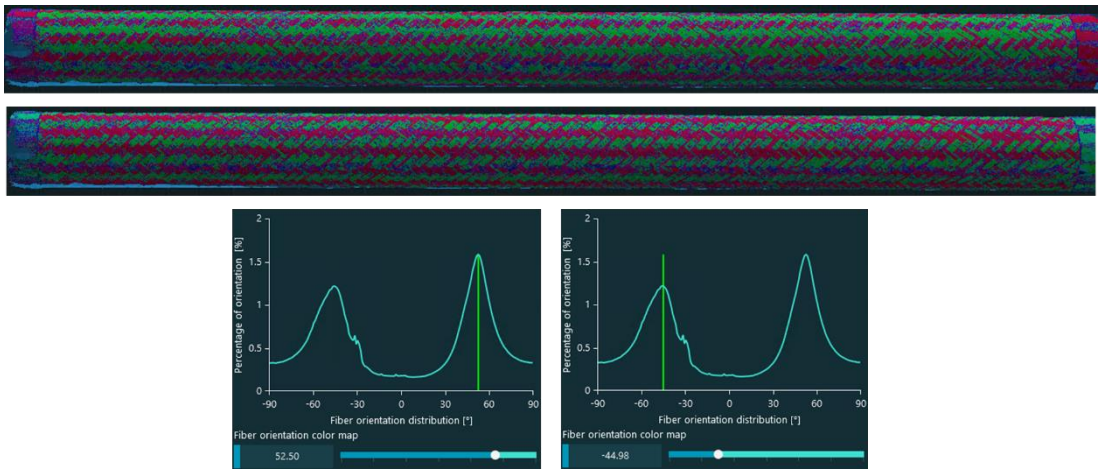

Figure 3-13. Apodius 3D scan data for braided fabric showing two angle peaks at 52.50 ° and -44.98 °.

3.5.1.2 Braid Thickness

Figure 3-14 presents a comparison of methods for measuring braid fabric thickness. Microscopy data was collected through a method of casting the fabric within Gurit Prime 20LV resin, whilst applying minimal external pressure to the structure to minimise potential thickness changes. The results show a large level of overlap between the two methods in calculating the thickness of the fabric, validating the laser scanning method for thickness measurements. The microscopy measurements show, on average, a lower fabric thickness than the laser scanning. This is to be expected due to difficulties in measuring the maximum thickness point when measuring a 2D image of the cross-section of the braid. This is not a problem for the laser scanner as it is able to detect a maximum thickness point over a larger slice of the braid. Additionally, contact with the braid is required when casting due to the requirement for the resin to flow into the yarns, although kept at a minimum, can compact the yarns to lead to small reductions in the braid thickness. The laser scanning solution requires no contact with the fabric post-braiding.

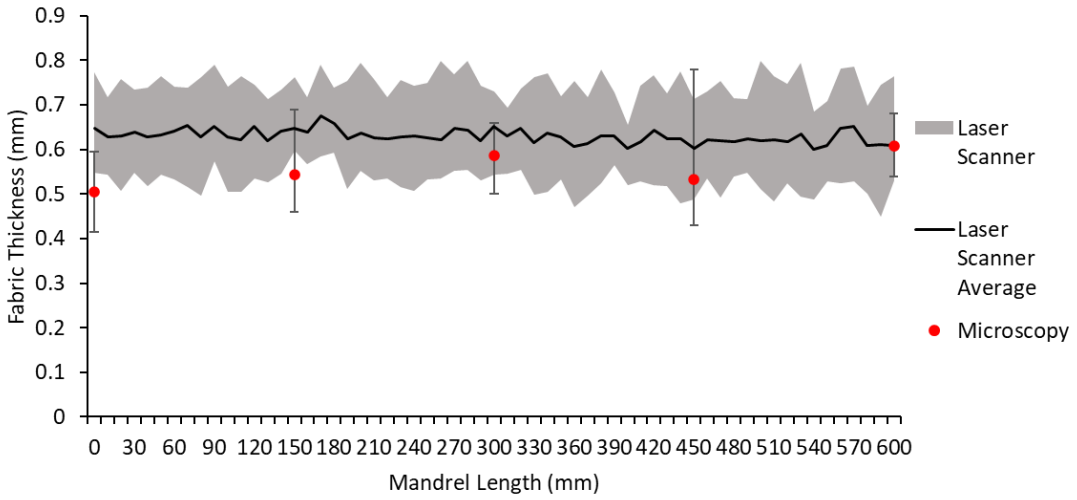

Figure 3-14. Braid thickness measurements using laser scanning and microscopy.

3.6 Conclusions

The methods used for experimental measurement and testing have been outlined in this chapter. This has ensured repeatable and comparable results throughout the study. Methods for quantifying the braid architecture have been presented with traditional techniques such as optical microscopy and 2D ImageJ image analysis as well as novel methods for detecting braid angle and fabric thickness using OpenCV and laser scanning. A wide range of techniques is required to enable the most appropriate method to be used to gather the required data. The following studies explain the methods used in each case. All methods have been validated against various methods showing a good level of agreement in both braid angle and fabric thickness.

4 Effect of twist on simple mandrels

When braiding components, it is common practice to control the tension and the layup of the fibres during the winding process. Kyosev [15] gives an overview of the practice of winding. Incorrect winding parameters can have a significant impact on the quality of the braid and the level of damage induced on the fibres. Applying a measured level of twist to the fibres during the winding process has been recommended by manufacturers but limited literature in academic journals has been published to support this. In this chapter, the effect of varying the level of twist on 12K fibres during winding has been investigated on simple circular mandrels, braiding on 48-carrier and 192-carrier axial braiders. The process of applying to twist during the winding process has been outlined in Chapter 3, Section 3.2.

4.1 Methodology

4.1.1 Winding Preparation

In total 4 levels of twist were selected for this study, 0, 3, 5 and 7 twists per meter (tpm). It is noted that any extra level of twist added to the fibres resulted in excess damage during the winding process. This is due to the sizing applied to the fibres during production, increasing the stiffness of the yarns and limiting the ability to flex the yarns without inducing damage. Intermediary levels of twist were chosen to understand the progressive behaviour of the yarn geometry with the addition of twist. T700SC-60E 12K Toray fibres were used, with winding completed on the Cezoma VLS-87 bobbin winder and the Eurocarbon Twist machine. The twist level referenced in this study is in addition to any twist applied by the manufacturer and gained during the braiding process.

4.1.2 Fabric Construction

Braided samples have been produced using a Steeger HS 140/48 48-carrier axial braider at the University of Nottingham (UoN) and the Eurocarbon 192-carrier axial braider at the National Composites Centre (NCC), both using a regular (2:2-1) braid pattern. Three constant circular cross-section mandrels have been selected for this study. A 32 mm and 50 mm diameter straight pipe mandrels were used on the 48-carrier braider at the University of Nottingham, in addition to a 200 mm diameter

mandrel used to investigate the effects of braider scale on the resultant architecture. This was braided using a 192-carrier braider at the NCC.

This study has been constructed with 4 parts, to develop a full understanding of the effect of additional twist on the resultant braided fabrics and components. This study enables the effect to be understood in small and larger braiders and in both dry preforms and infused panels. The aims and methodologies in each part are outlined below.

4.1.3 Dry Fibre Architecture

Aim: Investigate changes to dry braid architecture in 4-layer braided preforms on a 48-carrier braider at 0 tpm and 5 tpm.

Braided fabrics, produced on a 50 mm diameter mandrel, were analysed layer by layer using images, laser scanning and Apodius scanning. Methodologies for each of these techniques are outlined in Chapter 3. The stability of the braid angle, layer thickness and nesting between layers has been investigated. Braider process parameters for the braider are given in *Table 4-1*, to achieve a target angle of 45 degrees.

Table 4-1. Braider process parameters for samples produced in part A.

Fabric ID	Twist Per Meter (tpm)	Mandrel Diameter (mm)	Braider speed (rpm)	Take-up speed (mm/s)	Number of Layers	Repeats
1	0	50	2.23	4.636	4	3
2	5	50	2.23	4.636	4	3

4.1.4 Infused Architecture

Aim: Investigate the changes to flat infused 4-layer infused panels on a 48-carrier braider at different twist levels.

(a) (b) (c)

Figure 4-1. Methodology for sample production showing (a) braiding, (b) flattened fabrics cut from mandrel and (c) vacuum infusion process.

Within this part, 4-layer infused panels were produced from braid layers cut from the mandrel, using vacuum infusion. Each layer was braided independently to an overall length of 800 mm, secured, cut from the mandrel and flattened. The braid angle was analysed at 50 mm internals over the length before and after the removal process. This allowed the structure to be monitored and a sample length of 350 mm to be cut from a stabilised region of the braid. Each fabric was laid into a 4-layer preform. Analysis of the braid angle before and after cutting and flattening of the fabric shows no statistical changes to the architecture regarding yarn width and braid angle. *Table 4-2* outlines the parameters used for producing the braided fabrics within this study.

Table 4-2. Braiding parameters used for samples collected in part B.

Fabric ID	Twist Per Meter (tpm)	Mandrel Diameter (mm)	Braider speed (rpm)	Take-up speed (mm/s)	Layers per laminate
1	0	32	3.66	5	4
2	0	50	2.33	5	4
3	3	32	3.66	5	4
4	3	50	2.33	5	4
5	5	32	3.66	5	4
6	5	50	2.33	5	4

Two identical preforms were produced for each fabric with one being infused using a vacuum infusion process, shown in *Figure 4-1*, using Gurit Prime 20LV resin, while another being cast in the same Gurit Prime 20LV resin with no compaction pressure. This process allowed differences in yarn shape, arising from the moulding process, to be investigated. Samples were potted and imaged, using the methodology outlined in Chapter 3, Section 3.3.

4.1.5 192-Carrier Braider

Aim: Investigate the effect of braider size on the dry fabric preform at different twist levels.

Corresponding studies have been completed on a 192-carrier braider, investigating the effect of the scale of the braider on the resultant architecture. This has been completed using 0 tpm and 7 tpm fibres. The mandrel size has been scaled in relation to the scale of the braider with a 200 mm diameter mandrel used on a 192-carrier, as outlined in Chapter 3, Section 3.1.2. Yarn width and fabric thickness have been compared across braiders.

4.1.6 Yarn Damage

Aim: Qualify differences in yarn damage at different twist levels after braiding.

There have been many attempts to quantify yarn damage within the composites industry, however a repeatable standardised test has not been developed. Bulat et al. [101] states that damage is measured by the disintegration of the yarn. The condition of the yarn is related to the sizing, a chemical binder protecting each filament and adhered within each fibre yarn. Plonka et al. [102] concluded that the sizing integrity is key to the strength of the resin-fibre interface. Damage is expected within a braided fabric due to the process of the fibres during manufacturing. Lee et al. [103] recognises the repeated abrasion and bending of the fibres as the most prominent damage sources, unavoidable during the winding and braiding process. This has been echoed by Archer et al. [104] highlighting the rewinding process as a large contributor to fibre damage, demonstrating 5-6% degradation during this process.

Within this study, low reflective images of the braid surface have been taken using the Apodius 2D scanner camera to categorise the damage on the dry preform for each twist level. Ebel et al. [105] proposed a visual scale for the damage as shown in *Table 4-3.*

Table 4-3. Fibre damage levels as given by Ebel et al. [105]

Damage Level	Visual Description
0	Virgin fibre, no damage seen
1	Sizing degradation
2	Filament protrusion
3	Filament bundle protrusion
4	Sever damage
5	Broken yarn

4.2 Results and discussion

4.2.1 Dry Fibre Architecture Results

For the results presented in *Figure 4-2*, the methodology outlined in Chapter 3.4.4 has been used. A target angle of 45 was used for all fabrics, using a mandrel diameter of 50 mm. Braid angle measurements were taken at 20 mm internals along the length of the mandrel.

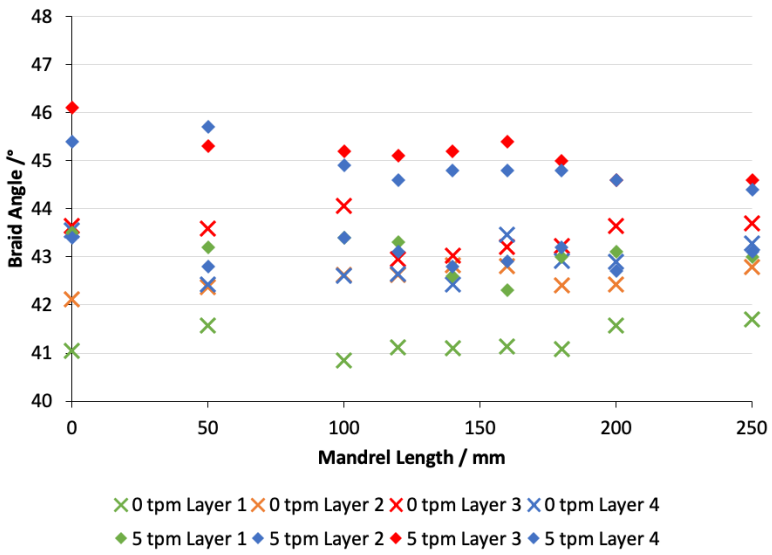

Figure 4-2. Measured braid angle data for 0 tpm and 5 tpm braided preform on 48-carrier axial braider.

Figure 4-2 highlights a minor effect on the braid angle for the difference in twist levels. Data shows a small reduction in the braid angle for 0 tpm, with a difference of 2-3° between twist levels for each layer. The reasoning behind this is expected to be due to variation in the levels of friction between fibres, leading to a change in the slip behaviour of the fibres between each other and the mandrel. This, as shown in subsequent sections, is due to a decrease in the yarn width for twisted yarns,

reducing the contact surface area between yarns. Between layers, minimal differences in braid angle are measured, with a minor trend towards a larger braid angle for the additional layers. This minimal increase is expected due to a small increase in mandrel radius with each subsequent layer added. Taking into consideration variation between tests, there appears to be very little statistical variation in the braid angle outside of the deemed variations within the braiding process. This was as expected, as the variables for braid angle typically do not include variables for yarn geometry unless jamming has occurred within the fabric, which was avoided within this study. It is noted that the grouping of the first and second layers and the third and fourth layers within 5 tpm fabrics is due to the decrease in coverage factor for these fabrics, allowing for a layer of nesting, possibly artificially affecting the braid angle.

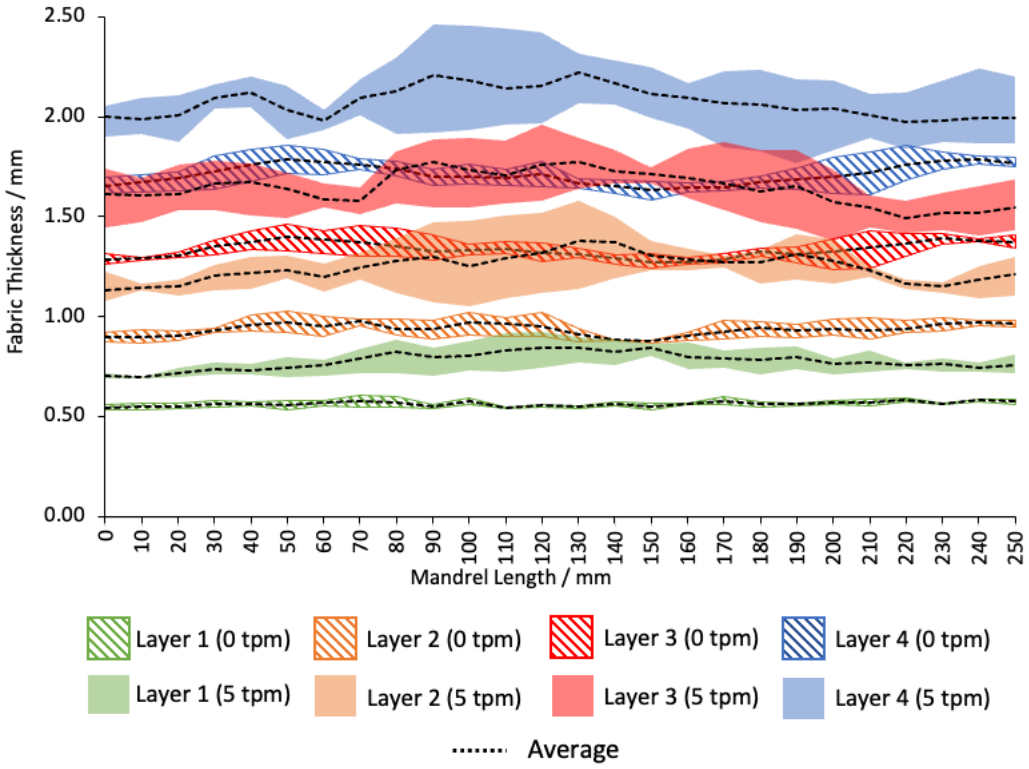

Figure 4-3. Measured preform thickness for 0 tpm and 5 tpm braided preforms on a 48-carrier axial braider.

Greater local variability is seen within the fabric thickness than within the braid angle. Fabric thickness data, presented in *Figure 4-3*, shows a significant effect between the levels of twist, both in terms of the thickness of the layers and the consistency of

the thickness of the fabrics. Analysis of the first layer shows an increase of 36% between 0 tpm and 5 tpm samples, with thickness increasing from 0.55 mm to 0.75 mm. This is seen to continue through each subsequent layer, with an average increase of 25% between 0 tpm and 5 tpm samples for all layers.

Using the assumption that the thickness of each subsequent layer is the same as the first layer, the level of nesting between the layers can be calculated. Nesting is defined as the percentage of the layer above, within the original boundary of the layer below (See Appendix F for derivation). Greater levels of nesting are observed within 5 tpm fabrics with an average nesting level of 44% compared to 33% for 0 tpm. However, this increase in nesting does not negate the increase in thickness of the yarns, leading to an increase in the total thickness of 4 layers of 0.35 mm from 1.72 mm to 2.07 mm. This would have a significant effect on tool requirements for RTM tool void thickness during post-processing.

Importantly consistency is observed within the 0 tpm fabrics, as presented in the spread of data in *Figure 4-3*. Comparing layer 1 for each twist level, the 0 tpm fabric has a standard deviation of 0.03 mm compared to 0.06 mm for the 5 tpm fabric. This increased to 0.07 mm in layer 4 for 0 tpm, with the 5 tpm samples increasing to 0.16 mm. The standard deviation is expected to increase with additional layers due to the greater levels of variation of the surface being braided onto. Increased nesting, damage to lower layers and local variations in braid architecture and yarn geometry all affect the subsequent layers. This could lead to significant problems for the prediction of a multilayer component, often braided between 8-12 layers.

4.2.2 Infused Architecture Results

During the infusion process, significant changes to yarn geometry are often observed. This can be due to external pressure applied to cause consolidation of the yarns and layer or due to resin flow and lubrication of the layer during the injection of resin. As discussed, changes in dry preform geometry can be seen in dry fabric preforms, particularly within thickness data for changes in twist levels. This has led to Part B of this study investigating the effects seen during the infusion process, using the vacuum infusion process. Optical microscopy images of samples outlined in *Table 4-2*

are presented below. The method for the collection is outlined in Chapter 3, Section 3.3.

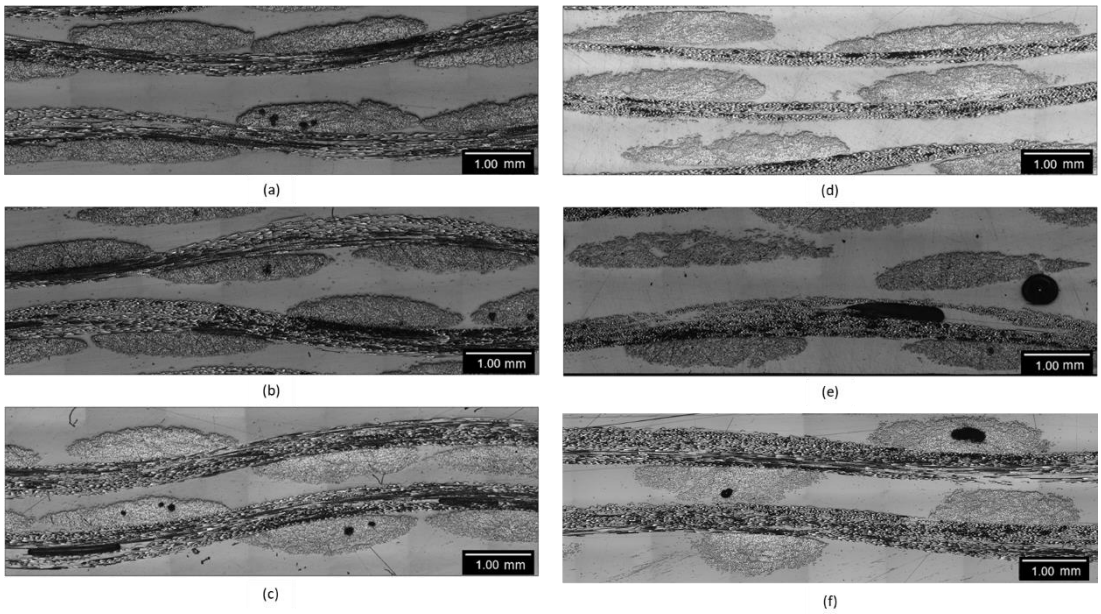

Figure 4-4. Optical Microscopy images of yarn cross-sections of dry preform braided fabrics. (a) 0 tpm, (b) 3 tpm 32mm, (c) 5 tpm all on a 32 mm ∅ mandrel and (d) 0 tpm 50 mm, (e) 3 tpm 50 mm and (f) 5 tpm all on a 50 mm ∅ mandrel.

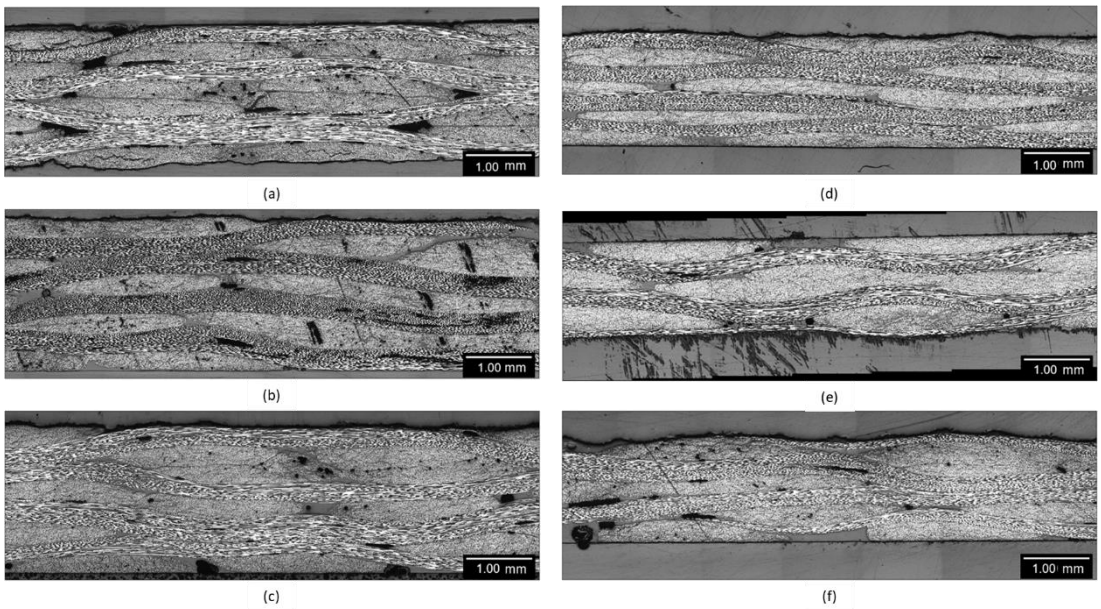

Figure 4-5. Optical Microscopy images of yarn cross-sections of infused preform braided fabrics. (a) 0 tpm, (b) 3 tpm 32mm, (c) 5 tpm all on a 32 mm ∅ mandrel and (d) 0 tpm 50 mm, (e) 3 tpm 50 mm and (f) 5 tpm all on a 50 mm ∅ mandrel.

Changes to yarn width and thickness at different twist levels for dry preforms and infused panels are presented in *Figure 4-6* and Figure *4-7*. This shows little change to the width of the yarns in samples braided on the 32 mm diameter mandrel for both an increase in twist level and post the infusion process. As predicted the high level of coverage (<99%) has caused lateral compaction of the fibres during the braiding process, resulting in decreased levels of fibre spread during the infusion process. Alternatively, samples braided on the 50 mm diameter mandrel show a reduction of 20% in the yarn width between 0 tpm and 5 tpm. This was expected from the thickness data observed in Part A, with the assumption of yarns having a constant cross-sectional area when braiding with lower coverages.

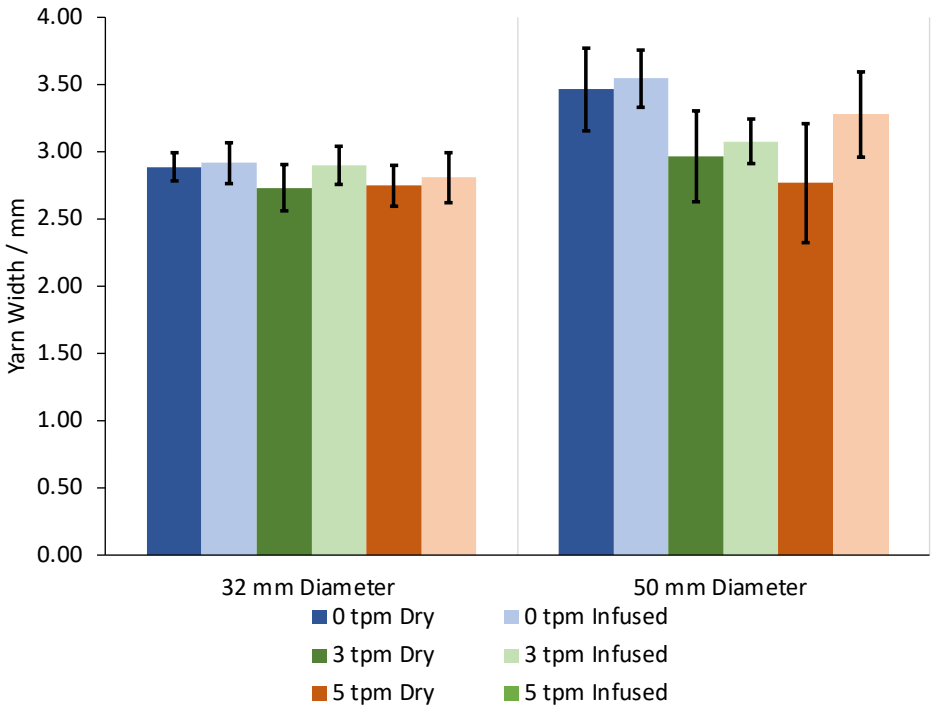

Figure 4-6. Effect of twist on yarn width for dry and infused laminate.

Typically, during an infusion process yarn thickness compaction and yarn spread would be expected due to the pressure applied to the fabric. This can clearly be seen in the 5 tpm 50 mm infused sample, with an 18.3% increase in yarn width and a 37.2% reduction in yarn thickness. Yarns with no additional twist show similar levels of yarn thickness reduction but minimal width increases post-infusion. Reduced initial yarn width for twisted samples increases the gaps between yarns within the fabric, encouraging yarns to spread or nest during the infusion process. Additionally, during the twisting process the sizing on the yarns, which helps hold the yarns shape and

bundle of fibres together, may have experienced additional damage. Once an external pressure from the infusion process is applied the yarns can spread more easily. Further investigations into the behaviour of the yarns post-braiding would need to be conducted to fully understand the mechanisms behind this phenomenon. Yarn thickness compaction, presented in *Figure 4-7*, is seen to be stable across all samples with an average percentage reduction of 29% for samples braided on the 32 mm mandrel and a 36% reduction for samples braided on the 50 mm mandrel.

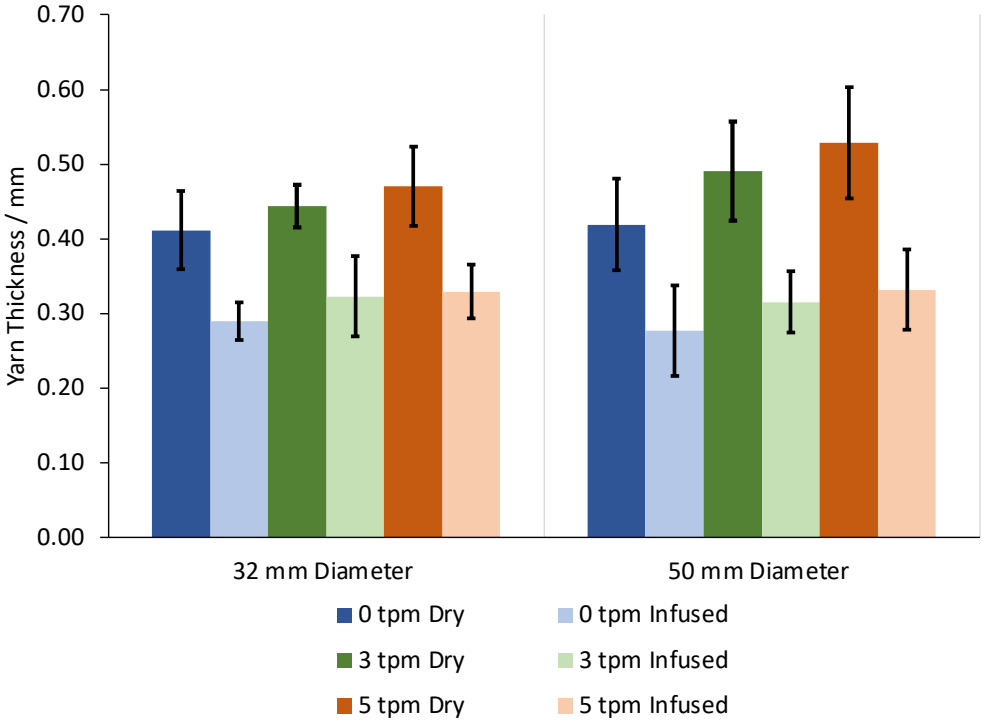

Figure 4-7. Effect of twist on yarn thickness for dry and infused laminate.

Yarn thickness levels have converged for infused braids on both mandrels, indicating variation in the yarn volume fraction values due to differences in the yarn widths measured. Difficulties arise in the measuring of yarn volume fractions from microscopy data due to the requirement of determining the total area of the yarn. Therefore, lenticular-shaped yarns have been modelled in TexGen with yarn width and thickness taken from *Figure 4-6* and Figure *4-7* using T700 12K yarns with a fibre diameter of 7µm. The results of this are presented in *Table 4-4*. This shows a marginal increase in volume fraction for untwisted samples but has little statistical differences due to the variability of yarn geometry. A significant increase in yarn volume fraction is observed for infused yarns, as expected due to the compaction pressure applied

during the infusion process. This shows initial yarn geometry has little effect on the yarns ability to reduce cross-sectional shape and increase yarn volume fraction.

Table 4-4. Predicted yarn volume fractions based on geometry measured.

Yarn Sample	Dry Yarn Volume fraction (%)	Infused Yarn Volume Fraction (%)
32 mm 0 tpm	47.8	72.4
32 mm 3 tpm	47.2	66.0
32 mm 5 tpm	43.9	66.1
50 mm 0 tpm	38.7	61.8
50 mm 3 tpm	39.0	63.0
50 mm 5 tpm	38.6	58.0

In addition to changes to the yarn geometry, the overall thickness of the composite panel was analysed, as shown in *Figure 4-8*. This analysis shows little difference in the panel thickness for different twist levels, as expected due to similarities in the yarn thickness data for the range of twist levels.

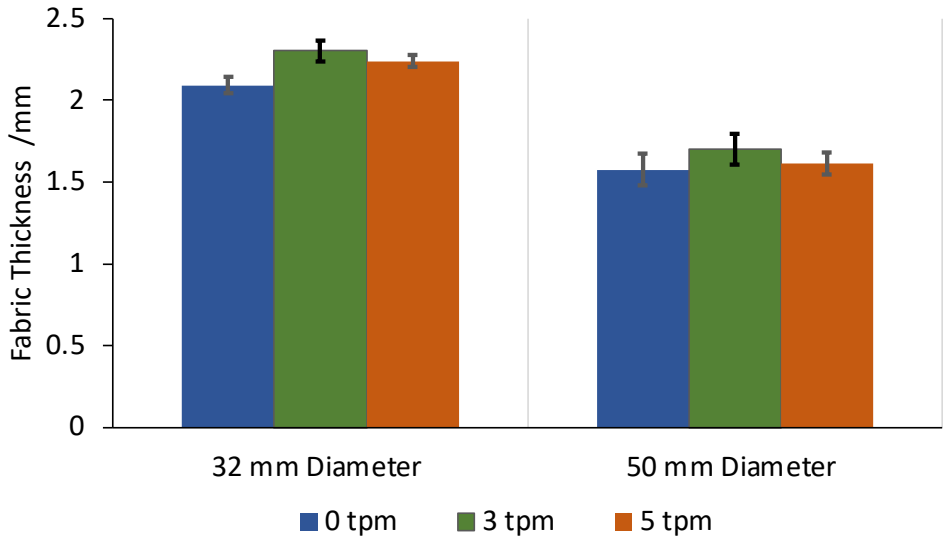

Figure 4-8. Effect of twist on 4-layer laminate thickness.

A difference is observed in the thickness of the panels produced from different sizes of mandrels, with the panels produced from 50 mm mandrels on average 26% thinner. This results from a lower coverage fabric allowing for greater nesting between the layers. Microscopy data presented in *Figure 4-5* shows increased voids for the equivalent fabric produced on 32 mm mandrels. This is due to increased yarn density causing resin penetration between layers to be harder. Observationally an

increase in resin-rich areas is seen for increased twist samples in *Figure 4-5*, due to gaps within the fabric. This increase in gaps for braided fabrics is due to the reduction in yarn width and can be seen in *Figure 4-9* and is similarly reported by Cheung et al. [44]. Both effects would be seen to have detrimental effects on the mechanical properties of the composite. This is seen in a reduction in fibre volume fraction from 48.1% to 42.6% between samples shown in *Figure 4-5 (d)* and *Figure 4-5 (f)* respectively.

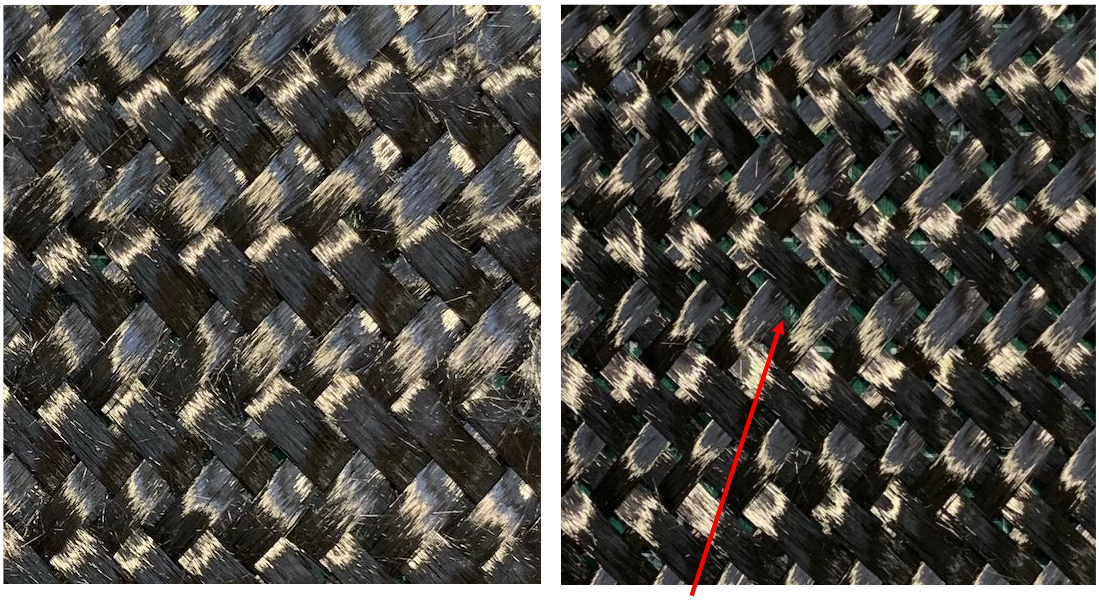

Figure 4-9: Images of (a) 0 tpm fabric and (b) 5 tpm fabric produced on a 50 mm mandrel showing larger gaps in the fabric, leading to resin-rich areas within the infusion process

4.2.3 192-Carrier Braider Results

A small amount of academic research has shown the effect of scale on the resultant braiding architecture. With a greater number of fibres and a larger diameter mandrel, braiding on a 192-carrier braider and comparing to data collected on the 48-carrier braider has been completed in this section.

Single-layer fabrics were produced on a 200 mm diameter circular mandrel with 0 tpm and 7 tpm fibres. A total length of 1.5 metres of braid was produced for each run to ensure a stabilised fabric for the measurements. This location was determined as the point at which 4 consecutive braid angle measurements were within a 2° range

of the target angle. In this case, fabrics were manufactured to a 45° angle. Images were collected from a stabilised region at 50 mm intervals over the length. Processing of these images was conducted within ImageJ software. Each fabric was repeated three times to gather an average yarn geometry. Yarn width measurements are presented in *Figure 4-10*.

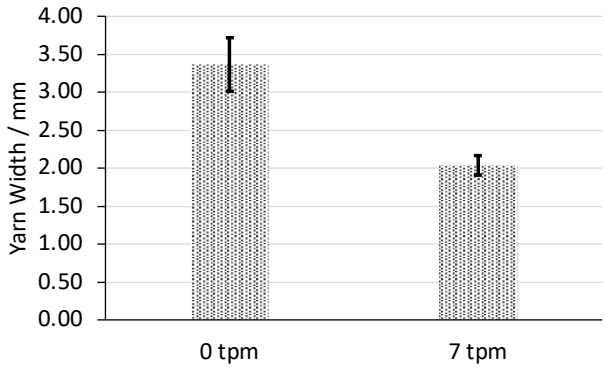

Figure 4-10: Yarn Width data for 0 tpm and 7 tpm yarns braided using a 192-carrier braider on a 200 mm diameter straight pipe.

Data shows a similar trend to those presented for fabrics produced using the 48-carrier braider. Twisted fibres show a significant reduction in the measured yarn width when compared to untwisted fibres. Braids produced using 0 tpm fibres show an average yarn width of 3.36 mm compared to 2.03 mm for the same fabrics produced with 7 tpm fibres. Additionally, reductions are seen in the variability of the yarn widths with an increase in twist levels leading to greater confidence in the predicted shape and a greater level of consistency in the fabric.

Comparing data between braiders for 0 tpm fibres, there are no statistical differences in the yarn width from the different braiders. An average yarn width of 3.46 mm for fabrics produced using the 48-carrier braider compared with an average yarn width of 3.36 mm using the 192-carrier braider. As with data from Part B, the addition of excess twist during the winding phase is seen to have a significant effect on the resultant yarn width, with a 39% reduction in yarn width for fabrics produced with 7 tpm yarns, compared to 0 tpm yarns.

This data supports the theory that the scale of the braider haves a negligible effect on the geometry of the yarns and fabric produced. *Figure 4-11* shows a full range of

measured yarn widths from 0-7 tpm T700-60E 12K carbon fibres. This shows a linear reduction in yarn width for an increase in twist level. This indicates the ability to manufacture scaled prototypes models before full scale manufacture is developed. However further comparison of similar twist levels is required to understand the full effects of the scale of the braider.

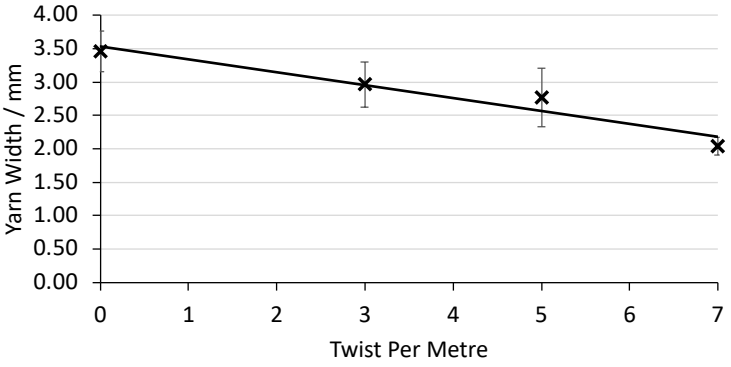

Figure 4-11: Relationship between additional twist during winding and yarn width in braided fabrics.0, 3 and 5 tpm data taken from 48-carrier braider and 7 tpm data taken from 192-carrier braider.

4.2.4 Yarn Damage Results

Figure 4-12 shows typical images taken of the surface of the braids using the Apodius 2D low reflective camera. An increase in fibre damage is observed in braids with lower levels of twist. This is determined by the increase in the level of stray fibres on the surface. The results of this may have negative effects on the mechanical properties of the composite as the fibre-resin boundary will be impacted. Using the scale presented by Ebel in *Table 4-3*, the 0 tpm fabrics would be classified as level 2 damage, whereas the 5 tpm samples would be level 1. Cheung et al. [44] presents tensile data for untwisted and twisted braided composites, showing an increase in maximum tensile load for twisted samples. This is theorised to be due to excess damage in untwisted samples.

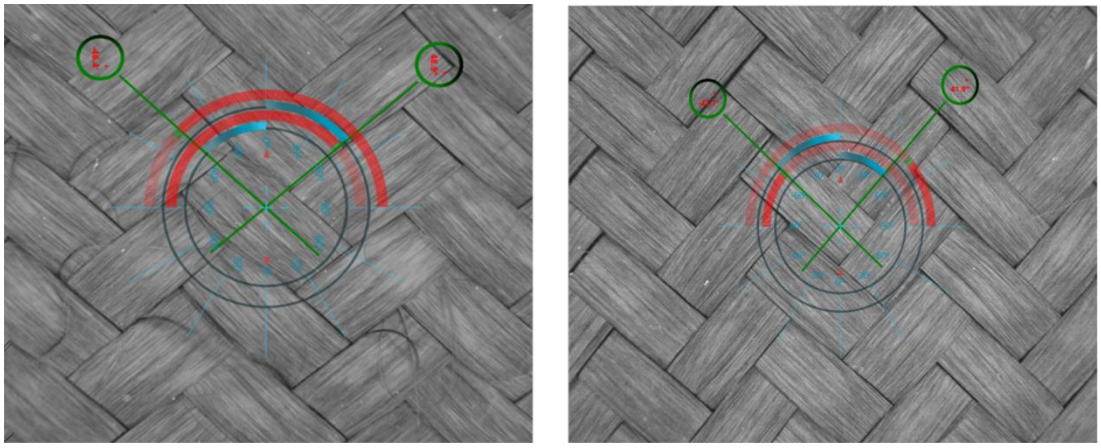

Figure 4-12. Sample low reflective images of braids at 0 tpm and 5 tpm.

The mechanism behind the increase in filament breakages in the yarns can be explained by increased friction in the cross-over regions due to the increase in surface area of the 0 tpm fibres as they cross, shown in *Figure 4-13*. This causes an increased lateral force on the yarn, damaging the sizing on the yarn, splitting the yarns apart and damaging the fibres. Additional damage will occur with the same mechanism on the guide ring.

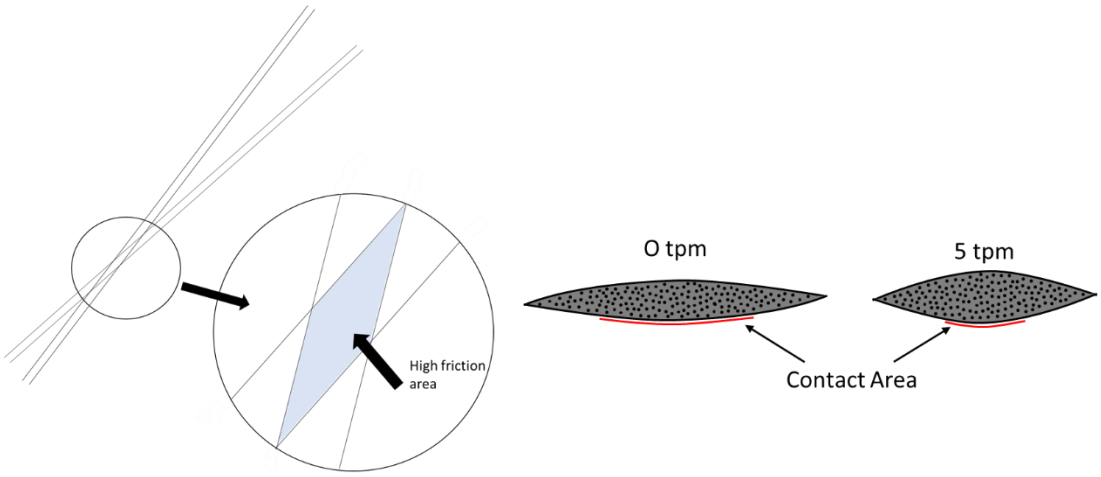

Figure 4-13. Increases in frictional forces on flatter 0 tpm yarns within the cross-over regions in the braiding process leading to an increase in filament damage within the fibres.

Further observations have been made for the overall process of braiding with different twist levels. An increase in yarn breakages was seen in 0 tpm yarns compared to 5 tpm. Investigation of the bobbins during yarn breaks shows an increase in the agglomeration of broken filaments on the bobbins known as a fibrous

ring, as shown in *Figure 4-14*. This would impede the unwinding of the yarns during the braiding process, causing the tension within the yarns to rise to an excessive level, leading to yarn breakages. This process was not seen during the braiding of the 5 tpm yarns. Yarn breakages can cause a significant reduction in the mechanical properties of the composite if left within the structure [106], or an increased level of wastage of fibres if the braid is required to be started again to produce a defect-free fabric.

Figure 4-14. Fibrous ring observed during braiding on 0 tpm fibres causing yarn breakages.

4.3 Conclusions

The findings show twist has a significant effect on the geometry of the yarns after braiding. Trends show higher twist levels lead to narrower and thicker fibres during the braiding process but with higher levels of variability within the braid. Data has shown minor effects of the braid angle but larger effects on coverage factor and preform thickness. Greater variability of yarn geometry and preform thickness has the potential to lead to further problems in the manufacture of components when using RTM infusion, however this has not been investigated within this study.

The change in geometry before and after the infusion process has been presented, with little difference being seen in the overall thickness of the composite panel for different twist levels. This is explained by an increase in fibre spread as a result of the pressure applied to the sample, as well as increased layer-to-layer nesting within the sample. A decrease in composite quality for increased twist levels was observed with an increase in resin-rich areas and voids within the panels, potentially having significant effects on the mechanical properties of the composites.

Comparisons between scales of braider have been presented with emphasis on yarn width and fabric thickness. This indicates yarn widths are not affected by an increase

in the size of the braider, with similar widths presented for both braiders using 0 tpm yarns. This leads to the conclusion of scale tests are able to be conducted with results transferable to larger studies.

Finally, the level of damage to the yarns was observed between twist levels, with an increase in damage for lower twist level samples. This is expected to be due to two mechanisms. (1) The unwinding of the bobbins leads to damage to the portion of the yarn being unwound and the portions on the surface of the bobbin, this leads to agglomeration of broken filaments on the surface of the bobbin, causing the yarn to be unable to unwind and breaking the yarn. (2) Once leaving the carrier the shape of the 0 tpm yarns causes filament separation as the fibres slide along each other during braiding, leading to an increase in broken filaments within the braid.

Work presented in this chapter enables a fundamental understanding of the process and effects of twist on stabilised braids. This is expanded in Chapter 5 to investigate the effect on conical-shaped mandrels, understanding how diverging and converging sections affects the braid architecture.

5 Effect of twist on complex mandrels

As covered in the previous Chapter, applying a measured level of twist to the fibres during the winding process can significantly affect the architecture of the braid in both dry and infused fabrics. To expand this work, the effect on complex mandrels has been investigated to understand the effects of conical sections of a mandrel on the braid architecture, including how converging and diverging conical sections result in changes within the braid. Similar work has been completed by Du and Popper [32], showing some changes to the architecture for diverging and converging conical sections. However, this was limited to a single speed profile, unrealistic under typical braiding requirements. This work was extended by Ravenhorst [41] investigating complex mandrel shapes including conical sections. This was limited to braiding on a converging conical section with a slope angle of 10°. The present study has been conducted using a 48-carrier braider and a 192-carrier braider to quantify the effect of scale on the braid architecture.

5.1 Methodology

5.1.1 Braiding Parameters

Two prismatic conical sections were used within this study on a 48-carrier braider to understand the effect of slope angle on changes in braid architecture. Du et al. [32] shows a significant improvement in the stability of the braid over the conical sections for mandrels with smaller slope angles at constant speeds. This research will add to this, demonstrating the effect of conical sections with a constant target braid angle of 45° along the length of the mandrel. This is achieved by varying the take-up speed during variable cross-sections. The geometry of the mandrels is shown in *Figure 5-1.*

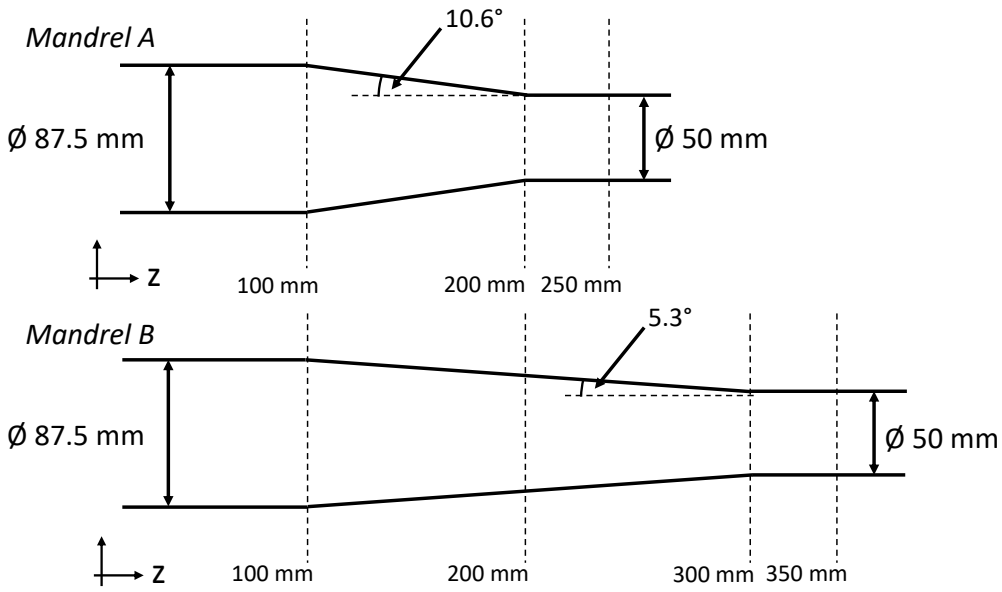

Figure 5-1. Mandrel geometry for braiding on 48-carrier braider.

Braiding of the mandrels will be conducted with 0 twists per meter (tpm) and 5 tpm yarns wound using the technique outlined in Chapter 3, Section 2.0. Toray T700SC-60E 12K fibres have been used, enabling a comparison of the data to the previous study using circular mandrels. Each mandrel was braided with 4 layers, with data gathered after each layer. Braiding was conducted in in both directions of the mandrel, with diverging and converging conical sections presented in the results section. Definition of the mandrel geometry for each is shown in *Figure 5-2.*

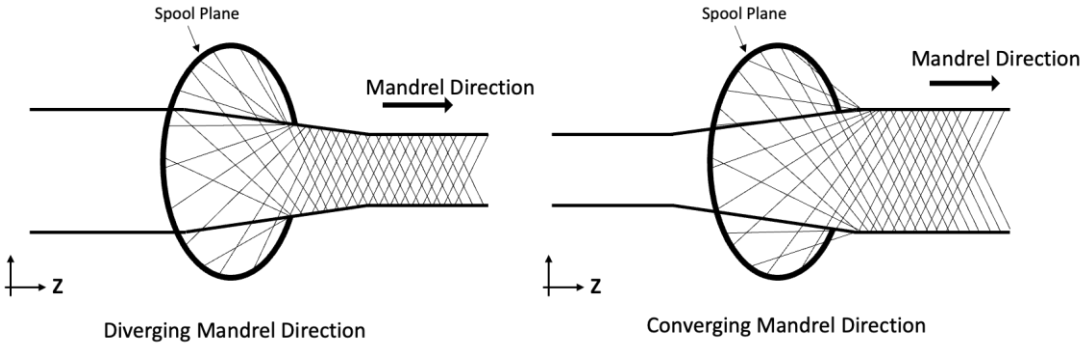

Figure 5-2: Mandrel braiding directions for diverging and converging conical sections.

As previously mentioned, the braiding conducted within this study aims to achieve a constant angle over the length of the mandrel. To achieve this, changes have been made to the mandrel take-up speed as the cross-section of the mandrel changes.

Figure 5-3 shows the take-up speed for Mandrel A and B, with a constant horn gear speed of 21.3 RPM.

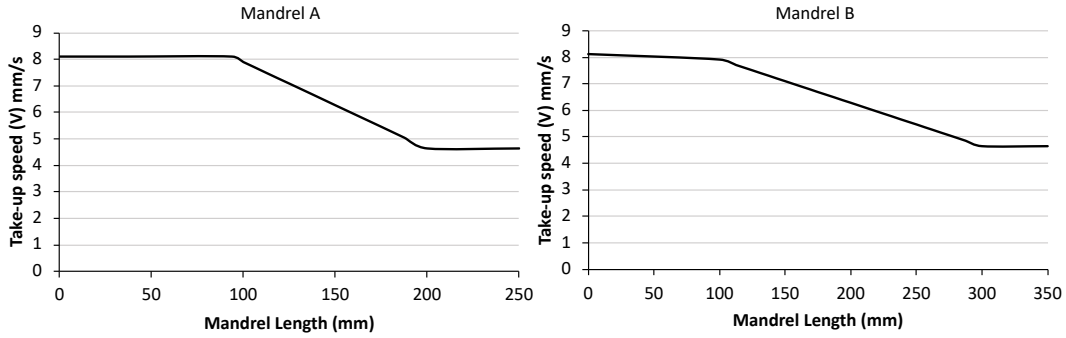

Figure 5-3: Speed profile for mandrel length for Mandrel A and Mandrel B. Data based on analytical models.

In addition to braiding on a 48-carrier braider, the work has been completed using a 192-carrier braider with 0 tpm and 7 tpm fibres. The geometry of the mandrel used, Mandrel C, is given in *Figure 5-4*. Due to limitations single layer data was collected on the larger braider.

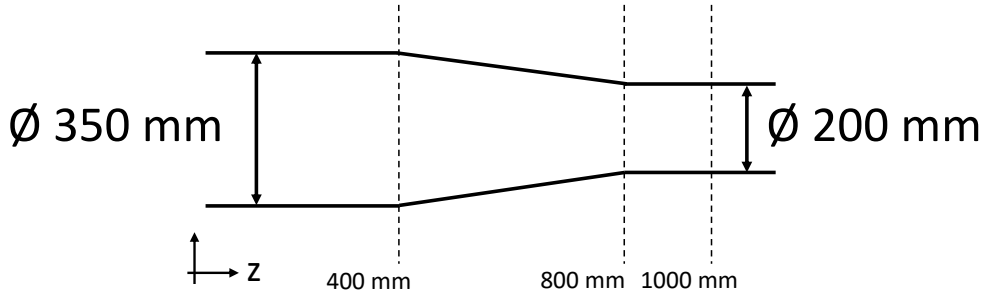

Figure 5-4. Mandrel C geometry for braiding on 192-carrier braider. Axial lengths are given in mm.

5.2 Results and Discussion

The results presented within this section are taken over 3 repeats. Braid angle and fabric thickness have been measured on mandrels A and B to understand the effect of yarn twist on complex mandrels with respect to the braid architecture. Results are compared to a similar study completed on a simple circular mandrel presented in Chapter 4.

5.2.1 Mandrel A

Measured braid angles from data collected from fabrics produced on Mandrel A are presented in *Figure 5-5*. Results are shown for converging and diverging conical sections.

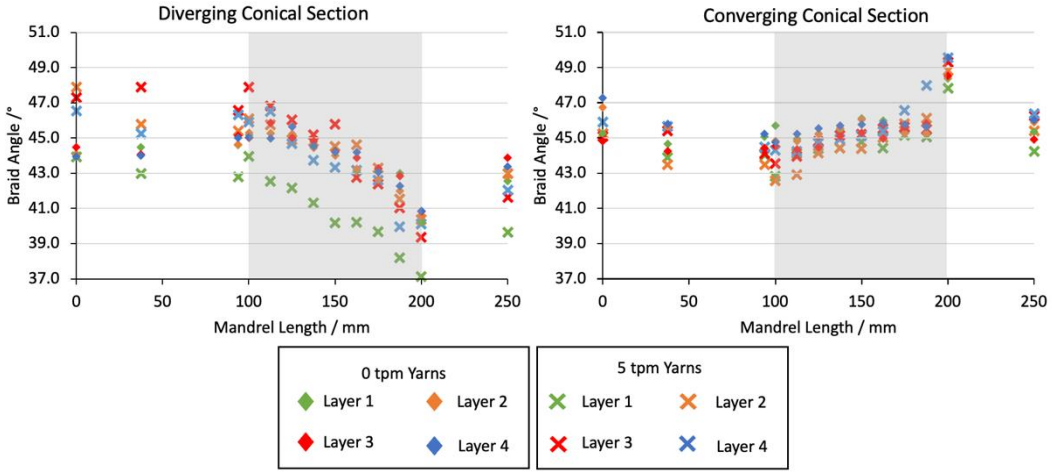

Figure 5-5. Measured braid angles over converging and diverging conical sections for 4-layer biaxial braids on Mandrel A, variable cross-section shown in grey.

Although braider parameters have been adjusted to compensate for changes in cross-section, the results show an influence of mandrel geometry on the braid angle. Braid angles are seen to clearly deviate from the target angle during the conical section, shown in grey in *Figure 5-5*, before returning close to the target following a period of stability in the cross-section of the mandrel. The results from this study echo those results from Du et al. [32], with less deviation in braid angles measured for converging sections in both twist levels, with a maximum 13% deviation from the target angle compared to an 18% maximum deviation for diverging sections. The maximum deviation values are observed at the end of the sloped section of the mandrel for braiding in both directions and are repeated in all layers of the braid, represented by an axial length of 200mm in *Figure 5-5*. This difference is caused by yarns slipping on the mandrel during the braiding process, seen to be more severe on diverging sections. As the braid is being formed, the fell point is being forced wider as the mandrel progresses, destabilising the braid being formed and leading to yarns slipping on the surface. This is not seen in the converging samples as the fell point diameter is decreasing as the braid processes, leading to a more stable braid.

Braid angle deviation is seen to occur in opposite directions when braiding in different directions, with angles increasing for converging sections and decreasing for diverging sections. For diverging conical sections sharp geometrical changes required end of the sloped section causes the yarns to bend significantly, as shown in *Figure 5-6*, for the yarns to maintain contact with the mandrel. This sharp change causes the yarns to slip within the braid, decreasing the braid angle. This will have some influence on the braid angle further down the slope as the yarn moves with diminishing effects as the braid constrains the fibres. Measurements are taken post-braiding and thus are not able to capture the braid angle at the fell point in real time to quantify the level of slippage in the braid as it is formed. Observations in fabric thickness presented in *Figure 5-8*, show a sharp reduction in fabric thickness corresponding to this location. The bending and slipping of the yarns cause compaction and spreading of the cross-sectional shape of the yarns leading to a reduction in the thickness of the overall fabric. This is seen in all layers across both 0 tpm and 5 tpm tests as seen in *Figure 5-8* at axial lengths of 200 mm. This effect may lead to post processing issues, during infusion. The reduction in thickness will create regions of high-volume fraction within the fabric, leading to decreased permeability. The high levels of thickness variation along the length of the mandrel will cause issues across the whole length, with race-tracking possibly occurring in regions of increased thickness.

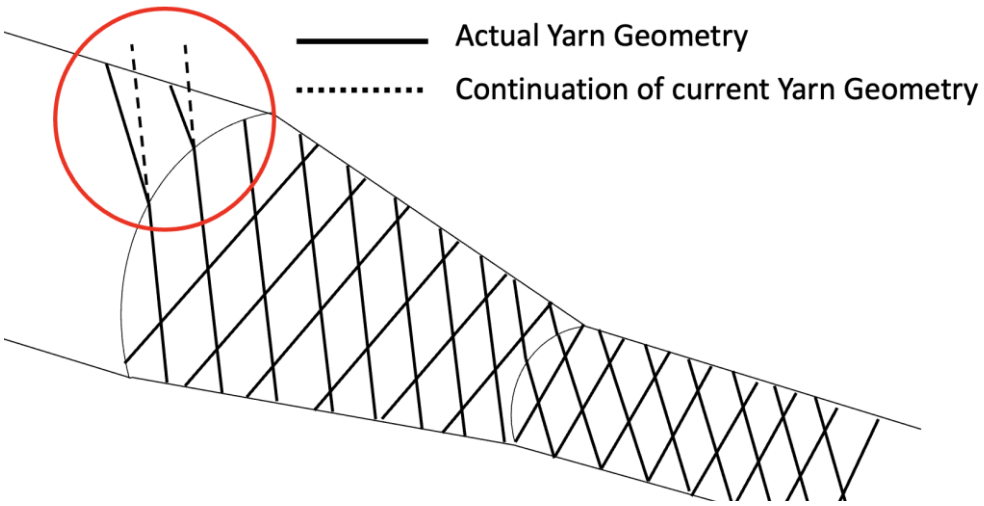

Figure 5-6: Changes in yarn geometry at end of sloped section for diverging conical mandrels.

Concerning the sharp peak braid angle seen on converging conical sections, the results indicate the braid is not following the contours of the mandrel causing the increase in braid angle. In observations of the fabric thickness, presented in *Figure 5-8*, a peak in fabric thickness correlates to this point, indicative of the bridging of the yarns across this section. Ravenhorst [41] is seen to reverse the speed profile of the mandrel in such sections to combat this bridging effect.

Comparing twist levels within *Figure 5-5*, minimal differences can be seen between 0 tpm and 5 tpm for the converging section. Similar trends, indicating bridging of the fabric, can be seen at the base of the sloped section. Alternatively, when comparing diverging sections, greater instability between layers of the fabric is observed within 5 tpm samples. This is the result of reduced coverage of the fabric produced for twisted yarn fabrics. Decreased yarn widths increase the spacing between yarns, giving rise to greater chance of excessive yarn slippage. This effect is shown in Figure 5-7 with a surface profile scan shown for braids produced at each end of the mandrel. This explains the discrepancies between 0 tpm and 5 tpm measurements for diverging sections. These results show that effects of yarn twist levels can be observed within the braid angle for complex mandrels, with both the yarns being braided and the direction of the sloped sections leading to changes in the braid angle. To further understand changes to the fabric, thickness measurements were taken for each layer of the braid using a laser scanner. The technique for this is outlined in Chapter 3, Section 3.4.3. The results of this are presented in *Figure 5-8*. A reduction in fabric thickness is seen for fabrics produced with untwisted yarns, aligned with results presented for simple mandrels in Chapter 4. However, changes in mandrel geometry have led to instability in the fabric thickness for both converging and diverging conical sections.

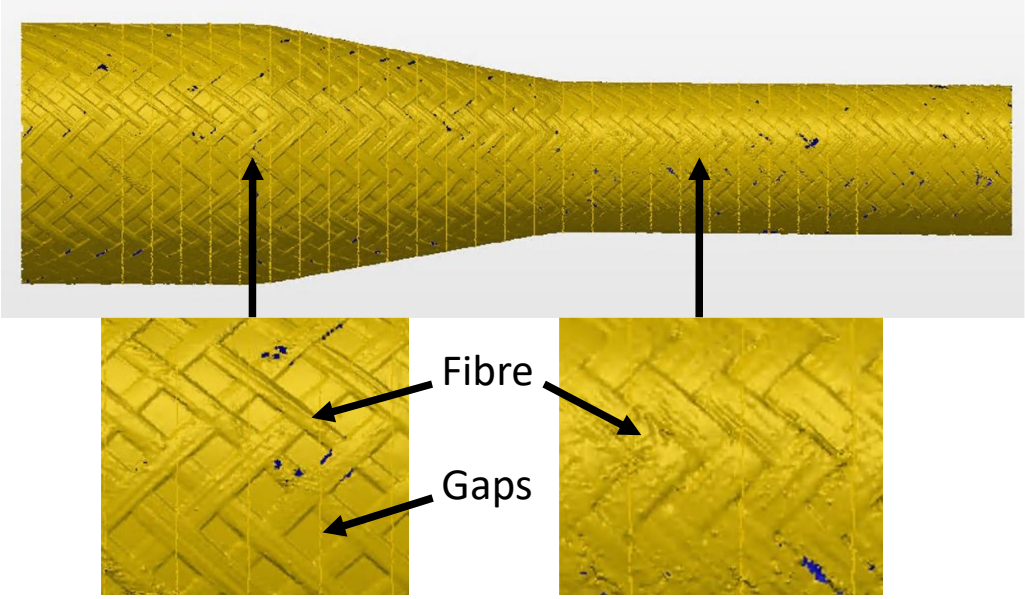

Figure 5-7: Representative image of scan data from braid with profiles shown on larger and smaller diameters.

All braids show a high level of repeatability for the measured thickness of a single layer with an average standard deviation of 0.02 mm for thickness measured between the first layers of 5 tpm yarns on a converging section. Similar results are seen across all tests. This repeatability is lost in all subsequent layers of the fabric with increased variability in fabric thickness clearly seen in layer 4 compared with layer 1 for all samples. This is expected as the braid is formed on an uneven surface for each subsequent layer, due to the presence of previous layers of braided fabric. Equivalent effects are seen in the data presented in Chapter 4. This uneven and unpredictable braid surface, particularly in lower coverage regions, causes unpredictability within the fabric. Measurements taken in the areas of highest coverage, for example, 0-100 mm axial length on a diverging direction mandrel show high levels of repeatability. With higher coverage, the yarns have less ability to slip between yarns or move within the braided structure, improving repeatability. The reduction in the coverage experienced using twisted yarns shows an increase in the variability of the braided fabric.

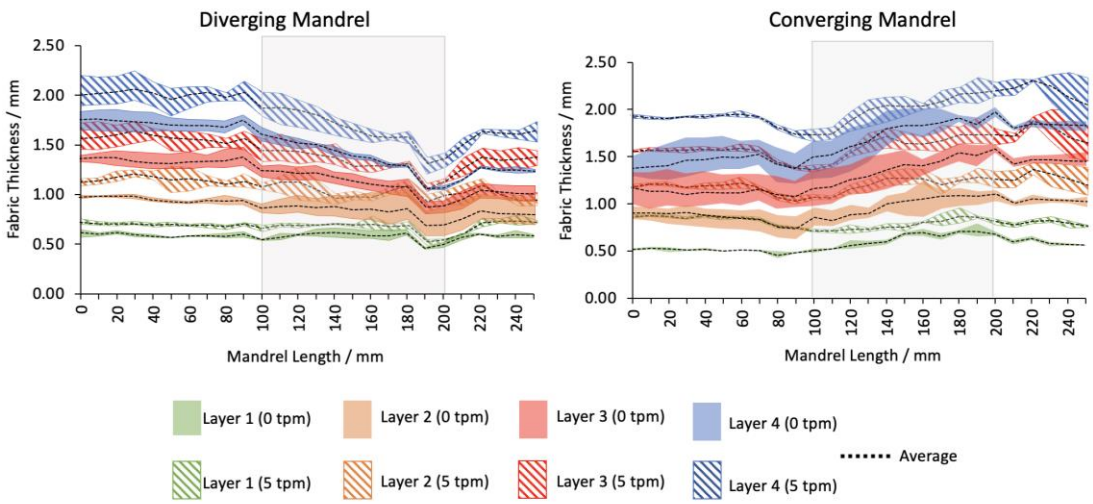

Figure 5-8: Measured fabric thickness for diverging and converging conical sections using mandrel A. Results are presented for fibres with 0 tpm and 5 tpm. The conical section of the mandrel is highlighted in grey.

0 tpm fabrics are shown to lead to thinner fabrics compared to the equivalent 5 tpm fabrics. A 4-layer average thickness of 1.47 mm and 1.53 is observed for 0 tpm samples on diverging and converging conical sections respectively. This is increased to 1.76 mm and 1.87 mm for equivalent 5 tpm fabrics. This has knock-on effects for the prediction of cavity size for tpm tooling with twisted fabrics requiring fewer layers of fabric to fill the cavity thickness.

The direction of braiding has little effect on the fabric thickness with similar trends seen for equivalent spots on braided formed in each direction, with each fabric increasing in thickness at smaller diameter sections. This is caused by increased coverage limiting the spread of the yarns during the braiding process.

Overall, it can be seen that complex mandrel shape has a significant effect on the architecture of the resultant braided fabric, with both the conical shape and profile affecting the fabric.

5.2.2 Mandrel B

To investigate this effect further, a similar conical section has been braided with a shallower cone angle as seen in Mandrel B. This enables the effect of the severity of complexity in the mandrel to be linked to the stability of the braided fabric. The results for this are presented below.

Comparing results from Mandrel B presented in *Figure 5-9* to the equivalent fabrics in *Figure 5-5*, significant increases in braid angle stability can be seen. Previous fabrics showed large levels of deviation from the target angles across the sloped section of mandrels in all cases. This is reduced to a negatable deviation for those produced on the shallower conical section, equivalent to those presented in Chapter 4 on simple constant cross-sectional mandrels. The stability seen in the braid angle indicates limited yarn slippage during braiding, enabling the conclusion that cone angles of 5 degrees or less, result in more predictable and stable braiding with respect to the braid angle.

Observing 0 tpm yarns compared to 5 tpm fibres limited conclusions can be drawn with a similar spread of braid angles across all 4 layers and similar trends, echoing the results of the simple mandrel results.

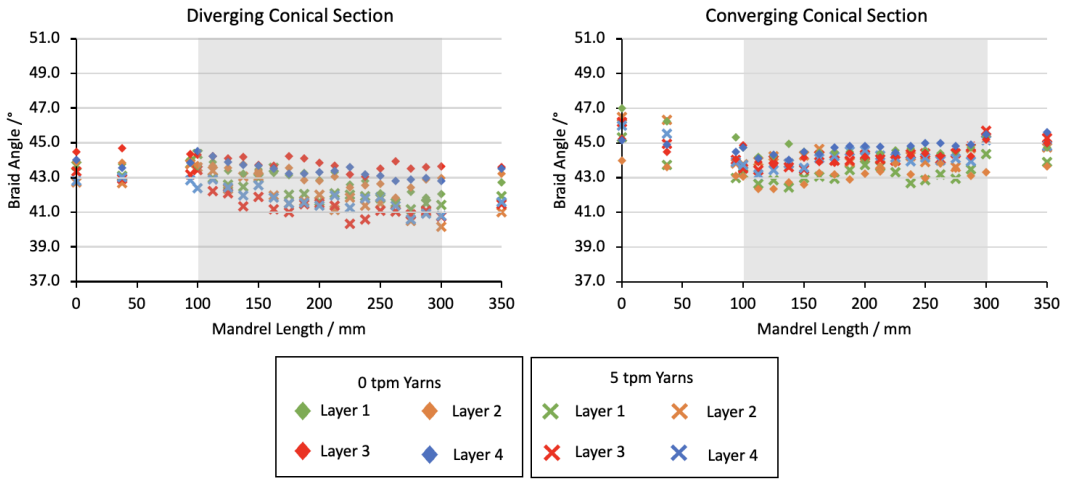

Figure 5-9: Measured braid angles over diverging and converging conical sections for 4-layer biaxial braids on Mandrel B, variable cross-section shown in grey.

To investigate these differences further, fabric thickness measurements are presented in *Figure 5-10* showing greater variability between twist levels, braiding direction and when compared to simple mandrels. As with all samples braided within this study, fabrics produced using 0 tpm fibres are shown to be thinner than the equivalent fabrics produced using twisted yarns. This resultant increase in fabric thickness is seen across all layers leading to the conclusion twist must be controlled and measured during the winding process to ensure accurate predictions of the fabric thickness, resulting in accurate design for RTM tooling to create composite parts.

Similar trends are seen across samples for braiding direction, compared to those produced on Mandrel A. Thickness is seen to decrease with an increase in mandrel radius. This is caused by the yarn spreading due to decreases in the cover factor of the fabric. This effect is less severe with the larger conical section, as there is less overall fibre slippage adding to the effect. A similar peak in thickness at the base of the conical section at an axial length of 300 mm, is seen for fabrics produced on converging conical sections. This is indicative of bridging in the fabric on the mandrel shape.

Additionally, the same effect of increased instability in additional layers can be seen for fabrics produced on Mandrel B. This is explained through braids being formed on an uneven surface for layers 2-4, compared to the smooth mandrel surface for layer 1 fabrics, similar to those presented for Mandrel A.

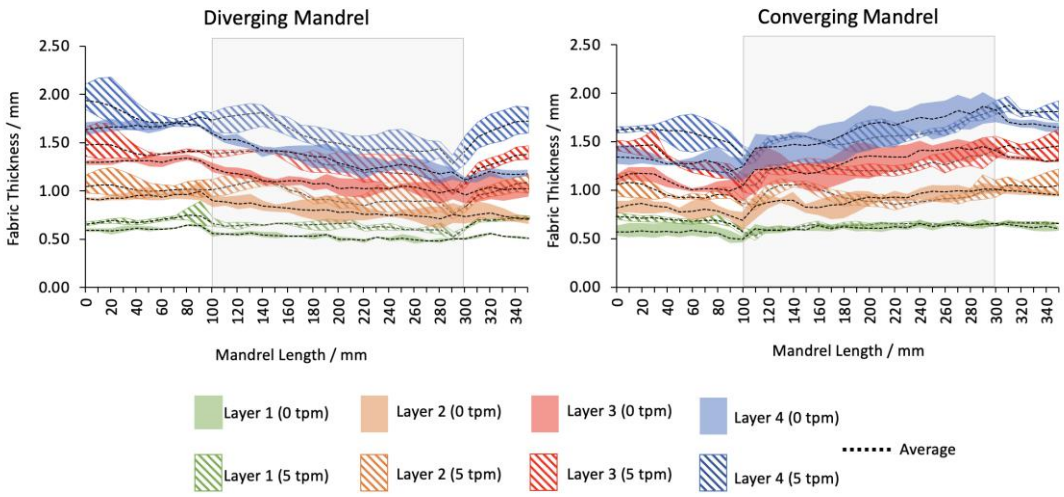

Figure 5-10: Measured fabric thickness for diverging and converging conical sections using mandrel B. Results presented for fibres with 0 tpm and 5 tpm. The conical section of the mandrel is highlighted in grey.

Results from these studies show how the mandrel slope affects the resultant braids, with increased slope angles leading to destabilised braided fabrics. With greater deviance in braid angle and fabric thickness, along with observed increased levels of yarn slipping after being deposited on the mandrel, the understanding is reached that there is a limit to the slope angle that is possible to braid without causing unacceptable levels of distortion and instability to the braided fabric. *Figure 5-11*

shows a braided fabric with excessive levels of yarn slippage and fibre spreading due to the extreme changes in mandrel geometry. This leads to unsuitable braids for composite components. Future work within this area of research should be aimed at determining this limit and the parameters which affect this.

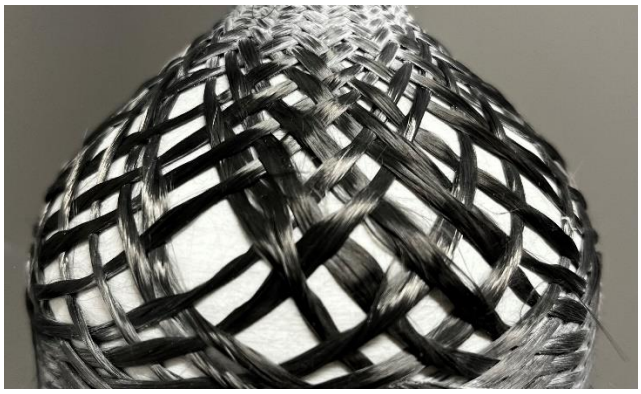

Figure 5-11. The effect of change in radius on braid architecture: an extreme example of fibre spreading/slipping due to a rapid change in geometry.

5.2.3 Braider Configuration

To investigate the effects of the braider scale on complex conical sections, Mandrel C as shown in *Figure 5-4*, has been braided on a 192-carrier braider using both 0 tpm and 7 tpm yarns. Braid angle measurements for single-layer fabrics have been taken at 50 mm intervals along the length of the mandrel. With the same slope angle as Mandrel A, results have been compared between mandrels. Similarly, fabrics have been produced with converging and diverging conical sections to investigate the effects on the resultant fabrics. The results of this study are given in *Figure 5-12*.

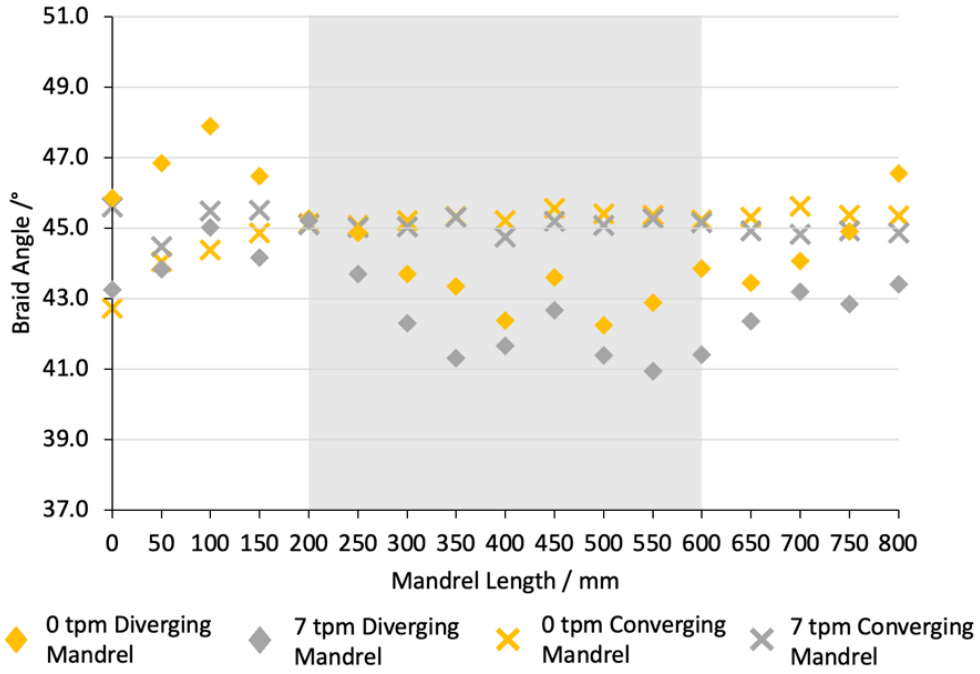

Figure 5-12: Braid angle measurements for single layer braids produced on Mandrel C, the sloped section of the mandrel shown in grey.

Results show some similar trends with data from Mandrel A, with greater levels of stability within the braid for samples braided on converging conical sections, compared to those on diverging sections. Fabrics produced on converging conical sections are seen to stabilise quickly and remain at this level throughout the conical section. Little fibre slippage is evident with the braid able to adapt to changes in the mandrel to remain constant. This is expected on larger-scale braiders, as there is a greater amount of time for the braid to react to speed changes in the mandrel and produce a consistent fabric. Additional stability is seen towards the end of the sloped section compared to measurements taken on Mandrel A. This is a result of limited bridging taking place during the braiding process. Larger mandrels enable the braid to be more reactive to the shape of the mandrel, reducing the likelihood of bridging the fabric.

This increased stability is not repeated for fabrics produced using diverging conical sections with instability seen across the whole length of the mandrel. The reasons for instability within constant cross-sections are not fully understood. It is evident that within the conical section large levels of braid angle deviation are experienced,

supporting data from Mandrel A showing large levels of fibre slippage during this portion of the mandrel.

In addition to braid angle, yarn width has been investigated using the 192-carrier braider on conical and straight pipe mandrels with the results presented in *Figure 5-13*. These results echo those presented in Chapter 4, showing a significant reduction in yarn width for twisted fabrics, with a 39% reduction in yarn width for 7 tpm samples compared to 0 tpm samples. Greater levels of variability are seen in 0 tpm samples as expected, due to the reduction in yarn density as shown in Chapter 4. These results show that although greater levels of fibre slippage are seen on diverging conical sections, this is not leading to yarn spread during this process, particularly evident in the twisted samples with almost identical results for all three mandrels. This is expected as the added twist limits the ability of the yarn to spread on the mandrel.

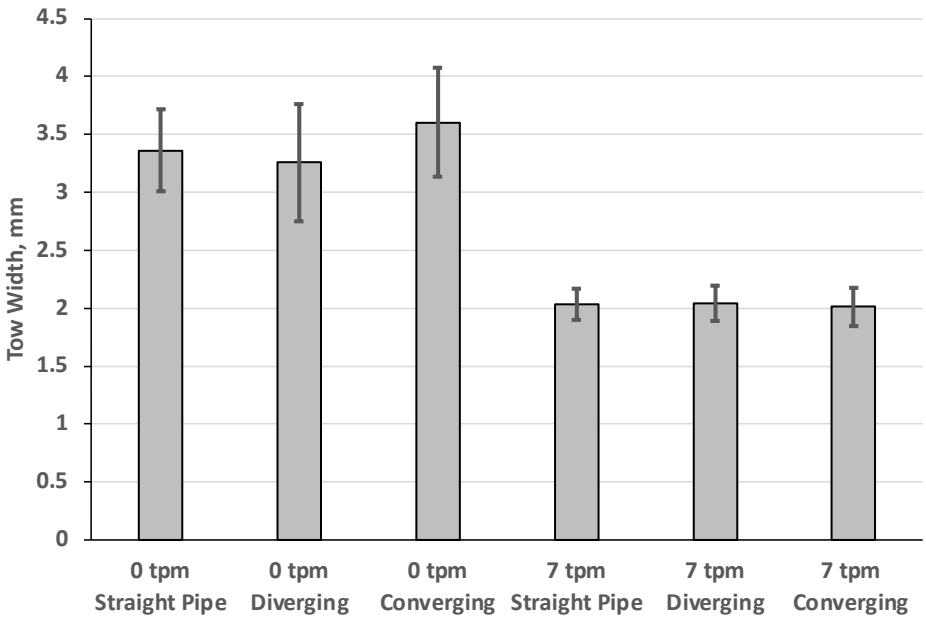

Figure 5-13: Average yarn width measurements from Mandrel C and a 200 mm diameter straight pipe for 0 tpm and 7 tpm yarns.

This study has shown that the scale of the braider has limited effects on the consistency of the braid for converging conical sections with a small increase in stability, with little effect on diverging conical sections. The significance of this study highlights the ability to test mandrel shapes and complexities on smaller, cheaper

braiders with the ability to scale the results for larger production-scale braiders. This helps reduce development and testing costs during the design phase.

5.3 Conclusions

Results presented in this chapter show the effect of complex mandrel shape on the resultant braided fabric concerning braid angle and fabric thickness. Both have significant effects on the infusion of fabrics using RTM and the mechanical performance of the composite. Understanding how the complex changes in mandrel shape affect the braid is vital in designing the optimum shape and braiding process for structural composite components. Braids were produced initially on two mandrels with variations in the slope angle in the conical section of the mandrel. The direction of the braiding has additionally been investigated to understand how previous and future changes to the mandrel geometry affect the braided fabric. Typical analytical models depend on consistent mandrel cross-section and braiding parameters to predict the geometry of the fabric.

All results for mandrel A show significant effects due to the sloped section of the mandrel compared to similar stabilised braided fabrics presented in Chapter 4. Braid angles show significant deviance from the target angle with braiding in both directions with a greater effect seen in diverging sections. This instability within the fabric was echoed in the thickness data. The same study conducted on Mandrel B, with a reduced slope angle, showed an increase in the stability within the fabric, especially regarding the braid angle. Within both studies, it is seen that defects or instabilities in lower layers of fabric are echoed and often magnified in subsequent layers. This leads to the conclusion that each layer should be inspected upon braiding to ensure these defects do not lead to detrimental effects once braiding is completed.

A twin study completed on a larger scale 192-carrier braider echoed the results produced on the smaller braider, showing the ability to scale mandrels and fabrics between braider sizes. This is particularly significant when in early design or testing phases with the ability to optimise the process using smaller, cheaper machines before scaling to full production on larger braiders.

Additional work on this topic would include investigating the point at which the slope angle of the mandrel becomes large enough to lead to an unacceptable braided fabric. This has been observed within braiding projects but is yet to be determined as a relationship between mandrel slope and braiding parameters.

The work presented in chapters 4 and 5 shows the need for the twist level to be controlled through the rewinding process in order to develop correct fabrics and mould tools. To date, there is limited ability to predict this additional twists effects on the braided fabric's properties. Chapters 6, 7 and 8 aim to address this through the development of tools within TexGen to predict the braided unit cell geometry and the resultant properties.

6 Geometrical Modelling

A review of the current methods for modelling braided fabrics and predicting their properties has been outlined in Chapter 2. This highlights the need for a predictive geometrical model of the structure of the fabric to enable fast and efficient optimisation of the braid. To address this, a new model has been developed within TexGen [83] to predict the structure of the fabric using key physical process parameters such as the configuration of the braider and the yarns being used. The use of TexGen has allowed for realistic, variable yarn cross-sections and complex yarn geometries to be modelled to represent a unit cell of braided 2D biaxial fabric. This chapter will explain the formation of this model and the variations available for building representative unit cells of biaxial braided fabrics.

6.1 Introduction

Braided fabrics have often been overlooked when designing composite components due to limitations in the prediction of properties. Work has been done on multiple scales to predict the resultant fabric and its properties. Ravenhorst [66] developed BraidSim, a kinematic modelling software, to predict the fibre angle and coverage of complex mandrels with both forward and inverse solutions. Additionally, a meso-scale modelling technique was developed for triaxial braided fabrics with the aim of predicting multilayer fabric thickness. Errors were seen on fabrics with multiple plies due to the difficulty in predicting nesting between layers. Kyosev [77] developed TexMind, a software package designed to model braids and allow for machine configuration tools to predict the pattern of the braid. CATIA Composite Braiding Designer (CBA) [72] can predict the coverage, fibre angle and fabric thickness for the fabrics on complex mandrels. Due to assumptions in yarn shape, the internal structure cannot be analysed. WiseTex [81] is capable of meso-scale modelling of 2D braided unit cells, however, is limited due to restrictions on the yarn paths and yarn cross sections. Braid CAM developed by Melanka & Carey [74] can be used to predict the mechanical properties for a range of braid angles for the three typical braid patterns. This model uses a volume averaging stiffness method to account for yarn undulation and the orientations of the yarns.

Typically, most methods for modelling and predicting the properties of the braided fabric assume a flat representative unit cell (RUC). Limited academic research has been conducted on the assumption of a curved unit cell, often seen in overbraided components. Pickett et al. [64] uses an explicit FE method for simulating the braiding process and predicting mechanical properties, however the assumption of circular yarn shape and timescale to run simulations limits the usage of such models. Ayranci [107] uses a modified classical laminate theory model to analyse the effect of the unit cell radius in the prediction of mechanical properties, showing up to a 7% difference in longitudinal modulus for curved models. This was reinforced by Nagaraju et al. [108] showing a significant difference in stiffness coefficients for curved unit cells using a modified TexGen braided unit cell.

As discussed, there are many methods to model braided fabrics however there is limited customisation for specific braiding cases. This research aims to use experimental quantification of the structure of braided fabrics to build a method within TexGen. This allows for a highly customised biaxial braided fabric to be modelled to a high level of geometrical detail, including variations to the cross-section. This method has been implemented for flat fabrics as well as curved fabrics, following the curvature of the mandrel. Using TexGen meshing functions, the permeability and mechanical properties of the fabrics can be evaluated, with results for mechanical properties presented in Chapters 7 and 8.

6.2 Unit Cell Modelling

When modelling fabrics, it is unrealistic to model the fibres on the whole structure of the component, therefore the fabric is represented by a unit cell, the smallest repetitive unit in a fabric. Due to the process of producing a braided fabric, there are levels of variation in yarn geometry as detailed by Czichos et al. [109]. Therefore, the unit cell modelled is an idealised model of the fabric. As these variations are only minor within the fabric, unit cell modelling can be assumed to give a relatively accurate prediction of the local architecture. Several studies have conducted a multi-scale model to use the mechanical properties determined from unit cell analysis in the macro-scale analysis [48, 110]. This study shows the fundamental steps needed to create an RUC of biaxial braided fabric and the automated process within TexGen.

New classes have been developed within TexGen, *CTextileBraid* and *CTextileBraidCurved*, which are inherited classes of *CTextile*. Building the system within the TexGen source code allows the model to take advantage of the current systems such as meshing, exporting and yarn building functions as shown within the API reference in *Figure 6-1*. Building of braided unit cells can be conducted through two routes: GUI (Graphical User Interface) or Python scripting. Previously it has been possible to create a custom braided fabric through the Python scripting method, however no analytical models were included with yarn locations, paths and cross-sections. These analytical models had to be manually programmed, limiting its suitability. An example of this and a new Python scripting method are outlined in Appendix D.

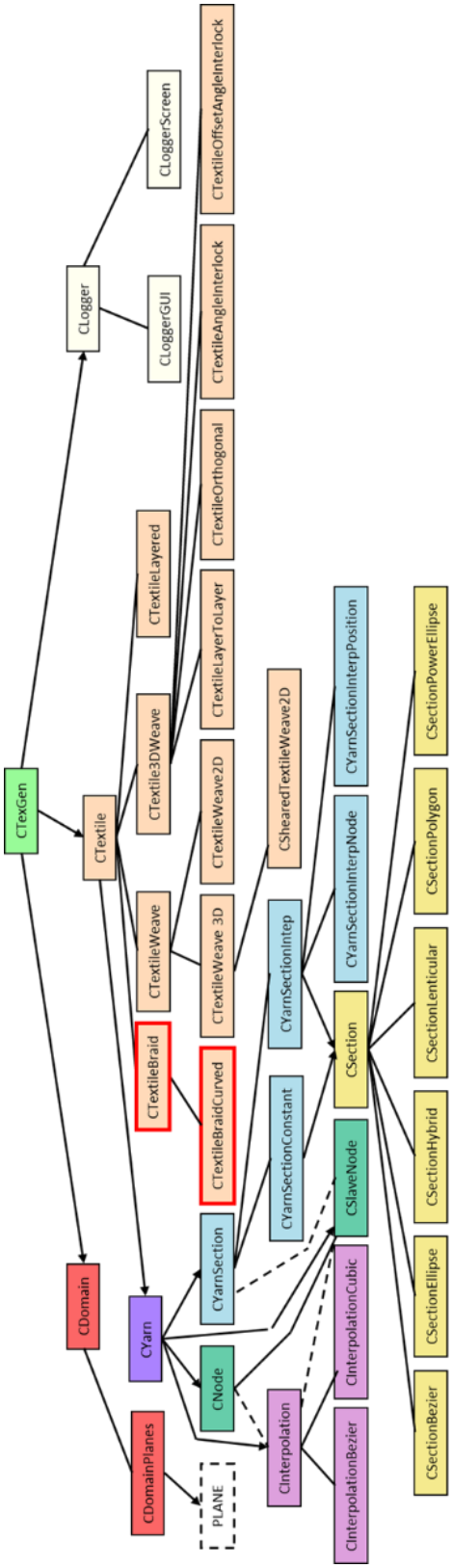

Figure 6-1. API reference for TexGen with the addition of CTextileBraid and CTextileBraidCurved API's outlined in red.

CTextileBraid is a predictive model that uses key physical process parameters to accurately model the unit cell. *Figure 6-2* shows the GUI interface used for creating braided unit cells within TexGen. The required inputs to the model are:

- The number of yarns required for the unit cell.
- Yarn width.
- Yarn thickness.
- Radius (or equivalent radius) of the mandrel.
- Horn gear velocity.
- The number of horn gears.
- Take-velocity of the mandrel.
- The pattern of the fabric.

The techniques for producing biaxial, braided unit cells within TexGen will be discussed in the following sections.

Figure 6-2. TexGen GUI for building unit cells for biaxial braided fabrics.

6.2.1 Braid Angle and Coverage Prediction

An analytical model developed by Du & Popper [59] has been used to predict the key characteristics of the braid from the input process parameters. The model assumes each yarn forms a helical path around the mandrel, with the braid angle being predicted using Eq. (6.1). This was then expanded on by Potluri et al. [89] in Eq. (6.2) to directly link braid angle to machine input parameters, such as the average angular velocity of the horn gears around their own centres, ω_h, and the number of horn

gears, N_h, as these are directly measurable and controllable parameters when braiding. The model was analysed against braids on a 48-carrier Steeger axial braider and showed an error of 1-2 degrees for stabilised fabrics. Results for this can be found in Chapter 4.

$$\alpha = tan^{-1}\left(\frac{\omega R}{v}\right) \tag{6.1}$$

$$\alpha = tan^{-1}\left(\frac{2\omega_h R}{N_h v}\right) \tag{6.2}$$

Further to the braid angle, the coverage of the fabric needs to be calculated to determine the spacing between the yarns. An expression for biaxial fabrics is presented in Eq. (6.3) with terms outlined in *Figure 6-3*. The derivation of this is shown in Chapter 2, Section 2.1.3. n_c is defined as the number of carriers, typically twice the number of horn gears.

$$CF = 1 - \left(1 - \frac{w_y n_c}{4\pi R cos(\alpha)}\right)^2 \tag{6.3}$$

This model is valid while the fabric has not jammed. This is identified when

$\frac{w_y n_c}{4\pi R cos(\alpha)} \leq 1$. At this point, the fabric is assumed to have 100% coverage. Further customisation is possible to model jammed fabrics with yarn overlap. Assuming the spacing between the weft and warp yarns is equal to the spacing between yarns, x_g is defined by Eq. (6.4).

$$x_g = \frac{\frac{1}{1-CF} - {w_y}^2}{2w_y} \tag{6.4}$$

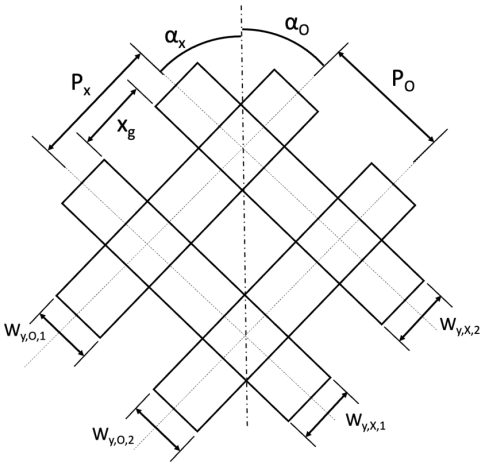

Figure 6-3. Definition of coverage factor for biaxial braided composite fabric

6.2.2 Yarn Paths and Node Locations

The yarn paths within TexGen are defined as one-dimensional lines representing the yarn's centreline in three-dimensional space. As the aim of the study is to model the fabric at the unit cell level, the yarn is assumed to be repeatable and only modelled at the smallest repeatable length. The yarn path can be described by a discrete number of positions along the length of the yarn, known as master nodes, and an interpolation is conducted between these. Master nodes are located at the cross-over points of the yarns, this ensures the required pattern of the fabric can be achieved by altering the vertical location of the nodes.

The interpolation functions used within TexGen have at least continuity C^1, meaning that there are no gaps within the yarn paths and the tangents to the yarn paths vary smoothly. To solve this, splines are used, with Bezier, Natural Cubic and linear being used in TexGen. An example of each is shown in *Figure 6-4*. In addition to continuity C^1, the interpolations also preserve C^0, to ensure repeatability of the yarns can be maintained.

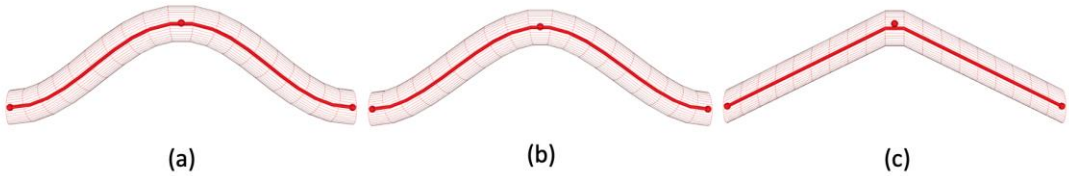

Figure 6-4. Different interpolation techniques within TexGen between three master nodes are shown. (a) Bezier, (b) Natural Cubic and (c) Linear.

A Bezier spline was chosen to predict the yarn path between the nodes, defined by Eq. (6.5). This ensures the yarn paths do not interpolate above the required thickness of the fabric and maintain a smooth path between the nodes. The interpolation is defined by 4 points within 3D space, $\boldsymbol{P}_1$, $\boldsymbol{P}_2$, $\boldsymbol{P}_3$ and $\boldsymbol{P}_4$. With the curve starting at $\boldsymbol{P}_1$ and heading towards $\boldsymbol{P}_2$ before turning and arriving at $\boldsymbol{P}_4$ from the direction of $\boldsymbol{P}_3$. Sherburn [82] outlines alternative interpolation techniques used in TexGen.

$$B(t) = \boldsymbol{P}_1(1-t)^3 + 3\boldsymbol{P}_2 t(1-t)^2 + 3\boldsymbol{P}_3 t^2(1-t) + \boldsymbol{P}_4 t^3 \qquad 0 \leq t \leq 1 \qquad (6.5)$$

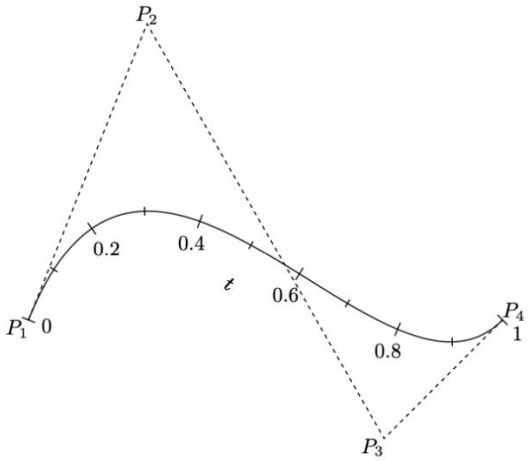

Figure 6-5. Cubic Bezier curve

Using the interpolation function, braid angle (α) and yarn gaps (x_g) outlined in the previous section, the location of the master nodes are calculated by Eq. (6.6 - 6.8) and yarn paths are defined for the biaxial braid. Master nodes are located at the cross-over points of weft and warp yarns, with slave nodes used to define the spline in the yarn path. There is assumed to be no gap between the yarns at the cross-over point due to the tension in the yarn during the braiding process.

$$x = x_g \sin(\alpha) \tag{6.6}$$

$$y = x_g \cos(\alpha) \tag{6.7}$$

$$z = \begin{Bmatrix} \frac{t_f}{4} \ if\ yarn\ is\ below \\ \frac{3t_f}{4} \ if\ yarn\ is\ above \end{Bmatrix} \tag{6.8}$$

In addition to the location of the master nodes, a vector describing the direction of the yarn at the node is required within TexGen. This is assumed to be concentric with the yarn path and is defined by Eq. (6.9 – 6.11). The z-direction can be assumed to be flat due to the interpolation function used, assuming the fabric does not rise above or below the defined fabric thickness. The outcome of this can be seen in *Figure 6-6* for a typical biaxial braided fabric.

$$\vec{x} = \sin(\alpha) \tag{6.9}$$

$$\vec{y} = \cos(\alpha) \tag{6.10}$$

$$\vec{z} = 0 \tag{6.11}$$

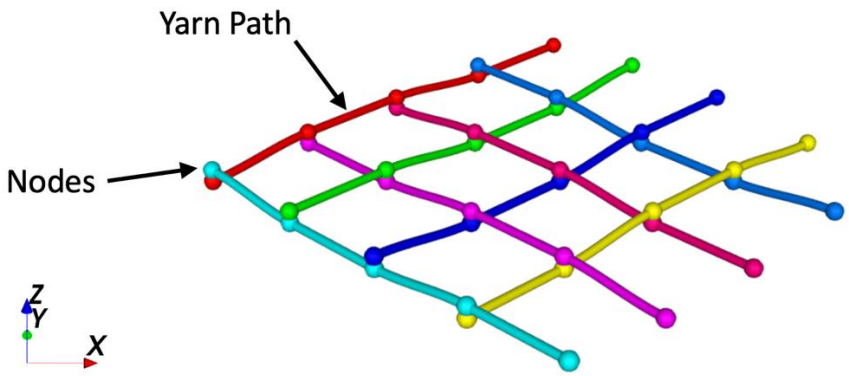

Figure 6-6. Master node locations and yarn paths for typical biaxial braided fabric within TexGen.

6.2.3 Yarn cross-section

Yarn cross-sections are defined as the 2D shape of the yarn when cut by a plane perpendicular to the yarn path tangent. Within this model, the yarns are treated as solid volumes, rather than defining the fibres individually. Therefore, the cross-section is approximated to be the smallest region that encompasses all fibres within the yarn. Multiple shapes can be defined within TexGen such as rectangular, circular, ellipse and power ellipse. Within this study optical microscopy data was used to understand the cross-sectional shape of braided yarns. This follows the procedure outlined in Chapter 3, Section 3.3.

Optical microscopy was performed on dry braided fabrics with a low coverage factor, ensuring that jamming between yarns would not affect the cross-sectional shape. Toray 12K T700 carbon fibres were used for braiding on a 48-carrier axial braider. *Figure 6-7* shows an example of this with two yarn cross-sections shown. Various assumptions of cross-sections have been used across the literature from rectangular [72] assumptions to lenticular [111] or power ellipse. Data from the optical microscopy showed the power ellipse sectional definition captures the shape of the yarn and allows for freedom in changes to the cross-sectional shape to match the style of yarns used.

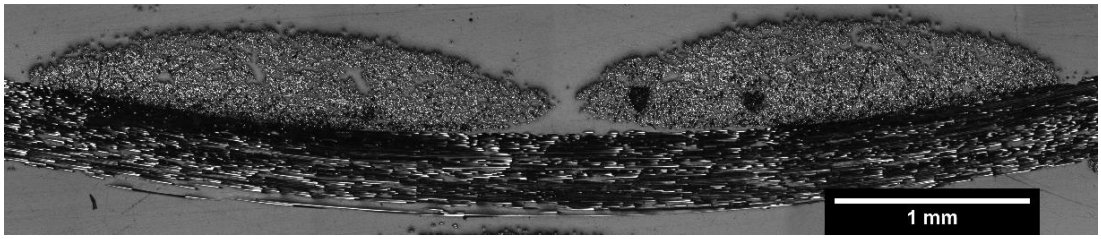

Figure 6-7. Optical microscopy of biaxial braided dry fabric showing a cross-sectional shape

The power-ellipse section is a modification of an ellipse section where the y-coordinate is assumed a power n to allow for the section to resemble a rectangular shape, when n < 1 or a shape similar to that of the lenticular cross-section when n > 1. Eq. (6.12) and (6.13), define the cross-section.

$$x(v) = \frac{w_y}{2}\cos(2\pi v) \qquad 0 \le v \le 1 \tag{6.12}$$

$$y(v) = \begin{Bmatrix} \frac{t_y}{2} sin(2\pi v)^n \\ -\frac{t_y}{2}(-\sin(2\pi v))^n \end{Bmatrix} \qquad \begin{matrix} if\ 0 \le v < 0.5 \\ if\ 0.5 \le v \le 1 \end{matrix} \tag{6.13}$$

Further investigation was conducted for the change in yarn shape during a vacuum infusion process. Samples with the same fibres and braiding parameters were produced as 4-layer biaxial braided panels and infused under vacuum pressure to compact and investigate yarn cross-sectional changes. The optical microscopy results of this are shown in *Figure 6-8*, showing a significant change to the cross-section, resembling a lenticular cross-section compared to that of the dry fabric. The changes seen here can be represented through the change of the power value within the power ellipse.

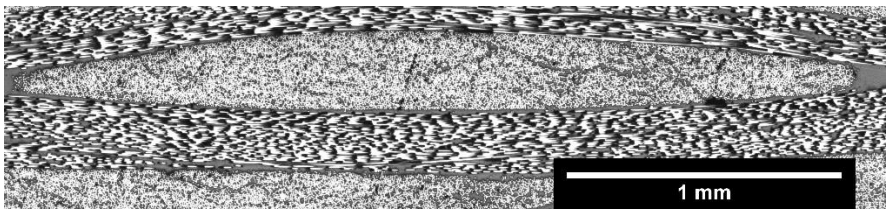

Figure 6-8. Optical microscopy of yarn cross-section of vacuum infused yarn.

Once the cross-section has been defined for the yarn, this is applied at the master node locations within the model, and the yarn surface can be defined. This requires an interpolation function of the yarn surface to be defined, with two options used within the model.

6.2.3.1 Constant cross-section

For a constant cross-section, the yarn is assumed to be constant along the length of the yarn. This can be used for simple models of braided fabrics however due to tension applied during the braiding process, is not realistic to the fabric.

6.2.3.2 Interpolated cross-sections

To model the geometry of the yarn more realistically within the braided fabric, an interpolated cross-section is used. Within this model, the cross-sections are defined at set positions along the length of the yarn, typically at the master and slave node locations and interpolated between the specified points. The interpolation between two points with cross-sections A(t) and B(t) can be defined by the cross-sections C(t, μ) defined in Eq. (6.14).

$$C(t,\mu) = A(t) + \big(B(t) - A(t)\big)\mu \quad 0 \le t \le 1 \qquad 0 \le \mu \le 1 \qquad (6.14)$$

Where μ varies linearly from 0 to 1 between the cross-sections A(t) and B(t). To ensure the linear interpolation can be used, both sections A(t) and B(t), must be defined in a similar manner. Within this case, each cross-section is defined by 40 points in the local x-y plane for the cross-section, which is the translated into the global X-Y-Z coordinates using the location and direction of the master or slave node. An extreme example of a yarn with interpolation between three different cross-sections is presented in *Figure 6-9* .

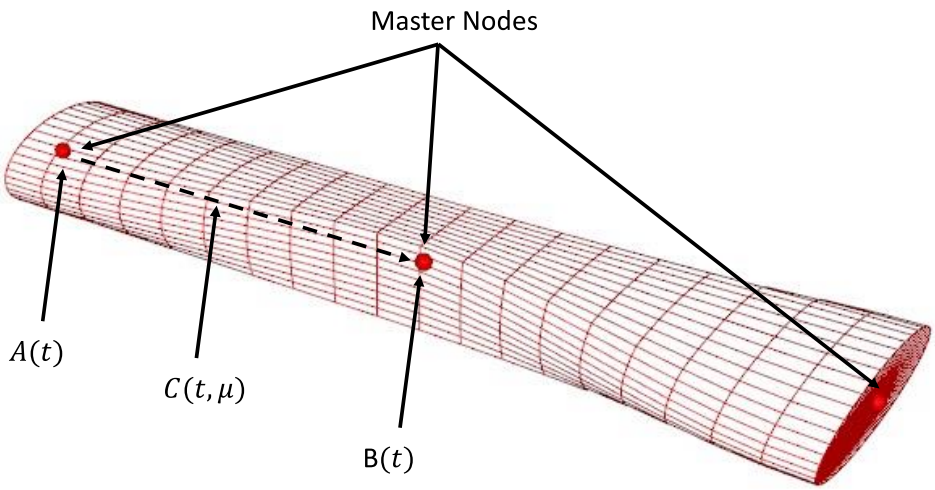

Figure 6-9. Yarn with different cross-sections at each master node (shown) and interpolation between each.

6.2.4 Repeats

Within TexGen, only the smallest repeatable size of the fabric is defined; the unit cell. This reduces the need to duplicate data, however there are occasions when larger samples of the fabric are needed to be modelled. Therefore, two repeats within the yarns are used to enable this. Firstly, due to continuity C^0, the first and last nodes of the yarn have identical cross-sections and node directional data. Therefore, the yarns can be repeated along the length of the yarn to produce an infinitely long yarn. Secondly, the yarns will repeat in the x-y plane to represent additional yarns in the fabric with the same properties. *Figure 6-10* shows the effect of the repeats for a sample fabric.

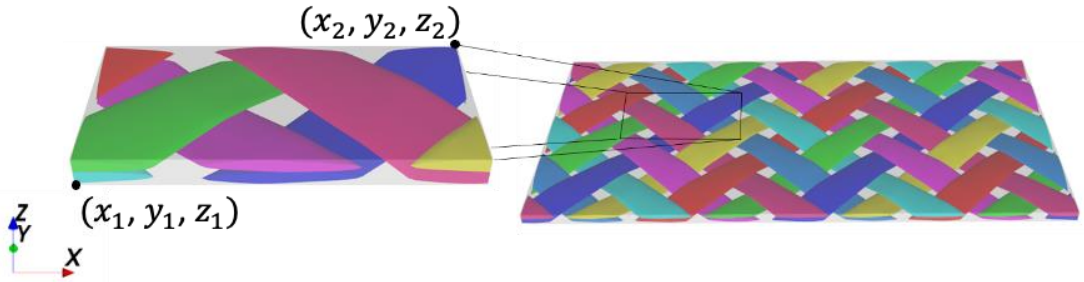

Figure 6-10. Biaxial braided fabric modelled in TexGen using repeats defined by the unit cell.

6.2.5 Domain

For most analyses of fabrics, a finite size of the fabric is required, usually the unit cell. To define this, a domain is assigned to the model. The domain is specified by 6 planes with values outside the internal space considered outside the domain and thus the fabric is not modelled in those regions. Typically, the domain is specified by a minimum point (x_1, y_1, z_1) and a maximum point (x_2, y_2, z_2), as seen in *Figure 6-10.* The model will automatically assume this is the size of the unit cell however adjustments can be made for a custom sized domain. For example, a model of consisting of two unit cells may be used to check periodic boundaries in a FE model.

6.2.6 Model Refinement

The process outlined so far produces a basic model of a biaxial braided fabric. Node locations and yarn paths are defined, cross-sections are defined at node locations with interpolations between sections and a domain is applied to constrain and define

the unit cell. Upon inspection of various models, a series of intersections between yarns were identified. To quantify these problems, the 'render intersections' function within TexGen was used. This identifies locations of intersections between yarns using the *PointInsideYarn* function [82]. The current section addresses these issues to produce a realistic model of a braided fabric and reduce these intersections.

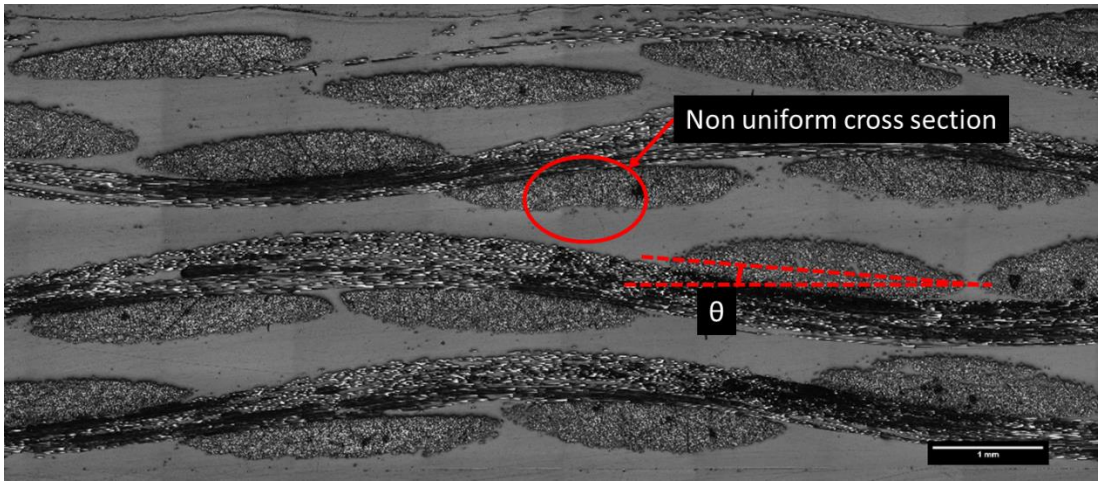

Figure 6-11. Optical microscopy of dry biaxial braid showing rotation in the cross-section.

Optical microscopy data in *Figure 6-11* reveals rotations within the yarns and non-uniform cross-sectional shapes. This is caused by the interaction of the yarns during braiding and the undulations within the pattern of the fabric. To solve this within the model, a rotation can be applied to the cross-section. The function iterates through each yarn and identifies locations where a rotation would be required. This happens if the transverse yarn is undulating between the top and bottom of the fabric. If required the angle of rotation, θ, is defined by Eq. (6.15), where t_f is defined as the fabric thickness.

$$\theta = tan^{-1}\left({t_f}/{2x_g}\right) \tag{6.15}$$

Secondly, the initial model assumes a constant cross-section along the length of the yarn. However, as seen in multiple microscopy samples the cross-section has small adjustments due to interactions with other yarns and the typically low levels of sizing on yarns used in braiding. To address this a second refinement step, *CorrectInterference*, is used to adjust the cross-sectional shape at each of the Master

and mid-point nodes to reduce this. *CorrectInterference* calculates a line segment from a point lying on the edge of the yarn cross-section, $\boldsymbol{P}_i$, to the centre of the yarn, $\boldsymbol{P}_c$. If this line intersects with the transverse yarn, the position of $\boldsymbol{P}_i$ is moved to the intersection point. This is an iterative procedure over each of the Master and Slave nodes within the yarn to produce a complex yarn shape as seen in *Figure 6-12*, showing an applied rotation and a change to the cross-sectional shape to reduce the intersections. A large level of intersections can be seen in the red yarn before refinement. The function is seen to reduce intersections by up to 100% depending on the depth of the intersection and the yarn geometry.

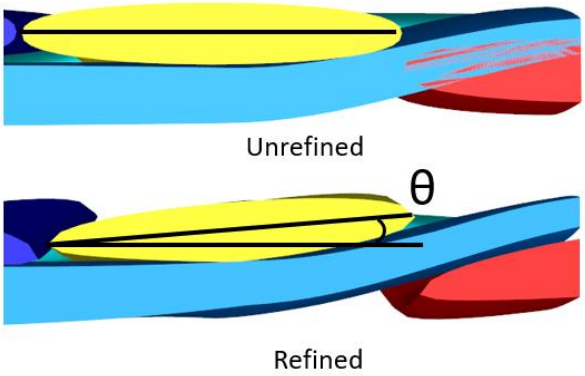

Figure 6-12. Changes to the cross-sectional shape from the refinement function for braids within TexGen.

6.2.7 Fabric Construction

The previous sections have outlined the methods used to predict and build a unit cell of a biaxial braided fabric within TexGen. The model is able to predict key architecture parameters such as braid angle, coverage and yarn shape. An optional refine function has been developed to adapt the rotations and cross-sections to realistically represent the yarns. *Figure 6-13* shows an overview of this process as a flow diagram.

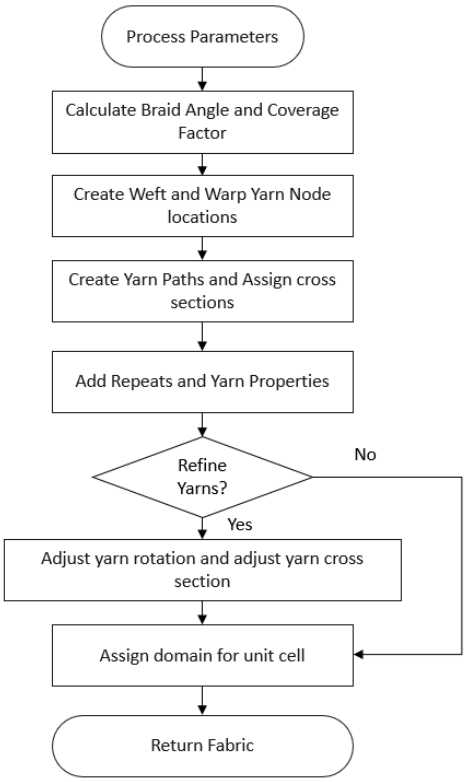

Figure 6-13. Flow chart for the generation of biaxial braided fabrics with optional yarn refinement in TexGen.

6.2.8 Model Validation

To validate the model, it has been compared to a sample of braided fabric. The fabric was constructed using data outlined in *Table 6-1*.

Table 6-1. Braiding process parameters.

Yarn Width (mm)	Yarn Thickness (mm)	Carrier Speed (rad/s)	Take-up Speed (m/s)	Mandrel Diameter (mm)	Predicted Angle (°)	Measured Angle (°)
2.73	0.44	0.383	0.005	32	44	46

A visual comparison of the cross-sections of the yarns from optical microscopy, an unrefined model and a refined model respectively is presented in *Figure 6-14.* This shows a good agreement for both cross-sectional shape and rotation within the refined model. Changes to both rotation and yarn cross-section can be clearly seen in all four yarns, reducing all intersections in the model.

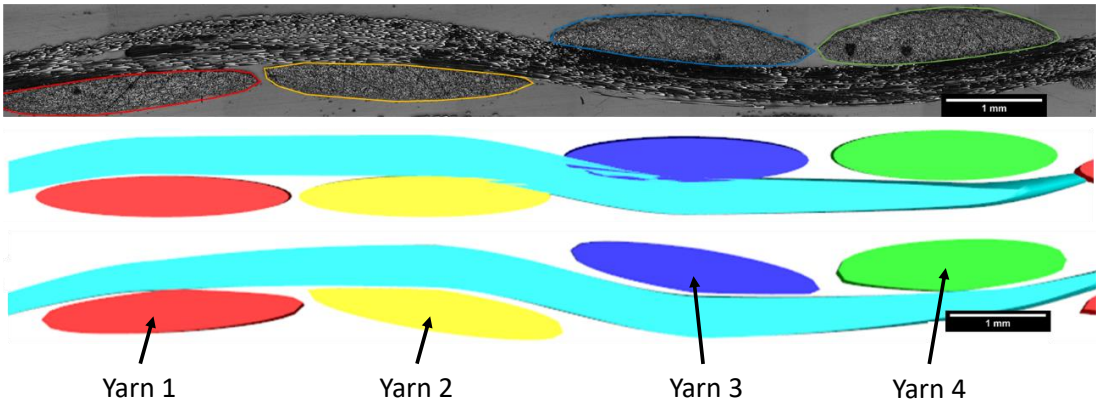

Figure 6-14. Comparison of optical microscopy data to predicted yarn structure for biaxial braid.

To further inspect the yarn data, the yarns volume fraction data are compared in *Table 6-2*. To calculate volume fraction for the optical microscopy data, individual yarns were cropped from the image and the colour threshold function was used within ImageJ as the yarns appear white within the image with the matrix showing as grey. Overall, the predicted volume fraction is close to that of the measured value. The greater error experienced within yarns 3 and 4 is explained by the greater than predicted thickness of the yarns, suspected to be due to the lack of compaction force from the alternative yarn. Freedoms within TexGen allow for this to be modified manually by the user for a greater representation of the fabric. However, it is noted that during an infusion process under pressure, this difference is minimal and therefore has not been automatically modelled into TexGen.

Table 6-2. Comparison of predicted and measured yarn volume fraction data.

	Predicted Yarn Vol. Fraction	**Yarn Vol. Fraction**
Yarn 1	0.527	0.527
Yarn 2	0.527	0.529
Yarn 3	0.527	0.447
Yarn 4	0.527	0.447

6.2.9 Analysis and Exportation

Once the model is built within TexGen, a range of analyses can be conducted within TexGen and as exportation to other software packages, such as Abaqus. Within TexGen the fibre volume fraction and yarn volume fraction can be calculated. The

textile can be exported as the following in both dry fabric and as an infused component in ways detailed in *Figure 6-15*.

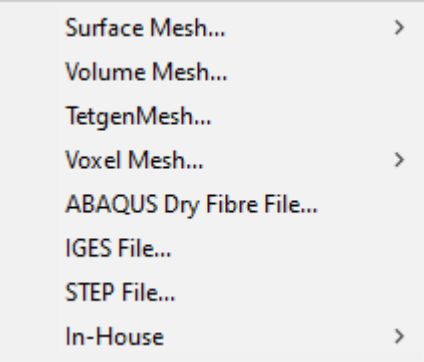

Figure 6-15. Export options for textiles within TexGen.

Voxel mesh analysis is used for the calculation of the elastic properties of the unit cell. This divides the model into equal-sized rectangular elements with such elements either taking the properties of the yarn or the matrix. This is conducted using the *PointInsideYarn* function to determine if the centre of the element is within the yarn or matrix of the TexGen model and apply the appropriate properties. The export will automatically apply periodic boundary conditions [112] for Abaqus analysis. An additional refinement layer developed by Matveev et al. [113] can be applied to refine the size of the voxel elements close to the boundary of the yarn, giving a greater definition to the yarn geometry.

6.3 Curved unit cells

As outlined in the introduction of this chapter, little academic research has been conducted on the effect of radius on unit cell analysis. Initial work indicates the potential of significant differences in mechanical properties for fabrics produced on small radii curves, which can be typical within the braiding industry. To investigate this a new class, *CTextileBraidCurved*, has been developed within this study to model such unit cells. This is an inherited class of *CTextileBraid*, allowing for the use of many of the functions previously stated. This section explains the differences in modelling for curved unit cells.

6.3.1 Yarn paths and node locations for curved unit cells

Calculation of the braid angle and the coverage of the fabric is done in the same method as explained in 6.2.1. For the curved unit cells a polar coordinate system,

RθZ, has been implemented in TexGen. Due to limitations in the rendering module, the final coordinates must be specified within cartesian coordinates. Eq. (6.16 – 6.19) are used for the coordinate transform. t_f is defined as the fabric thickness.

$$R = \begin{Bmatrix} r + \frac{t_f}{4} \; if \; yarn \; is \; below \\ r + \frac{3t_f}{4} \; if \; yarn \; is \; above \end{Bmatrix} \tag{6.16}$$

$$\theta = \frac{\pi}{N_h} \tag{6.17}$$

$$Z = x_g \cos(\alpha) \tag{6.18}$$

$$x = Rsin(\theta)$$

$$y = Rcos(\theta) \tag{6.19}$$

$$z = x_g \cos(\alpha)$$

Master node locations are defined at the cross-over points between the weft and warp yarns, using the polar coordinate systems along with the braid angle and distance between the centre lines of the yarns. Unlike the flat yarns, the direction of the nodes cannot be assumed to be flat due to the curvature. The direction of the nodes is defined as the directional vector between the current node and the next node in the yarn. Yarn paths are interpolated by a Bezier spline, defined in section 6.2.2. *Figure 6-16* shows the nodes and yarn paths for a curved unit cell.

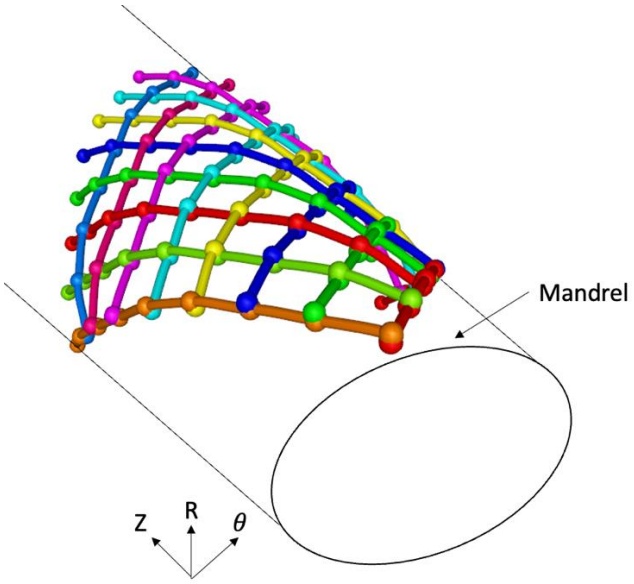

Figure 6-16. Nodes and yarn paths for a curved unit cell around a 10 mm mandrel.

6.3.2 Yarn cross-section

Yarn cross-sections are defined in the same way as the flat unit cell, as power ellipse sections. However, due to the curvature of the unit cell, an initial rotation is needed to match this. This uses the theta coordinate of the master node to define the rotation of the yarn, β, as seen in *Figure 6-17*. The yarn cross-section is interpolated between the yarns to ensure it smoothly transitions between the master nodes.

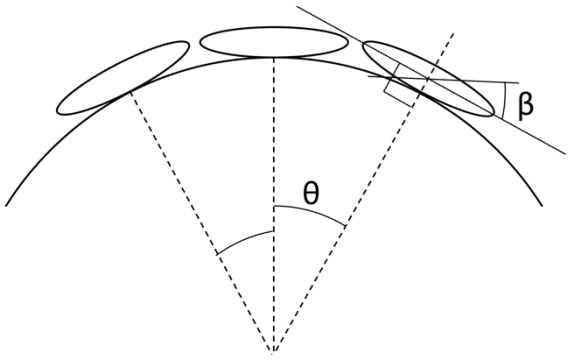

Figure 6-17. Initial rotation of yarns within the curved model.

6.3.3 Domain

As explained in section 6.2.5 the standard domain within TexGen is defined as a series of flat planes. With the curved fabrics recently developed domain system, *CPrismDomain*, has been used. Initially, the domain is defined through a series of points, as shown in *Figure 6-18*. The location of these points is dependent on the parameters of the fabric such as braid angle, coverage, mandrel size and fabric thickness. Following this, the domain is then extruded along the axis of the fabric to the size of a unit cell.

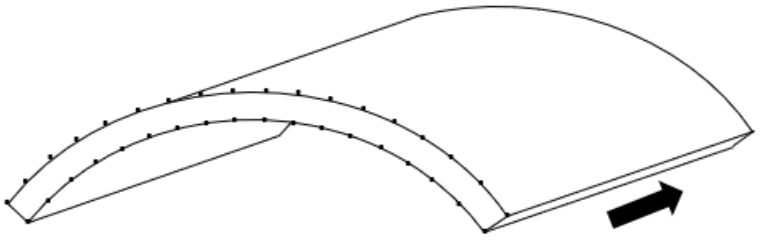

Figure 6-18. Definition of a curved domain using CPrismDomain.

6.3.4 Curved unit cell fabric construction

The construction method is very similar for the curved fabrics compared to the flat as the node locations are defined and paths interpolated between those with the

appropriate cross-sections applied to the yarns. Finally, the domain is assigned, and the unit cell is constructed. Additionally, a refinement function has been implemented for the curved fabrics, which follows the same method outlined for the flat fabrics, taking into consideration the initial rotation applied to the yarns for the curvature of the mandrel. *Figure 6-19* shows the process to model a curved unit cell.

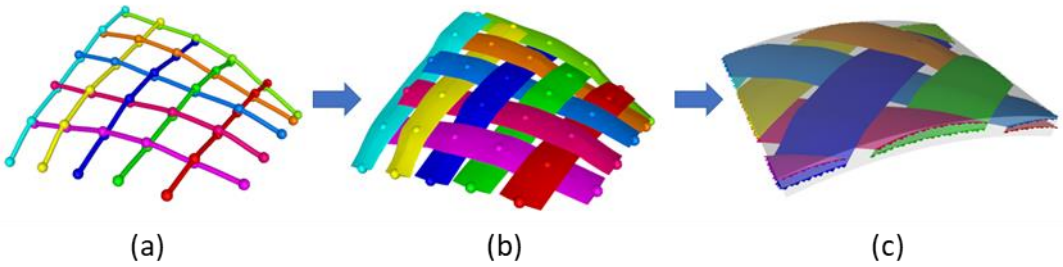

Figure 6-19. Generation of a curved biaxial braid unit cell. (a) Node Locations and paths are defined, (b) cross-sections are applied to yarns and refinement to shape and (c) the domain is applied and the unit cell defined.

6.4 Multi-layer fabrics

Nesting is commonly seen in multilayer braided fabrics to varying degrees [27]. Additionally, the level of nesting within the dry fabric can vary along the length of the braid, as seen in Chapter 4, affecting the volume fraction, and leading to effects on the permeability and mechanical properties of the component. A method has been developed to model fabrics with multiple layers. This may include multiple braid layers or axial fibres, as seen in *Figure 6-20*.

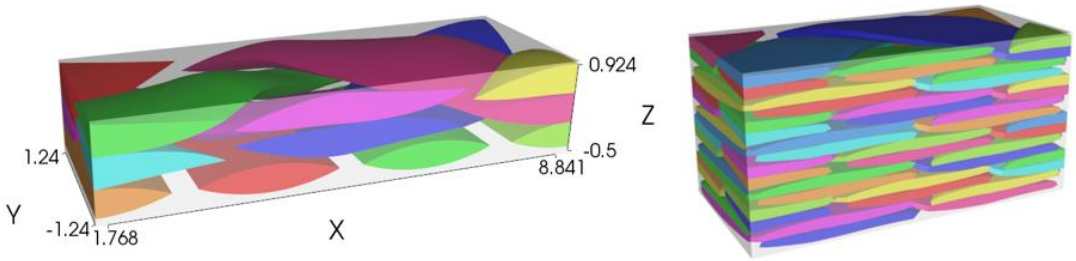

Figure 6-20. Example of multi-layer fabrics produced using TexGen. Left: Biaxial braided layer with an axial fibre layer. Right: 8-layer baixial braided fabric with nesting between layers.

6.4.1 Compaction of braided fabrics

The level of nesting and offset of the layers can be specified within TexGen, however interactions between yarns and tool surfaces or the fabric can be exported as a dry fabric to Abaqus to simulate compaction behaviour. C3D6 6-node linear triangular prism elements were used to model the yarns with boundary conditions to ensure periodicity is maintained during the compaction procedure. This enables unit cell analysis after compaction to be conducted. *Figure 6-21* shows the compaction on a 2-layer braided fabric produced using TexGen. The increased nesting between layers can be clearly seen within the compacted fabric. Two rigid plates (not shown in *Figure 6-21*) were placed above and below the fabric with a target void size specified to simulate an example of closed mould tool void spacing. Deformation of the yarn shape can be seen due to interactions between yarns and between yarns and the tool surfaces, matching similar work seen in infused samples.

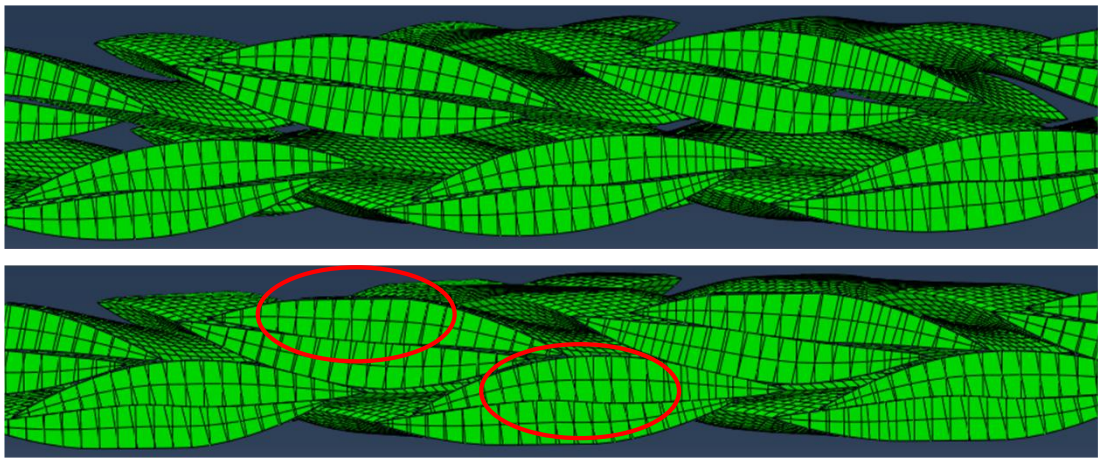

Figure 6-21. Fabric compaction of 2-layer braid produced using TexGen, yarn deformations highlighted.

Prediction of final composite geometry is complex due to many different variables within the infusion process including offset of additional layers, imperfections within the material and voids and resin-rich areas from the infusion. For validation of compaction optical microscopy images of a 4-layer infused panel have been compared to a simulation using a fabric produced in TexGen from the predictive models outlined above. Each layer was initially offset by a yarn width to encourage nesting. This is often typical when braiding as the additional layer settles within the ingress between the yarns in the lower layer. A comparison between the predicted

geometry (green) and actual yarn geometry (blue) is presented in *Figure 6-22*. This shows a good agreement of the yarns with variability coming from the lateral offset of the layers, with interaction between weft and warp yarns being captured within the prediction and resin-rich areas. Additional disagreement can be seen in the void areas within the top two layers as this cannot be captured during the simulation but has a significant impact on the yarn shape. Further refinement of this methodology could include incorporating the high fidelity model, proposed by Thompson et al. [114] to model the yarns using a multi-chain element to capture the yarn spreading and bending to a greater degree of accuracy.

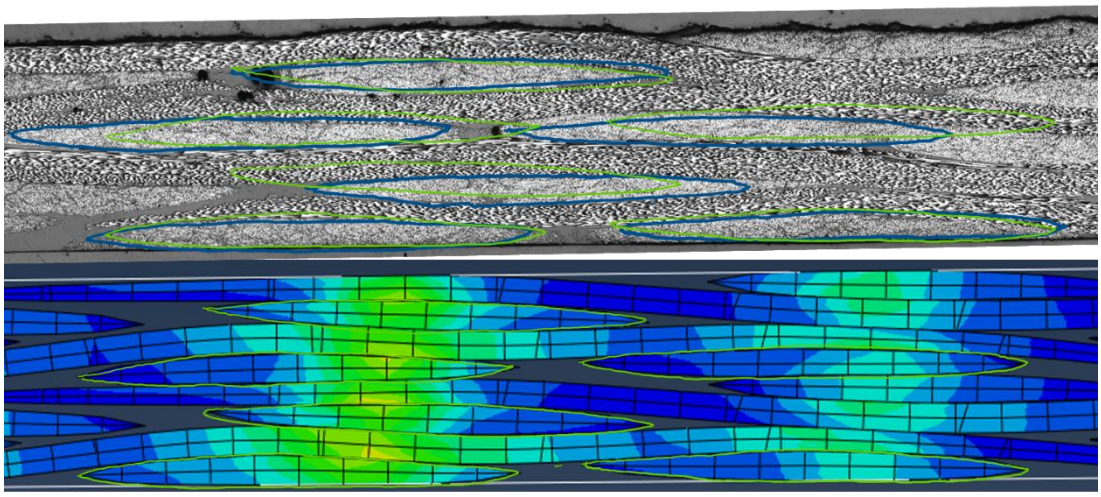

Figure 6-22. Compaction simulation compared to optical microscopy images. Predicted yarn geometry is shown in green, and actual yarn geometry is shown in blue.

From the compacted fabric within Abaqus, an import function has been written to import the deformed geometry back into TexGen as a native model. This allows for the use of the functions within TexGen such as mechanical property analysis, permeability analysis, volume fraction analysis and changes in properties.

6.5 Conclusion

Difficulty in the prediction of the properties of braided fabrics and composites is a key reason for the slower uptake within production components. The novel tools developed within the current section allow for the building of geometrical models of biaxial braided fabrics using a predictive approach for the braid architecture.

Braid architecture including braid angle, coverage and yarn geometry is predicted using a range of models to allow for the analysis of the dry fabric and the infused composite. This has been validated against optical microscopy of braided examples showing good agreement between the predicted yarn shape and experimental geometry.

A curved unit cell methodology has been developed to enable the prediction of the braid architecture on a circular mandrel, using polar coordinates for the prediction of the geometry. Similar refinement functions have been implemented to produce a realistic yarn geometry and a new domain function applied to allow for further analysis.

The model has been expanded to allow for multilayer fabrics, including multi-style layups with alternative braid architectures and axial fibres within the model. Further, a compaction methodology has been detailed for the prediction of nesting and change in yarn shape from the compaction process. Compacted results can be imported back into TexGen for further analysis, including mechanical and permeability analysis.

Chapters 7 and 8 use the tools developed within this section to predict the mechanical properties of the braided composite, comparing the influence of curved unit cells (Chapter 7) and modelling the effects of twist during the winding of yarns within the composite (Chapter 8).

7 Influence of curvature on mechanical properties

Within meso-scale modelling, unit cells are typically considered to be flat sections of the composite to predict the mechanical properties. Although this is generally the case for many fabrics, such as woven and NCF fabrics, overbraiding rarely produces flat sections that are large enough to consider flat unit cell analysis. In Chapter 7 (TexGen) a method was developed for modelling a braided fabric on a curved mandrel, a typical case for overbraiding. Within this chapter, the influence of curvature on elastic mechanical properties is investigated and compared to the traditional method of assuming a flat fabric.

7.1 Introduction

The production method and suitability of the materials lead to braided components often being used in tubular structures, with the offset angle between fibres making the energy absorption properties desirable for items such as automotive chassis components. This can lead to issues with the traditional method of predicting the mechanical properties through unit cell analysis. Ayranci et al. [107] evaluated the effect of the radius of curvature on the longitudinal and shear elastic modulus and in-plane Poisson's ratio. The model was split into three regions: matrix only, undulating yarns and non-undulating yarns. The model also used a modified classical laminate plate theory to calculate the stiffness of each region. The overall stiffness matrix of the braided unit cell was calculated as the sum of the stiffness matrices for the regions. Results showed good agreement with the experimental values with a reduction in the predicted modulus for curved unit cells compared to the equivalent flat fabric. A similar study has been presented by Nagaraju et al. [108] investigating the effect of the curvature on the extensional stiffness matrix of 2D braided tubes. This focuses on SiC/SiC composite and carbon/epoxy composite tubes, researching the effect of the ratio of thickness to the inner radius on the stiffness. Models were produced as flat unit cells within TexGen and exported as voxel meshed FE models. The curvature was then implemented as the models were mapped into a polar coordinate system to model a curved representative unit cell (RUC). This work was in agreement with Ayranci, showing a predicted drop in stiffness for curved unit cells,

with a greater effect seen in the carbon/epoxy models compared to the SiC/SiC models.

The present work shows a methodology for predicting elastic mechanical properties from TexGen models for both flat and curved RUCs with appropriate periodic boundary conditions. The effect of curvature is presented for a case study and compared to results found in the literature.

7.2 Micro-mechanical modelling

7.2.1 Flat Unit Cell

The method for evaluating the mechanical properties of flat RUCs has been given in detail by Li & Sitnikova [112] with an outline provided below. Periodicity within the unit cells is assumed to be translational along the x-plane, y-plane and z-plane. This can be simplified for the assumption of single-layer unit cell analysis. The periodic boundary conditions are applied to the faces, edges and vertices as outlined below, with terms outlined in *Figure 7-1*.

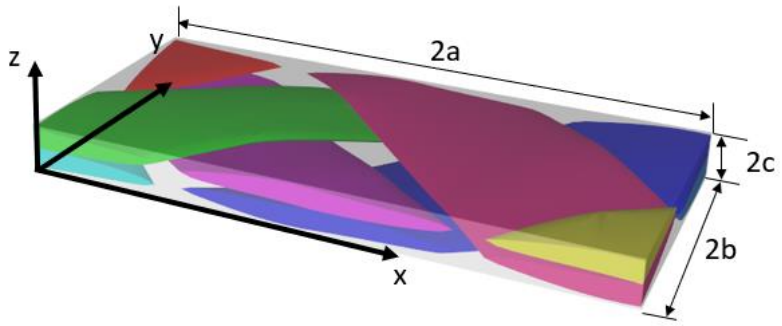

Figure 7-1. A flat unit cell of a braided composite with a rectangular coordinate system.

Within the unit cell there are three translations along the coordinate axis through the lengths shown in *Figure 7-1.* Generalised boundary conditions for the three faces of the unit cell are given in Eq. (7.1-7.3) where ϵ^0 is defined as the macroscopic strains. See nomenclature section for full definition.

$$(u|_{x=a} - u|_{x=-a})|_{y,z} = 2a\varepsilon_x^0$$

$$(v|_{x=a} - v|_{x=-a})|_{y,z} = 0 \qquad (7.1)$$

$$(w|_{x=a} - w|_{x=-a})|_{y,z} = 0$$

$$\left(u|_{y=b} - u|_{y=-b}\right)|_{x,z} = 2b\gamma_{xy}^0$$

$$\left(v|_{y=b} - v|_{y=-b}\right)|_{x,z} = 2b\varepsilon_y^0 \tag{7.2}$$

$$\left(w|_{y=b} - w|_{y=-b}\right)|_{x,z} = 0$$

$$(u|_{z=c} - u|_{z=-c})|_{x,y} = 2c\gamma_{xz}^0$$

$$(v|_{z=c} - v|_{z=-c})|_{x,y} = 2c\gamma_{yz}^0 \tag{7.3}$$

$$(w|_{z=c} - w|_{z=-c})|_{x,y} = 2c\varepsilon_z^0$$

Concentrated forces (generalised with dimension force x length) can be applied for each degree of freedom leading to macroscopic stresses, σ^0, being applied to the unit cells. The relationship between the concentrated forces and macroscopic stresses can be explained by a simple energy equivalence consideration. When a force, F_x, is applied to the degree of freedom ε_x^0 of a unit cell, while all other degrees of freedom are free from constraints, the work done is defined as

$$W = \frac{1}{2} F_x \varepsilon_x^0 \tag{7.4}$$

The strain energy stored in the unit cell can be expressed as

$$E = \frac{1}{2}\int_V \sigma_x^0 \varepsilon_x^0 \, dV \; = \frac{1}{2} V \sigma_x^0 \varepsilon_x^0 \tag{7.5}$$

Where V is defined as the volume of the unit cell. Using Eq. (7.4 – 7.5) the relationship between the force and the macroscopic stress for each degree of freedom can be defined as

$$\sigma_x^0 = F_x/V, \quad \sigma_y^0 = F_y/V, \quad \sigma_z^0 = F_z/V,$$

$$\tau_{yz}^0 = F_{yz}/V, \; \tau_{zx}^0 = F_{zx}/V, \; \tau_{xy}^0 = F_{xy}/V \tag{7.6}$$

From this, the effective elastic material properties can be obtained in terms of the independent degrees of freedom and the applied loads.

$$E_x^0 = \frac{\sigma_x^0}{\varepsilon_x^0} = \frac{F_x}{V\varepsilon_x^0}$$

$$\nu_{xy}^0 = \; -\frac{\varepsilon_y^0}{\varepsilon_x^0} \tag{7.7}$$

$$\nu_{xz}^0 = -\frac{\varepsilon_z^0}{\varepsilon_x^0}$$

When $F_y = F_z = F_{yz} = F_{zx} = F_{xy} = 0$

$$E_y^0 = \frac{\sigma_y^0}{\varepsilon_y^0} = \frac{F_y}{V\varepsilon_y^0}$$

$$\nu_{yx}^0 = -\frac{\varepsilon_x^0}{\varepsilon_y^0} \tag{7.8}$$

$$\nu_{yz}^0 = -\frac{\varepsilon_z^0}{\varepsilon_y^0}$$

When $F_x = F_z = F_{yz} = F_{zx} = F_{xy} = 0$

$$E_z^0 = \frac{\sigma_z^0}{\varepsilon_z^0} = \frac{F_z}{V\varepsilon_z^0}$$

$$\nu_{zx}^0 = -\frac{\varepsilon_x^0}{\varepsilon_z^0} \tag{7.9}$$

$$\nu_{zy}^0 = -\frac{\varepsilon_y^0}{\varepsilon_z^0}$$

When $F_x = F_y = F_{yz} = F_{zx} = F_{xy} = 0$

$$G_{xy}^0 = \frac{\tau_{xy}^0}{\gamma_{xy}^0} = \frac{F_{xy}}{V\gamma_{xy}^0}$$

$$G_{yz}^0 = \frac{\tau_{yz}^0}{\gamma_{yz}^0} = \frac{F_{yz}}{V\gamma_{yz}^0} \tag{7.10}$$

$$G_{zx}^0 = \frac{\tau_{zx}^0}{\gamma_{zx}^0} = \frac{F_{zx}}{V\gamma_{zx}^0}$$

7.2.2 Curved Unit Cell

The boundary conditions outlined in the previous section are only valid for unit cells with translational symmetry, not present in curved models. Alternatively, rotational symmetry is seen within the curved RUC and therefore appropriate periodic boundary conditions are required. This section outlines those boundary conditions and the method to calculate the effective elastic properties of the unit cells.

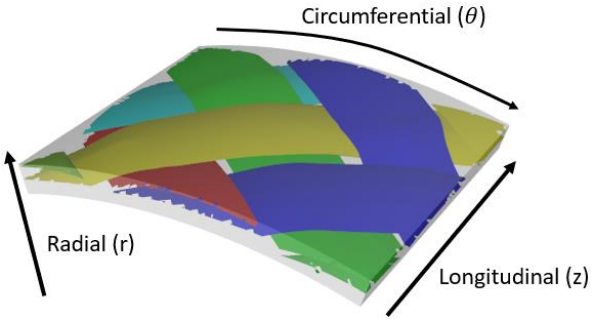

Figure 7-2. A curved unit cell of a braided composite with a polar coordinate system.

Within the cylindrical coordinate system, shown in *Figure 7-2*, the kinematic equations for deformation are defined as.

$$\varepsilon_r = \frac{\partial u_r}{\partial r}$$

$$\varepsilon_\theta = \frac{u_r}{r} + \frac{1}{r}\frac{\partial u_\theta}{\partial \theta} \tag{7.11}$$

$$\gamma_{r\theta} = \frac{1}{r}\frac{\partial u_r}{\partial \theta} + \frac{\partial u_\theta}{\partial r} + \frac{u_\theta}{r}$$

Unlike within a rectangular coordinate system, in a cylindrical coordinate system with a strain field periodic in the circumferential direction, the in-plane displacements, u_r and u_θ will have the same periodic characteristics. Therefore, the following periodic boundary conditions can be applied.

$$u_z|_{\theta=\alpha} = u_z|_{\theta=-\alpha}$$

$$u_r|_{\theta=\alpha} = u_r|_{\theta=-\alpha} \tag{7.12}$$

$$u_\theta|_{\theta=\alpha} = u_\theta|_{\theta=-\alpha}$$

Within the longitudinal direction, the periodicity leads to the following relative displacement boundary conditions.

$$u_z|_{z=b} - u_z|_{z=-b} = 2b\varepsilon_z^0$$

$$u_r|_{z=b} - u_r|_{z=-b} = 0 \tag{7.13}$$

$$u_\theta|_{z=b} - u_\theta|_{z=-b} = 2\phi r$$

Where ϕ is the relative angle of twist about the z-axis. The longitudinal modulus can be calculated using the same procedure as outlined in the previous section in Eq. (7.9). However, the shear modulus is obtained using Eq. (7.14).

$$G = \frac{nT}{J\phi/2b} \tag{7.14}$$

Where n is the number of periods over the circumference, T is the torque applied and J is the polar moment of inertia.

7.3 Meshing

There are two main meshing techniques for unit cell analysis, conformal and voxel meshing, as presented in *Figure 7-3*. Conformal meshing allows for the exact geometry of the yarns and matrix to be captured within the mesh, however due to the geometry of reinforced fabrics, this method can lead to incorrect aspect ratios within the mesh and requires a fine mesh which is computationally expensive. Voxel meshing splits the unit cell into an equal-sized 3D grid with elements either assigned as matrix or yarn material. This has the advantages of being computationally cheap and easy to apply periodic boundary conditions as nodes match on opposite sides of the unit cell. The key downside to this method is the inability to perfectly represent the geometry of the yarns as there is a stepped interface between the yarns and the matrix. However, for the analysis required within this study, a voxel mesh has been chosen. This is due to the reduced computational resources required when using a voxel mesh and the requirement of having nodes in the same position on opposite sides of the unit cell for the boundary conditions. This is easily obtained through voxel meshing but can be difficult and time consuming when using free meshing for conformal meshing.

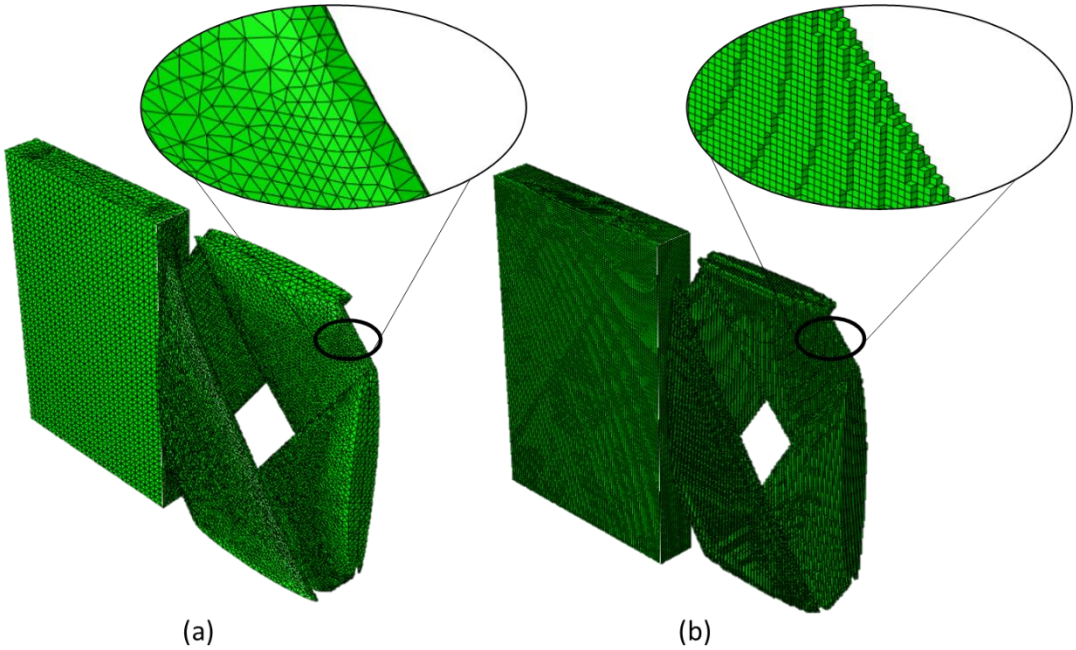

Figure 7-3. Meshing Techniques of braided unit cells with and without pure matrix material. (a) conformal mesh and (b) voxel mesh.

Two methods have been investigated for meshing curved geometry using voxel meshing: stepped boundary and wedge-shaped element voxels. Both methods can be seen in *Figure 7-4*. Both meshing systems allow for the accurate representation of the yarn geometry, whilst due to the rotational symmetry present within the curved models, the stepped boundary is invalid as it will only allow for translational boundary conditions. Therefore, the wedge-shaped voxel meshing technique has been implemented in TexGen and used within this study. This algorithm uses the *PointInsideYarn* function to determine if the centre of the element is within the yarn or matrix material and assigns the required properties accordingly.

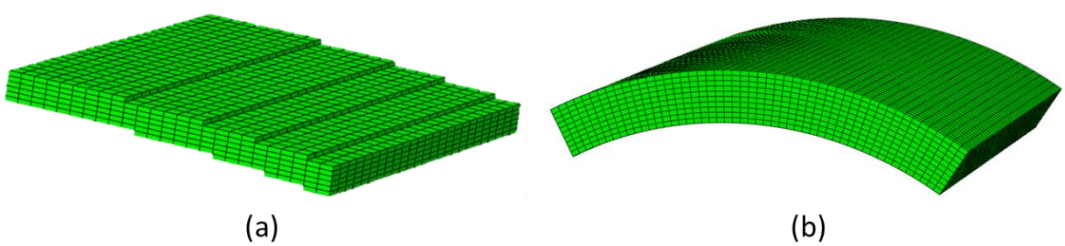

Figure 7-4. Voxel meshing of curved geometry, (a) stepped boundary and (b) wedge-shaped elements.

Nagaraju et al. [108] exported the fabrics as flat unit cells and used a polar transformation to produce the curved unit cell. Due to distortions in the elements,

inaccuracies can occur in the local volume fraction within each element. This value is key to accurately predicting the elastic properties of the yarns in each element using the Chamis equations. The curved voxel mesh algorithm has been written to accurately represent the curved fabric without having to be translated between coordinate systems.

The node sets have been identified for opposite faces, edges and vertices, with the required boundary conditions written into the Abaqus input file. An eight-node brick linear hexahedron element (C3D8) was used in the analysis. Both flat and curved fabrics have been meshed using this technique, with simulations for flat fabrics being conducted in a cartesian coordinate system in Abaqus, while curved fabrics are conducted in a polar coordinate system within Abaqus. While exporting the FE mesh, TexGen generates two additional files. The orientation file (.ori extensions) contains the fibre orientation data for each element and the element data file (.eld extension) contains the local yarn volume fraction data for each element. Elastic properties of each element within the yarns were calculated using Chamis Equations (7.16). This semi-empirical approach does not require any micro-mechanical modelling and is often used for its simplicity.

$$E_1 = V_f E_{f,1} + (1 - V_f) E_m$$

$$E_2 = E_3 = \frac{E_m}{1 - \sqrt{V_f}\left(1 - {E_m}/{E_{f,22}}\right)}$$

$$G_{12} = G_{13} = \frac{G_m}{1 - \sqrt{V_f}\left(1 - {G_m}/{G_{f,12}}\right)} \tag{7.15}$$

$$G_{23} = \frac{G_m}{1 - \sqrt{V_f}\left(1 - {G_m}/{G_{f,23}}\right)}$$

$$\nu_{12} = \nu_{13} = V_f \nu_{f,12} + (1 - V_f)\nu_m$$

$$\nu_{23} = V_f \nu_{f,23} + \left(1 - V_f\right)(2\nu_m - \frac{\nu_{12}}{E_1} E_2)$$

7.3.1 Mesh Refinement

Due to the stepped nature of the voxel mesh at the boundaries between yarns and matrix, unrealistic stress concentrations and inaccurate geometry can occur if a

coarse mesh is used for the analysis. Therefore, a mesh refinement study was completed to optimise the predicted values with the computational expense, shown in *Figure 7-5*. As the equivalent curved models are of the same size, only flat models have been used for the mesh refinement system. Additionally, it is best practice to use cubic elements to reduce inaccurate stresses across the length and height of the element.

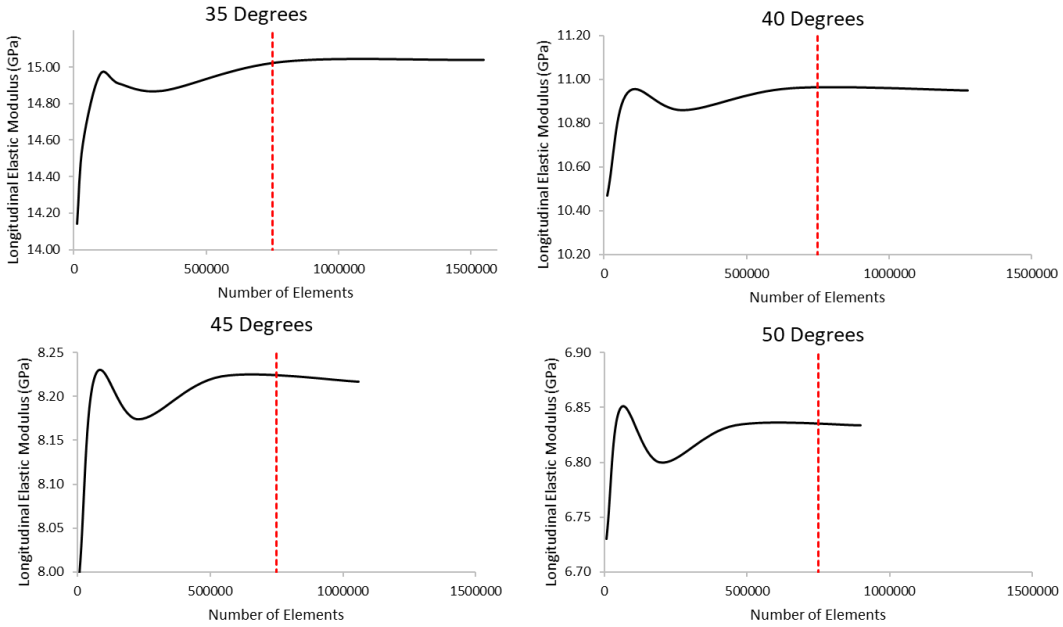

Figure 7-5. Results of mesh refinement study showing a requirement of 750,000 elements.

This study shows a requirement of a minimum of 750,000 elements within the models to converge on a constant value for the longitudinal elastic modulus. The time taken to export a mesh of this size is around 90-100 seconds with a simulation time of around 1500 seconds running on 6 CPU cores. A key factor in the size of the mesh is the number of elements within the thickness of the mesh. This is due to the lenticular shape of the yarns requiring a small element size to capture the cross-sectional shape accurately.

The initial over prediction in the stiffness seen in the mesh refinement graphs is explained by fluctuations in the fibre volume fraction within the unit cell, shown in *Figure 7-6*. This is due to the inaccuracy in following the geometry of the yarn cross-

section. The prediction of fibre volume fraction echoes the modulus prediction values.

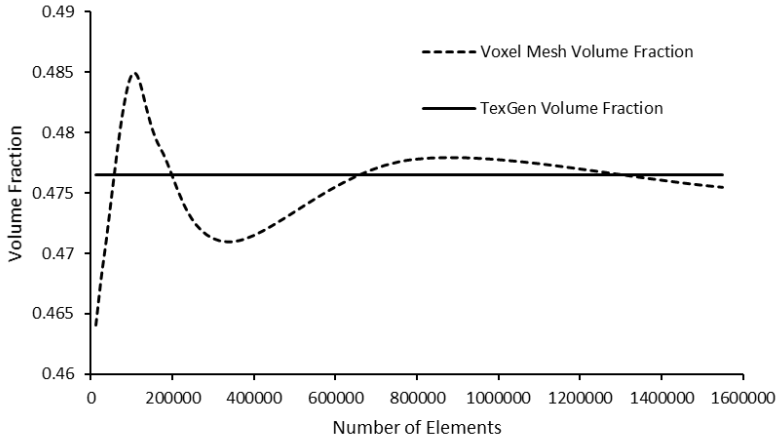

Figure 7-6. Measured volume fraction from voxel mesh compared to the predicted value from conformal mesh.

7.4 Results and discussion

In this section, the proposed curved unit cell model is compared against equivalent flat fabrics for the longitudinal modulus and shear modulus. Elastic modulus for flat fabrics is calculated using Eq. (7.7-7.9). For curved unit cells longitudinal modulus is calculated using Eq. (7.9) and the shear modulus calculated using Eq. (7.14). Four braid angles were chosen, 35, 40, 45 and 50 degrees at a radius of curvature of 10 mm. Yarns within the study were modelled as HexTow AS4 fibres [115] with a yarn width of 2.7 mm and a yarn thickness of 0.35 mm. The properties of the fibres and matrix used within this study are given in *Table 7-1*. The data for this study has been replicated from Ayranci et al. [116], to allow for the comparison of techniques used and validation against experimental data.

Table 7-1. Elastic properties of fibre and matrix. Data adopted from Ayranci et al. [116]. Moduli are given in GPa.

	E_{11}	E_{22}	E_{33}	G_{12}	G_{13}	G_{23}	ν_{12}	ν_{13}	ν_{23}
Carbon Fibre	228	40	40	24	24	24	0.26	0.24	0.1
Matrix	4.2	-	-	1.62	-	-	0.3	-	-

A comparison of predicted elastic properties for both a flat unit cell and a curved equivalent on a 10 mm radius at a range of braid angles is presented in *Figure 7-7*. This shows a significant reduction in both longitudinal elastic modulus and in-plane shear modulus. A 10.5% reduction in longitudinal modulus has been observed for modules with a 35° braid angle. This is seen to reduce with an increase in braid angle, an expected result as the influence of the orthogonal nature of the yarns decreases and an increase in the influence of the isotropic matrix material. Similar results are seen within the shear modulus with a maximum of an 8% reduction in modulus predicted for the curved model.

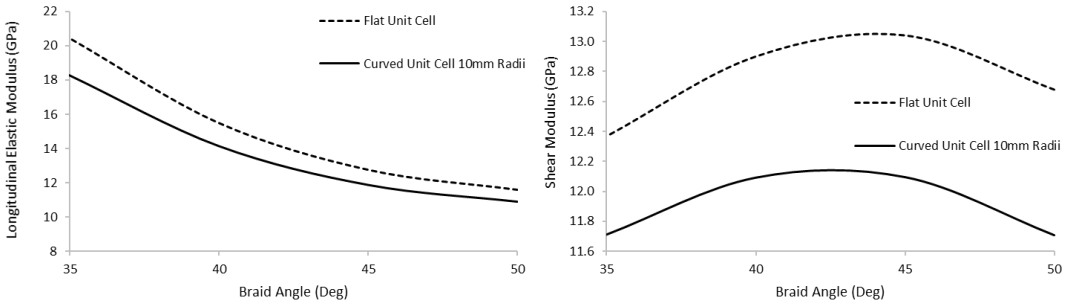

Figure 7-7. Comparison of predicted longitudinal and in-plane shear modulus of flat and curved unit cells for equivalent fabrics with yarn thickness = 0.35 mm.

Changes to the model allow for the influence of fabric thickness to be investigated. The thickness of the yarns has been increased to 0.5 mm, whilst other properties are maintained. This has been a reduction in yarn volume fraction from 0.67 to 0.47. The effects can be seen in *Figure 7-8*. Similar effects are seen in the reduction of the elastic properties for the curved model with a reduction of 10% in the longitudinal elastic modulus.

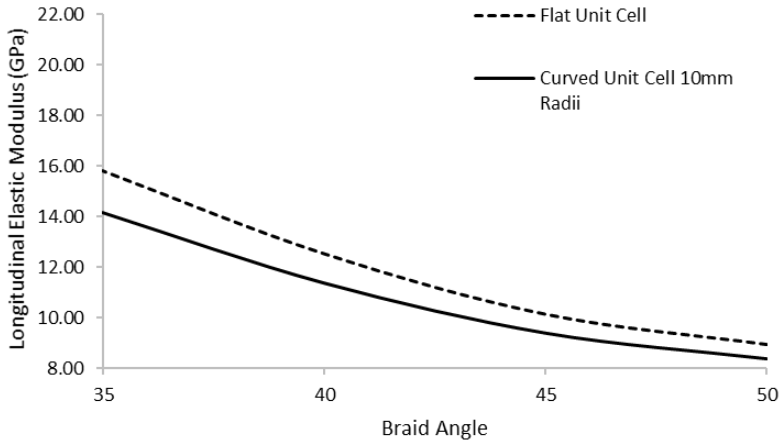

Figure 7-8. Comparison of predicted longitudinal modulus of flat and curved unit cells for equivalent fabrics with yarn thickness = 0.5 mm.

The effect on mandrel radius has been investigated for braid angles between 35 and 50 degrees, on mandrels with an 8 mm radius to 280 mm radius. The results of this can be seen in *Figure 7-9*. This shows a significant decrease in the difference between flat and curved predicted longitudinal elastic modulus with an increase in mandrel radius. Once again lower braid angles are shown to have greater effects on the difference in predicted properties due to the greater influence of yarns on the elastic properties.

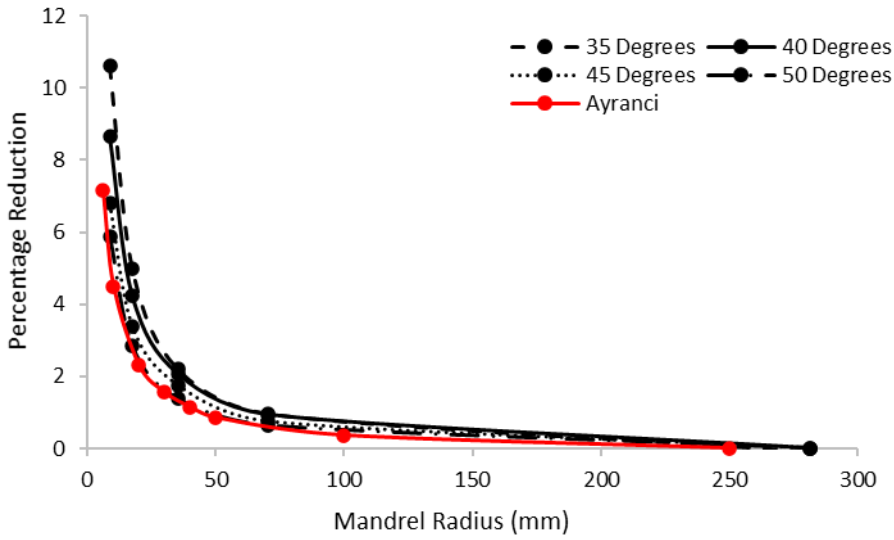

Figure 7-9. Effect of mandrel radius on the difference of longitudinal elastic modulus at a range of braid angles compared to values presented in [116].

The findings from this study have been compared to that in [116] showing similar reductions in longitudinal elastic modulus, with negligible difference in modulus seen for mandrel radii larger than 280 mm. This means for fabrics produced on this size mandrel a flat model will be appropriate for the prediction of mechanical properties. It is noted that the values presented by Ayranci are described as the 'average percentage difference to flat model for E_{xx}' explaining the small differences to the small braid angle values presented in this study. Work presented in [116] has been compared to experimental values, showing agreement within 3%, indicating the methodology presented within this study would lead to comparable results.

7.5 Conclusions

A new methodology for predicting elastic properties of curved braided unit cells has been presented within this chapter. A new meshing algorithm has been implemented within TexGen to allow for wedge shaped voxel meshes to be generated to capture the curvature of the model being tested.

The work presented in this chapter shows a significant difference in the calculated elastic properties for braids manufactured on small-scale radii. A reduction of up to 10.5% has been observed for the longitudinal elastic modulus for braids produced on a 10 mm radius mandrel. This is seen to be present at a variety of braid angles, with a greater effect seen at smaller angles. The influence of curvature on the calculated properties is seen to decrease significantly with an increase in mandrel radius and a negligible difference is seen for models with a 280 mm radius.

Similar effects have been observed with respect to the shear modulus, with a 7.5% difference evident on samples with a 10 mm radius mandrel. Results show a peak difference at a braid angle of 45 degrees, with a reduction seen on either side of this value.

Although experimental validation has not been completed, this work has been compared to similar studies, with a good agreement with the literature for the influence of mandrel radius on the reduction in predicted longitudinal modulus.

8 Mechanical Properties of Braided Composites using Twisted Yarns

Previous chapters have highlighted the geometrical differences between untwisted and low-level twisted yarns during the braiding process on simple mandrels (Chapter 4) and conical mandrels (Chapter 5). A novel methodology has been developed for the prediction and geometrical modelling of braided fabrics, which has been presented in Chapter 6, showing a new module within TexGen. This chapter builds upon this work to investigate the effects of twisted carbon fibres on the mechanical properties of the braided fabric. This is experimentally tested on 0 tpm and 7 tpm samples with modulus and strength presented. A novel framework is presented for the prediction of mechanical properties using models developed within the thesis. This framework is validated against the experimental data collected and expanded to investigate the wider effect of twist within fibres for a range of braid angles and yarn geometry.

8.1 Introduction

When compared to conventional unidirectional and woven laminates, braided laminates provide superior toughness and fatigue strength. In unidirectional laminates, cracks are able to propagate readily along the fibres, whereas the interlacing pattern of the yarns in braided fabrics acts as crack arresters [33]. Additionally, braided composites have good torsional and shear stiffness, and increased transverse moduli and strength whilst offering near net-shaped manufacture. This makes braided fabrics often very appealing, creating the requirement to understand the mechanical properties in further detail.

A range of studies have focused on the mechanical performance of twisted yarns, both in terms of yarn properties [117] and fabric properties [118]. Academic research has largely focused on the effects within Kevlar and glass fibres. As a result of increased levels of twist applied to yarns, a decrease in mechanical properties is reported. Weinberg et al. [119] reports a reduction in strength and modulus for additional twist levels in Kevlar 29/epoxy yarns. This is echoed by Rao et al. [117] showing a decrease in modulus and an initial peak in strength, degrading past twist angles greater than 7°. High levels of twist are seen to reduce the strength, stiffness and permeability of the yarns due to increased difficulty in resin impregnation [120].

It is noted that this effect has been described for high levels of twist, as often used in natural fibres, rather than the low levels of twist being investigated in this study. Cheung et al. [44] experimentally measured the effect of adding up to an additional twist to fibres prior to braiding on mechanical properties. Braided tubular composites were created on PTFE cores and subjected to tensile loading. Results show a small increase in Young's Modulus in fully twisted samples. This level of twist would not be expected on carbon fibre yarns due to the brittle nature of the fibre, with excessive damage experienced at levels above 7-10 tpm in 12K HST40 carbon fibres. Dalfi et al. [118] studied the effects of yarn twist on S-glass yarns for twist levels between 0-40 tpm, showing a small, but not statistically significant reduction in the modulus of elasticity for an increase in twist level. Naik et al. [121] developed an analytical methodology for the prediction of mechanical properties of twisted glass fibre woven composites. An optimum twist angle of 5° is concluded to balance ease of manufacture with mechanical properties. Wolfhart et al. [122] investigated the effects of low levels of twist in carbon fibre braided composites, using 0, 5 and 10 tpm yarns. Samples were tested in ±45° and 0°/90° directions. No significant improvements in modulus could be seen when normalised to 60% volume fraction, with minor improvements in strength for untwisted samples.

8.2 Methodology

To assess the effect of low levels of twist within braided yarns, specimens with 0 tpm and 7 tpm were prepared. Tenax HTS40 12K fibres [123] were used for the manufacture of braided preforms. As with previous studies, alternative direction yarns have been twisted with opposite twist directions (S or Z twist – See Chapter 3.1 for definition). The direction of the twist has not been investigated within this study. The preforms were produced using a 192-carrier axial braider. A regular 2:2-1 braiding pattern was used, with a braid angle of 45° and a coverage factor of 96% for each fabric was achieved. Once braided, the fabrics were cut along the take-up direction, flattened and placed in a mould, with 6 layers of fabric used within each panel. Resin infusion was conducted using Epikote Resin MGS RIMR with the properties of both the fibres and matrix given in *Table 8-1*. Three identical panels for each twist level were produced to enable 30 coupons of each twist level for testing.

Volume fractions for each panel were calculated, showing a consistent volume fraction of 54% between panels.

Table 8-1: Fibre and matrix properties.

	Tensile Modulus (GPa)	**Tensile Strength (MPa)**	**Tensile strain at break (%)**	**Fibre Diameter (μm)**
Carbon Fibre [123]	240	4400	1.8	7
Matrix [124]	3.0	70	8.0	-

Testing was conducted in alignment with the BS EN ISO 527-4:2021 [125] standard for the production of samples and tensile testing. Rectangular samples were cut from the composite panels along the fibre direction to create 0°/90° coupons. Although not indicative of the loading direction of braided components, this method allowed for greater inspection of the changes to the properties. This is due to the fibre preparation and the effects this may cause on the matrix/fibre boundaries, thus making loading in this direction a good indicator of the performance of a composite component prepared with each twist level. Loading within the bias fibre direction encourages failure to be dominated by the fibres rather than the matrix, as is often the case during loading off fibre directions. Samples had a nominal width of 25 mm and a thickness of 3.90 mm for twisted yarns and 2.33 mm for untwisted yarns, following specifications outlined in [125]. Samples were a total length of 210 mm with a gauge length of 110 mm. Tabs produced from a glass fibre/resin laminate were bonded to the ends for gripping within the machine as shown in *Figure 8-1*, in compliance with the standard.

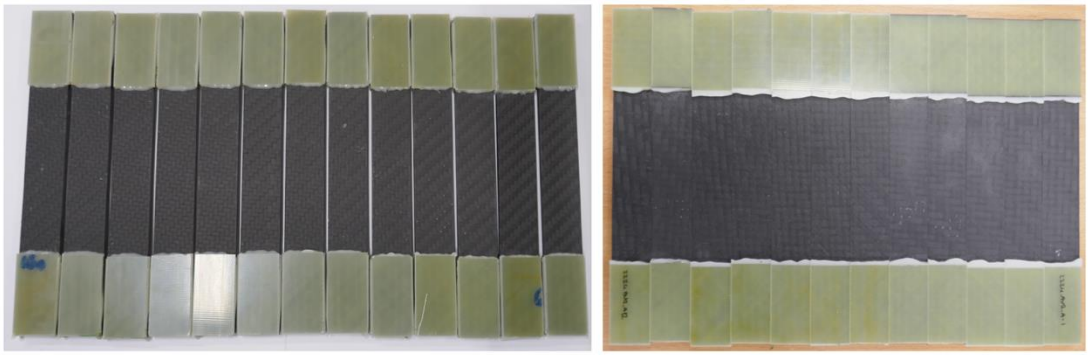

Figure 8-1: Samples of coupons manufactured for tensile testing. (a) untwisted yarns and (b) twisted yarns.

Testing was undertaken using a Shimadzu AG-X+ testing machine with a 100KN load cell [126]. An Epsilon E96524 Extensometer and Imetrum Video Strain Gauge were used to measure strain during the test, as shown in *Figure 8-2*. The speed of the test is defined as strain controlled to ensure a strain rate as close to 1% of the gauge length per minute, leading to a cross-head movement of 2 mm/min in compliance with BS EN ISO 527-4:2021[125].

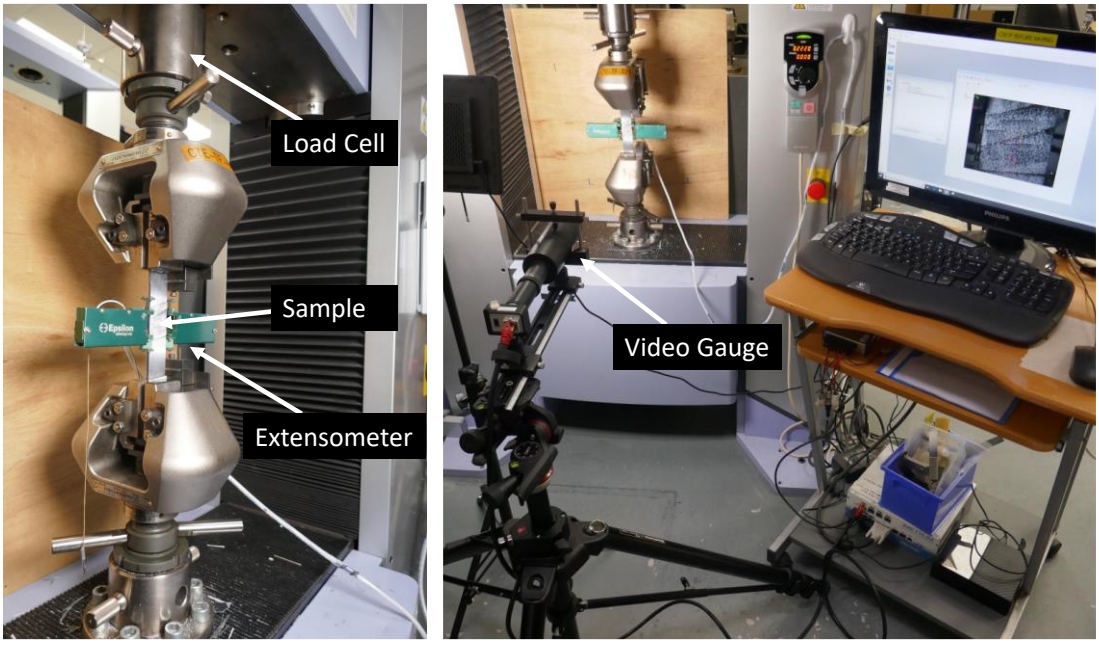

Figure 8-2: Testing setup for tensile testing composite coupons using a video strain gauge.

The tensile modulus of each sample has been calculated with the method outlined in [127] using a linear regression method. This defines the tensile modulus as:

$$E_t = \frac{d\sigma}{d\varepsilon} \tag{8.1}$$

Where $\frac{d\sigma}{d\varepsilon}$ is the slope of a least-squares regression line fit to the part of the stress/strain curve in the strain interval $0.0005\ (0.05\%) \leq \varepsilon \leq 0.0025\ (0.25\%)$, expressed in megapascals (MPa). Full details on the methodology are presented in Appendix F.

Figure 8-3 shows an indicative response for a composite with the key regions of interest highlighted. As previously defined, the region for modulus calculation is represented between $\varepsilon_1\ and\ \varepsilon_2$. Tensile strength is defined as the first local maximum observed during the tensile test as defined in BS EN ISO 527-4:2021. Serviceability failure will occur within the structure prior to this point and is defined as the end of the linear portion of the stress-strain response. As previously discussed, strain measurements were gathered using an extensometer. Large levels of noise are expected in the readings due to the small levels of strain being induced within the sample. Therefore, a Gaussian filter has been applied to the data, with both raw and filtered data presented in *Figure 8-3*. See Appendix F for methodology.

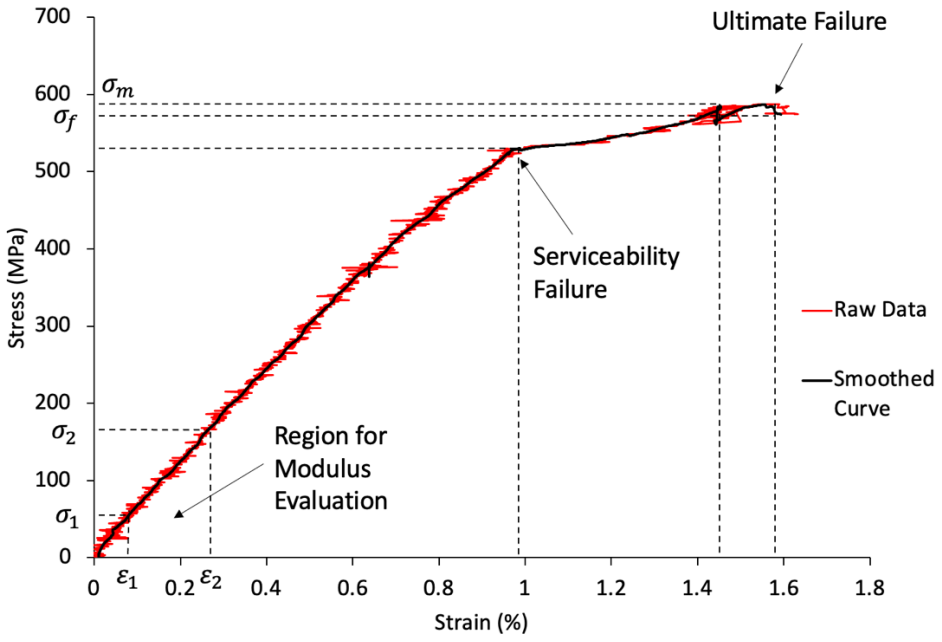

Figure 8-3: Indicative Stress/strain response for composite specimens showing region for modulus calculation, serviceability failure and ultimate failure. Data shows raw data gathered from a video strain gauge and smoothed data using a Gaussian smoothing filter.

8.3 Results

Initial inspection of the results shows a low level of strain noise within the samples. This can be seen in the raw data in *Figure 8-3*. This indicates a high level of confidence in the strain measurements, gauge placement and tab bonding to the sample. Additionally, many samples show serviceability failure within the specimen, indicated by a sudden jump in strain before a redistribution of stress within the sample followed by the failure of the coupon. This phenomenon is caused within composite panels loaded in the fibre direction. Internal fibres within the composite fail leading to the transfer of loads to surrounding fibres until the specimen is unable to maintain loading and total failure is caused. An example of the stress-strain response within this region is shown in *Figure 8-4*

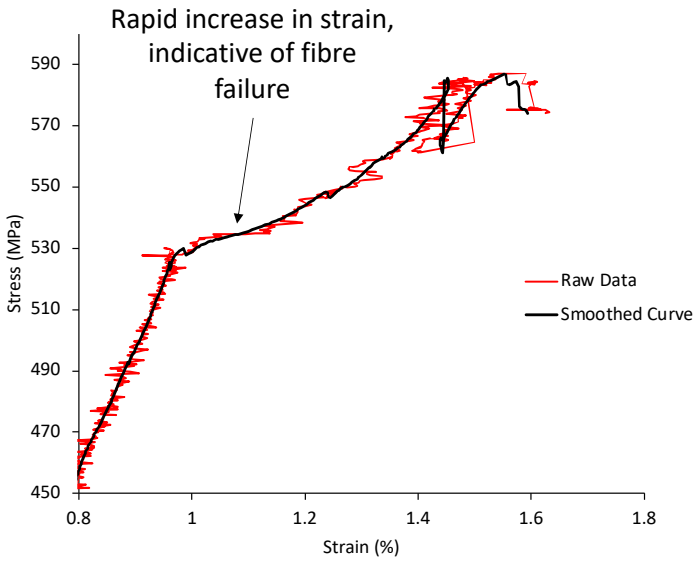

Figure 8-4: Serviceability failure regions within composite stress-strain response.

Results have been averaged for both twisted and untwisted samples with the stress strain response displayed in *Figure 8-5*. Untwisted yarns show brittle failure of the composite, indicated by a sudden failure of the coupon. Twisted fibres display a pseudo-ductile failure. This can be seen in the elongation of the twisted sample response in *Figure 8-5* between the serviceability failure and ultimate failure stresses. Greater average tensile failure strain values are measured for twisted yarns (1.47% strain) compared to untwisted yarns (1.17% strain).

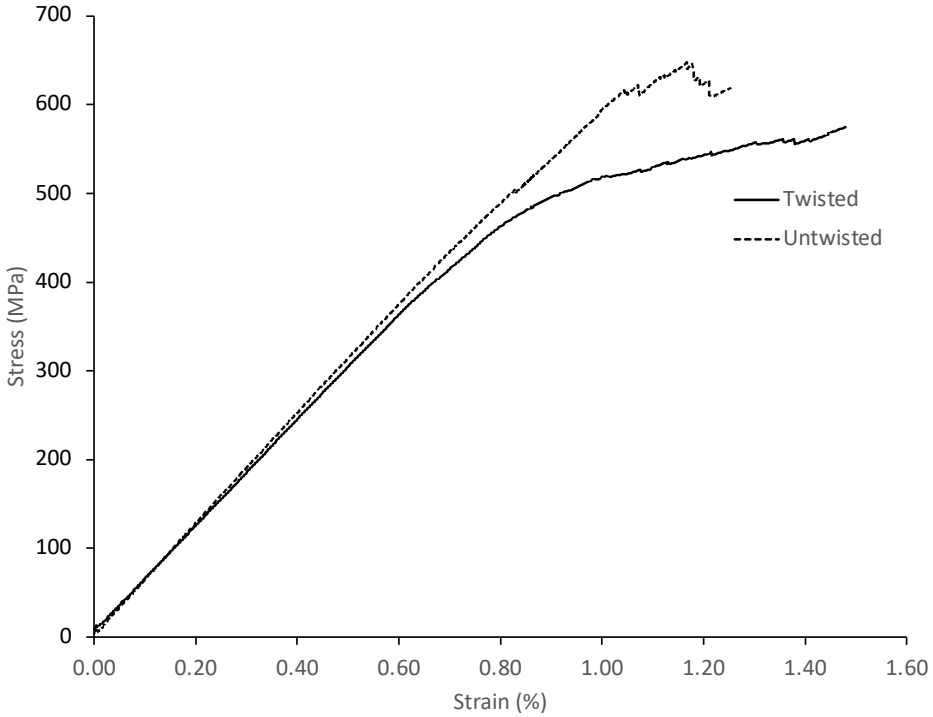

Figure 8-5: Average tensile stress/strain response for untwisted and twisted fibres, loaded along the fibre direction.

Inspection of failure locations across samples shows that both composites fail laterally within the gage length, indicating both successful bonding of the tabs and purely tensile loading within the test. Additionally, failed coupons show the causes behind the failure profiles seen in *Figure 8-5*. Untwisted yarn coupons, presented in *Figure 8-6,* show linear failure within the gauge region with little to no indication of delamination of fabric layers within the failed samples. This indicates a sudden failure event within the yarns of the test sample, as evidenced in the stress-strain profile. Alternatively, twisted yarn coupons, presented in *Figure 8-7*, clearly show a level of delamination between the layers in the side profile views. This delamination of the layers absorbs the stress within the structure and causes the pseudo-ductile failure as seen within the stress-strain profile. This effect is likely caused by the added thickness of the yarns within the sample. This causes a weakened bond between the layers of the fabrics and greater levels of crimp within the yarns causing the delamination process during loading.

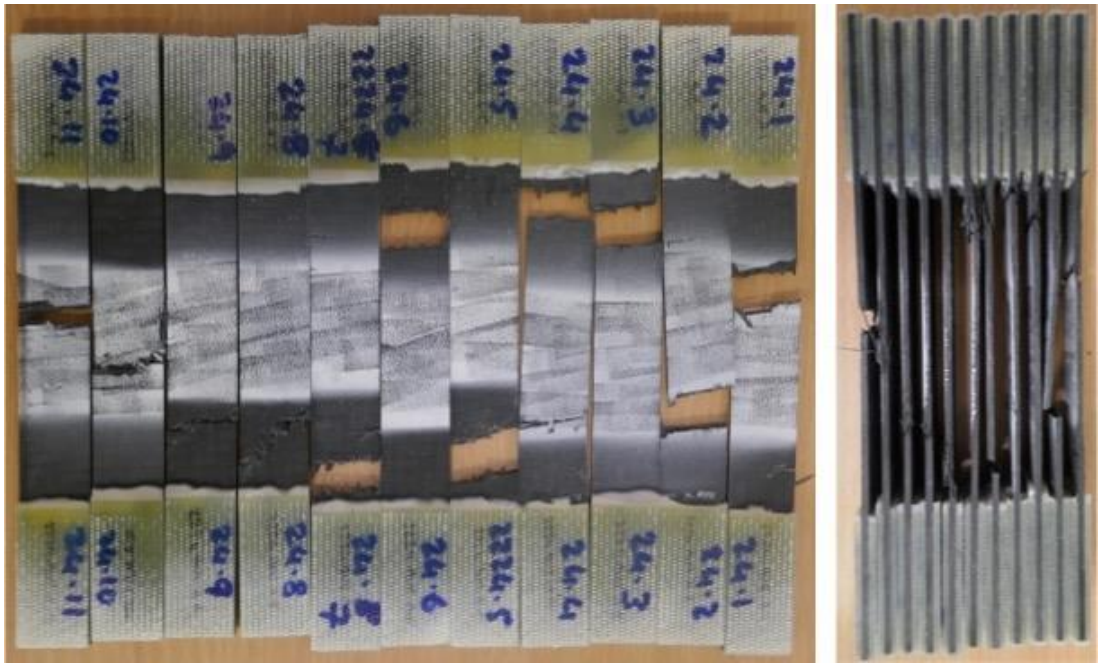

Figure 8-6: Sample images of failure of coupons for untwisted fibres. Failure shows linear cracks in the gauge regions with little evidence of delamination between layers during testing.

Figure 8-7: Sample images of failure of coupons for twisted yarns. Failure shows linear cracks in the gauge regions with evidence of delamination between layers during testing.

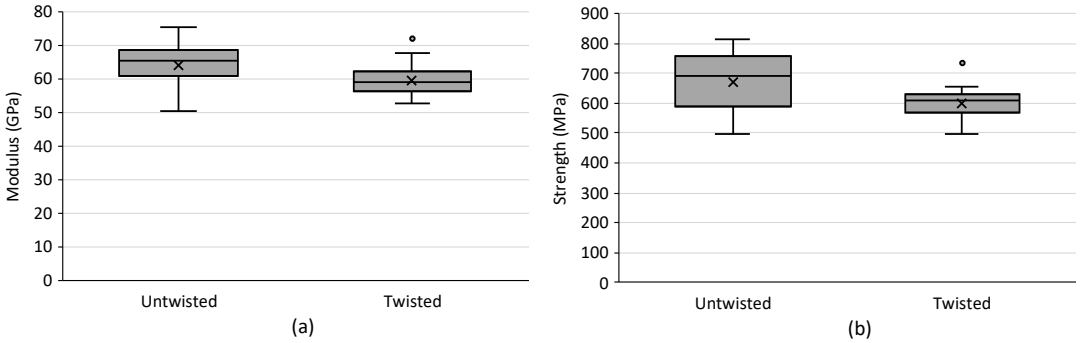

Figure 8-8: Statistical analysis of experimental results for (a) modulus and (b) strength.

Using methods outlined in [125] and detailed in the previous section, the tensile modulus and tensile strength have been determined for each specimen, see Appendix F for the analysed data. Analysis of the tensile modulus measurements shows a high level of data alignment, with average values of r^2 of 0.99 and 0.97 for untwisted and twisted samples respectively. These results are presented in *Figure 8-8*. Minimal differences are evidenced for the tensile modulus across the two samples, with a small increase between median values for untwisted samples, 65.65 GPa to 59.15 GPa for twisted. When comparing the range of values for each sample, a decrease in the interquartile range (IQR) and total range can be seen for twisted samples, 5.81 GPa compared to 7.40 GPa for untwisted. The twist is seen to have a greater effect on the tensile strength compared to the modulus, with a reduction of the median strength value from 690.67 MPa to 611.11 MPa. Similar to the modulus results, a reduction in the IQR is measured for the strength of twisted samples from 160.51 MPa for untwisted yarns to 53.06 MPa for twisted samples. The reduction in variability of results is linked to the reduction in yarn geometry variability presented in Chapter 4. The results presented show that a more consistent fabric and yarn geometry leads to a more predictable stress-strain response from the composite.

Due to loading in the fibre direction during the testing, a reduction in strength is an indication of a weakening of the interfacial fibre/matrix boundary [128]. This prevents fibre pull-out during loading as the weak matrix around the fibres fails due to stress within the structure. Results in Chapter 4, Section 4.2.4 showed an increase in damage to the surface of the yarns and sizing in the yarns. Previous studies have

shown a decrease in mechanical performance due to damage caused to the sizing, with the interfacial fibre/matrix boundary being damaged once infused [102].

An increase in yarn thickness through the inclusion of twist with the yarns causes increased levels of crimp within the fabric, leading to off-axis loading during the tensile test. Multiple studies have shown an increase in yarn crimp within a sample reduces the strength of the composite [31], as echoed by the results of this study.

The results presented in this study agree with similar studies presented in the literature [119, 122]. Other studies have shown increases in mechanical properties for low levels of twist but have presented finding using alternative fibres such as Kevlar and natural fibres.

8.4 Modelling

The ability to predict the effects of changes in fibre preparation is key for an industrial setting, creating the opportunity to adjust a design or develop a new product quickly and with reduced costs. The methodology outlined in Chapter 6 allows for this prediction and modelling of yarn geometry in 2D biaxial braids. To expand and validate this work, a methodology for modelling and testing the effects of changes in fabric geometry due to twisting in braided samples is presented for a range of braided fabrics and compared to experimental results. Validation of the meshing technique is presented, comparing stress distribution between conformal and voxel meshing.

8.4.1 Meshing Techniques

Various meshing techniques have been used in a range of studies for the prediction of the mechanical properties of composite materials. The complex geometry of the yarns and matrix material often leads to difficulties in accurately representing the geometry whilst maintaining an efficient meshing technique. As shown in previous sections, the small differences in yarn geometry can have effects on both the modulus and the strength of the composite. Prediction of the mechanical response of composite materials is a highly researched area with multiple methodologies being implemented for this. Nobeen et al. [129] focused on micro-damage modelling in biaxial braided composites, using 3D Hashin and Stassi failure criteria. Braided unit

cells are meshed using a conformal mesh with eight-node brick elements (C3D8R) with reduced integration, and six-node wedge (C3D6) elements or four-node tetrahedron element (C3D4) elements are used for the yarns. Xiao et al. [55] focused on the strength prediction of a triaxial braid, showing good agreement with experimental data for initial failure when using a similar conformal mesh. Binienda et al. [56] incorporated a damage progression model with Hashin failure criteria to predict failure behaviour in triaxial braids. Dauda et al. [57] presented tension, compression and shear tests on braided composites and characterised their properties. These studies have shown that conformal meshing can lead to good predictions of the strength and failure of braided unit cells. Due to the nature of conformal meshing, the complexity of the FE model is increased with increased element numbers and time to run. Additionally, difficulty arises when applying periodic boundary conditions. This is due to the difficulty in matching node pairs on opposite faces. In most cases, no periodic boundary conditions are used with pinned loading at the base of the unit cell with a displacement applied to the upper surface. A detailed comparison between using Periodic Boundary Conditions (PBC) and non-periodic boundary conditions for braided unit cells showed minimal differences in the case of uniaxial loading condition [130, 131]. However, some studies have opted to use a voxel mesh for the strength prediction. Zhang et al. [54] allected to use a voxel mesh for the prediction of failure modelling within triaxial braided composites.

All models that aim to predict the strength of the composite rely on a failure criterion for the onset of failure within their models. This is often taken as 3D Hashin failure [132], however many others have been developed such as Tsai-Wu [133] or Tsai-Hill failure [134]. This leads to the results being intrinsically linked to the failure criterion applied, rather than the stress distribution within the unit cell. To avoid this, the study presented shows the properties of the unit cell within the elastic region only, with modulus being the main objective.

This study looks at two different meshing techniques: conformal and voxel meshing. Through comparing stress distributions within tensile loading, localised regions of stress concentrations can be investigated, with their effects on the tensile properties of the unit cell.

8.4.1.1 Boundary Conditions

The application of loading and boundary conditions is important for the simulation of mechanical properties. Typically, PBCs have been used for mechanical analysis, as outlined by Li et al. [112]. However, for the PBC to be valid there must be identical nodal coordinates on opposite sides of the model, allowing for a constraint equation to tie each nodal pair together. This is easily achievable in voxel meshing, however for complex conformal meshing this is not possible. Therefore, a simple non-periodic boundary condition has been used within this study. In this situation, the lateral sides of the unit cell were not constrained, with a pinned boundary condition applied to the bottom surface and a displacement applied to the upper surface, as seen in *Figure 8-9*. The boundary conditions used within this simulation have been used in multiple other studies [96, 129].

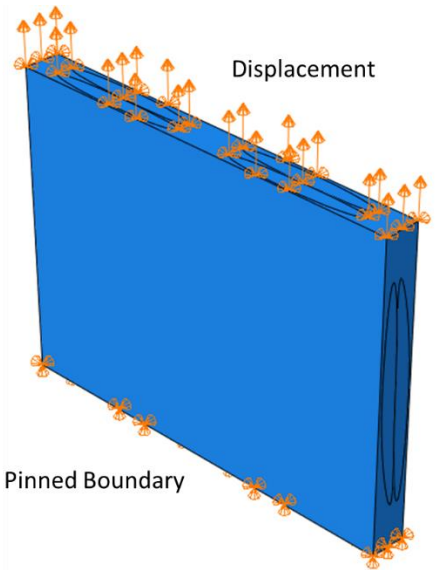

Figure 8-9. Boundary conditions applied to a meso-scale braid unit cell.

8.4.1.2 Conformal Mesh

Conformal meshing allows for the complex geometry of the yarns within the unit cell to be accurately captured within the mesh. However, this can often lead to complexities in meshing the matrix material due to the complex geometrical shape. From TexGen, the unit cell is exported as a .step file, capturing the surface mesh of the yarns within the unit cell. This is imported into Abaqus as a single part with boundaries between yarns and matrix material to enable the yarn material and matrix material to be assigned, an example of this can be seen in *Figure 8-10*. The

mesh is generated within Abaqus using 4-node linear tetrahedron elements (C3D4) to capture the complex shape of the part.

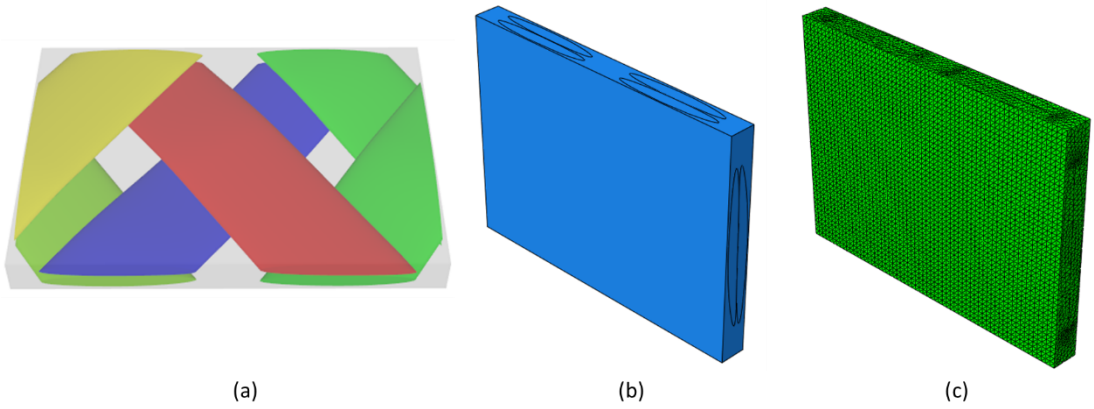

Figure 8-10. Example of a biaxial braid unit cell created in (a) TexGen, (b) imported into Abaqus and (c) meshed using conformal mesh.

8.4.1.3 Voxel Mesh

The use of voxel meshing for representing complex composite geometries has been demonstrated in multiple studies [54]. Artificial stresses can occur on multi-material boundaries when using voxel meshes due to the stepped, block-like representation of a smooth boundary. Attempts at smoothing this artificial stress have been conducted by Fang et al. [135]. Voxel meshing is conducted within TexGen, assigning eight-node brick elements (C3D8) with local yarn volume fractions and fibre orientations imported into Abaqus for accurate prediction of mechanical properties within the yarns.

8.4.1.4 Material Model

The braided composites studied within this present study are simulated using Toray 12K T700s yarns. *Table 8-2* presents the properties of each of the components within the model. Longitudinal properties and matrix properties have been taken from the manufacturer data sheets with the transverse and shear properties of the T700s carbon fibre described by Li et al. [49]. The properties of the yarns are calculated using the Chamis model [46] for the infused yarns. The yarn volume fraction for each yarn is output from TexGen, using fibre diameter data and yarn area data.

Table 8-2. Mechanical properties of composite components

	E_{11}	E_{22}	E_{33}	G_{12}	G_{13}	G_{23}	**Fibre Diameter (µm)**
Carbon Fibre	230	15	15	24	24	5.03	7
Matrix	3.5	-	-	1.0	-	-	-

8.4.2 Results

A conformal mesh comprised of 1.3 million elements was used, alongside a voxel mesh containing 1.1 million elements to gain the resolution required to capture the yarn geometry correctly. (See Chapter 7 for evidence). *Figure 8-11* shows the results of the von Mises stress within the yarns of the structure for a range of strain values. Each model uses the same loading and boundary conditions. Inspection of the unit cells for each strain value shows an agreement between the values for the stress within the yarns.

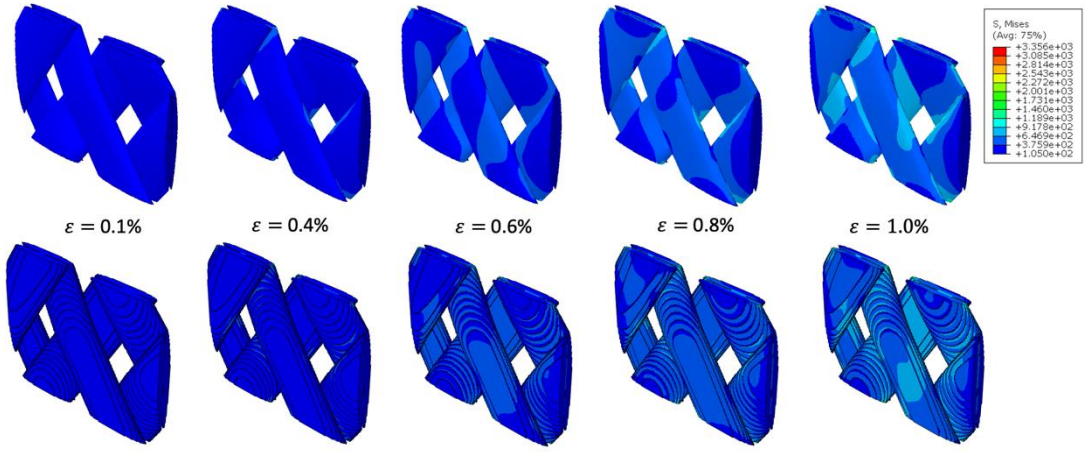

Figure 8-11: Comparison of von Mises stress in MPa within the yarns for a conformal and voxel mesh unit cell for a range of strain values from 0.1%-1.0% strain.

Some evidence of mesh created stress concentrations can be seen in the voxel mesh when compared to the conformal mesh, as highlighted in *Figure 8-12*. To evaluate the impact of these stress concentrations, the tensile modulus of both techniques has been compared with a 4% increase in calculated modulus for the voxel mesh. This is within an acceptable level, indicating the mesh created stress concentrations are having limited effects on the properties. This may require further research if

failure modelling is expected as they may cause localised areas of failure, having the potential to significantly impact the stress-strain response of the system.

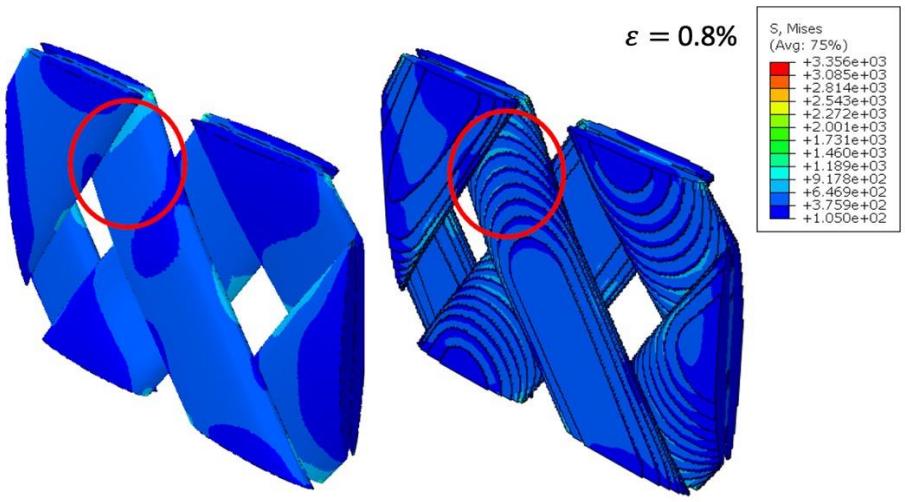

(a) (b)

Figure 8-12: Stress distribution within (a) conformal and (b) voxel meshing. Evidence of mesh created stress concentrations within the voxel mesh as highlighted in red at higher levels of strain. Stress given in MPa.

The final conclusions on the meshing technique show minimal advantages to using a conformal mesh over a voxel mesh for elastic property prediction, with limited effects on the internal stress values within the structure. Due to the complex nature of the yarn shape, a large number of elements are required for the conformal mesh with problems often occurring in relation to element size ratio with regions between upper and lower fibres. This can often cause problems within the meshing of the system, requiring input to ensure a stable mesh can be created. Additionally, the difficulty in applying periodic boundary conditions using the conformal meshing technique leads to the decision to use a voxel mesh for subsequent mechanical property simulations.

8.4.3 Validation of TexGen Models

The previous section displays the validity of using the voxel meshing technique for the mechanical property analysis of braided models. To validate the TexGen modelling technique developed within the study, mechanical elastic properties have been compared to experimental results presented in Section 8.3.

Table 8-3: Yarn geometry data of tensile coupons

Twist Level (tpm)	Yarn Width (mm)	Yarn Thickness (mm)
0	3.54	0.20
7	2.30	0.35

For this analysis, single-layer models of the braided structure were produced using the methodology outlined in Chapter 6 to simulate the production of a fabric with a braid angle of 45°. This has been rotated to replicate the coupon direction tested within Section 8.3, results of this can be seen in *Figure 8-13*. Yarn geometry data is given in *Table 8-3* for each level of twist.

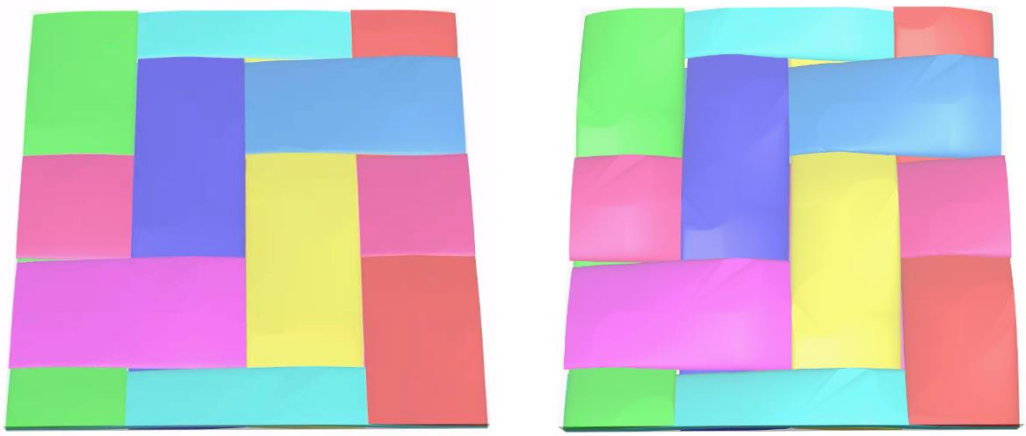

Figure 8-13: TexGen models of (a) untwisted and (b) twisted braided fabrics used for validation.

Analysis of the TexGen models shows fibre volume fractions comparable to the measured experimental values, with a predicted value of 55% for untwisted and 52% for twisted models compared to a value of 54% for experimental samples.

Predicted elastic values were calculated using mechanical data presented in *Table 8-1* and voxel meshing. Boundary conditions are outlined by Li in [112] for the testing of unit cells using Abaqus.

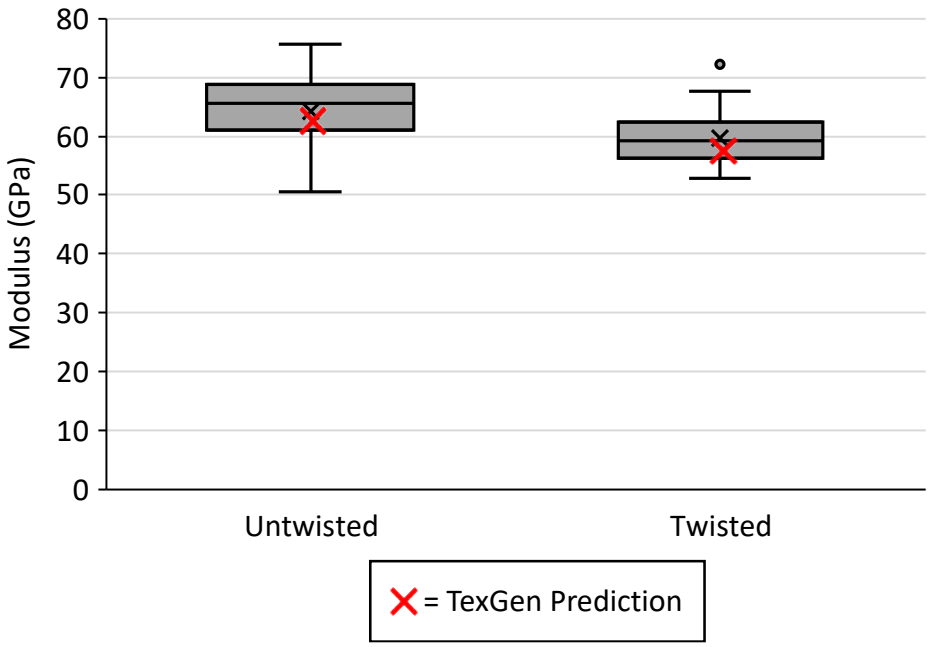

Figure 8-14: Predicted elastic tensile modulus values compared against experimental values presented in Section 8.3.

Results show good validation of the predicted elastic modulus, with a value of 62.7 GPa and 57.4 GPa for untwisted and twisted samples respectively. This is compared to a medium value of 65.65 GPa and 59.15 GPa for experimental values. This shows a high level of confidence in the TexGen predictive model, with minimal differences between values. Predictive results match the small decrease in modulus experienced in twisted models. This relates partially to the reduction in the yarn volume fraction and partially due to the increased level of undulation within the fibres. Models use localised yarn directions for the prediction of mechanical properties within Abaqus, leading to greater off-plane properties at the detriment of in-plane properties.

This methodology shows a high level of confidence in the ability to predict composite elastic properties modelled using the methodology outlined in Chapter 6 compared to experimental values. Further sections investigate the effect of twist further simulating a range of braided unit cells for mechanical analysis.

8.5 Predictive Modelling

Following the validation of the methodology in Section 8.4.3 a range of biaxial braided unit cells have been modelled using the method presented in Chapter 6 to predict yarn geometry and braid architecture. The elastic mechanical properties for

these resultant models have been simulated and compared between different levels of twist.

For this study a range of braid angles, 35°, 40°, 45°, 50° and 55° with constant coverage have been modelled. Twist levels of 0, 3 and 5 tpm are used. Yarn geometry has been defined using data presented in Chapter 4 with a summary given in Table 8-4.

Table 8-4. Yarn Geometry Data

Twist Level (tpm)	Yarn Width (mm)	Yarn Thickness (mm)
0	3.54	0.28
3	3.07	0.32
5	2.77	0.33

Figure 8-15 presents the TexGen unit cells produced using different twist levels at 45° braid angle. This shows the significant difference in the architecture, expected to lead to significant differences in the elastic properties of the composite. Voxel meshing ensures nodes are equivalent on opposite sides of the unit cell, enabling the easy usage of periodic boundary conditions (PBC) when estimating the mechanical properties. Li et al. [112] defines the boundary conditions used within this study.

Due to the block-shaped nature of voxel meshing, complex geometries often require highly refined models to avoid large artificial stress concentrations. Due to this, a mesh refinement study was completed which showed a minimum voxel size of 0.03 mm^3. This led to 20 elements, representing the thickness of the fabric, for the 0 tpm sample. This is typically the limiting factor when meshing braided fabrics due to the requirement to capture the lenticular shape of the yarn with the required resolution. Additional elements are used in the twisted models due to the increase in thickness.

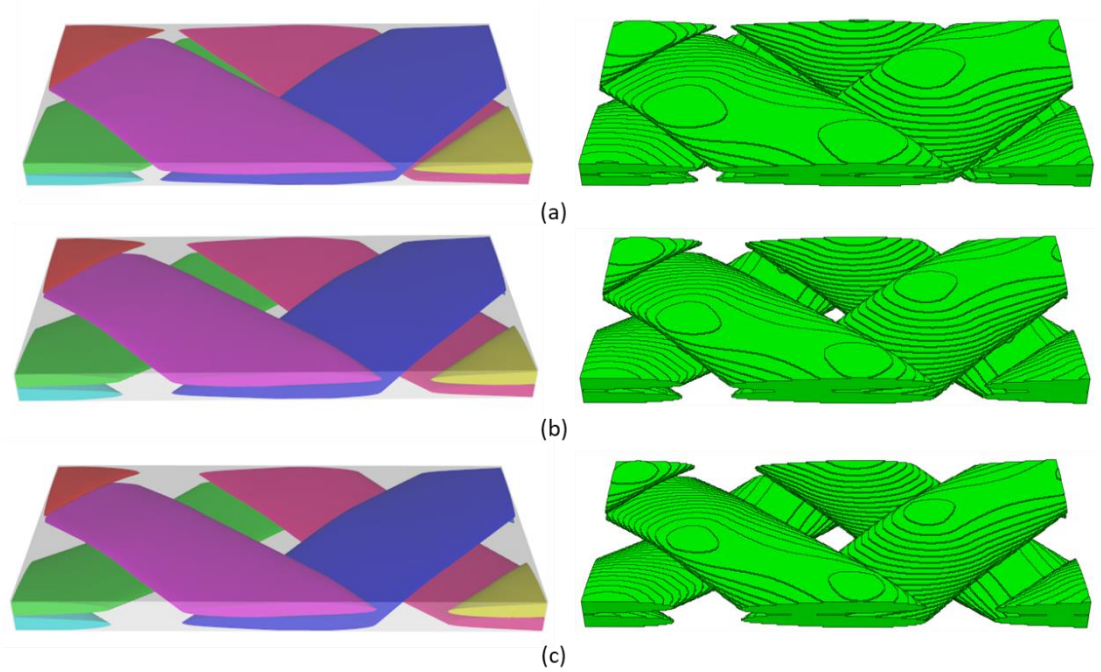

Figure 8-15. Biaxial braid unit cells and voxel mesh with 3 levels of twist, (a) 0 tpm, (b) 3 tpm and (c) 5 tpm.

Changes in yarn volume fraction between the different twist levels have been observed using the yarn volume fraction prediction tool within TexGen, with a 7% increase in yarn volume fraction between 0 tpm and 5 tpm yarns. This shows that the twisting of the yarn leads to the compaction of the total area. However, when measuring on a global scale of the unit cell, the total volume fraction is seen to decrease by up to 17% between 0 and 5 tpm samples. The full data is given in *Table 8-5*. Following modelling using functions within TexGen, models are exported using voxel meshing to capture the changes in yarn geometry.

Table 8-5. Local yarn and fibre volume fraction calculated from TexGen.

	0 tpm	**3 tpm**	**5 tpm**
Local Volume Fraction	0.61	0.62	0.65
Fibre Volume Fraction	0.394	0.349	0.330

Material properties for the components are detailed in *Table 8-6*. The Chamis model [46] is used for estimating the mechanical properties of the yarns, using the yarn volume fractions calculated within TexGen. Results from Section 8.3 show a minor

reduction in the stiffness and strength of twisted yarns. To capture this within the model a reduction factor has been applied to the yarns. This is based on the orientation of the individual filaments in the yarn. Filaments towards the outer edges of the yarns show a greater change in the orientation with relation to the longitudinal direction for yarns with twist applied. The reduction factor is calculated using the cosθ or Gegauff's classic model [117]. In this, the stiffness of the twisted yarn is calculated using Eq. (8.1) where E_{11}, E_f and θ are defined as the yarn modulus in the longitudinal direction, the elastic modulus of the filament and the surface yarn twist angle (2° for 5 tpm fibres) respectively.

$$E_{11} = E_f \cos^2 \theta \tag{8.1}$$

Table 8-6. Material properties for components in the braided models.

	E_{11}	E_{22}	v_{12}	v_{23}	G_{12}
Carbon Fibre	228	40	0.26	0.1	24
Matrix	4.2	-	0.3	-	1.62

8.5.1 Results

Using the proposed models the longitudinal, transverse and in-plane shear modulus has been estimated and presented in *Figure 8-16*, *Figure 8-17* and *Figure 8-18* respectively.

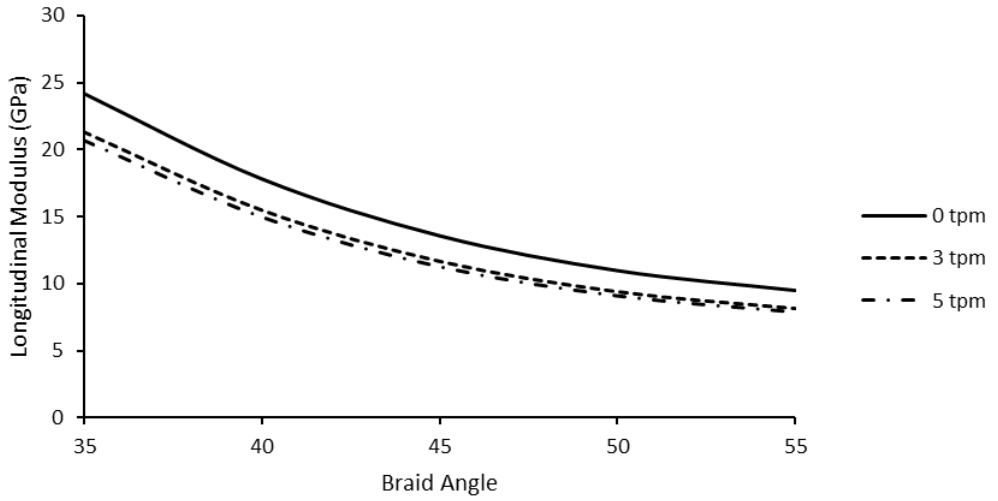

Figure 8-16. Influence of low levels of twist in yarns on longitudinal modulus for biaxial braided composites.

Results in *Figure 8-16* show a reduction in longitudinal elastic modulus for an increase in twist levels, with an average reduction of 16.7% between 0 tpm and 5 tpm in the longitudinal modulus. This is primarily due to the decrease in the fibre volume fraction of the composite, a key factor in the elastic performance. This difference is greater in smaller braid angle models, due to the greater influence of the yarns superior longitudinal properties, compared to the transverse properties and matrix properties. Such effects were not seen in the experimental results presented in Section 8.3 as the coverage factor and volume fraction were kept constant between samples. Similar effects are seen in the transverse, *Figure 8-17*, and in-plane shear modulus, *Figure 8-18*. Critically, the differences between 3 tpm results and 5 tpm show little differences in the mechanical properties, indicating a non-linear relationship with a point at which adding additional twist had a negligible effect on the mechanical properties. This is proposed to be due to the limit on the packing density of the yarns, meaning an additional twist would not alter the geometry of the yarn.

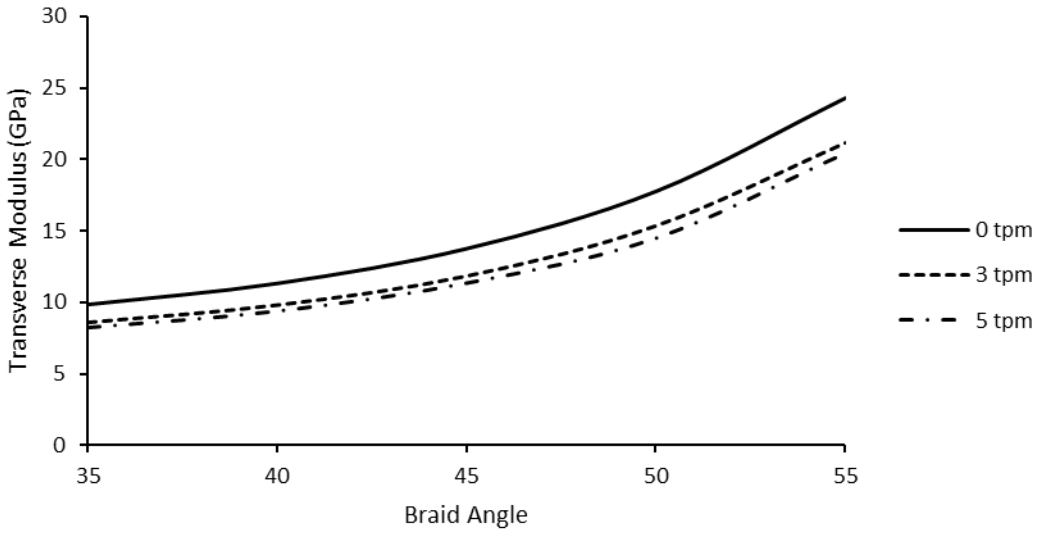

Figure 8-17. Influence of low levels of twist in yarns on transverse modulus for biaxial braided composites.

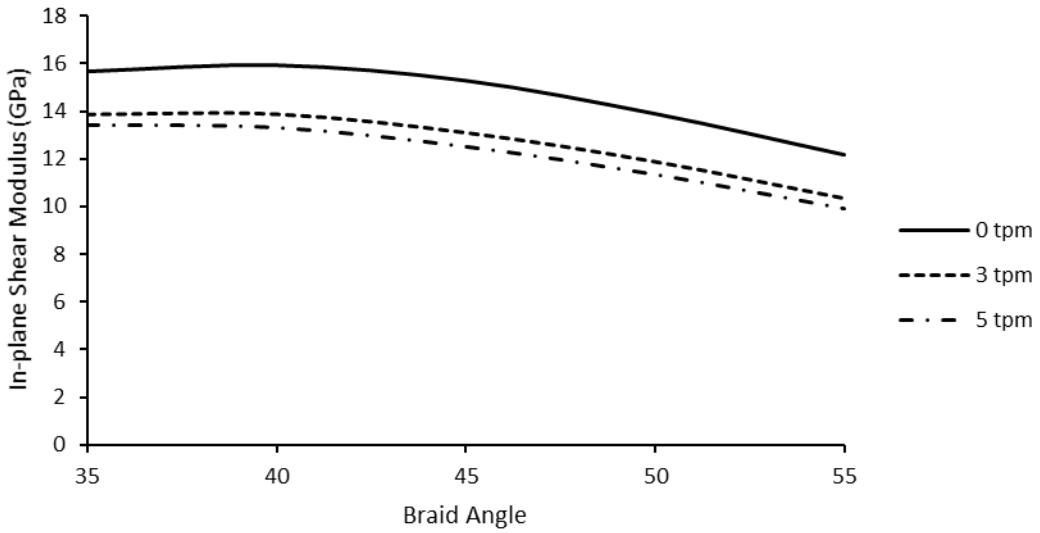

Figure 8-18. Influence of low levels of twist in yarns on in-plane shear modulus for biaxial braided composites.

In addition to the elastic and shear modulus the effect on in-plane Poisson's ratio was investigated, presented in *Figure 8-19*, displaying no effect due to the twist level within the fibres.

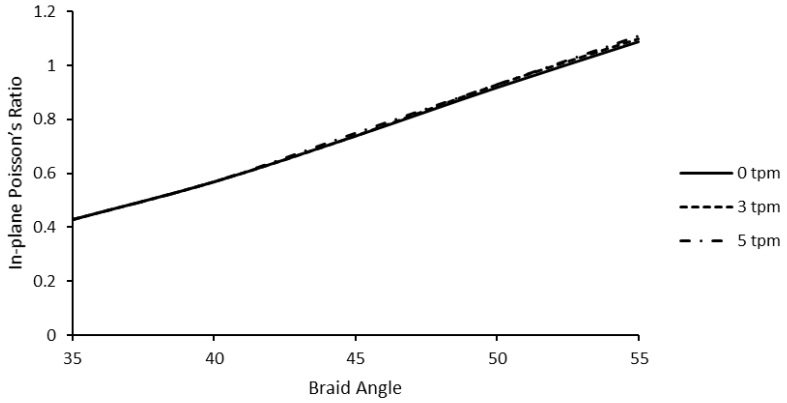

Figure 8-19: Influence of low levels of twist in yarns on in-plane Poisson's ratio for biaxial braided composites.

The coverage factor is a key parameter designers must consider when designing braided composite components. Twist level has a significant effect on this, potentially leading to large reductions in the mechanical performance of the component. This can be addressed through the increase in the number of yarns within the fabric or a reduction in the diameter of the mandrel being braided.

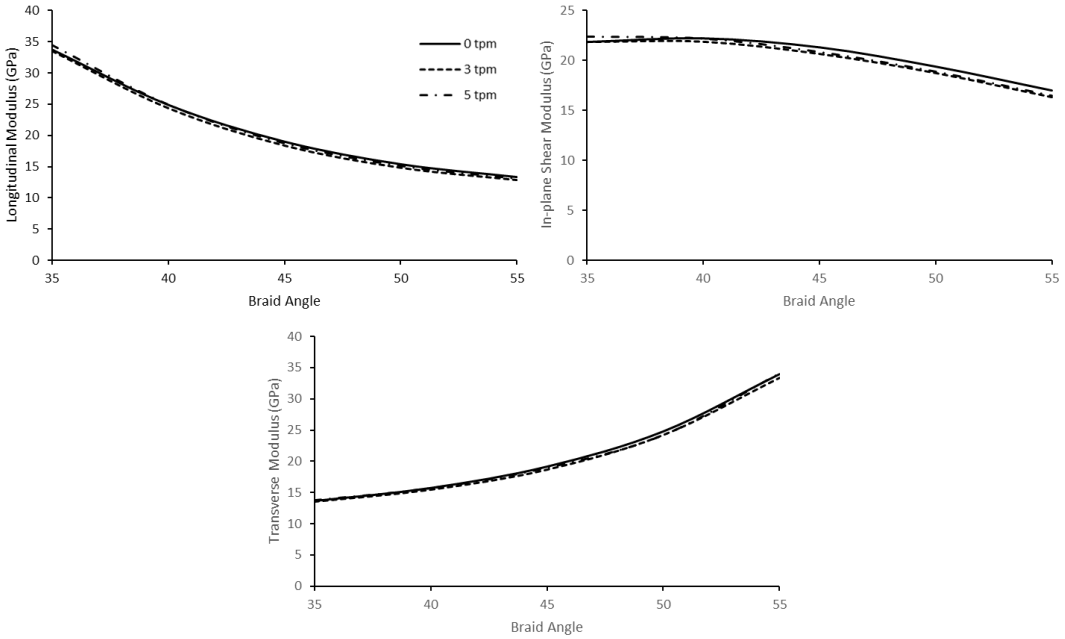

Figure 8-20. Mechanical properties of 3 twist levels normalised to 55% volume fraction.

To investigate the effect of yarn geometry changes, within models produced in TexGen volume fractions have been normalised to 55% for all braided samples, with the results presented in *Figure 8-20*. This shows minimal differences in the mechanical properties between different twist levels, with an average 3% reduction in longitudinal modulus for 5 tpm samples. This reflects much of the research previously conducted, showing small effects on elastic modulus, but no statistically large differences at low levels of twist as experienced in these tests.

8.6 Conclusions

Previous chapters have investigated the effects of yarn twist on the geometry of the yarns and the architecture of the fabric (Chapters 4 & 5) showing significant effects. The development of novel predictive tools for the geometry of the braided fabric has been outlined in Chapter 6, enabling the flexibility to test multiple configurations and fabric properties in the early design stages. The current chapter has combined data and methodologies from these chapters to investigate the effects of yarn twist during the winding process on the mechanical properties of the fabric. Predictions and experimental data have been presented, with an additional investigation into the

meshing techniques to give justification for the predictive models with the conclusions from this work outlined below.

Tensile testing experimental results using 0 tpm and 7 tpm yarns show minimal differences in the tensile modulus and strength, with a small reduction in both properties for twisted samples. Stress-strain response post-serviceability failure is seen to diverge between the two twist levels, with an increase in tensile failure strain values for twisted samples. This is evidenced by pseudo-ductile behaviour caused by the delamination of the fabric layers at high levels of strain. This behaviour was not evidenced using untwisted samples with a brittle sudden failure with images of failed samples showing little evidence of delamination between layers. Key findings from this study were incorporated into the modelling of braided fabrics presented with a material property reduction factor applied to the twisted yarns using Gegauff's classic model, causing a minimal reduction in the mechanical properties of the yarns.

A comparison of meshing techniques has been presented using both conformal and voxel meshing to evaluate local mesh-created stress concentrations. Although minor levels of stress concentrations are observed in voxel meshed samples, this has minimal effect on the predicted tensile modulus. Voxel meshing has been recommended for these samples due to the ability to apply periodic boundary conditions.

Validation of the TexGen modelling technique developed within Chapter 6, shows a high level of confidence between the predicted and experimental results. This shows good levels of accuracy in the geometry predictions for yarn shape and undulations for both twist levels.

Modelling the behaviour of the composites using models produced in TexGen shows a reduction in mechanical properties with an increase in twist level. This is resultant of (1) a reduction in the mechanical properties applied to the yarns and (2) a decrease in the overall volume fraction of the unit cell through the increase in yarn thickness. The presented results have been normalised to a volume fraction of 55% to negate these effects and show a minimal reduction in the tensile and shear modulus for

twisted composites. This modelling behaviour was conducted using voxel meshing of the unit cell from TexGen.

9 Discussion and Conclusion

The composites industry is set to continue its rapid expansion in the following decades with greater emphasis being placed on lightweight, strong materials for a range of applications, in particular the energy and transport sectors. As this trend continues, designers are required to develop new fabric architectures and manufacturing methods to improve the efficiency of the production and materials being used. Current methods in the industry lead to large amounts of wasted materials and inefficient use of raw materials for the production of structural components.

The use of braided fabrics has seen growth in the previous decade with manufacturers beginning to invest and develop components using this technique. Much academic research has been conducted over the past 25 years to develop braided fabrics and composites aimed at encouraging industrial partners to invest in and use braided fabrics. Even with this research, take up in the technology has been slow and sparingly used within structures. Much of this is believed to be due to the lack of data and tools for designers when in the early design stages of components. Without the ability to easily test and validate material properties and component performance, designers have often chosen alternative, more developed manufacturing techniques such as woven or prepreg composites.

This thesis aimed to address these problems through the development of a methodology to accurately predict the yarn geometry in biaxial braided fabrics from process parameters and to develop a framework for the prediction of mechanical properties of the resultant fabrics. Through the range of studies presented in this work the aim has been achieved. Novel designer tools have been presented within this thesis to predict the geometry of a braided fabric, using data from experimental studies conducted on a range of mandrel shapes and braider scales, alongside existing models, and studies. A new expansion to TexGen geometrical modelling software has been detailed and validated, with the ability to develop both flat and curved braided unit cells. Methodologies have been outlined for the prediction of properties, with a particular focus on the effects of yarn pre-preparation technique for the addition of twist to yarns.

The present chapter summarises the outcomes of this thesis in relation to the objectives outlined in Chapter 1, Section 1.3.1.

9.1 Effect of yarn twist

To enable the development of predictive tools for braided fabrics, the parameters affecting the architecture need to be understood. A critical review of the academic literature presented in Chapter 2 showed many of these factors. These include the relative speeds of the braider, the take-up speed of the mandrel, the size of the braider, the configuration of the carrier, the style of the braider, the mandrel shape and the yarns being used. Companies producing braided fabrics have often used the technique of adding twist to the yarns during the rewinding process with little explanation in academic research to quantify the effect this has on the resultant braid. The technique is required for many natural fibres with high levels of twist seen in the winding process, such as flax. This thesis hypothesised that a low level of controlled twist applied to carbon fibres during the winding process could affect the resultant braid geometry and give designers the ability to control the braid architecture through the twist.

A systematic review of the effects of the addition of twist on the geometry of both dry and infused fabrics has been presented in Chapters 4 and 5, on simple circular mandrels and conical mandrels respectively. This study shows that the addition of twist has no statistical effect on the braid angle of the fabric when braiding on circular mandrels. This is critical for the ability to design with a range of twist levels as the braid angle has a large influence on the mechanical properties of the fabric [57]. However, the inclusion of 5 twists per metre in the yarns is seen to increase the thickness of the fabric from 0.55 mm to 0.75 mm. With this increase in thickness, a subsequent decrease in the width of the yarns is observed. This impacts the coverage of the fabric on the mandrel, in addition to the post-braiding manufacturing techniques. With RTM being the most common post-processing method used for braiding, an accurate prediction of the fabric thickness is required for tool design. This leads to the recommendation of controlling the level of twist induced in the fabric to ensure post-processing techniques are not impacted by a change in fabric thickness. Effects of the induced twist in the yarns are seen to continue post infusion

with optical microscopy images showing, changes to the infused yarn geometry presented in Chapter 4.

Trends in conical mandrel shapes have been presented with the direction of braiding investigated, showing large differences in the braid angle. Converging conical sections are seen to produce more consistent braid architectures compared with identical diverging conical sections. This effect is seen to span across braider sizes, with similar effects seen on a 48-carrier braider compared to a 192-carrier braider.

9.1.1 Conclusions

The key implications of this study are as follows: (1) Inclusion of low levels of twist produces more consistent, narrower, thicker yarns within a braided fabric, with minimal effect on the braid angle. (2) Increased levels of nesting between layers with less consistency are observed in fabrics produced with low levels of twist due to decreased coverage in each fabric layer. (3) Increased levels of surface level damage is observed within untwisted samples with increased stray fibres on the surface of the braid. (4) Conical direction significantly affects the resultant braid geometry with the mandrel geometry being the dominant factor in fabric geometry compared to the twist level in the yarns. (5) Converging conical sections results in more consistent fabric geometry with (6) an increase in consistency for a decrease in conical angle. (7) Similar effects are observed across braider geometries enabling the use of cheaper and smaller braiders for initial investigatory studies to reduce waste and expenditure in the development of novel braided components.

9.2 Effect of Braider Geometry

A novel study has been conducted within this thesis to investigate the effects of braider scale on the resultant braid architecture. Two braiders, a 48-carrier axial and a 192-carrier axial braider have been utilised with similar fabrics produced on both. This allows scale production tests for braided fabrics to be investigated, enabling cheaper, reduced-scale testing to be completed before final production.

9.2.1 Conclusions

The results from this have shown the braid angle and yarn width have been constant throughout the scaling process, with both braider and mandrel scaled during the process.

9.3 Geometrical Modelling of Braided Fabrics

Using key data presented in Chapters 4 and 5, alongside a range of academic studies critically reviewed in Chapter 2, a novel methodology for the prediction and modelling of geometrical unit cells for biaxial braided fabrics has been presented in Chapter 6. This work is built within the modelling software TexGen, used in a wide range of industries for the prediction of fabric geometries. Within this, two new functions CTextileBraid and CTextileBraidCurved have been developed for the automatic prediction and modelling of both flat and curved geometry biaxial braided unit cells. This gives designers an easy, validated method for the prediction of the braid geometry, modelling the complex geometrical changes to yarns along their length induced from the braiding process. Freedom is given to the designer to manipulate the yarn geometry. This allows for investigations into the effects of the inclusion of twist or other parameters on the braided fabric. Use cases have been outlined for this model, including the modelling of complex fabrics such as a mixture of braided geometries or the inclusion of axial yarn layers to the fabric.

9.3.1 Conclusions

Fabrics can be exported in a range of file formats for the applications required including (1) compaction simulations, (2) elastic mechanical property prediction, (3) permeability predictions and (4) mechanical performance and failure prediction simulations. This range of applications gives designers the tools they require for the use of braided fabrics during the design process for structural components, encouraging greater use of braids in industrial applications.

9.4 Effects of Curvature on Mechanical Properties

The majority of fabric simulations are based on flat geometrical unit cells with idealised geometry. In many applications, this is a justified assumption due to the typical flat nature of components produced using composite materials. However, for overbraided components, this is often not justified as components are braided

around small diameter mandrels often with the production of circular or near circular components. Due to this disparity between the actual geometry of the component and the model used for the prediction of properties, a novel approach to modelling the unit cell with the inclusion of a radius of curvature has been developed and validated in Chapter 7.

The inclusion of a radius of curvature shows a significant effect on the elastic properties of the unit cell, showing a reduction of up to 10.5% for the tensile modulus with the inclusion of a radius of curvature of 8 mm. This effect is shown to rapidly reduce with an increase in radius, showing little to no difference for unit cells with a radius of curvatures above 250 mm.

9.4.1 Conclusions

The implications of this study show: (1) The final geometry of the unit cell must be considered when predicting the final properties of the braided fabric being used. (2) Fabric properties in locations of significant geometrical changes such as corners must be taken into consideration with the expectation of a reduction in performance in these areas.

9.5 Mechanical Performance of Twisted Fabrics

Observations in Chapter 4 showed the geometrical effect of the inclusion of low levels of twist within braided fabrics. To further this investigation, the effects on the mechanical performance have been conducted with the results presented in Chapter 8.

To quantify the effects of twist on mechanical properties, two approaches have been taken, experimental and modelling. Coupon samples produced using 0 twists per metre and 7 twists per metre were tensile tested along the bias fibre direction in a 0/90° configuration. This ensured the direct comparison of yarn changes, ensuring loading was fibre dominated. Minor reductions in both modulus and strength are seen for samples with the inclusion of twist, indicating a negative effect on the interfacial fibre/matrix boundary. Results from Chapter 4 show a greater consistency in yarn and fabric geometry for fabrics produced using twisted yarns, which has been translated into greater consistency for the mechanical properties, with a reduction

in the interquartile range for both modulus and strength in composites produced with twisted yarns.

An investigation into the methodology for the meshing of unit cells was presented to understand how the voxel meshing technique, used for elastic property predictions, may lead to localised stress concentrations due to the shape of the mesh. Although some localised stress concentrations were observed for voxel meshing when compared to conformal meshing, the generalised trends of stress distribution across the yarns within the structure matched well. These stress concentrations could be seen to have minimal effect on the measured tensile modulus of the composite, leading recommendation of voxel meshing, with periodic boundary conditions for the modelling of braided unit cells.

Using the results from the experimental data, a prediction for the mechanical properties of a range of twist levels and braid angles is presented. This shows a reduction in elastic and shear modulus for composites produced using twisted yarns. This effect is seen to be caused primarily by the reduction in fibre volume fraction due to the thicker, narrower yarns used in twisted samples.

9.5.1 Conclusions

The implications of this study are as follows: (1) the inclusion of low levels of twist in carbon fibre/epoxy composites negatively affects the mechanical performance of the composite with regard to the tensile modulus and strength. (2) the excess damage observed for untwisted samples has not had detrimental effects on the mechanical performance as hypothesised within Chapter 4. (3) localised stress concentrations within a voxel mesh have minimal effect on the predicted tensile modulus whilst still matching the generalised stress concentrations across the fabric. (4) Methodologies for the development of geometrical models of the braided unit cell within TexGen, correctly allow designers to test the influence of yarn geometry on the elastic mechanical properties of the composite.

9.6 Recommendations for future studies

Following the work conducted within this thesis the following areas of future work have been identified.

1. Study on the prediction of failure within braided unit cells with the inclusion of low levels of twist.

Many studies have attempted to predict the strength of composites through the inclusion of a failure criterion within a FE model of the fabric. A future study is proposed to incorporate such criteria within models produced using CTextileBraid and CTextileBraidCurved to validate the geometry of the unit cells further.

2. Development of triaxial Braided Unit Cells.

The work conducted within this study has focused on biaxial braided fabrics. An investigation is proposed for the development of designer tools within TexGen for triaxial braided unit cells. Further work is required to understand the complex changes to yarn geometry due to the inclusion of axial fibres within the braid.

3. An optimisation algorithm for braided fabrics.

Recent studies have focused on the development of optimisation algorithms within TexGen for woven fabrics. A study is proposed for the development of similar tools for braided geometries, allowing for the investigation of complex fabric architectures.

4. Prediction of braided fabric geometry on complex geometry.

Current methods for the prediction of braid architecture on complex mandrel geometries either negate the effects of fibre slippage, shown to be significant within this thesis or require complex and resource-intensive FE modelling. The development of tools for designers to predict the occurrence of fibre slippage due to yarn geometry and mandrel geometry is proposed to increase the ease of development of complex braided components.

A Appendix A

Various parameters can be controlled during the braiding process such as spring tension, mandrel location, winding technique and braiding speeds. For the purposes of this thesis, numerous small-scale tests have been undertaken using a 48-carrier braider and Kuka robot to understand how these may affect the braid architecture to achieve the required set-up for further in-depth experimental studies. This chapter outlines each of those studies.

A.1 Carrier Spring Tensioner

As outlined within Chapter 2 (lit review) the carriers have two main functions; control the tension of the yarn and move the yarn around in a sinusoidal motion. Two sets of springs are available for the braider used in this study. The compressive stiffness of both sets of springs was calculated using hooke's law. A mass was applied to the spring, with deformation measured.

Table A-1. Measured Spring stiffness values for two spring sets.

Spring Set	Stiffness (N/m)
Spring 1	11.35
Spring 2	38.79

With significantly different stiffness values each set was used to braid a 75 mm diameter circular mandrel with the results given below.

A.1.1 Results

The braid angle was measured using the image processing method outlined in Chapter 3 at 4 points along the length of the mandrel. The results shown are an average of the measured angle from the top, side and bottom of the mandrel, with no significant variation seen around the circumference of the mandrel.

Results show spring tension has a large impact on both the consistency and value of the braid angle. The lower tension springs show a higher braid angle, with an average of 64 degrees, with little variation over the 600 mm length. Alternatively, the stiffer springs show a range of braid angles with little consistency. This can be explained

through inspection of the resultant braid and observations during the braiding process.

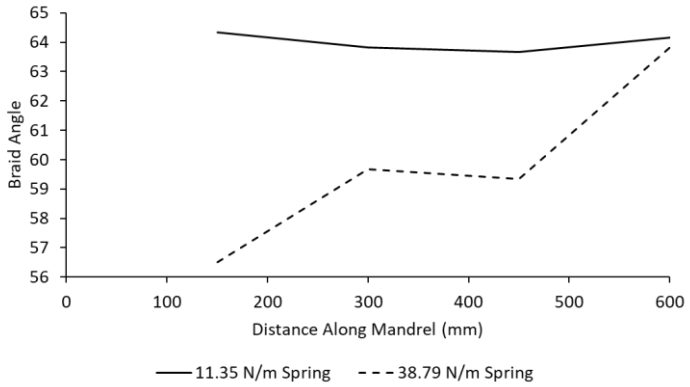

Figure A-1: Effect of spring tension on the measured braid angle.

The stiffer springs were 'too stiff' for the material being used and resulted in excessive damage to the yarns and braided fabric. As the tension was too great within the braiding process, yarns were unable to be pulled from the carriers, decreasing the braid angle, and causing damage. This resulted in an unusable fabric once braided. This damage is shown in *Figure A-2.*

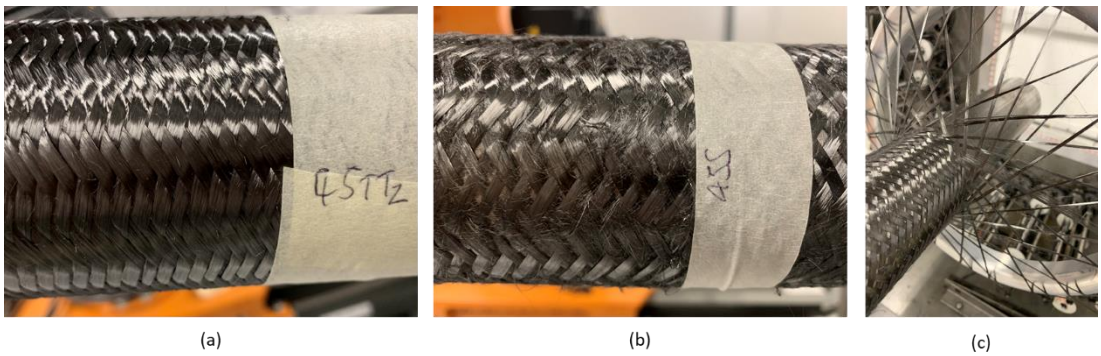

Figure A-2. Effect of spring stiffness on braided fabric. (a) Braid using 11.35 N/m spring, (b) braid using 38.79 N/m springs and (c) damage shown during braiding to yarns with 38.79 N/m springs

From this test, it can be seen that the springs with a stiffness of 11.35 N/m were required to produce a viable braided fabric and have been used on all subsequent tests within this thesis.

A.2 Braider Consistency

Braiding has unavoidable variability in the production of fabrics. There are many areas which can affect this, the winding process, yarn variability, braider speed

variations and local frictional changes. A small study was conducted to investigate on both a 48-carrier and 192-carrier braider how much variability is expected between braids with the same configurations.

Braider speeds and mandrel sizes are given in *Table A-2*. Each braid was repeated 3 times with angle measurements taken along the length.

Table A-2. Braid parameters

		48-carrier		192-carrier
Mandrel Diameter (mm)	75	75	75	200
Carrier Speed (rpm)	1.8	2.3	2.9	
Take up Speed (mm/s)	3.5	3.5	3.5	

A.2.1 Results

As expected there are small levels of variability within the braided fabrics however overall a good level of consistency is seen across three samples with a 2° range for the 48-carrier braider. It is noted most samples had a larger than average braid angle at the start of the mandrel as the fabric requires a stabilisation length. This length is dependent on a number of factors and has been investigated by Grimes et al. [136].

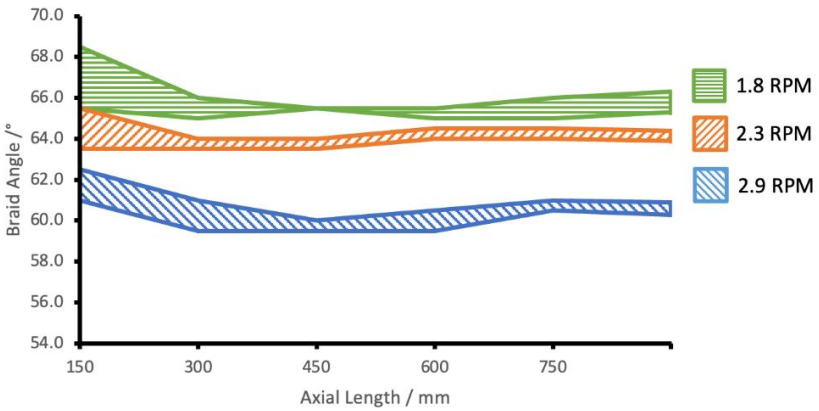

Figure A-3. Braid angle measurements for a 48-carrier braider.

Results for braiding on the larger 192 carrier braider are given in *Figure A-4*, showing similar levels of consistency following an initial period of instability as the braid conforms to the required braid angle.

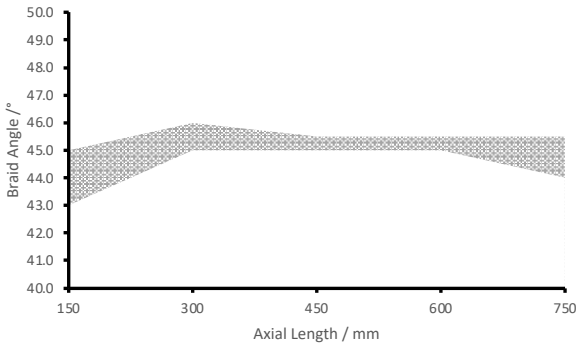

Figure A-4: Braid angle measurements for 192-carrier braider.

A.3 Mandrel Shape

Previous tests presented were conducted using a circular mandrel. Various studies have shown the effects mandrel shape on the braid architecture [9, 137, 138]. A small study was conducted using a 48-carrier braider and a 75 mm square mandrel to investigate the effects of the braid angle on the top, sides and bottom surfaces of the braid being formed. Four different braider speeds, 1.8 RPM, 2.3 RPM, 2.6 RPM and 2.9 RPM with a constant take-up speed of 3.5 mm/s.

A.3.1 Results

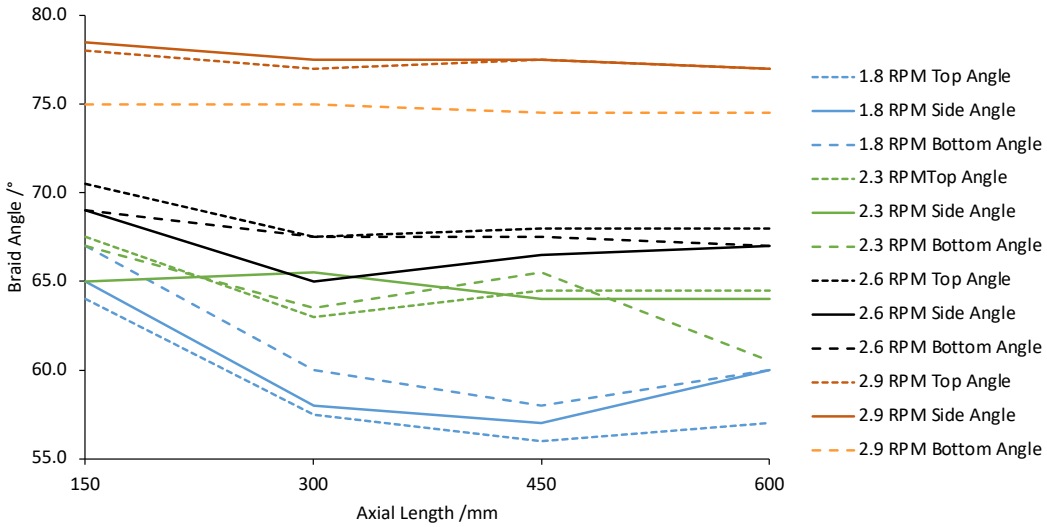

Figure A-5: Measured braid angle using square mandrel on top, side and bottom surfaces at various braider speeds.

Results show little statistical difference in the braid angle with respect to the top, side, and bottom surfaces. Inspection of images taken from these braids shows minimal deviation of the braid from the usual path with a straight yarn shown in

Figure A-6. This is suspected to be caused by the small mandrel size in comparison to the yarns. Literature has shown using larger braiders an “S-Shaped” yarn is likely to appear using rectangular-shaped mandrels.

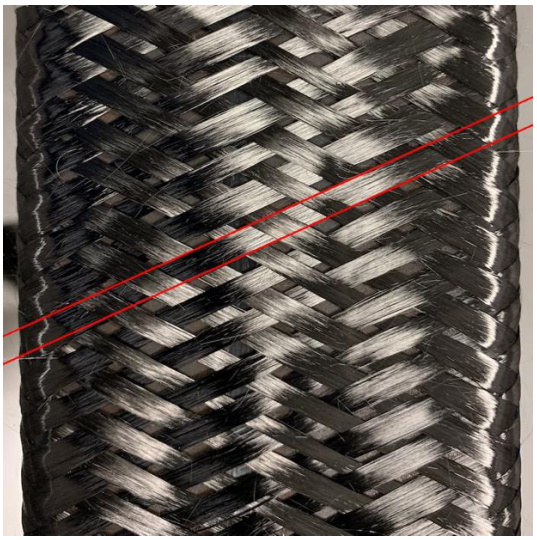

Figure A-6: Image of braid taken from square mandrel with yarn path highlighted in red.

A.4 Apodius 2D Vision sensor validation

Braid angles from two flat fabrics were measured using both ImageJ and the Apodius 2D vision sensor. The angle measurements can be seen in Figure A-7. This shows a high level of agreement between the two methods with 1.0 ° agreement between both methods. This highlights the repeatability and accuracy of using the Apodius 2D vision sensor to detect the braid angle.

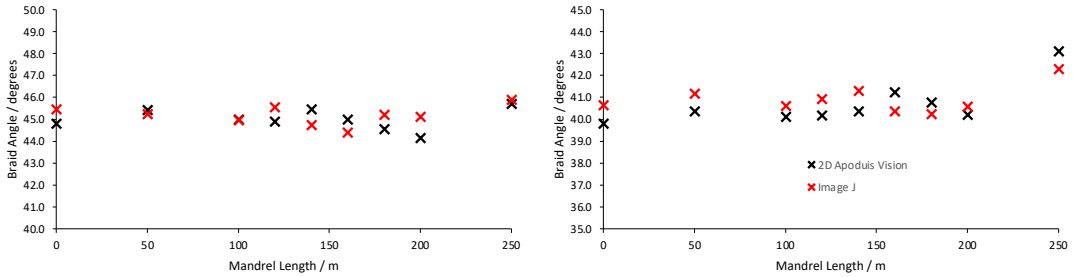

Figure A-7: Measured braid angles for two fabrics using ImageJ manual measurements and Apodius 2D Vision sensor.

A.5 Conclusions

The small studies presented in this chapter confirm the braider parameters used within the main study of this work. Carrier tensioning systems have been investigated with results leading to the use of 11.35 N/m springs within the tensioning system. Additionally, the consistency of the braider has been proven to be within 2 degrees for multiple tests on single-layer braids. This is vital for the ability to make judgements from the normal variable experienced in braiding for various changes in parameters within this study.

B. Appendix B

This section outlines the code used for automatic recognition and measurement of the braid angle using image processing algorithms. An explanation is given in Chapter 3 with the code explained below. The image processing code used for this analysis is OpenCV [100]

Table B-1: Sample MATLAB Code for the detection of braid angle from image data.

B1	import cv2 import numpy as np import math import statistics
B2	number = '0' img=cv2.imread(number+'.jpg')
B3	bilateral_blur = cv2.bilateralFilter(img, 25,200,200) cv2.imwrite('bilateral'+number+'.jpg', bilateral_blur)
B4	img_gray = cv2.cvtColor(img, cv2.COLOR_BGR2GRAY) edges=cv2.Canny(image=img_gray, threshold1=10, threshold2=200) cv2.imwrite('Canny Edge Detection'+number+'.jpg', edges)

B5	lines = cv2.HoughLines(edges, 1, np.pi/180, 100, None, 0, 0)
	thetas=[]
	#Draw the lines
	if lines is not None:
	  for i in range(0, len(lines)):
	  rho = lines[i][0][0]
	  theta = lines[i][0][1]
	  thetas.append(lines[i][0][1])
	  a = math.cos(theta)
	  b = math.sin(theta)
	  x0 = a * rho
	  y0 = b * rho
	  pt1 = (int(x0+1000*(-b)), int(y0+1000*(a)))
	  pt2 = (int(x0-1000*(-b)), int(y0-1000*(a)))
	
	  cv2.line(img, pt1, pt2, (0,0,255), 3, cv2.LINE_AA)
	
	cv2.imwrite("Detected Lines(in red)"+number+".jpg", img)

B6	linesP = cv2.HoughLinesP(edges, 1, np.pi/360,70,None, 40, 5)
	anglePos=[]
	angleNeg=[]
	thetas=[]
	lines=[]
	if linesP is not None:
	  for i in range(0, len(linesP)):
	  l =linesP[i][0]
	  theta=math.degrees((math.atan((l[2]-l[0])/(l[3]-l[1]))))
	  thetas.append(theta)
	  if theta>=37 and theta<=48:
	  anglePos.append(theta)
	  cv2.line(imgP, (l[0], l[1]), (l[2], l[3]), (0,0,255), 2, cv2.LINE_AA)
	  if theta<=-37 and theta>=-48:
	  angleNeg.append(theta)

	cv2.line(imgP, (l[0], l[1]), (l[2], l[3]), (0,0,255), 2, cv2.LINE_AA) lines.append([l[0],l[1],l[2],l[3]]) cv2.imwrite("P Detected Lines(in red)"+number+".jpg", imgP)
B7	Average_Pos=statistics.mean(anglePos) Average_Neg=statistics.mean(angleNeg) braid_angle=(Average_Pos+(-1*Average_Neg))/2

B1

This loads the required functions and classes into the Python script used for this analysis.

B2

This defined the location along the axis (in this case 0 mm) and loads in the correct image of the braid.

B3

This applies the bilateral filter to the image using three threshold values. These have been tested to gain a blur within the yarns without distorting the edges of the yarns for analysis. This then saves a new .jpeg file with this blur applied.

B4

The blurred image has a greyscale filter applied to aid in the edge detection. A canny edge detection is then applied to the image to automatically detect the edges of the yarns and saved into a new .jpeg file.

B5/6

A Hough transform is applied to the image to detect the lines within the edges image. This is then plotted back onto the images. Two different Hough transforms are completed for reference. In A6 a precise Hough transform is completed with the start and end of each of the lines detected and superimposed onto the image. In this, the lines that are not sensible to measure are excluded from the list to ensure only the edges of the yarns are detected. Due to reflections in the images, it can be likely there are edges detected that do not correspond to the edge of yarns. By filtering the results to only results within a boundary the true braid angle can be measured. This value must be manually adjusted by the user.

B7

The average positive and negative yarns are calculated with the values used to calculate the braid angle. In order to gather a true braid angle the size of the image of the braid being inspected must be small to ensure variations in the braid angle are not included in this value. The author recommends using a length between 10-20mm for the images.

C. Appendix C

This section contains the code developed for the prediction of fabric thickness using a laser scanner. The full method is outlined in Chapter 3 with the code explained below.

Table C-1: Sample MATLAB code for the calculation of fabric thickness using point-cloud data.

C1	%layer 1
	[x,y,z]=textread('Big_Cone_BtS_0tpm_layer1(1)-0.txt','%f,%f,%f');
	figure;
	pcshow([x(:),y(:),z(:)]);
	title('0 deg');
	ylabel('Y');

C2	width=min(y(:))-max(y(:));
	ymin=max(y(:))+(width/2)-10;
	for j = 1:1
	  h=1;
	  x1=[];
	  y1=[];
	  z1=[];
	  ymax=ymin+20;
	  for ii = 1:d(1)
	  if y(ii,1)>=ymin && y(ii,1)<=ymax
	  x1(h)=x(ii,1);
	  y1(h)=y(ii,1);
	  z1(h)=z(ii,1);
	  h=h+1;
	  end
	  end
	  figure;
	  pcshow([x1(:),y1(:),z1(:)]);
	end

C3	zmin=489;
	dia0deg=[];
	maxX=[];
	minX=[];

C4	for j = 1:36
	  h=1;
	  x2=[];
	  y2=[];
	  z2=[];
	  zmax=zmin+10;
	  for ii = 1:d(2)
	  if z1(1,ii)>=zmin && z1(1,ii)<=zmax
	  x2(h)=x1(1,ii);
	  y2(h)=y1(1,ii);
	  z2(h)=z1(1,ii);
	  h=h+1;

```
        end
    end
    zmin=zmin+10;
    [Max IMax] = max(x2);
    [Min IMin] = min(x2);
    dia0deg(j)=(max(x2)-min(x2));
end
```

C1

This loads in the point cloud .txt file into the Matlab workspace and plots the point cloud, labelling the plot and the y-axis to ensure the orientation is correct.

C2

The first two lines in this section calculate the centre plane corresponding to the y-axis and the direction the measurement should be taken. The 'slice' of material is taken to be 20 mm in width so the ymin is set to be 10 less with ymax defined as ymin+20. The for loop works through the points in the total point cloud and checks to see if they fall within these limits. If the point is within the slice the coordinate is saved in the new coordinates x1,y1,z1. The output from this is then plotted as a visual check.

C3

The zmin is set in the coordinate system which corresponds to 0 in the axial length of the data. This should be adjusted for each scan to ensure the results are in the same coordinate system. This then sets up empty arrays for the data in A4.

C4

The number of iterations in the for loop (j=1:36) is defined by the length of the mandrel being measured, in this case between 0 and 350mm is being measured. This then sets up a third coordinate system x2,y2,z2 to hold values in the correct z slice of data. The slice size (zmax=zmin+10) is defined by the user and is explained in Eq. (3.1). This gathers all points within this section and evaluates the maximum and minimum points to gather the distance between them. This is iterative along the length of the mandrel saving the data into the array dia0deg. This can then be exported and taken away from the mandrel measurement to calculate fabric thickness.

D. Appendix D

The code below is a standard code for the manual production of a triaxial braid within TexGen available prior to the work completed within this thesis. This requires user input to calculate node locations, yarn rotations and cross-section and incorporates no machine parameters in the production of the unit cell.

Table D-1: Python script example for manual production of a braided unit cell within TexGen.

D1	from TexGen.Core import * import math
D2	Textile = CTextile()
D3	Yarns = [CYarn(), CYarn(), CYarn()]
D4	Yarns[0].AddNode(CNode(XYZ(0, 0, 0))) Yarns[0].AddNode(CNode(XYZ(0.5, 0.2887, 0.2))) Yarns[0].AddNode(CNode(XYZ(1, 0.5774, 0.2))) Yarns[0].AddNode(CNode(XYZ(1.5, 0.8660, 0))) Yarns[0].AddNode(CNode(XYZ(2, 1.1547, 0))) Yarns[1].AddNode(CNode(XYZ(0, 0, 0.2))) Yarns[1].AddNode(CNode(XYZ(0.5, -0.2887, 0))) Yarns[1].AddNode(CNode(XYZ(1, -0.5774, 0))) Yarns[1].AddNode(CNode(XYZ(1.5, -0.8660, 0.2))) Yarns[1].AddNode(CNode(XYZ(2, -1.1547, 0.2))) Yarns[2].AddNode(CNode(XYZ(-0.25, 0, 0.1))) Yarns[2].AddNode(CNode(XYZ(-0.25, 0.57735, 0.1)))
D5	AngledSection = CSectionLenticular(0.45, 0.13) AngledYarnSection = CYarnSectionInterpPosition(True, True) RotationAngle = math.radians(12) AngledYarnSection.AddSection(1.0/8.0, CSectionRotated(AngledSection, -RotationAngle)) AngledYarnSection.AddSection(5.0/8.0, CSectionRotated(AngledSection, RotationAngle))
D6	AngledYarnSection.AddSection(0.0/4.0, AngledSection) AngledYarnSection.AddSection(1.0/4.0, AngledSection) AngledYarnSection.AddSection(2.0/4.0, AngledSection) AngledYarnSection.AddSection(3.0/4.0, AngledSection) Yarns[0].AssignSection(AngledYarnSection) Yarns[1].AssignSection(AngledYarnSection)
D7	Yarns[0].AddRepeat(XYZ(2, 0, 0)) Yarns[1].AddRepeat(XYZ(2, 0, 0))
D8	StraightSection = CSectionLenticular(0.6, 0.15) Yarns[2].AssignSection(CYarnSectionConstant(StraightSection)) Yarns[2].AddRepeat(XYZ(1, 0, 0))

D9	for Yarn in Yarns:
	  Yarn.AssignInterpolation(CInterpolationCubic())
	  Yarn.SetResolution(20)
	  Yarn.AddRepeat(XYZ(0, 0.57735, 0))
	  Textile.AddYarn(Yarn)

D10	Textile.AssignDomain(CDomainPlanes(XYZ(0+0.25, 0, -0.1), XYZ(2+0.25, 1, 0.3)))
D11	AddTextile("triaxialbraid", Textile)

D1

Imports TexGen and Math Library into the system

D2

Creates a Textiles using the class CTextile

D3

Creates a Python list names Yarns with three CYarn

D4

Adds Nodes to each of the yarns with the global coordinates. Yarn[0] and Yarn[1] correspond to the bias yarns and Yarn[2] corresponds to the axial yarns

D5

This section relates to applying a lenticular cross-section with a width of 0.45 mm and a thickness of 0.13 mm. A rotation of 12 degrees is then applied to the cross-section and applied to sections $1/8^{th}$ and $5/8^{th}$ along the yarns at +/- rotation angles.

D6

Unrotated angles are then applied at other sections of the yarn with this applied to Yarn[0] and Yarn[1]

D7

Repeats are applied to Yarn[0] and Yarn[1] in the x direction

D8

Lenticular sections are applied to the straight yarns with a width of 0.6 mm and a thickness of 0.15 mm. with a constant cross-section applied and a repeat in the X direction.

D9

A loop iterates through each yarn with an interpolation assigned, a yarn resolution set, a repeat vector and the yarns added to the textile.

D10

A domain is applied for a unit cell of the fabric with X,Y,Z coordinates given.

D11

Textile is added to the viewport in TexGen for rendering with the name ‘triaxialbraid’.

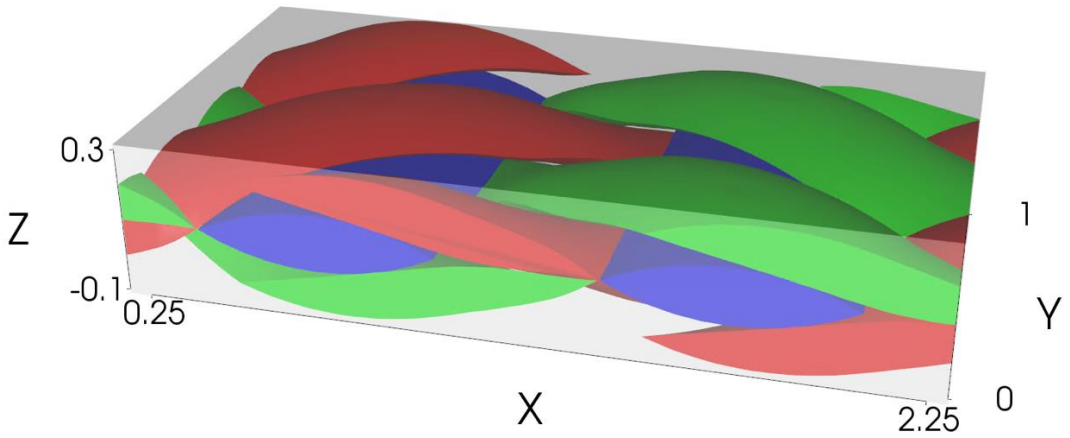

Figure D-1: Render of triaxial braid produced using the code outlined in Table D-1.

Through the development of CTextileBraid and CTextileBraidCurved as outlined in Chapter 6 of this thesis, braided unit cells cannot be predicted using TexGen with geometry, yarn cross-sectional shape and node locations predicted within the unit cell using machine parameters and basic yarn width and fabric thickness. An example of a new Python script for the production of a biaxial braided unit cell is given below with an explanation.

Table D-2: Python script example for automatic production of a braided unit cell within TexGen using studies outlined within this thesis.

D1.1	from TexGen.Core import *
D2.1	braid = CTextileBraid(4, 4, 3.5, 0.225, 0.45, 0.08, 5.49559, 88, 0.01, bool(1), bool(0))
D3.1	braid.SwapPosition(0, 0) braid.SwapPosition(0, 3) braid.SwapPosition(1, 2) braid.SwapPosition(1, 3) braid.SwapPosition(2, 1) braid.SwapPosition(2, 2) braid.SwapPosition(3, 0) braid.SwapPosition(3, 1) braid.AssignDefaultDomain(False, True)
D4.1	AddTextile("Braid 2 EPIKOTE",braid)

D1.1

Imports TexGen core module

D2.1

Sets up a new fabric called 'braid' using the CTextileBraid class (a subset of the CTextile class) using the following inputs:

CTextileBraid(int iNumWeftYarns, int iNumWarpYarns, double dWidth, double dHeight, double dThickness, double dRadius, double dHornGearVelocity, int iNumHornGear, double dVelocity, bool bRefine, bool bAdjustSpacing);

In this case this is set to: 4 weft yarns, 4 warp yarns, 3.5 mm yarn width, 0.225 mm yarn thickness, 0.45 fabric thickness, 0.08 m radius mandrel, 5.49559 rpm braider speed, 88 horn gears, 0.01 m/s take up speed with the refine function active but no adjusting of the spacing between the yarns.

D3.1

This sets the pattern of the braid, swapping the yarns between each other to achieve the desired pattern.

D4.1

Textile is added to the renderer with the name 'Braid 2 EPIKOTE'

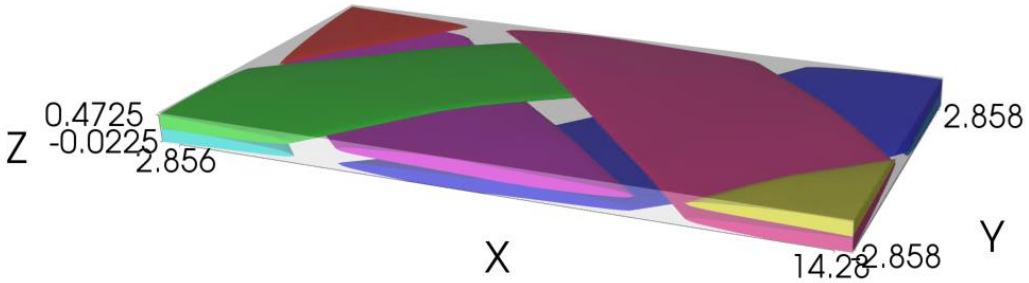

Figure D-2: Rendered image of the braid produced through the code outlined in Table D-2

E. Appendix E

Nesting is defined as additional layers of fabric within a component containing fibres within the layers below. Nesting within multilayers of braids has been evidenced for both fabrics produced on mandrels and within flat fabrics infused using vacuum infusion.

Nesting helps to increase the volume fraction of the composite as gaps between fibres within the layer below are filled by those above, reducing the number of resin-rich areas and creating a more densely packed composite. This settling of the yarns within gaps in the layer below can often lead to distortions in the yarn shape, often making it difficult to distinguish the boundaries of the yarns within microscopy images.

This section outlines the quantification of nesting within components as referred to within the main body of the thesis. Nesting is referred to as a percentage and is defined as the percentage of the layer that is 'inside' the layer below. Therefore 0% nesting refers to the situation where none of the yarns from the layer above is within the layer below, as shown in *Figure E-1 (a).*

Eq. (E.1) defines the level of nesting with relation to the depth of the 2nd layer inside the 1st, defined as Δh, and the thickness of 1 layer t_1.

$$Nesting = \frac{\Delta h}{t_1}\, x\, 100 \tag{E.1}$$

Δh can often not be measured without microscopy or μCT data. Therefore, this can be related to the absolute thickness of the component with 2 layers, t_2, through Eq. (E.2).

$$\Delta h = nt_1 - t_2 \tag{E.2}$$

Where n is the number of layers of fabric.

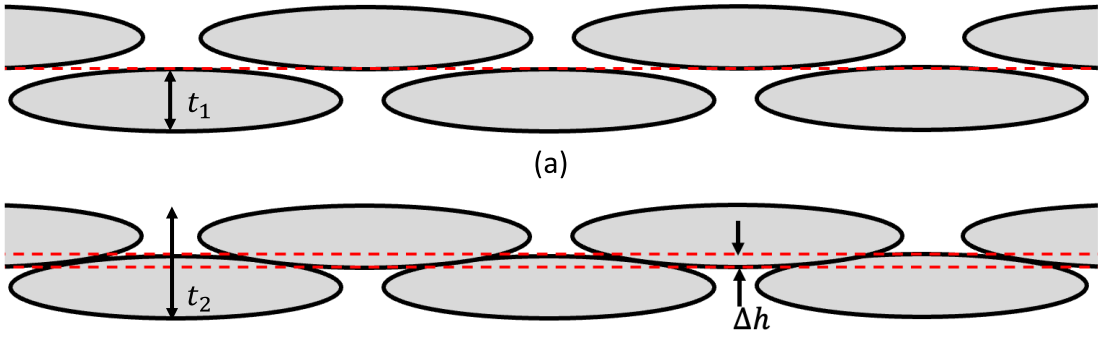

Figure E-1: Levels of nesting between layers of yarns. (a) shows 0% nesting with (b) showing nesting between the layers, with the second layer within the 1st by a height Δh.

F. Appendix F

As defined in BS EN ISO 527-1:2019 Plastics. Determination of tensile properties - General principles [127]. The modulus of the polymer can be determined as the gradient of the line of linear regression for the region of strain between 0.05% and 0.25%. The results below show the calculated tensile modulus using this method for each sample as well as the tensile strength and modulus calculated through the testing house CTE.

F.1 Tensile Testing Results

Table F-1: Obtained mechanical properties for untwisted samples. Tensile strength and modulus supplied by testing house CTE. *E calculated using linear regression method.

Twist Level	CTE Specimen ID	0° Tensile Strength (MPa)	0° Tensile Modulus (GPa)	E (GPa) *	R^2	Notes
Untwisted	2224-AUR-A-1**	754.12	56.16	-	-	*Imetrum strain data transfer error*
Untwisted	2224-AUR-A-2	669.47	54.95	61.08	0.9930	
Untwisted	2224-AUR-A-3	624.65	57.36	75.65	0.9917	
Untwisted	2224-AUR-A-4	697.81	53.71	65.55	0.9961	
Untwisted	2224-AUR-A-5	781.06	59.37	68.17	0.9969	
Untwisted	2224-AUR-A-6	624.08	58.60	67.90	0.9937	
Untwisted	2224-AUR-A-7	593.61	53.52	60.88	0.9942	
Untwisted	2224-AUR-A-8	541.94	49.15	51.82	0.9901	
Untwisted	2224-AUR-A-9	498.18	46.05	50.61	0.9919	
Untwisted	2224-AUR-A-10	533.08	47.08	51.56	0.9915	
Untwisted	2224-AUR-A-11	747.88	57.32	62.96	0.9954	
Untwisted	2222-AUR-A-1	679.72	55.12	69.31	0.9932	
Untwisted	2222-AUR-A-2	717.95	52.33	70.82	0.9953	
Untwisted	2222-AUR-A-3	742.69	52.68	64.28	0.9927	
Untwisted	2222-AUR-A-4	639.36	49.43	52.74	0.9930	
Untwisted	2222-AUR-A-5	690.69	52.17	53.46	0.9926	
Untwisted	2222-AUR-A-6	671.61	56.36	66.80	0.9928	
Untwisted	2222-AUR-A-7	694.20	52.19	60.88	0.9959	
Untwisted	2222-AUR-A-8	729.23	53.35	69.05	0.9918	*ext jump at ~5200usn due to specimen failing; 1000-5000usn Poissons*

Untwisted	2222-AUR-A-9	791.53	55.04	63.25	0.9951	
Untwisted	2222-AUR-A-10	788.85	54.72	72.76	0.9967	
Untwisted	2223-AUR-A-1	748.35	64.77	68.98	0.9862	
Untwisted	2223-AUR-A-2	782.23	61.62	62.83	0.9957	
Untwisted	2223-AUR-A-3	761.64	56.72	66.23	0.9921	*ext jump at ~5900usn due to specimen failing; 1000-5000usn Poissons*
Untwisted	2223-AUR-A-4	813.31	59.92	64.78	0.9974	
Untwisted	2223-AUR-A-5	787.81	58.98	68.25	0.9939	
Untwisted	2223-AUR-A-6	643.56	55.45	67.48	0.9932	
Untwisted	2223-AUR-A-7	583.68	54.85	65.76	0.9891	
Untwisted	2223-AUR-A-8	519.45	54.38	63.95	0.9925	*ext jump at ~4000usn due to specimen failing. Poissons 1000-3000usn*
Untwisted	2223-AUR-A-9	538.16	52.39	66.35	0.9920	
Untwisted	2223-AUR-A-10	518.09	60.16	70.40	0.9916	*ext jump at ~4000usn due to specimen failing. Poissons 1000-3000usn*
Untwisted	2223-AUR-A-11	763.51	63.72	73.27	0.9930	
Untwisted	2223-AUR-A-12	526.44	55.41	60.59	0.9963	

**2224-AUR-A-1 had a transfer error for the final strain data. Testing house gathered modulus and strength but raw data was unavailable for linear Regression.

Table F-2: Obtained mechanical properties for twisted samples. Tensile strength and modulus supplied by testing house CTE. *E calculated using linear regression method.

Twist Level	CTE Specimen ID	0° Tensile Strength (MPa)	0° Tensile Modulus (GPa)	E(GPa)*	R^2	Notes
Twisted	2225-AUR-A-1	507.72	57.20	63.28	0.9746	
Twisted	2225-AUR-A-2	537.74	56.26	62.18	0.9531	
Twisted	2225-AUR-A-3	587.09	54.79	59.01	0.9761	
Twisted	2225-AUR-A-4	559.25	57.39	64.44	0.9768	
Twisted	2225-AUR-A-5	565.93	58.80	63.40	0.9700	
Twisted	2225-AUR-A-6	595.29	58.22	67.76	0.9718	
Twisted	2225-AUR-A-7	616.56	55.10	59.34	0.9647	

Twisted	2225-AUR-A-8	611.33	59.07	72.18	0.9733	
Twisted	2225-AUR-A-9	641.51	59.70	63.86	0.9715	
Twisted	2225-AUR-A-10	595.26	59.34	58.71	0.9826	
Twisted	2226-AUR-A-1	586.70	53.23	53.36	0.9615	
Twisted	2226-AUR-A-2	634.41	56.02	53.69	0.9875	
Twisted	2226-AUR-A-3	623.73	55.14	54.55	0.9869	
Twisted	2226-AUR-A-4	655.74	54.52	59.15	0.9887	
Twisted	2226-AUR-A-5	627.27	54.63	52.89	0.9864	
Twisted	2226-AUR-A-6	603.52	57.00	59.59	0.9793	
Twisted	2226-AUR-A-7	622.11	56.99	61.33	0.9785	
Twisted	2226-AUR-A-8	495.77	56.67	56.36	0.9860	
Twisted	2226-AUR-A-9	621.21	57.37	64.91	0.9878	
Twisted	2226-AUR-A-10	586.33	56.68	55.65	0.9882	
Twisted	2227-AUR-A-1	736.57	57.98	58.58	0.9803	
Twisted	2227-AUR-A-2	627.81	54.93	59.59	0.9836	
Twisted	2227-AUR-A-3	574.41	58.83	55.63	0.9884	
Twisted	2227-AUR-A-4	620.28	61.63	57.16	0.9871	*ext jump at ~4500usn due to specimen failing; 1000-4000usn Poissons*
Twisted	2227-AUR-A-5	611.11	56.50	56.25	0.9831	
Twisted	2227-AUR-A-6	583.42	56.07	54.78	0.9828	
Twisted	2227-AUR-A-7	530.58	53.71	59.13	0.9834	*ext jump at ~4200usn due to specimen failing; 1000-4000usn Poissons*
Twisted	2227-AUR-A-8	529.95	54.12	58.89	0.7086	*ext jump at ~4000usn due to specimen failing; 1000-4000usn Poissons*
Twisted	2227-AUR-A-9	562.11	56.07	59.55	0.9840	
Twisted	2227-AUR-A-10	632.27	53.13	60.14	0.9847	*ext jump at ~4600usn due to specimen failing; 1000-4000usn Poissons*
Twisted	2227-AUR-A-11	658.03	54.72	57.62	0.9722	*ext jump at ~5000usn due to specimen failing; 1000-*

						5000usn Poissons
Twisted	2227-AUR-A-12	642.47	60.37	61.05	0.9883	
Twisted	2227-AUR-A-13	627.47	61.18	62.84	0.9836	

F.2 Collection of Results

F1	data=readmatrix("2224_AUR_A_2_refined.csv"); slope_data=[];

F2	h=1;
	for i=1:length(data)
	  if data(i,2)>=0.05 && data(i,2)<=0.25
	  slope_data(h,1)=data(i,1);
	  slope_data(h,2)=data(i,2)/100;
	  h=h+1;
	  end
	end

F3	p = polyfit(slope_data(:,2), slope_data(:,1),1); E=p(1)/1000;

F4	plot(slope_data(:,2), slope_data(:,1),'.',slope_data(:,2),f,'-')
	xlabel('Strain (%)');
	ylabel('Stress (MPa)');
	title('2224 AUR A 2 refined');
	legend('data', 'linear regression');

F5	r= corrcoef(slope_data(:,2), slope_data(:,1)); rsquared=r(2)^2;

F1

Read in the stress-strain data for each sample from a .csv file

F2

Filter the data to include only data corresponding to strain values between 0.05% and 0.25% strain.

F3

Use MATLAB Polyfit function to calculate a linear line of best fit for the data. Young's Modulus is defined as the slope of this line and is expressed in GPa.

F4

Raw data for this region and the line of best fit are plotted, an example of this is shown in *Figure F-1.*

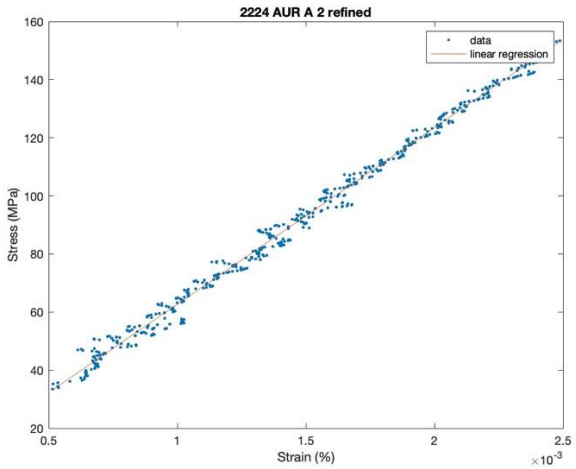

Figure F-1: Stress/Strain response for untwisted sample in strain regions between 0.05% and 0.25%. Line of best fit plotted for data.

F5

Coefficient of correlation and coefficient of determination were calculated for the line of best fit with the corresponding data.

F.3 Smoothing Strain Data

Strain data gathered from the extensometer contains small degrees of noise due to the scale of the strain being applied to the sample (max 1.8% strain). This noise can clearly be seen in the raw data of *Figure F-2*. To produce a smooth stress-strain response for the tensile samples a Gaussian smoothing filter has been applied, using MATLAB [139], to the strain data. This has resulted in the smoothed data lines seen in Figure F-2.

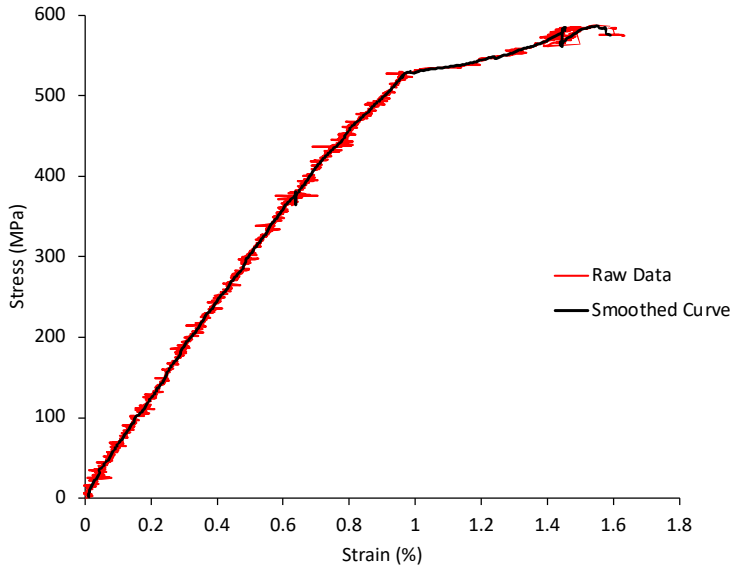

Figure F-2: Stress-strain response with raw data and smoothed curve for tensile sample.

F.4 Average Data

To combine multiple stress-strain response data a common value of strain is required. The extensometer used for the testing leads to small levels of noise within the sample, as seen previously, with non-uniform gaps for the strain measurement. Therefore, a MATLAB script was developed to use the smoothed data presented in Section G.3 to interpolate the data and calculate data at set strain values, allowing the corresponding stress values to be averaged.

Table F-3: MATLAB script developed for the smoothing of strain data and interpolation of data at set strain values.

F1.1	data=readmatrix('2222_AUR_A_10.csv');

F2.1	data(1,:)=[];
	data(2,:)=[];
	data(3,:)=[];
	strain=data(:,2);
	stress=data(:,1);

F3.1	SS=smoothdata(strain,'gaussian',70);
F4.1	[x,idx] = unique(SS) ; y = stress(idx) ; xi = 0:3e-4:max(x); xi=xi.'; yi = interp1(x,y,xi) ;

F1.1

This reads in the stress-strain data, in this case for sample 2222_AUR_A_10.

F2.1

The first three lines removed the first three lines within the csv file that corresponds to the title rows within the file.

Stress and strain data are then defined in their own variables.

F3.1

A Gaussian filter is applied to the strain data.

F4.1

This section first removes any duplicate values of strain and reads the corresponding stress values from the values of strain. New stress-strain values are then calculated for each 0.0003 % strain value using the interp1 function in MATLAB. The results of this are shown in *Figure F-3.*

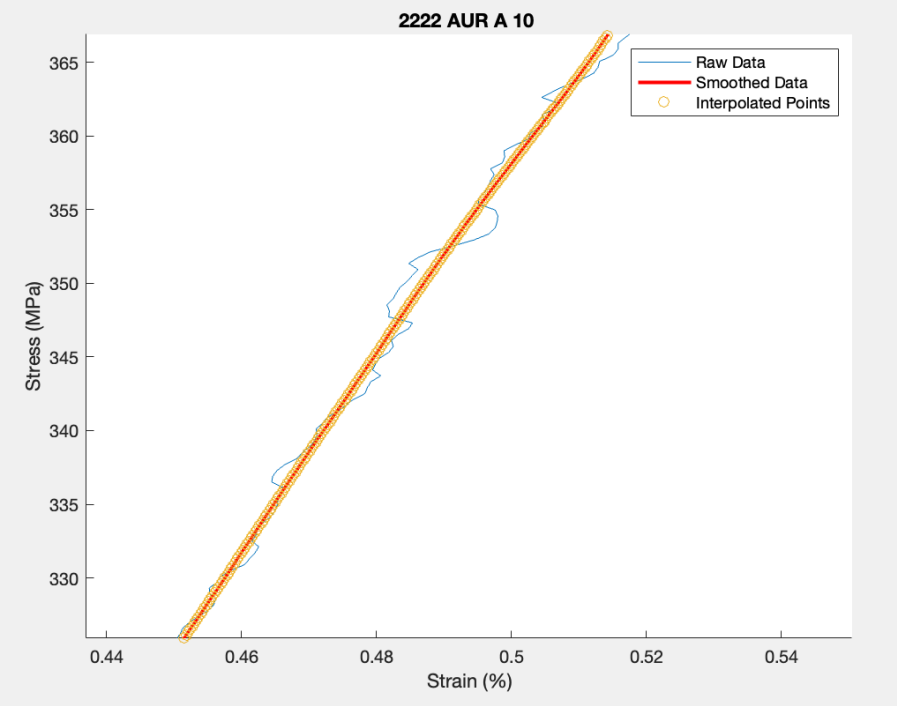

Figure F-3: Section of stress-strain response with raw data, smoothed data and interpolated data.

G. Appendix G

Other references of work completed by the author on the topic:

TexGen branch including code developed throughout this study. This is capable of being compiled: https://github.com/matthewphd

TexGen modelling of braided fabric referenced with images used. [140]

Presentation and conference paper presented at ECCM 2022 Lausanne.[141]

Presentation and conference paper presented at ECCM 2022 Lausanne. [142]

Poster Presentation at ACM5 conference Bristol 2022 [143]

References

[1] "Braided carbon wheels for the Porsche 911 Turbo S Exclusive Series," in *World première: exclusive innovation with spectacular look for enhanced driving dynamics*, ed. Porsche Newsroom: Porsche, 2017.

[2] G. Gardiner. "DigiProp positions Dowty Propellers and its customers for sustainable, next-generation platforms." https://www.compositesworld.com/news/digiprop-positions-dowty-propellers-and-its-customers-for-sustainable-next-generation-platforms (accessed 20/08/2022, 2022).

[3] A. Erber, "High Volume Automotive Applications Addressed by the Braiding Technology," in *JEC World Conference 2017*, Paris, March 2017.

[4] C. Braiding. "Anti-Microbial Grab Poles." https://compositebraiding.com/projects/anti-microbial-grab-poles/ (accessed 20/08/2022, 2022).

[5] "A&P Technology - History." https://www.braider.com/About/History.aspx (accessed 20/08/22, 2022).

[6] J. H. Van Ravenhorst and R. Akkerman, "Circular braiding take-up speed generation using inverse kinematics," *Composites Part A: Applied Science and Manufacturing,* Article vol. 64, pp. 147-158, 2014, doi: 10.1016/j.compositesa.2014.04.020.

[7] J. Rosenbaum, *Flechten: Rationelle Fertigung faserverstärkter Kunststoffbauteile*. Köln, 1991.

[8] A. P. Technology. "Megabraiders." https://www.braider.com/About/Megabraiders.aspx (accessed 24/04/23, 2023).

[9] J. F. A. Kessels and R. Akkerman, "Prediction of the yarn trajectories on complex braided preforms," *Composites Part A: Applied Science and Manufacturing,* Article vol. 33, no. 8, pp. 1073-1081, 2002, doi: 10.1016/S1359-835X(02)00075-1.

[10] A. Gessler, "Braided reinforcements for composites," in *Composite Reinforcements for Optimum Performance*, 2011, pp. 116-156.

[11] Y. Kyosev, "Braiding Machine Components," in *Braiding Technology for Textiles*: Woodhead Publishing, 2015, ch. 6, pp. 113-150.

[12] W. A. Douglass, *Braiding and Braiding Machinery*. Centrex Publishing Company; Cleaver-Hume Press, 1964.

[13] Y. Kyosev, "Carriers for Braiding Machines," in *Braiding Technology for Textiles*: Woodhead Publishing, 2015, ch. 7, pp. 153-175.

[14] G. Ma, D. J. Branscomb, and D. G. Beale, "Modeling of the tensioning system on a braiding machine carrier," *Mechanism and Machine Theory,* Article vol. 47, no. 1, pp. 46-61, 2012, doi: 10.1016/j.mechmachtheory.2011.08.008.

[15] Y. Kyosev, "Yarn Winding Operations in Braiding," in *Braiding Technology for Textiles*: Woodhead Publishing, 2015, ch. 10, pp. 231-254.

[16] "Semi automatic bobbin winding machine SP 280 Eco." Herzog. https://herzog-online.com/bobbin-winding-machines/ (accessed 23/09/23, 2023).

[17] C. Ebel and T. Hans, "Interaction of braiding ring geometry and fiber lay-up in the braiding process," ed: Inistitue for Carbon Composites, 2014.
[18] A. A. Head, J. W. Peter, and T. C. Story, "Forming Ring with Adjustable Diameter for Braid Production and Method of Braid Production," USA Patent Appl. US 6.679,152 B1, 2004.
[19] Y. Kyosev, *Recent Developments in Braiding and Narrow Weaving*, 1st ed. Cham, SWITZERLAND: Springer, 2016.
[20] V. Reimer, A. S. Dyagilev, and T. Gries, "Effect of Vibration Mechanism Operating Conditions on the Structure of a Braided Preform," *Fibre Chemistry,* journal article vol. 49, no. 5, pp. 330-333, January 01 2018, doi: 10.1007/s10692-018-9892-4.
[21] A. Gessler, "5 - Braided reinforcements for composites," in *Composite Reinforcements for Optimum Performance*, P. Boisse Ed.: Woodhead Publishing, 2011, pp. 116-156.
[22] Y. Kyosev, "Patterning of Bradied Products," in *Braiding Technology for Textiles*: Woodhead Publishing, 2015, ch. 2, pp. 27-46.
[23] T. Sontag, H. Yang, T. Gries, and F. Ko, "Recent advances in 3D braiding technology," in *Advances in 3D Textiles*, 2015, pp. 153-181.
[24] G. Némoz, L. Dréano, and D. Bigaud, "3D braided preforms for shaped composite material," in *European Space Agency, (Special Publication) ESA SP*, 2005, 581 ed., pp. 259-264.
[25] G. Grave, K. Birkefeld, T. V. Reden, K. Drechsler, Y. Kyosev, and A. Rathjens, "Simulation of 3D Overbraiding - Solutions and Challenges," presented at the Second World Conference on 3D Fabrics and their Application, Greenville, 2009.
[26] G. Guyader, A. Gabor, and P. Hamelin, "Analysis of 2D and 3D circular braiding processes: Modeling the interaction between the process parameters and the pre-form architecture," *Mechanism and Machine Theory,* vol. 69, pp. 90-104, 2013/11/01/ 2013, doi: https://doi.org/10.1016/j.mechmachtheory.2013.04.015.
[27] K. Birkefeld, M. Röder, T. Von Reden, M. Bulat, and K. Drechsler, "Characterization of biaxial and triaxial braids: Fiber architecture and mechanical properties," *Applied Composite Materials,* Article vol. 19, no. 3-4, pp. 259-273, 2012, doi: 10.1007/s10443-011-9190-2.
[28] M. Wolfahrt, G. Printer, S. Zaremba, T. V. Reden, and C. Edel, "Effect of preform architecture on the mechanical and fatigue behavior of braided composites for generating design allowables," presented at the 30th International Jubilee Conference of SAMPE Europe, Paris, 2009.
[29] D. Liu *et al.*, "Estimating the elastic modulus of unidirectional over-braided multilayer composites," *Textile Research Journal,* vol. 92, no. 13-14, pp. 2410-2423, doi: 10.1177/00405175221080702.
[30] P. Middendorf, B. V. D. Broucke, A. Gebler, F. Maidl, and C. Metzner, "14. Material Characterization of Non-Crimp Braided CFRP for Aeronautic Applications.," in *Recent Advances in Textile Composites - Proceedings of the 9th International Conference on Textile Composites: (TEXCOMP9)*, 2008.
[31] C. Metzner, A. Gessler, C. Weimer, U. Beier, and P. Middendorf, *Performance assessments on unidirectional braided CFRP materials*. 2014.

[32] G. W. Du and P. Popper, "Analysis of a circular braiding process for complex shapes," *Journal of the Textile Institute,* Article vol. 85, no. 3, pp. 316-337, 1994, doi: 10.1080/00405009408631277.

[33] P. Potluri, A. Rawal, M. Rivaldi, and I. Porat, "Geometrical modelling and control of a triaxial braiding machine for producing 3D preforms," *Composites Part A: Applied Science and Manufacturing,* vol. 34, no. 6, pp. 481-492, 2003/06/01/ 2003, doi: https://doi.org/10.1016/S1359-835X(03)00061-7.

[34] *BS ISO 10122:2014 - Reinforcement materials. Tubular braided sleeves. Basis for a specification*. 2014.

[35] C. A. Schneider, W. S. Rasband, and K. W. Eliceiri, "NIH Image to ImageJ: 25 years of image analysis," *Nature Methods,* vol. 9, no. 7, pp. 671-675, 2012/07/01 2012, doi: 10.1038/nmeth.2089.

[36] *Image Porcessing Toolbox version: 11.6 (R2022b)*. (2018). The MathWorks Inc. [Online]. Available: https://www.mathworks.com

[37] P. Monnot, J. Lévesque, and L. Laberge Lebel, "Automated braiding of a complex aircraft fuselage frame using a non-circular braiding model," *Composites Part A: Applied Science and Manufacturing,* vol. 102, pp. 48-63, 2017/11/01/ 2017, doi: https://doi.org/10.1016/j.compositesa.2017.07.011.

[38] M. Pipan, A. Kos, and N. Herakovic, "Adaptive Algorithum for the Quality Control of Braiding Sleeving," *Advances in Mechanical Engineering,* vol. 2014, 2014, doi: https://journals.sagepub.com/doi/10.1155/2014/812060.

[39] A. J. Hunt and J. P. Carey, "A machine vision system for the braid angle measurement of tubular braided structures," *Textile Research Journal,* vol. 89, no. 14, pp. 2919-2937, 2019, doi: https://doi.org/10.1177/0040517518803792.

[40] S. Zambal, W. Palfinger, M. Stöger, and C. Eitzinger, "Accurate fibre orientation measurement for carbon fibre surfaces," *Pattern Recognition,* vol. 48, no. 11, pp. 3324-3332, 2015/11/01/ 2015, doi: https://doi.org/10.1016/j.patcog.2014.11.009.

[41] J. H. Van Ravenhorst, "Design Tools for Circular Overbraiding of Complex Mandrels," Degree of Doctor Dissertation, University of Twente, 2018.

[42] S. Chen and N. A. Warrior, "An Innovative Approach to Manufacturing Closed-Section Composite Profiles," 2019. [Online]. Available: https://cimcomp.ac.uk/research/an-innovative-approach-to-manufacturing-closed-section-composite-profiles/.

[43] A. Torun, G. Hoffmann, A. Mountasir, and C. Cherif, "Effect of Twisting on Mechanical Properties of GF/PP Commingled Hybrid Yarns and UD-Composites," *Journal of Applied Polymer Science,* vol. 123, pp. 246-256, 01/05 2012, doi: 10.1002/app.34458.

[44] B. K. Cheung and J. P. Carey, "Improving two-dimensional braided composite tensile properties by including low angle yarn twist: Production, experimental verification, and modeling," *Journal of Engineered Fibers and Fabrics,* vol. 15, 2020, doi: 10.1177/1558925020946449.

[45] D. Brunnschweiler, "The Structure and Tensile Properties of Braids," *Journal of the Textile Institute Transactions,* vol. 45, no. 1, pp. T55-T77, 1954/01/01 1954, doi: 10.1080/19447025408662631.

[46] C. C. Chamis, "Mechanics of Composite Materials: Past, Present and Future," *Journal of Composites Technology & Research,* vol. 11, pp. 3-14, 1989.
[47] Z.-M. Huang, "Micromechanical Failure Analysis of Unidirectional Composites," *Failure Analysis,* 2018, doi: 10.5772/intechopen.80807.
[48] D. Zhang, L. Chen, Y. Sun, Y. Zhang, and K. Qian, "Multi-Scale Modeling of an Integrated 3D Braided Composite with Applications to Helicopter Arm," *Applied Composite Materials,* Article vol. 24, no. 5, pp. 1233-1250, 2017, doi: 10.1007/s10443-017-9584-x.
[49] X. Li, W. K. Binienda, and R. K. Goldberg, "Finite-Element Model for Failure Study of Two-Dimensional Triaxially Braided Composite," *Journal of Aerospace Engineering,* vol. 24, no. 2, pp. 170-180, 2011, doi: doi:10.1061/(ASCE)AS.1943-5525.0000029.
[50] T. Wehrkamp-Richter, N. V. De Carvalho, and S. T. Pinho, "Predicting the non-linear mechanical response of triaxial braided composites," *Composites Part A: Applied Science and Manufacturing,* vol. 114, pp. 117-135, 2018/11/01/ 2018, doi: https://doi.org/10.1016/j.compositesa.2018.08.011.
[51] L. Xu, C. Z. Jin, and S. K. Ha, "Ultimate strength prediction of braided textile composites using a multi-scale approach," *Journal of Composite Materials,* vol. 49, no. 4, pp. 477-494, 2015, doi: 10.1177/0021998314521062.
[52] J. Sun, G. Zhou, C. Zhou, and X. Wang, "In-plane shear investigation of 3D surface-core braided composites," *Composites Science and Technology,* vol. 135, pp. 54-66, 2016/10/27/ 2016, doi: https://doi.org/10.1016/j.compscitech.2016.09.011.
[53] Y. Ren, S. Zhang, H. Jiang, and J. Xiang, "Meso-Scale Progressive Damage Behavior Characterization of Triaxial Braided Composites under Quasi-Static Tensile Load," *Applied Composite Materials,* Article vol. 25, no. 2, pp. 335-352, 2018, doi: 10.1007/s10443-017-9623-7.
[54] C. Zhang, W. K. Binienda, R. K. Goldberg, and L. W. Kohlman, "Meso-scale failure modeling of single layer triaxial braided composite using finite element method," *Composites Part A: Applied Science and Manufacturing,* vol. 58, pp. 36-46, 2014/03/01/ 2014, doi: https://doi.org/10.1016/j.compositesa.2013.11.009.
[55] X. Xiao, H. G. Kia, and X. J. Gong, "Strength prediction of a triaxially braided composite," *Composites Part A: Applied Science and Manufacturing,* Article vol. 42, no. 8, pp. 1000-1006, 2011, doi: 10.1016/j.compositesa.2011.04.003.
[56] W. K. Binienda and X. Li, "Mesomechanical Model for Numerical Study of Two-Dimensional Triaxially Braided Composite," *Journal of Engineering Mechanics,* vol. 136, no. 11, pp. 1366-1379, 2010, doi: 10.1061/(ASCE)EM.1943-7889.0000181.
[57] B. Dauda, S. O. Oyadiji, and P. Potluri, "Characterising Mechanical Properties of Braided and Woven Textile Composite Beams," *Applied Composite Materials,* journal article vol. 16, no. 1, pp. 15-31, February 01 2009, doi: 10.1007/s10443-008-9073-3.
[58] T. J. Reinhart and A. I. H. Committee, *Engineered Materials Handbook: Composites*. ASM International, 1987.

[59] G.-W. Du and F. K. Ko, "Analysis and Design of 2D Braided Preforms for Composite Reinforcement," presented at the 9th International Conference on Composite Materials - Composite Design, Madrid, Spain, 1993.

[60] Q. Zhang, D. Beale, and R. M. Broughton, "Analysis of circular braiding process, part 1: Theoretical investigation of kinematics of the circular braiding process," *Journal of Manufacturing Science and Engineering, Transactions of the ASME,* Article vol. 121, no. 3, pp. 345-350, 1999, doi: 10.1115/1.2832687.

[61] Q. Zhang, D. Beale, R. M. Broughton, and S. Adanur, "Analysis of circular braiding process, part 2: Mechanics analysis of the circular braiding process and experiment," *Journal of Manufacturing Science and Engineering, Transactions of the ASME,* Article vol. 121, no. 3, pp. 351-359, 1999, doi: 10.1115/1.2832688.

[62] J. H. Van Ravenhorst and R. Akkerman, "A yarn interaction model for circular braiding," *Composites Part A: Applied Science and Manufacturing,* Article vol. 81, pp. 254-263, 2016, doi: 10.1016/j.compositesa.2015.11.026.

[63] J. Hajrasouliha, R. J. Nedoushan, M. Sheikhzadeh, W. Na, and W.-R. Yu, "Theoretical and experimental study of braid pattern in mandrels with arbitrary cross-sections," *Journal of Composite Materials,* vol. 52, no. 29, pp. 4009-4022, doi: 10.1177/0021998318773460.

[64] A. K. Pickett, J. Sirtautas, and A. Erber, "Braiding simulation and prediction of mechanical properties," *Applied Composite Materials,* Article vol. 16, no. 6, pp. 345-364, 2009, doi: 10.1007/s10443-009-9102-x.

[65] T. Hans, J. Cichosz, M. Brand, and R. Hinterhölzl, "Finite element simulation of the braiding process for arbitrary mandrel shapes," *Composites Part A: Applied Science and Manufacturing,* vol. 77, pp. 124-132, 2015/10/01/ 2015, doi: https://doi.org/10.1016/j.compositesa.2015.06.003.

[66] J. H. Van Ravenhorst. "BraidSim Virtual Braiding." https://www.braidsim.com/ (accessed 31/10/2018, 2018).

[67] Y. Wang and X. Sun, "Digital-element simulation of textile processes," *Composites Science and Technology,* vol. 61, no. 2, pp. 311-319, 2001/02/01/ 2001, doi: https://doi.org/10.1016/S0266-3538(00)00223-2.

[68] G. Zhou, X. Sun, and Y. Wang, "Multi-chain digital element analysis in textile mechanics," *Composites Science and Technology,* vol. 64, no. 2, pp. 239-244, 2004/02/01/ 2004, doi: https://doi.org/10.1016/S0266-3538(03)00258-6.

[69] A. J. Thompson, B. El Said, J. P. H. Belnoue, and S. R. Hallett, "Modelling process induced deformations in 0/90 non-crimp fabrics at the meso-scale," *Composites Science and Technology,* vol. 168, pp. 104-110, 2018/11/10/ 2018, doi: https://doi.org/10.1016/j.compscitech.2018.08.029.

[70] S. Joglekar and M. Pankow, "Modeling of 3D woven composites using the digital element approach for accurate prediction of kinking under compressive loads," *Composite Structures,* vol. 160, pp. 547-559, 2017/01/15/ 2017, doi: https://doi.org/10.1016/j.compstruct.2016.10.070.

[71] X. Sun, J. P.-H. Belnoue, A. Thompson, B. E. Said, and S. R. Hallett, "Dry Textile Forming Simulations: A Benchmarking Exercise," (in English), *Frontiers in Materials,* Original Research vol. 9, 2022-March-16 2022, doi: 10.3389/fmats.2022.831820.

[72] "CATIA Composite Braiding Designer (CBA)." https://cloud.academy.3ds.com/r2017x/role_cba.html (accessed 11/05/2021, 2021).
[73] G. Melanka. "Braid CAM Software Download." https://github.com/ElsevierSoftwareX/SOFTX-D-17-00056 (accessed 28/11/2018.
[74] G. W. Melenka and J. P. Carey, "Braid CAM: Braided composite analytical model," *SoftwareX,* Article vol. 7, pp. 23-27, 2018, doi: 10.1016/j.softx.2017.12.004.
[75] G. W. Melenka and J. P. Carey, "Development of a generalized analytical model for tubular braided-architecture composites," *Journal of Composite Materials,* Article vol. 51, no. 28, pp. 3861-3875, 2017, doi: 10.1177/0021998317695421.
[76] G. W. Melenka and J. P. Carey, "Experimental analysis of diamond and regular tubular braided composites using three-dimensional digital image correlation," *Journal of Composite Materials,* vol. 51, no. 28, pp. 3887-3907, 2017, doi: 10.1177/0021998317695418.
[77] *TexMind Braider*. (2018). [Online]. Available: http://texmind.com/wp/products/braider/
[78] F. Ning, P. Potluri, W. Yu, and J. Hearle, "Geometrical modeling of tubular braided structures using generalized rose curve," *Textile Research Journal,* Article vol. 87, no. 4, pp. 474-486, 2017, doi: 10.1177/0040517516632471.
[79] *Braided Composite Design App*. (2017). Google Play Store. [Online]. Available: https://play.google.com/store/apps/details?id=org.braidedcompositedesign.braidedcompositedesign&hl=en_GB
[80] J. P. Carey, *Handbook of advances in braided composite materials : theory, production, testing and applications / edited by Jason P. Carey*. Cambridge: Woodhead Publishing, 2017.
[81] *WiseTex Suite*. Composite Materials Group - CMG. [Online]. Available: https://www.mtm.kuleuven.be/Onderzoek/Composites/software/wisetex
[82] M. Sherburn, "Geometric and Mechanical Modelling of Textiles," Doctor of Philosophy PhD Thesis, University of Nottingham, 2007.
[83] *louisepb/TexGen: TexGen v3.12.2*. (2021). Zenodo. [Online]. Available: https://doi.org/10.5281/zenodo.4598477
[84] S. Li and A. Wongsto, "Unit cells for micromechanical analyses of particle-reinforced composites," *Mechanics of Materials,* vol. 36, no. 7, pp. 543-572, 2004/07/01/ 2004, doi: https://doi.org/10.1016/S0167-6636(03)00062-0.
[85] S. R. Swanson and L. V. Smith, "Comparison of the biaxial strength properties of braided and laminated carbon fiber composites," *Composites Part B: Engineering,* vol. 27, no. 1, pp. 71-77, 1996/01/01/ 1996, doi: https://doi.org/10.1016/1359-8368(95)00008-9.
[86] P. J. Falzon and I. Herszberg, "Mechanical performance of 2-D braided carbon/epoxy composites," *Composites Science and Technology,* vol. 58, no. 2, pp. 253-265, 1998/01/01/ 1998, doi: https://doi.org/10.1016/S0266-3538(97)00133-4.
[87] F. Heieck, F. Hermann, P. Middendorf, and K. Schladitz, "Influence of the cover factor of 2D biaxial and triaxial braided carbon composites on their in-plane

mechanical properties," *Composite Structures,* vol. 163, pp. 114-122, 2017/03/01/ 2017, doi: https://doi.org/10.1016/j.compstruct.2016.12.025.

[88] K. M. Charlebois, R. Boukhili, O. Zebdi, F. Trochu, and A. Gasmi, "Evaluation of the Physical and Mechanical Properties of Braided Fabrics and their Composites," *Journal of Reinforced Plastics and Composites,* vol. 24, no. 14, pp. 1539-1554, 2005, doi: 10.1177/0731684405050391.

[89] P. Potluri, A. Manan, M. Francke, and R. J. Day, "Flexural and torsional behaviour of biaxial and triaxial braided composite structures," *Composite Structures,* vol. 75, no. 1, pp. 377-386, 2006/09/01/ 2006, doi: https://doi.org/10.1016/j.compstruct.2006.04.046.

[90] Z. T. Kier, A. Salvi, G. Theis, A. M. Waas, and K. Shahwan, "Estimating mechanical properties of 2D triaxially braided textile composites based on microstructure properties," *Composites Part B: Engineering,* vol. 68, pp. 288-299, 2015/01/01 2015, doi: https://doi.org/10.1016/j.compositesb.2014.08.039.

[91] S. C. Quek, A. M. Waas, K. W. Shahwan, and V. Agaram, "Analysis of 2D triaxial flat braided textile composites," *International Journal of Mechanical Sciences,* Article vol. 45, no. 6-7, pp. 1077-1096, 2003, doi: 10.1016/j.ijmecsci.2003.09.003.

[92] A. Gurley, D. Beale, R. Broughton, and D. Branscomb, "The design of optimal lattice structures manufactured by maypole braiding," *Journal of Mechanical Design, Transactions of the ASME,* Article vol. 137, no. 10, 2015, Art no. 101401, doi: 10.1115/1.4031122.

[93] X. G. Yu and J. Z. Cui, "The prediction on mechanical properties of 4-step braided composites via two-scale method," *Composites Science and Technology,* Article vol. 67, no. 3-4, pp. 471-480, 2007, doi: 10.1016/j.compscitech.2006.08.028.

[94] A. Miravete *et al.*, "3D mesomechanical analysis of three-axial braided composite materials," *Composites Science and Technology,* vol. 66, no. 15, pp. 2954-2964, 2006/12/01 2006, doi: https://doi.org/10.1016/j.compscitech.2006.02.015.

[95] S. C. Quek, A. Waas, K. W. Shahwan, and V. Agaram, "Compressive response and failure of braided textile composites: Part 2—computations," *International Journal of Non-Linear Mechanics,* vol. 39, no. 4, pp. 649-663, 2004/06/01/ 2004, doi: https://doi.org/10.1016/S0020-7462(03)00019-2.

[96] C. Wang *et al.*, "Strength prediction for bi-axial braided composites by a multi-scale modelling approach," *Journal of Materials Science,* vol. 51, no. 12, pp. 6002-6018, 2016/06/01 2016, doi: 10.1007/s10853-016-9901-z.

[97] "KUKA KR C2 Edition05 Operating Instructions ", ed: KUKA, 2007.

[98] Eurocarbon. "Overbraiding " Eurocarbon. https://www.eurocarbon.com/composite-reinforcement/overbraiding-and-turn-key-solutions/ (accessed 30/03/23, 2023).

[99] G. M. Vélez-García, P. Wapperom, V. Kunc, D. G. Baird, and A. Zink-Sharp, "Sample preparation and image acquisition using optical-reflective microscopy in the measurement of fiber orientation in thermoplastic composites," *Journal of Microscopy,* Article vol. 248, no. 1, pp. 23-33, 2012, doi: 10.1111/j.1365-2818.2012.03646.x.

[100] G. Bradski, "The OpenCV Library," *Dr. Dobb's Journal of Software Tools,* 2000.
[101] M. Bulat, H. Ahlborn, F. Gnädinger, and D. Michaelis, "15 - Braided carbon fiber composites," in *Advances in Braiding Technology*, Y. Kyosev Ed.: Woodhead Publishing, 2016, pp. 383-394.
[102] R. Plonka, E. Mäder, S. L. Gao, C. Bellmann, V. Dutschk, and S. Zhandarov, "Adhesion of epoxy/glass fibre composites influenced by aging effects on sizings," *Composites Part A: Applied Science and Manufacturing,* vol. 35, no. 10, pp. 1207-1216, 2004/10/01 2004, doi: https://doi.org/10.1016/j.compositesa.2004.03.005.
[103] B. Lee, K. H. Leong, and I. Herszberg, "Effect of Weaving on the Tensile Properties of Carbon Fibre Tows and Woven Composites," *Journal of Reinforced Plastics and Composites,* vol. 20, no. 8, pp. 652-670, 2001, doi: 10.1177/073168401772679011.
[104] E. Archer, S. Buchanan, A. McIlhagger, and J. Quinn, "The effect of 3D weaving and consolidation on carbon fiber tows, fabrics, and composites," *Journal of Reinforced Plastics and Composites,* vol. 29, no. 20, pp. 3162-3170, 2010, doi: 10.1177/0731684410371405.
[105] C. Ebel, A. Mierzwa, and K. Kind, "13 - Yarn damage during braiding of reinforcement fibers for composites," in *Advances in Braiding Technology*, Y. Kyosev Ed.: Woodhead Publishing, 2016, pp. 319-354.
[106] A. Mierzwa, C. Ebel, and K. Drechsler, "Influence of yarn gaps on the mechanical performance of braided carbon fiber reinforced plastics," *Zeitschrift Kunststofftechnik/Journal of Plastics Technology,* vol. 2018, pp. 146-173, 01/01 2018, doi: 10.3139/O999.02022018.
[107] C. Ayranci and J. P. Carey, "Effect of diameter in predicting the elastic properties of 2D braided tubular composites," *Journal of Composite Materials,* Article vol. 44, no. 16, pp. 2031-2044, 2010, doi: 10.1177/0021998310369599.
[108] H. Thandaga Nagaraju, B. V. Sankar, G. Subhash, N. H. Kim, and R. T. Haftka, "Effect of curvature on extensional stiffness matrix of 2-D braided composite tubes," *Composites Part A: Applied Science and Manufacturing,* vol. 147, p. 106422, 2021/08/01 2021, doi: https://doi.org/10.1016/j.compositesa.2021.106422.
[109] R. Czichos, O. Bareiro, A. K. Pickett, P. Middendorf, and T. Gries, "Experimental and numerical studies of process variabilities in biaxial carbon fiber braids," *International Journal of Material Forming,* vol. 14, no. 1, pp. 39-54, 2021/01/01 2021, doi: 10.1007/s12289-020-01541-4.
[110] H. Jiang, Y. Ren, Z. Liu, S. Zhang, and G. Yu, "Multi-scale analysis for mechanical properties of fiber bundle and damage characteristics of 2D triaxially braided composite panel under shear loading," *Thin-Walled Structures,* Article vol. 132, pp. 276-286, 2018, doi: 10.1016/j.tws.2018.08.022.
[111] G. Balokas, B. Kriegesmann, S. Czichon, and R. Rolfes, "A variable-fidelity hybrid surrogate approach for quantifying uncertainties in the nonlinear response of braided composites," *Computer Methods in Applied Mechanics and Engineering,* vol. 381, p. 113851, 2021/08/01 2021, doi: https://doi.org/10.1016/j.cma.2021.113851.

[112] S. Li and E. Sitnikova, "Chapter 6 - Formulation of unit cells," in *Representative Volume Elements and Unit Cells*, S. Li and E. Sitnikova Eds.: Woodhead Publishing, 2020, pp. 107-187.
[113] M. Y. Matveev, L. P. Brown, and A. C. Long, "Efficient meshing technique for textile composites unit cells of arbitrary complexity," *Composite Structures,* vol. 254, p. 112757, 2020/12/15 2020, doi: https://doi.org/10.1016/j.compstruct.2020.112757.
[114] A. Thompson, B. Elsaid, D. Ivanov, J. Belnoue, and S. Hallett, "High fidelity modelling of the compression behaviour of 2D woven fabrics," *International Journal of Solids and Structures,* vol. 154, 06/01 2017, doi: 10.1016/j.ijsolstr.2017.06.027.
[115] "HexTow AS4 Carbon Fibre Product Datsheet," ed: Hexcel, 2023.
[116] C. Ayranci and J. P. Carey, "Predicting the longitudinal elastic modulus of braided tubular composites using a curved unit-cell geometry," *Composites Part B: Engineering,* vol. 41, no. 3, pp. 229-235, 2010/04/01 2010, doi: https://doi.org/10.1016/j.compositesb.2009.10.006.
[117] Y. Rao and R. J. Farris, "A modeling and experimental study of the influence of twist on the mechanical properties of high-performance fiber yarns," *Journal of Applied Polymer Science,* vol. 77, no. 9, pp. 1938-1949, 2000, doi: https://onlinelibrary.wiley.com/doi/10.1002/1097-4628(20000829)77:9%3C1938::AID-APP9%3E3.0.CO;2-D.
[118] H. K. Dalfi, M. Tausif, and Z. yousaf, "Effect of twist level on the mechanical performance of S-glass yarns and non-crimp cross-ply composites," *Journal of Industrial Textiles,* vol. 51, no. 2, pp. 2921-2943, 2022, doi: 10.1177/1528083720987206.
[119] A. Weinberg and P. Schwartz, "Twist effect on the mechanical behaviour of Kevlar 29/epoxy strands," *Journal of Materials Science Letters - J MATER SCI LETT,* vol. 6, pp. 832-834, 07/01 1987, doi: 10.1007/BF01729028.
[120] S. Goutianos, T. Peijs, B. Nystrom, and M. Skrifvars, "Development of Flax Fibre based Textile Reinforcements for Composite Applications," *Applied Composite Materials,* vol. 13, no. 4, pp. 199-215, 2006/07/01 2006, doi: 10.1007/s10443-006-9010-2.
[121] N. K. Naik and R. Kuchibhotla, "Analytical study of strength and failure behaviour of plain weave fabric composites made of twisted yarns," *Composites Part A: Applied Science and Manufacturing,* vol. 33, no. 5, pp. 697-708, 2002/05/01/ 2002, doi: https://doi.org/10.1016/S1359-835X(02)00012-X.
[122] M. Wolfahrt, J. Grosser, M. Fleischmann, and M. Schubert, "Characterization of the Mechanical and Fatigue Behavior of Braided Composites Made of Twisted Yarns," *Materials Science Forum,* vol. 825-826, pp. 876-882, 2015, doi: 10.4028/www.scientific.net/MSF.825-826.876.
[123] "Product Datasheet - Tenax HTS40 ", ed: Teijin Carbon, 2020.
[124] "EPIKOTETM Resin MGS RIMR035c Datasheet," ed: Westlake Epox, 2022.
[125] *BS EN ISO 527-4:2021 Plastics. Determination of tensile properties. Test conditions for isotropic and orthotropic fibre-reinforced plastic composites*, B. S. Institution, London, 2021.
[126] "Autograph AGS-X Series Datasheet," ed: Shimadzu.

[127] *BS EN ISO 527-1:2019 Plastics. Determination of tensile properties. General principles*, B. S. Institute, London, 2019.
[128] S. Huang, Q. Fu, L. Yan, and B. Kasal, "Characterization of interfacial properties between fibre and polymer matrix in composite materials – A critical review," *Journal of Materials Research and Technology,* vol. 13, pp. 1441-1484, 2021/07/01/ 2021, doi: https://doi.org/10.1016/j.jmrt.2021.05.076.
[129] N. S. Nobeen *et al.*, "Constituent materials micro-damage modeling in predicting progressive failure of braided fiber composites," *Composite Structures,* vol. 145, pp. 194-202, 2016/06/10/ 2016, doi: https://doi.org/10.1016/j.compstruct.2016.02.078.
[130] S. Song, A. M. Waas, K. W. Shahwan, X. Xiao, and O. Faruque, "Braided textile composites under compressive loads: Modeling the response, strength and degradation," *Composites Science and Technology,* Article vol. 67, no. 15-16, pp. 3059-3070, 2007, doi: 10.1016/j.compscitech.2007.06.008.
[131] G. Al Kassem and D. Weichert, "Micromechanical material models for polymer composites through advanced numerical simulation techniques," *PAMM,* vol. 9, no. 1, pp. 413-414, 2009, doi: https://doi.org/10.1002/pamm.200910180.
[132] Z. Hashin, "Failure Criteria for Unidirectional Fiber Composites," *Journal of Applied Mechanics,* vol. 47, no. 2, pp. 329-334, 1980, doi: 10.1115/1.3153664.
[133] S. W. Tsai and E. M. Wu, "A General Theory of Strength for Anisotropic Materials," *Journal of Composite Materials,* vol. 5, no. 1, pp. 58-80, 1971, doi: 10.1177/002199837100500106.
[134] I. M. Daniel, J.-J. Luo, and P. M. Schubel, "Three-dimensional characterization of textile composites," *Composites Part B: Engineering,* vol. 39, no. 1, pp. 13-19, 2008/01/01 2008, doi: https://doi.org/10.1016/j.compositesb.2007.02.002.
[135] G. Fang, B. El Said, D. Ivanov, and S. R. Hallett, "Smoothing artificial stress concentrations in voxel-based models of textile composites," *Composites Part A: Applied Science and Manufacturing,* vol. 80, pp. 270-284, 2016/01/01 2016, doi: https://doi.org/10.1016/j.compositesa.2015.10.025.
[136] B. Grimes, P. Giddings, and N. Warrior, "A computational and experimental analysis of the influence of guide ring size on fibre architecture in the braiding process," presented at the International Conference on Manufacturing of Advanced Composites, Online, 2021.
[137] A. Pickett, A. Erber, T. Von Reden, and K. Drechsler, "Comparison of analytical and finite element simulation of 2D braiding," *Plastics, Rubber and Composites,* Conference Paper vol. 38, no. 9-10, pp. 387-395, 2009, doi: 10.1179/146580109X12540995045769.
[138] A. Fouladi and R. Jafari Nedoushan, "Prediction and optimization of yarn path in braiding of mandrels with flat faces," *Journal of Composite Materials,* vol. 52, no. 5, pp. 581-592, 2018, doi: 10.1177/0021998317710812.
[139] T. M. Inc., "Smoothdata - Matlab Documentation," ed. Mathworks 2022.
[140] S. S. Roy and P. Potluri, "7 - Braiding and filament winding," in *Design and Manufacture of Structural Composites*, L. Harper and M. Clifford Eds.: Woodhead Publishing, 2023, pp. 145-187.

[141] M. Thompson, K. Rengaraj, L. Brown, and N. Warrior, "TexGen - Geometrical Modelling of Biaxial Braided Fabrics," presented at the ECCM20 - The 20th European Conference on Composite Materials, Lausanne, 2022.
[142] B. Grimes, M. Thompson, P. Giddings, and N. Warrior, "Braiding Characterisation and Optimisation: Complex Geometries," presented at the ECCM20 - The 20th European Conference on Composite Materials, Lausanne, 2022.
[143] M. Thompson, B. Grimes, K. Rengaraj, and N. Warrior, "Effect of Winding Twist on Multilayer Braided Composites," presented at the ACM5 2022, Bristol, UK, April 2022, 2022.